NOCTURNAL MEASUREMENTS OF HONO, NO_2 AND NO_3 BY DIFFERENTIAL OPTICAL ABSORPTION SPECTROSCOPY IN POLLUTED MARINE AND URBAN ATMOSPHERES

PATRYK RAJMUND WOJTAL

A DISSERTATION SUBMITTED TO THE FACULTY OF GRADUATE STUDIES
IN PARTIAL FULFILMENT OF THE REQUIREMENTS
FOR THE DEGREE OF

DOCTOR OF PHILOSOPHY

GRADUATE PROGRAM IN CHEMISTRY
YORK UNIVERSITY
TORONTO, ONTARIO
DECEMBER 2013

NOCTURNAL MEASUREMENTS OF HONO, NO_2 AND NO_3 BY DIFFERENTIAL OPTICAL ABSORPTION SPECTROSCOPY IN POLLUTED MARINE AND URBAN ATMOSPHERES

by **Patryk Rajmund Wojtal**

Examination Committee Members:

1. Dr. Robert McLaren
2. Dr. Geoffrey Harris
3. Dr. Donald Hastie
4. Dr. Jennifer G. Murphy
5. Dr. Peter A. Taylor

Abstract

Nitrogen oxides are ubiquitous throughout the lower atmosphere and significantly affect the chemistry of the atmosphere, air quality, and climate. A data set obtained using differential optical absorption spectroscopy (DOAS) was analyzed in order to quantify the NO_3, HONO and NO_2 concentrations at Saturna Island, and concentrations of N_2O_5 were calculated. Nocturnal measurements of NO_3, NO_2 and HONO were also performed using active-DOAS at York University.

A method for calculating the lifetimes of NO_3 without assuming a steady-state approximation was determined and non steady-state lifetimes of NO_3 were calculated for both studies. The direct (via NO_3) and indirect (via N_2O_5) rate loss constants of NO_3 from the combined nocturnal reservoir (NO_3+N_2O_5) were determined as a function of time of night. Measurements of HONO over the polluted open ocean were performed for the first time. Rapidly established steady-states of HONO were observed, persisting throughout the night until sunrise. During the steady-state period ($d[\mathrm{HONO}]/dt \approx 0$), HONO was independent of the air mass source and NO_2, leading to a zero-order HONO formation with respect to NO_2, contrary to expectations. Potential reservoirs of HONO were explored and a conceptual model for

HONO formation over aqueous surfaces was hypothesized. Subsequently, nocturnal measurements of HONO in the urban area were made at York University for a total of 242 nights. This urban data set showed two types of HONO behavior. Firstly, a steady-state behavior was clearly observed for a subset of the data-set, similar to that observed in the aqueous environment at Saturna. Secondly, HONO concentrations were observed to highly correlate with NO_2 for another subset of the data-set ($d([\mathrm{HONO}]/[\mathrm{NO_2}])/dt \approx 0$), showing evidence of first-order behavior as expected for the accepted heterogeneous NO_2 hydrolysis mechanism of HONO formation ($2NO_2 + H_2O \rightarrow HONO + HNO_3$). Steady-states of HONO were observed during atmospherically unstable nights, while HONO was strongly correlated with NO_2 during stable nights. It was discovered that the main parameters distinguishing these two types of behavior were atmospheric stability and NO_2 concentration.

Acknowledgements

This work would not be possible without the assistance and support of many individuals throughout the years. First and foremost, I would like to acknowledge my supervisor, Dr. Robert McLaren. His patience, encouragement, endless ideas, and scientific discussions have greatly shaped this thesis and provided me with an excellent scientific role model. I would also like to thank my graduate committee members, Dr. Michael Mozurkewich and Dr. Geoffrey Harris who have given me great guidance and helped give structure to my projects. I would also like to thank my external examiner Dr. Jennifer Murphy, my internal examiner Dr. Peter Taylor and defense committee member Dr. Donald Hastie for taking the time to read my thesis and for providing feedback. I am especially thankful to Dr. Peter Taylor for providing meteorological measurements at York University which greatly augmented the presented analysis.

I would also like to thank the current and previous group members which I have worked with over the years, especially Jamie Halla and Ibraheem Nuaaman for the exchange of ideas and scientific discussions. I am grateful for being able to be a part of the Center for Atmospheric Chemistry (CAC) at York University which has a wonderful group of closely knit researchers and graduate students. Special thanks to Carol Weldon for taking care of the administrative side of the research.

Above all, I would like to thank my family which has allowed me to get to where I am and have always supported me unquestionably. Very special thanks to my beautiful wife, Caroline Guimarães whose love and support have made this experience so much more enjoyable and brightened up every day. I would also like to thank Caroline Guimarães and Dr. Robert McLaren for carefully editing my thesis and providing outstanding feedback.

Table of Contents

List of Tables

List of Figures

Abbreviations

a.g.l. -above ground level

a.s.l. - above sea level

BL - Boundary Layer

CAPMon - Canadian Air and Precipitation Monitoring Network

CFCs - ChloroFluoroCarbons

DC - Dark Current

DOAS - Differential Optical Absorption Spectroscopy

DOASIS - DOAS Intelligent System

DMS - DiMethyl Sulphide

EC - Environment Canada

EDT - Eastern Daylight Time

EMOS - Earth and space science and engineering Meteorological Observation Station

FWHM - Full Width Half Maximum

HC - HydroCarbon

LFV - Lower Fraser Valley

LST - Local Standard time

MAX-DOAS - Multi AXis Differential Optical Absorption Spectroscopy

MBL - Marine Boundary Layer

NBL - Nocturnal Boundary Layer

NCAR - National Center for Atmospheric Research

PDT - Pacific Daylight Time

PBL - Planetary Boundary Layer

PM - Particulate Matter

$PM_{2.5}$ - Particulate Matter with aerodynamic diameter up to 2.5 μm

ppb - parts per billion

ppm - parts per million

ppt - parts per trillion

RH - Relative Humidity

SML - Surface Micro-Layer

SNL - Surface Nano-Layer

SCD - Slant Column Density

SZA - Solar Zenith Angle

$\Delta T_{9.5-1}$ - ΔTemperature ($T_{9.5m} - T_{1m}$)

TUV - Tropospheric Ultraviolet and Visible radiative transfer column model

VCD - Vertical Column Density

VOCs - Volatile Organic Compounds

WD - Wind Direction

WS - Wind Speed

1 Introduction

The study of atmospheric chemistry and physics became a scientific discipline in the 18th century, when the first measurements of the composition of the atmosphere were made. Initial measurements focused on the identification and quantification of the major atmospheric constituents such as N_2, O_2, H_2O, CO_2 and the noble gases. Currently, the motivations to study the chemistry and composition of the atmosphere are related to the anthropogenic influences that have led to environmental and health degradation over the past two centuries, coinciding with the industrial revolution. Anthropogenic activity has disrupted the natural balance of the atmosphere's composition and has led to numerous environmental crises, with some of the most severe summarized below:

1. The first reported air pollution events occurred in London, United Kingdom between 1850s − 1950s. The London *smog* events[1] were caused by the widespread burning of sulfur-containing coal for domestic and industrial heating. Under the right conditions, the smoke and sulfur dioxide (SO_2) produced from the burning of coal can combine with fog to create industrial smog. In the presence of a

---

[1] The observation of smoke and fog during these pollution events coined the phenomenon as 'smog'.

low inversion, the dense acidic fog resulted in ∼4,000 deaths in London over a 4-day span. These events reoccurred for nearly 100 years until the necessary technology was developed to allow for the desulfurization of coal and crude oil (Wilkins, 1954; Bell et al., 2004a).

2. Occurrences of a very different type of smog events were reported in the San Joaquin Valley and Los Angeles, USA, in the late 1940s. These photochemical smog events that led to crop damage and severe irritation of the eyes and respiratory tract of both humans and animals were attributed to the enhanced photo-chemical production of ozone (O_3) and carbonyl compounds during sunny days with high temperatures. The O_3 enhancement was caused by the continuous increase of anthropogenic emissions of nitrogen oxides (NO_x), carbon monoxide (CO) and volatile organic compounds (VOCs) (Middleton et al., 1950; Haagen-Smit, 1952).

3. Forest decline and lake acidification in developed countries were observed and found to be linked with increased anthropogenic emissions of nitrogen dioxide (NO_2) and SO_2. Aqueous phase oxidation of NO_2 and SO_2 to nitric acid (HNO_3) and H_2SO_4, respectively, led to the deposition of these acids in various ecosystems as *acid rain* (Likens et al., 1979).

4. The stratospheric *ozone hole* over Antarctica was discovered in 1985 (Farman et al., 1985). The deterioration of the stratospheric ozone layer, which is responsible for the absorption of the majority of the Sun's UV-radiation, was predicted

and attributed to catalyzed O_3-destructing processes initiated by halogenated species (Molina and Rowland, 1974). Extremely stable halogen-containing compounds, chlorofluorocarbons (CFCs), were industrially produced and served as coolants and spray can propellants. These species have a relatively long lifetime, allowing for their transportation to the stratosphere, where the catalytic destruction of O_3 is initiated upon photolysis of CFCs at short wavelengths. Every spring, the ozone column over Antarctica is reduced to less than one third of its unperturbed value. Despite the aggressive global phasing out of CFC production, it was estimated that another three decades are required before normal levels are observed once again (Solomon, 1999).

5. The most recently debated atmospheric phenomenon pertains to the impacts of climate change due to aerosols and greenhouse gases such as CO_2, CH_4, N_2O, O_3 and CFCs. Anthropogenic emissions are believed to have reached a level where an impact on global surface temperatures and on the global water cycle have become very likely. Additional repercussions of climate change include a decrease in the thickness and extent of the Arctic sea ice; risk of significant biodiversity loss due to species extinction in many tropical areas; significant changes in water availability for human consumption, agriculture and energy generation; increased risk of inland flash floods; increased frequency of coastal flooding and erosion from storms and sea level rise; increased frequency, intensity and duration of heat waves in cities in which such phenomenon is currently

experienced, among others. (McCarthy, 2001; IPCC, 2007).

The atmospheric issues outlined above have had a large impact on scientific research, public perception of air pollution, and government regulations. Despite the numerous environmental issues faced to date, many positive results can be attributed to atmospheric research, such as the halt of a planned fleet of supersonic passenger aircraft, predicted to generate substantial loss of stratospheric ozone due to NO_x emissions (Johnston, 1971), the implementation of automobile catalytic converters that has greatly reduced NO_x emissions (Taylor, 1984), the phasing out of lead in gasoline (Lovei, 1998), the Montreal protocol on phasing out the production of numerous CFCs responsible for stratospheric ozone depletion (Penner, 1999), the removal of SO_2 from exhaust flue gases from fossil-fuel power plants (Lefohn et al., 1999) and the ultra-deep desulfurization of refinery streams for ultra-clean (ultra-low-sulfur) gasoline, diesel fuels and jet fuels (Song, 2003).

1.1 Atmospheric Composition and Structure

The Earth's atmosphere consists of a layer of gases enveloping the planet and is essential for its habitability as we know it. The atmosphere has evolved from primarily consisting of H_2O in the earliest stages of the Earth's development, to the current O_2-rich atmosphere. The Earth's biological era was marked by the simultaneous decrease of atmospheric CO_2 and the increase of O_2 due to life processes ~2.0 Ga years ago, leading to the transformation of a previously reducing atmosphere into an oxidative environment (Kasting, 1993). The atmosphere is essential for the protection of lifeforms on Earth, absorbing ultraviolet solar radiation while warming the surface and retaining heat through the greenhouse effect. The major constituents of the current atmosphere are molecular nitrogen (N_2) and oxygen (O_2), comprising >99% of the dry, unpolluted atmosphere. A summary of the atmosphere's major constituents is shown in Table 1.1.

Table 1.1: Main gaseous constituents of the dry, unpolluted atmosphere. The mixing ratio volume (%) of water vapor ranges from 0.001 − 5%.

Gaseous Species	Chemical formula	Mixing ratio (ppmv)	Mixing ratio vol. %
Nitrogen	N_2	7.808×10^5	78.08
Oxygen	O_2	2.095×10^5	20.95
Argon	Ar	9.340×10^3	0.9340
Carbon dioxide	CO_2	394.5	0.03945
Neon	Ne	18.18	0.001818
Helium	He	5.24	0.000524
Methane	CH_4	1.79	0.000179
Krypton	Kr	1.14	0.000114
Xenon	Xe	0.9	0.00009
Hydrogen	H_2	0.5	0.00005
Nitrous oxide	N_2O	0.3	0.00003
Carbon monoxide	CO	0.1	0.00001
Ozone	O_3	0.04	0.000004
Nitrogen dioxide	NO_2	0.001	0.0000001

The structure of the atmosphere is characterized by an exponential decrease of pressure with height and a variation of temperature that delineates the atmosphere into four layers; the troposphere, stratosphere, mesosphere, and thermosphere, as shown in Figure 1.1.

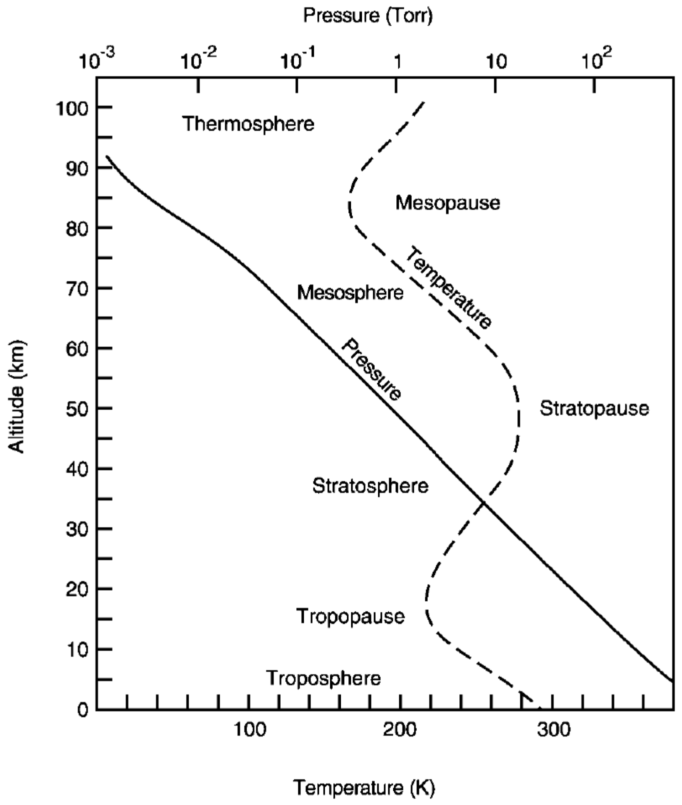

Figure 1.1: Typical variation of temperature and pressure with altitude for a mid-latitude region (Finlayson-Pitts and Pitts Jr, 1999).

The troposphere is the region of the atmosphere closest to the Earth's surface, where most pollutants and their sources are located. The troposphere extends from the ground to heights of ∼10 km for high latitude regions and ∼20 km for equatorial regions. This layer is identified by a vertical temperature decrease of ∼10 °C km^{-1}

and contains ~80% of the total mass of the atmosphere. The stratosphere is located above the troposphere and extends to ~50 km a.s.l. This layer contains the majority of atmospheric O_3, whose absorption of UV-radiation results in an increase of temperature with height. In the mesosphere, the temperature once again decreases with height according to the adiabatic lapse rate (~10 °C km^{-1}). This layer extends from the stratosphere to ~85 km, height which marks the beginning of the thermosphere. The thermosphere extends >85 km a.s.l. and is characterized by an increase in temperature with height due the absorbance of short UV and X-ray radiation by N_2 and O_2.

The planetary boundary layer (PBL) consists of the region of the troposphere which is closest to the surface and directly influenced by emissions on the planet. The typical diurnal variation of the PBL is shown in Figure 1.2. Temperature gradients caused by heat fluxes from the diurnal variance of solar radiation are the driving force of the structure and dynamics of the PBL. Atmospheric turbulence driven by wind shear and convection lead to a well mixed PBL during the daytime. After sunset, radiative cooling occurs and the wind shear remains as the only driving force in the PBL, generally reducing mixing. A residual layer containing the air mass formerly in the convective mixed layer is decoupled from the ground as a shallow stable layer of air forms below. The nocturnal boundary layer is characterized by the formation of a temperature inversion in which warmer buoyant air remains above cooler dense air at the surface. Trace gases can accumulate within the low nocturnal inversion layer, until its subsequent breakup after sunrise and the reformation of a well mixed layer.

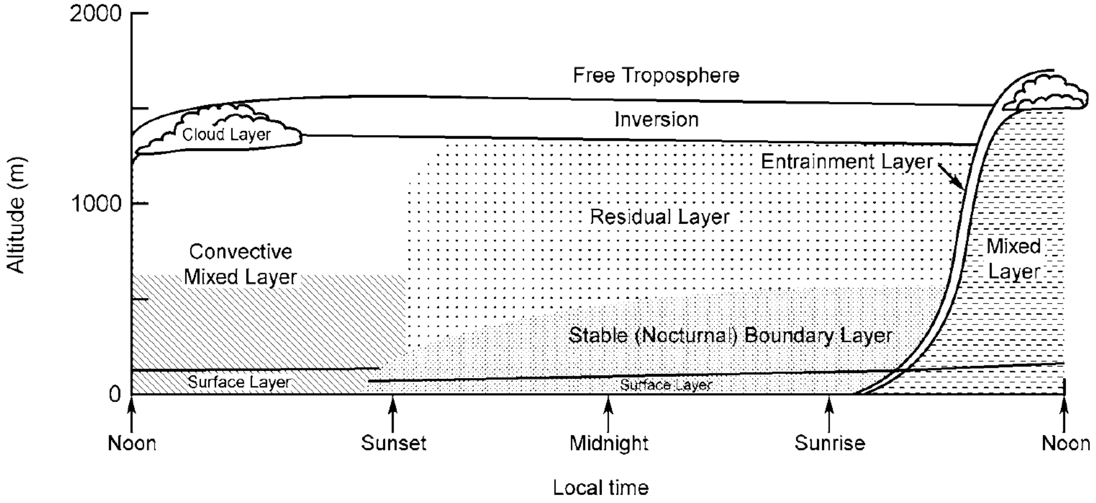

Figure 1.2: Schematic of the diurnal variation and dynamics of the planetary boundary layer (Stull, 1988).

1.2 Chemistry of the Troposphere

1.2.1 Nitrogen Oxides and Ozone

Nitrogen oxides (NO_x), defined as the sum of [NO] + [NO_2], are ubiquitous throughout the lower atmosphere and significantly affect the chemistry of the atmosphere, air quality, and climate (IPCC, 2007). Nitrogen oxides play a leading role in controlling the budget of tropospheric O_3, the abundance of OH-radicals, and the formation of nitrate aerosols.

The most significant species emitted via anthropogenic processes is nitric oxide (NO), produced through the reaction of N_2 and O_2 during high temperature combustion processes, as shown in R 1.1. Similarly, NO_2 is also produced from combustion processes in varying amounts, as shown by R 1.2.

$$\mathrm{N_2 + O_2 \longrightarrow 2\,NO^{\cdot}} \tag{R 1.1}$$

$$\mathrm{N_2 + 2\,O_2 \longrightarrow 2\,NO_2{}^{\cdot}} \tag{R 1.2}$$

The fraction of NO to NO_x emitted is dependent on the conditions, fuel, and type of combustion processes. NO_2 is emitted in smaller amounts, typically less than 10% of the total NO_x production, but can range from $1 - 30\%$ (Lenner, 1987).

Global emissions of NO_x were estimated to be 45.4 TgN yr^{-1} ($\times 10^{12}$ grams yr^{-1}) in 2005 from satellite based measurements and were shown to strongly vary with location and season (Miyazaki et al., 2012). In Canada, anthropogenic NO_x emissions were estimated to be 1.9 TgN yr^{-1} in 2011 and to steadily decrease each year by ~6% since 2003, according to the Canadian national pollutant release inventory. The decline of NO_x emissions in Canada is attributable to a reduction in transportation-related emissions due to the progressive introduction of new technology and cleaner fuels for vehicles. In addition, the observed emission reduction can be accounted by the significant reduction of emissions arising from electricity generation, which resulted from new regulations, as well as domestic and international agreements. The direct anthropogenic sources of NO_x emissions in Canada for 2011 were estimated to be 54.2% from transportation (road, off-road, rail, air and marine), 32.1% from industry, 12.9% from fuel for electricity and heating, and 0.6% from firewood burning, incineration and miscellaneous[2] (EC, 2012).

---

[2] These emissions do not include natural sources such as forest fires, lightning, biogenic emissions nor open sources such as prescribed burning.

The photolysis of NO_2 and the OH-radical catalyzed reactions between NO_x and hydrocarbon radicals are the major sources of anthropogenic O_3 in the troposphere. Tropospheric ozone acts as a greenhouse gas and influences the lifetime of some trace gases due to its oxidative nature. Tropospheric O_3 is also responsible for a variety of adverse health effects such as irritation of the respiratory system, reduction in lung function, aggravation of asthma, damage to the lining of the lungs, and increased susceptibility to respiratory infections and inflammation (Bell et al., 2004b).

The photolysis of NO_2 (λ <420 nm) in the troposphere produces the ground state of atomic oxygen with two unpaired electrons, $O(^3P)$, via the following reaction:

$$\mathrm{NO_2}^{\cdot} + h\nu \longrightarrow \mathrm{NO}^{\cdot} + \mathrm{O}(^3\mathrm{P}) \tag{R 1.3}$$

$O(^3P)$ rapidly reacts with O_2 to form tropospheric O_3 via:

$$\mathrm{O}(^3\mathrm{P}) + \mathrm{O_2} \xrightarrow{\mathrm{M}} \mathrm{O_3} \tag{R 1.4}$$

where a third body ($M = N_2$ or O_2) is required to dissipate the energy of the unstable O_3 molecule.

NO rapidly reacts with O_3 to produce NO_2:

$$\mathrm{NO}^{\cdot} + \mathrm{O_3} \longrightarrow \mathrm{NO_2}^{\cdot} + \mathrm{O_2} \tag{R 1.5}$$

Assuming a typical background level of tropospheric O_3 of 35 ppb and using the rate constant for Reaction R 1.5, $k_{(\mathrm{NO+O_3})} = 1.9 \times 10^{-14}\ \mathrm{cm^3\,molec^{-1}\,s^{-1}}$ at 298 K (Sander et al., 2006), the NO lifetime is estimated to be ~1 minute. In polluted urban environments, the O_3 concentration is frequently “titrated” to 0 ppb by NO during the nighttime, especially for nights during which a shallow and stable nocturnal boundary layer (NBL) is formed. In the absence of a nocturnal inversion, such a depletion may not occur due to dilution of NO into a much larger volume of air.

In the absence of organic compounds, the concentrations of NO, NO_2 and O_3 are in a photo-stationary state during the daytime defined by the Leighton ratio, given by the expression below.

$$\frac{[\mathrm{NO}][\mathrm{O_3}]}{[\mathrm{NO_2}]} = \frac{k_{(\mathrm{NO_2}+h\nu)}}{k_{(\mathrm{NO}+\mathrm{O_3})}} \tag{1.1}$$

Thus, the ratio of NO_2 to NO is given by:

$$\frac{[\mathrm{NO_2}]}{[\mathrm{NO}]} = [\mathrm{O_3}] \times \frac{k_{(\mathrm{NO}+\mathrm{O_3})}}{k_{(\mathrm{NO_2}+h\nu)}} \tag{1.2}$$

The sum of O_3 and NO_2, referred to as odd oxygen (O_x), is constant given that the concentrations of NO, NO_2 and O_3 are balanced by the Leighton ratio. The Leighton ratio is only valid when R 1.3 and R 1.5 are the main sinks for NO_2 and O_3, respectively. Thus, during sunrise and sunset periods, the photo-stationary state assumption is invalid, since the rate of photolysis of NO_2 is slow (Calvert and Stockwell, 1983).

In the absence of VOCs and free radicals, no net production of O_3 from R 1.3, R 1.4 and R 1.5 occurs. Deviations in the ratio are observed in the presence of VOCs, free radicals (primarily OH-radicals) and changing photolysis frequencies. In addition, major variations in the Leighton ratio take place throughout the day due to the varying frequency of NO_2 photolysis as a function of solar zenith angle (SZA). Non-chemical loss processes and fluxes of NO from the surface also affect the Leighton ratio (Carroll and Thompson, 1995), as well as occasions when the sinks of O_3 are more significant than R 1.5, such as ozone photolysis and O_3 reactions with NO_2, alkenes, HO_2 and OH.

Furthermore, oxidative species such as peroxy-radicals (RO_2 and HO_2) may oxidize NO to NO_2 through the following reactions:

$$RO_2^{\cdot} + NO^{\cdot} \longrightarrow NO_2^{\cdot} + RO^{\cdot} \tag{R 1.6}$$

$$HO_2^{\cdot} + NO^{\cdot} \longrightarrow NO_2^{\cdot} + OH^{\cdot} \tag{R 1.7}$$

When R 1.6 and R 1.7 are significant, the subsequent photolysis of NO_2 leads to a net production of O_3.

1.2.2 The Hydroxyl Radical and Volatile Organic Compounds

The hydroxyl-radical ($OH^{\cdot}$) is one of the most important species in the atmosphere due to its dominant role in initiating the oxidation of most of the natural and anthropogenic gases emitted into the atmosphere. The three most significant sources of tropospheric OH-radicals are the photolysis of O_3, HONO, and formaldehyde (HCHO). Minor additional sources include the photolysis of peroxides, other carbonyl compounds, and the reaction of O_3 with alkenes.

The generation of OH-radical through the photo-disassociation of O_3 ($\lambda \leq 320$ nm), shown in R 1.8, occurs via the production of the excited state oxygen atom, $O(^1D)$, which subsequently reacts with water vapor to produce OH (R 1.9). Alternatively, excited state oxygen atoms can be quenched by air molecules, as shown in

R 1.10.

$$O_3 + h\nu \longrightarrow O(^1D) + O_2 \qquad \text{(R 1.8)}$$

$$O(^1D) + H_2O \longrightarrow 2\,OH^{\cdot} \qquad \text{(R 1.9)}$$

$$O(^1D) \xrightarrow{M} O(^3P) \qquad \text{(R 1.10)}$$

The branching ratios of R 1.9 and R 1.10 depend on the concentration of water vapor in the atmosphere. At an ambient temperature of 300 K and 50% relative humidity, ~10% of $O(^1D)$ reacts with H_2O producing OH-radicals.

Photolysis of O_3 reaches a maximum at solar noon, marking the point when OH-radical production from ozone photolysis is at a maximum. Thus, as in the case of ozone photolysis, the relative contribution of the various sources of OH-radical depend primarily on the time of day and the chemical composition of the atmosphere. The daily production of OH-radicals from O_3 photolysis was estimated to be between 44 − 55% in remote and semi-polluted regions with low NO_x and VOC levels, while only 15 − 30% of the total OH-radical production was estimated to arise from the photolysis of O_3 in polluted environments (Alicke, 2000).

The photolysis of HONO is another significant source of OH-radicals during the daytime. HONO photolysis was estimated to contribute to 17 − 34% of the total OH production integrated over 24 hours in a polluted environment near Berlin, Germany (Alicke et al., 2003). HONO is known to accumulate during the nighttime and undergoes photolysis after sunrise, producing OH-radicals and NO:

$$HONO + h\nu \longrightarrow NO^{\cdot} + OH^{\cdot} \qquad \text{(R 1.11)}$$

Further details pertaining to HONO chemistry are discussed in Chapter 1.2.4.

Formaldehyde is the most abundant gas-phase carbonyl compound in the ambient atmosphere, with daytime mixing ratios ranging from several hundred ppt in remote and rural locations (Munger et al., 1995) and from 1 to 100 ppb in polluted urban environments (Fan and Dasgupta, 1994). The sources of HCHO include combustion processes and atmospheric oxidation of hydrocarbons, where HCHO is generally produced as a first or second generation product. The photolysis of HCHO ($\lambda < 370$ nm) produces $H^\cdot$ and $CHO^\cdot$ radicals (R 1.12a) that subsequently form HO_2 radicals (R 1.13 and R 1.14), which are rapidly converted to OH in the presence of NO, as shown in R 1.12a − R 1.15. In polluted urban environments, the photolysis of HCHO was observed to play a significant role in the OH-radical production, contributing to ~30% of the total daily production (Alicke, 2000).

$$\mathrm{HCHO} + h\nu \longrightarrow \mathrm{H}^\cdot + \mathrm{HCO}^\cdot \tag{R 1.12a}$$

$$\longrightarrow \mathrm{H_2} + \mathrm{CO} \tag{R 1.12b}$$

$$\mathrm{H}^\cdot + \mathrm{O_2} \longrightarrow \mathrm{HO_2}^\cdot \tag{R 1.13}$$

$$\mathrm{HCO}^\cdot + \mathrm{O_2} \longrightarrow \mathrm{HO_2}^\cdot + \mathrm{CO} \tag{R 1.14}$$

$$\mathrm{HO_2}^\cdot + \mathrm{NO}^\cdot \longrightarrow \mathrm{OH}^\cdot + \mathrm{NO_2}^\cdot \tag{R 1.15}$$

The reaction mechanism above also includes the oxidation of NO to NO_2 without the consumption of ozone, leading to a deviation in the Leighton ratio and a net production of O_3.

The photolysis of organic hydroperoxides (ROOH) and hydrogen peroxide (H_2O_2) are also minor contributors for the production of OH-radicals, as shown below:

$$\mathrm{H_2O_2} + h\nu \longrightarrow 2\,\mathrm{OH^{\cdot}} \qquad \text{(R 1.16)}$$

The two most dominant sinks of the OH-radical are its reaction with carbon monoxide (CO) and methane (CH_4). Assuming a mean global mixing ratio of [CO] = 80 ppb and [CH_4] = 1.8 ppm, and using the rate constant of OH reactions with CO ($k_{(\mathrm{CO+OH})} = 1.5 \times 10^{-13}\,\mathrm{cm^3\,molec^{-1}\,s^{-1}}$) and CH_4 ($k_{(\mathrm{CH_4+OH})} = 6.3 \times 10^{-15}\,\mathrm{cm^3\,molec^{-1}\,s^{-1}}$) at 298 K (Sander et al., 2006), 50% of the OH-radicals react with CO and 50% with CH_4. The reaction between CH_4 or any hydrocarbon (HC) with OH-radicals also lead to a net production of O_3, with sufficient NO_x. The reaction scheme for the OH-initiated oxidation of a hydrocarbon in the troposphere is as follows:

$$\mathrm{RH} + \mathrm{OH^{\cdot}} \longrightarrow \mathrm{R^{\cdot}} + \mathrm{H_2O} \qquad \text{(R 1.17)}$$

$$\mathrm{R^{\cdot}} + \mathrm{O_2} \xrightarrow{\mathrm{M}} \mathrm{RO_2{}^{\cdot}} \qquad \text{(R 1.18)}$$

$$\mathrm{RO_2{}^{\cdot}} + \mathrm{NO^{\cdot}} \longrightarrow \mathrm{RO^{\cdot}} + \mathrm{NO_2{}^{\cdot}} \qquad \text{(R 1.19)}$$

$$\mathrm{RO^{\cdot}} + \mathrm{O_2} \longrightarrow \mathrm{R'CHO} + \mathrm{HO_2{}^{\cdot}} \qquad \text{(R 1.20)}$$

$$\mathrm{HO_2{}^{\cdot}} + \mathrm{NO^{\cdot}} \longrightarrow \mathrm{OH^{\cdot}} + \mathrm{NO_2{}^{\cdot}} \qquad \text{(R 1.21)}$$

The overall net reaction is:

$$\mathrm{RH} + 2\,\mathrm{O_2} + 2\,\mathrm{NO^{\cdot}} \longrightarrow \mathrm{R'CHO} + \mathrm{H_2O} + 2\,\mathrm{NO_2{}^{\cdot}} \qquad \text{(R 1.22)}$$

Therefore, by combining the overall net reaction for the oxidation of hydrocarbons (R 1.22), the photolysis of NO_2 (R 1.3) and the reaction of O_3 with $O(^3P)$ (R 1.4), the overall net O_3 production becomes:

$$\mathrm{RH} + 4\,\mathrm{O_2} + 2\,h\nu \longrightarrow \mathrm{R'CHO} + \mathrm{H_2O} + 2\,\mathrm{O_3} \qquad \text{(R 1.23)}$$

Similar to the reaction of OH-radicals with hydrocarbons, the reaction of OH-radicals with CO also leads to the formation of tropospheric O_3 via the reaction scheme below, in which the OH-radical is also regenerated.

$$\mathrm{CO} + \mathrm{OH^{\cdot}} \longrightarrow \mathrm{CO_2} + \mathrm{H^{\cdot}} \qquad \text{(R 1.24)}$$

$$\mathrm{H^{\cdot}} + \mathrm{O_2} \xrightarrow{M} \mathrm{HO_2}^{\cdot} \qquad \text{(R 1.25)}$$

$$\mathrm{HO_2}^{\cdot} + \mathrm{NO} \longrightarrow \mathrm{NO_2} + \mathrm{OH^{\cdot}} \qquad \text{(R 1.26)}$$

The oxidation of CO, in combination with the photolysis of NO_2 (R 1.3) and the reaction of O_2 with $O(^3P)$ (R 1.4), yields a net production of ozone:

$$\mathrm{CO} + 2\,\mathrm{O_2} \longrightarrow \mathrm{CO_2} + \mathrm{O_3} \qquad \text{(R 1.27)}$$

The termination reactions of the OH-radical (or more generally expressed as HO_x = OH + HO_2) depend upon the availability of NO_x and VOCs. In polluted environments with a low VOC/NO_x ratio, the OH-radical reacts with NO_2, producing nitric acid:

$$\mathrm{OH^{\cdot}} + \mathrm{NO_2}^{\cdot} \xrightarrow{M} \mathrm{HNO_3} \qquad \text{(R 1.28)}$$

In less polluted environments with a high VOC/NO_x ratio, the self-reaction of peroxy radicals takes place due to the lack of NO, yielding:

$$HO_2^{\cdot} + HO_2^{\cdot} \longrightarrow HOOH \qquad \text{(R 1.29)}$$

In summary, by exclusively considering the concentrations of NO, NO_2 and O_3, no net production of O_3 is observed. When VOCs and CO are introduced, oxidizing agents such as HO_2 and RO_2 are formed and oxidation of NO to NO_2 occurs, leading to subsequent O_3 production. In order to obtain an overall decrease in the tropospheric O_3 concentration, a simultaneous reduction in both VOCs and NO_x is required in polluted environments.

1.2.3 The Nitrate Radical and Dinitrogen Pentoxide

The nitrate radical ($NO_3^{\cdot}$) is one of the primary oxidants of the nocturnal atmosphere. The first measurements of NO_3 were performed in a polluted atmosphere using differential optical absorption spectroscopy (DOAS), measuring mixing ratios as high as 355 ppt one hour after sunset (Platt et al., 1980b). The nitrate radical is a significant nocturnal oxidant in both marine and terrestrial environments for a variety of organic species including dimethyl sulphide (DMS), aldehydes, and various unsaturated hydrocarbons and aromatics. The 24-hour contribution of NO_3 to the oxidation of continental VOCs was previously estimated to be 28%, along with 55% and 17% for OH and O_3, respectively (Geyer et al., 2001).

NO_3 is formed by the reaction between NO_2 and O_3 (R 1.30), both of which are present at significant concentrations in polluted marine and urban environments.

$$NO_2^{\cdot} + O_3 \longrightarrow NO_3^{\cdot} + O_2 \tag{R 1.30}$$

During the daytime, NO_3 absorbs solar radiation in the red region of the visible spectrum (580 − 670 nm) and rapidly undergoes photo-disassociation with two possible pathways:

$$NO_3^{\cdot} + hv \longrightarrow NO_2^{\cdot} + O(^3P) \tag{R 1.31a}$$

$$\longrightarrow NO^{\cdot} + O_2 \tag{R 1.31b}$$

The quantum yield of (R 1.31a) dominates in the 570 − 585 nm wavelength region, gradually decreasing to zero at 635 nm where the quantum yield of (R 1.31b) is 1. During the daytime, NO_3 rapidly photolyzes and has a lifetime of approximately 5 seconds at a solar zenith angle of 0° (Wayne et al., 1991). The concentration of NO_3 is suppressed in urban environments by fresh NO_x emissions which rapidly titrate NO_3 by the following reaction:

$$NO_3^{\cdot} + NO^{\cdot} \longrightarrow 2\,NO_2^{\cdot} \tag{R 1.32}$$

Thus, the lifetime of the nitrate radical is shortest in close proximity of fresh NO_x sources. The lifetime is found to increase as NO reacts with O_3 (R 1.5) or peroxy radicals (R 1.7). Based on the rate constant for R 1.32, $k_{(NO_3+NO)} = 2.6\times 10^{-11}$ cm^3 molec^{-1} s^{-1} at 298 K, the lifetime of NO_3 in the presence of 1 ppb of NO is 1.5 seconds (Sander et al., 2006).

NO_3 rapidly reacts with several organic compounds, primarily terpenes and isoprene in rural environments and monoterpenes near forests (Atkinson, 1997). The initial step of such reactions is the addition of NO_3 to a double bond, forming a nitrato-radical intermediate as follows:

$$\mathrm{NO_3{}^{\cdot} + R_1C{=}CR_2 \longrightarrow R_1C(ONO_2)C^{\cdot}R_2} \tag{R 1.33}$$

The nitratoalkyl radical ($R_1C(ONO_2)C^{\cdot}R_2$) can produce an epoxide and NO_2 or react with O_2, forming a nitratoalkylperoxy radical ($R_1C(ONO_2)C(O_2{}^{\cdot})R_2$):

$$\mathrm{R_1C(ONO_2)C^{\cdot}R_2 \longrightarrow R_1COCR_2 + NO_2{}^{\cdot}} \tag{R 1.34}$$

$$\mathrm{R_1C(ONO_2)C^{\cdot}R_2 + O_2 \longrightarrow R_1C(ONO_2)C(O_2{}^{\cdot})R_2} \tag{R 1.35}$$

Subsequently, the nitratoalkylperoxy radical may react with NO, forming a nitratoalkoxy radical ($R_1C(ONO_2)C(O^{\cdot})R_2$) or dinitrate ($R_1C(ONO_2)C(ONO_2)R_2$) as follows:

$$\mathrm{R_1C(ONO_2)C(O_2{}^{\cdot})R_2 + NO^{\cdot} \longrightarrow R_1C(ONO_2)C(O^{\cdot})R_2 + NO_2{}^{\cdot}} \tag{R 1.36a}$$

$$\mathrm{\longrightarrow R_1C(ONO_2)C(ONO_2)R_2} \tag{R 1.36b}$$

In the absence of NO, the peroxy radical can react with other peroxy radicals to form nitratoperoxides, nitratocarbonyls and nitratoalcohols, yielding a large number of oxidative products (Seinfeld and Pandis, 2012).

The NO_3 radical is known to be a dominant sink for dimethyl sulphide in marine environments, surpassing even the contribution from the OH-radical during the daytime (Allan et al., 2000). DMS is released into the atmosphere by biological processes from phytoplankton in surface water (Charlson et al., 1987) and is estimated to account for ~60% of the total natural sulphur emission to the atmosphere (Andreae and Raemdonck, 1983). The reaction between NO_3 and DMS proceeds through hydrogen abstraction, producing HNO_3 via:

$$NO_3^{\cdot} + CH_3SCH_3 \longrightarrow CH_3SCH_2^{\cdot} + HNO_3 \qquad \text{(R 1.37)}$$

Additional minor sinks of the NO_3 radical include reactions on aerosol surfaces (Thomas et al., 1998) and dry deposition. Assuming conditions typical of a NBL with a height of 100 m and a NO_3 deposition velocity (ν_d) of 0.33 cm s^{-1}, the lifetime of NO_3 with respect to dry deposition was estimated to be ~10 hours (Geyer et al., 2001).

Vertical profiles of NO_3 were measured at a rural/suburban site impacted by anthropogenic emissions from a nearby urban center, by using a movable carriage allocated on a 300m tower (Brown et al., 2007). Mixing ratios of NO_3 as high as 100 ppt were measured at a height of 200 meters, while ground level mixing ratios below 5 ppt were observed. The elevated levels of NO_3 within the residual layer impact the chemistry in the layer overnight, as well as in the following morning when the nocturnal inversion layer is broken.

Upon NO_3 formation, a temperature dependent equilibrium is established with dinitrogen pentoxide (N_2O_5) in the presence of NO_2 via R 1.38, for which colder temperatures favor the stability of N_2O_5.

$$NO_3^{\cdot} + NO_2^{\cdot} \overset{M}{\rightleftharpoons} N_2O_5 \qquad \text{(R 1.38)}$$

Mixing ratios of N_2O_5 as high as 15 ppb were calculated in the Los Angeles area using simultaneous measurements of ambient NO_3 and NO_2, as well as the equilibrium constant for Reaction R 1.38 (Atkinson et al., 1986).

Significant amounts of N_2O_5 are ultimately converted to HNO_3 by hydrolysis via the following major heterogeneous channel:

$$N_2O_5 + H_2O_{(p)} \longrightarrow 2\,HNO_{3(p,g)} \qquad \text{(R 1.39)}$$

and minor homogeneous channel (Dentener and Crutzen, 1993):

$$N_2O_5 + H_2O_{(g)} \longrightarrow 2\,HNO_{3(g)} \qquad \text{(R 1.40)}$$

HNO_3 is removed from the atmosphere through dry and wet deposition and acts as the major global sink of NO_x. Modeling studies predict that between $50 - 90\%$ of the formation of HNO_3 occurs through R 1.39 and R 1.40 and by the adsorption of NO_3 on wet surfaces in the northern hemisphere (Dentener and Crutzen, 1993).

N_2O_5 is also known to react heterogeneously with sea salt aerosols in marine environments, producing $ClNO_2$ through (Finlayson-Pitts et al., 1989):

$$N_2O_5 + NaCl_{(s,aq)} \longrightarrow ClNO_{2(g,aq)} + NaNO_{3(s,aq)} \qquad \text{(R 1.41)}$$

The mixing ratio of gas-phase $ClNO_2$ has been recently measured to exceed 2 ppb in the MBL and was found to be correlated with the loss rate of N_2O_5 (Osthoff et al., 2008; Young et al., 2012).

In addition, recent studies have also shown that NO_2 and N_2O_5 can react heterogeneously with HCl on aerosol surfaces, producing ClNO and $ClNO_2$, respectively

(Raff et al., 2009). These reactions are thought to initiate with the auto-ionization of NO_2 and N_2O_5 upon their absorption onto the aerosol surfaces:

$$2\,NO_2{}^{\cdot} \longrightarrow NO^+NO_3^- \qquad (R\,1.42)$$

$$N_2O_5 \longrightarrow NO_2^+NO_3^- \qquad (R\,1.43)$$

The auto-ionization process is followed by the reaction of the ionized species with HCl:

$$NO^+NO_3^- + HCl \longrightarrow ClNO + HNO_3 \qquad (R\,1.44)$$

$$NO_2^+NO_3^- + HCl \longrightarrow ClNO_2 + HNO_3 \qquad (R\,1.45)$$

The resulting ClNO and $ClNO_2$ may accumulate overnight in a polluted marine environment, producing Cl-radicals upon photolysis in the following morning via:

$$ClNO + h\nu \longrightarrow Cl^{\cdot} + NO \qquad (R\,1.46)$$

$$ClNO_2 + h\nu \longrightarrow Cl^{\cdot} + NO_2 \qquad (R\,1.47)$$

Chlorine radicals have been shown to contribute to enhancements of O_3 formation in coastal urban areas (Knipping and Dabdub, 2003; Finley and Saltzman, 2006; Osthoff et al., 2008; Simon et al., 2009; Raff et al., 2009). The initial reaction of the Cl-radical with hydrocarbons (RH) is as follows:

$$Cl^{\cdot} + RH \longrightarrow R^{\cdot} + HCl \qquad (R\,1.48)$$

As previously discussed, the resulting hydrocarbon radical ($R^{\cdot}$) rapidly reacts with O_2, producing RO_2 (R 1.18). Subsequent reaction of RO_2 with NO leads to the formation of NO_2 (R 1.19), which produces O_3 upon photolysis (R 1.3).

1.2.4 Nitrous Acid

Nitrous acid (HONO) was first detected in a moderately polluted atmosphere in 1979 with mixing ratios as high as 0.8 ppb (Perner and Platt, 1979) and first detected in a polluted atmosphere shortly after with mixing ratios as high as 4.1 ppb (Platt et al., 1980a). HONO is a significant atmospheric constituent because of its role as a primary source of HO_x during the day. Contributions of HONO to the OH-radical budget were underestimated for a long period of time and consequently neglected in many modeling studies. This was mainly a result of the lack of ambient measurements of HONO and an incomplete understanding of the HONO formation mechanism and its kinetics. Photolysis of HONO was estimated to contribute to $17 - 34\%$ of the total OH-radical production integrated over 24-hours in polluted environments (Alicke et al., 2003). A recent study highlights the vertical dependence of this production with HONO contributing more highly in the lowest layer close to its source and less so at higher elevations in the PBL (Young et al., 2012).

HONO generally accumulates over the course of the night and rapidly photolyzes during sunrise ($300 \text{ nm} < \lambda < 405 \text{ nm}$) at a rate of J_{HONO}, producing OH-radicals and NO through the following reaction:

$$\text{HONO} + h\nu \longrightarrow \text{NO}^{\cdot} + \text{OH}^{\cdot} \qquad \text{(R 1.49)}$$

The concentration of HONO exhibits a strong diurnal variation with photolysis as the major sink during the daytime. Previous studies of HONO during the daytime observed mixing ratios between $5 - 150$ ppt in rural and semi-polluted environments

(Alicke, 2000). Recent studies of HONO reported daytime mixing ratios between 0.5 − 1.0 ppb at a non-urban site in China (Su et al., 2008), and daytime mixing ratios as high as 1.4 ppb during the wintertime in the Utah Basin over snow (Rappenglück et al., 2013). Shortly after sunset, the mixing ratio of HONO was observed to increase to several 100s of ppt in rural areas and to several ppb in polluted environments (Alicke, 2000), with mixing ratios as high as 15 ppb reported in the nocturnal polluted atmosphere in Los Angeles, USA (Winer and Biermann, 1994).

Several gas-phase reactions producing HONO have been proposed and examined in the past. HONO is known to be produced from the reaction between NO and OH via:

$$\mathrm{NO^{\cdot} + OH^{\cdot} \xrightarrow{M} HONO} \qquad \text{(R 1.50)}$$

This reaction can become significant in urban areas during the daytime, due to simultaneously high levels of OH-radical and NO, given the abundance of NO sources. During the daytime, the homogeneous formation of HONO (R 1.50) remains in a steady-state with the photolysis of HONO (R 1.49), rapidly established within ∼10 minutes of sunrise. Based on the rate constant for R 1.50, $k_{(\mathrm{NO+OH})} = 3.89 \times 10^{-12}\,\mathrm{cm^3\,molec^{-1}\,s^{-1}}$ (Sander et al., 2006), and assuming mixing ratios of [NO] = 25 ppb and [OH] = $2.0 \times 10^{6}\,\mathrm{molec\,cm^{-3}}$, the maximum HONO mixing ratio is 14 ppt for $J_{\mathrm{HONO}} = 2.0 \times 10^{-3}\,\mathrm{s^{-1}}$. During the nighttime, assuming mixing ratios of [NO] = 25 ppb and [OH] = $1.0 \times 10^{5}\,\mathrm{molec\,cm^{-3}}$, the formation rate of HONO becomes 32 ppt $\mathrm{h^{-1}}$. Therefore, this production reaction alone is insufficient to explain the observed mixing ratios of HONO.

Alternative homogeneous pathways involve the gas-phase reaction between NO_x and water vapor as follows:

$$NO^{\cdot} + NO_2{}^{\cdot} + H_2O \longrightarrow 2\,HONO \qquad \text{(R 1.51)}$$

$$2\,NO_2{}^{\cdot} + H_2O \longrightarrow HONO + HNO_3 \qquad \text{(R 1.52)}$$

The reaction rates for these 3-body collisions in the gas phase are $k_{(NO+NO_2+H_2O)} = 1.2 \times 10^{-34}\,cm^6\,molec^{-2}\,s^{-1}$ for Reaction R 1.51 (Wayne and Yost, 1951) and $\sim 10^{-40}\,cm^6\,molec^{-2}\,s^{-1}$ for Reaction R 1.52 (Chan et al., 1976). Both of these rates are much too slow to explain observed HONO mixing ratios under atmospherically relevant levels of NO_x. Reaction R 1.51 was also suggested to occur heterogeneously (Ferm et al., 1985; Calvert et al., 1994; Andres-Hernandez et al., 1996), however, many field and laboratory studies have observed high rates of HONO formation in the absence of NO, suggesting that this mechanism is not likely a dominant source of HONO (Platt, 1986; Alicke et al., 2002; Finlayson-Pitts et al., 2003b).

Previous studies have also shown that HONO is directly emitted from fuel combustion processes with a $HONO/NO_x$ ratio typically below 0.01, dependent upon vehicle and fuel type. The $HONO/NO_x$ ratio for modern gasoline cars with catalytic converters was found to be $< 0.0065 \pm 0.24$ (Kurtenbach et al., 2001) and < 0.0001 for gasoline engines under rich operating conditions (Kessler and Platt, 1984), unable to substantially account for the observed ambient HONO levels.

Since observations of direct emissions of HONO and known homogeneous formation reactions are insufficient to explain the observed HONO levels, studies have shifted their focus to heterogeneous production of HONO. Evidence for HONO formation over the ground surface was obtained from vertical gradient measurements of HONO between 0.25 and 2 m (Harrison and Kitto, 1994; Harrison et al., 1996). The authors observed negative gradients of HONO when $[NO_2]>10$ ppb and positive gradients when $[NO_2]<10$ ppb over a grass surface. The results were attributed to a balance between the heterogeneous formation of HONO from NO_2 on the ground and dry deposition of HONO. Another study used an active-DOAS system to probe the lowest 450 m of the planetary boundary layer (PBL) over Heidelberg, Germany (Veitel, 2002). The HONO mixing ratio and the HONO/NO_2 ratio were observed to decrease with altitude under nearly any atmospheric condition during both day and night periods, suggesting that the formation of HONO likely occurs on the ground.

A comparison between the ground surface area in the NBL and the surface area of aerosols was previously performed, concluding that the ground provides a much larger surface area (Yu et al., 2009; Stutz et al., 2004). The heterogeneous conversion of NO_2 to HONO on the surface of aerosols can become significant with an increase in height of the mixed layer and pollutant loading (Lammel, 1999). Previous studies have also suggested soot particles as a possible surface for the heterogeneous formation of HONO from NO_2 (Ammann et al., 1998; Kleffmann et al., 1999; Aubin and Abbatt, 2007). However, the formation rate on soot particles rapidly decreases with the deactivation of the carbonaceous surface.

Early studies determined a first-order dependence of the heterogeneous formation rate of HONO on the concentration of water vapor and NO_2 (Sakamaki et al., 1983;

Pitts et al., 1984; Jenkin et al., 1988; Kleffmann et al., 1999). These studies were generally performed under constant temperature, resulting in HONO formation rates proportional to relative humidity. However, more recent studies suggest that the formation of HONO is rather linked to the amount of surface water. Thus, the previous relative humidity dependence was observed since relative humidity is a surrogate for the amount of H_2O chemically or physically adsorbed onto surfaces where the heterogeneous formation occurs (Lammel, 1999; Finlayson-Pitts et al., 2003b). The heterogeneous formation reaction was observed to yield 50% HONO and 50% surface adsorbed HNO_3 for a variety of laboratory surfaces, with NO and N_2O as secondary products under high NO_2 levels, high surface to volume (S/V) ratios, or during long reaction times (Svensson et al., 1987; Kleffmann et al., 1998; Goodman et al., 1999).

Laboratory studies and observations within the nocturnal boundary layer suggest heterogeneous conversion of NO_2 on surface adsorbed water as the major nocturnal source of HONO with the following stoichiometry (Finlayson-Pitts et al., 2003b):

$$\mathrm{NO_2{}^{\cdot} + NO_2{}^{\cdot} + H_2O \longrightarrow HONO + HNO_3} \qquad \text{(R 1.53)}$$

An integrated mechanism was proposed by (Finlayson-Pitts et al., 2003b) and is shown in Figure 1.3. The authors proposed that the reaction initiates with the gas-phase formation of the NO_2 dimer, N_2O_4, which is adsorbed onto a thin aqueous surface and stabilized by two molecules of water. The reactive surface species was proposed to be asymmetric dinitrogen tetroxide, $ONONO_2$, formed by isomerization of symmetric N_2O_4. The asymmetric $ONONO_2$ can auto-ionize to generate $NO^+NO_3^-$,

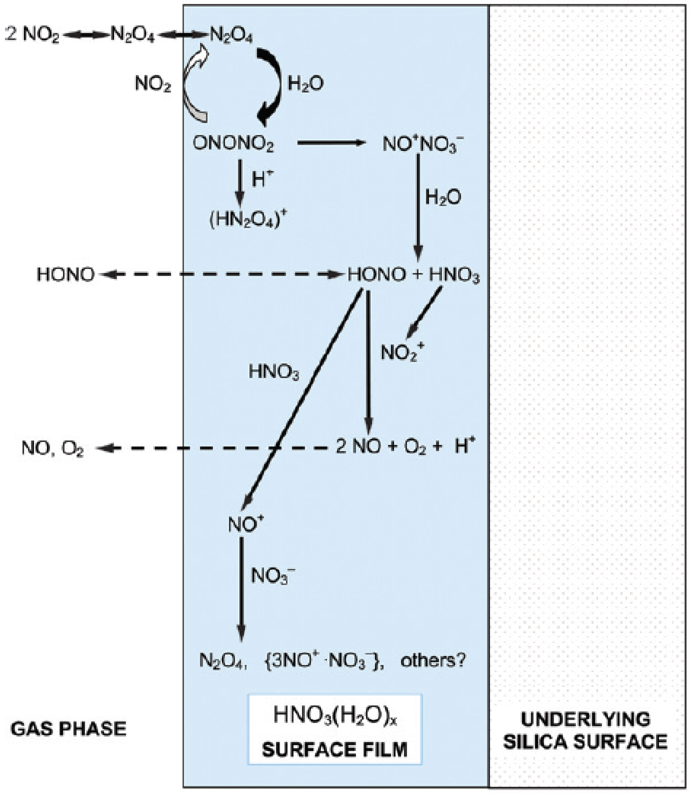

Figure 1.3: Reaction mechanism of the heterogeneous formation of HONO proposed by (Finlayson-Pitts et al., 2003b)

or a back reaction may occur with gas phase NO_2 to reform the symmetric N_2O_4. The $NO^+NO_3^-$ complex reacts with water to generate HONO, which partly escapes from the surface, as well as HNO_3 which remains in the aqueous phase, generating NO_2^+. In the mechanism, NO is also generated by the reaction of HONO with NO_2^+ and HONO may react with HNO_3, producing NO^+ on the surface. The proposed overall rate of HONO formation is first-order with respect to NO_2, +2 due to formation of N_2O_4, and -1 for back reaction of NO_2 with $ONONO_2$, reforming N_2O_4.

The HONO/NO_2 ratio is often used as an indicator of the conversion efficiency of NO_2 to HONO. Early studies in both rural and urban environments determined that the nighttime HONO concentration is generally higher in urban environments. However, when normalized to NO_2, similar results were found in both rural and urban regions, with HONO/NO_2 ratios ranging from 1.7 − 13% (Lammel and Cape, 1996). HONO/NO_2 ratios <1.0% are generally associated with direct HONO emissions from combustion processes (Kurtenbach et al., 2001). Ratios below 4% were observed in environments with low relative humidity (10−30% RH), whereas ratios up to 9% were determined in high relative humidity conditions (50−100% RH) (Stutz et al., 2004). Recently, HONO/NO_2 ratios as large as 30% were observed in the mountainous region of Nepal, for which the highly efficient conversion of NO_2 to HONO was attributed to the high concentration of pollutants and relative humidity, in combination with a low nocturnal inversion (Yu et al., 2009).

Relatively high daytime HONO mixing ratios have been recently reported, sparking great interest in the determination a daytime source of HONO strong enough to account for the observations (Su et al., 2008). In 2008, (Li et al., 2008) proposed the reaction between electronically excited NO_2 and water vapor as a major formation pathway for daytime HONO; however, such a reaction was shown to be a two photon process (Amedro et al., 2011), becoming insignificant under atmospherically relevant conditions (Wong et al., 2012). In addition, various photolytic substrates known to reduce NO_2 to HONO were proposed in order to explain daytime HONO mixing ratios. Examples include humic acid (Stemmler et al., 2006), organic films (Broske et al., 2003), soot (Aubin and Abbatt, 2007) and TiO_2 (Ndour et al., 2008).

(Su et al., 2011) proposed the partitioning of soil nitrite ions (NO_2^-) as a significant source of daytime HONO. Part of the nitrification process in soil converts ammonium (NH_4^+) to NO_2^- by nitrifying microbes via:

$$NH_4^+ + {}^3\!/\!_2\, O_2 \longrightarrow 2\, H^+ + H_2O + NO_2^- \tag{R 1.54}$$

Upon the depletion of molecular oxygen, nitrate becomes the primary oxygen source for microorganisms. The denitrification process reduces nitrate (NO_3^-) to NO_2^- by denitrifying microbes via:

$$2\, NO_3^- \longrightarrow 2\, NO_2^- + O_2 \tag{R 1.55}$$

The produced NO_2^- is only present in the aqueous phase and may undergo the following reversible acid-base reaction:

$$NO_2{}^-_{(aq)} + H^+{}_{(aq)} \longleftrightarrow HONO_{(aq)} \tag{R 1.56}$$

where HONO can reversibly partition from the aqueous phase of humid soil into the gas phase:

$$HONO_{(aq)} \longleftrightarrow HONO_{(g)} \tag{R 1.57}$$

Nevertheless, the proposed formation pathway is insufficient to explain the high HONO levels observed in urban areas with minimal soil surface coverage or during winter periods with snow ground cover, when microbe activity is at a minimum.

Another study found daytime HONO fluxes to be positively correlated with the product of leaf surface nitrate loading and the rate constant of nitrate photolysis (Zhou et al., 2011). The authors suggest that the photolysis of surface adsorbed

HNO_3 may explain the daytime levels of observed HONO, although the kinetics and mechanism remain poorly understood. To date, photo-chemical mechanisms have been unable to fully explain the daytime formation rates of HONO required to reproduce ambient observations (Sörgel et al., 2011b).

Apart from HONO photolysis during the daytime, additional sinks of HONO are not well understood nor characterized. Gradient measurements of HONO near the surface assume a balance between HONO production and loss at the surface, with irreversible deposition to the surface as the only major sink of HONO during the nighttime (Wong et al., 2011; Sorgel et al., 2011a). The extent of the dry deposition of HONO was proposed to be a function of the height of the NBL and stability (Geyer and Stutz, 2004; Wong and Stutz, 2010), where HONO deposition velocities between $0.08 - 3$ cm s^{-1} have been reported for a wide range of environments (Li et al., 2012). Currently, the fate of surface deposited HONO remains unknown.

In order to fully understand the day and nighttime HONO processes, a more comprehensive understanding of the nighttime formation mechanism, production and loss rates, as well as the fate of surface deposited HONO under various atmospheric conditions are required.

1.3 Differential Optical Absorption Spectroscopy

1.3.1 Overview of the DOAS Technique

Differential optical absorption spectroscopy is a spectroscopic technique that quantifies the attenuation of light by trace gases in the atmosphere and determines their concentration (Platt et al., 1979). DOAS is particularly useful for the detection of highly reactive trace gases due to the non-invasive nature of the technique. The technique quantifies the structured narrowband absorptions (typically <10 nm) of trace gases of atmospheric interest while ignoring the smooth broadband extinction features, such as Raleigh scattering, aerosol scattering or other smoothly varying instrumental functions.

A similar spectroscopic technique was first deployed by Noxon (Noxon, 1975; Noxon et al., 1979), who utilized sun and moonlight to measure NO_2 in the stratosphere and troposphere from ground-based absorption spectroscopy. The technique was subsequently modified to include an artificial light source, producing simultaneous measurement of atmospheric CH_2O, O_3, and NO_2 (Platt et al., 1979). The DOAS technique was the first to directly measure several radical species such as OH (Perner et al., 1976), NO_3 (Platt et al., 1980a), OClO, BrO (Sanders et al., 1989), IO (Alicke et al., 1999) and OIO (Allan et al., 2001) in ambient air in both the troposphere and stratosphere. The technique also led to the first reported measurements of HONO (Perner and Platt, 1979) and the first direct measurements of glyoxal (CHOCHO) (Platt et al., 1979).

Current application of the DOAS technique involves either a *passive*- or *active*-DOAS mode. The passive-DOAS technique utilizes a natural light source such as moonlight (Wagner et al., 2000), starlight (Naudet et al., 1981) or sunlight (Wagner et al., 2001), collecting either direct or stray light from the source. A popular application of the passive technique is multi-axis differential optical absorption spectroscopy (MAX-DOAS), which measures scattered sunlight from multiple viewing angles in order to determine the tropospheric vertical column density (VCD) of various trace gases (Hönninger et al., 2004; Halla, 2013). Active-DOAS utilities an artificial light source and is employed for measurement of trace gases in the lower troposphere or in laboratory kinetic studies. The technique utilizes a telescope which emits a collimated light beam through a defined path-length in the open atmosphere. For the presented work, an active-DOAS system was deployed in polluted marine and urban environments. Additional instrumental details are described in further detail in Chapter 2.

1.3.2 Theoretical Background of DOAS

The principle of operation of DOAS is based on Beer-Lambert's law (Plane and Smith, 1995):

$$I(\lambda) = I_o(\lambda) e^{-\sigma(\lambda) L c} \tag{1.3}$$

where $I_\circ(\lambda)$ is the initial light intensity and $I(\lambda)$ is the transmitted intensity of the light of wavelength λ after passing through an air sample of length L (cm) with concentration of analyte c (molecules cm^{-3}) and absorption cross-section $\sigma(\lambda)$. The optical density (D) of a layer of a given species is defined as:

$$D = \ln\left(\frac{I_o(\lambda)}{I(\lambda)}\right) = \sigma(\lambda)Lc \tag{1.4}$$

The concentration of the gas species is calculated by rearranging equation 1.3

$$c = \ln\left(\frac{I_o(\lambda)}{I(\lambda)}\right)(\sigma(\lambda)L)^{-1} \tag{1.5}$$

$$c = \frac{D}{\sigma(\lambda)L} \tag{1.6}$$

However, Equation 1.5 does not account for Mie and Rayleigh scattering of light in the atmosphere and must be extended in order to encompass the effects of these two processes. Mie scattering consists of light scattering by atmospheric aerosol particles whose dimensions are of the same order as the wavelength of incident light. Rayleigh scattering is defined as the scattering of photons by air molecules as light travels through the air parcel; being inversely proportional to the fourth power of the wavelength.

In order to include Rayleigh scattering effects, the Rayleigh extinction coefficient $\epsilon_R(\lambda)$ must be introduced:

$$\epsilon_R(\lambda) = \sigma_R(\lambda)n_{Air} \tag{1.7}$$

where n_{Air} is the number density of air (2.45×10^{19} molecules cm^{-3} at 20° and 1 atm) and

$$\sigma_R(\lambda) = \sigma_{RO}\,\lambda^{-4} \tag{1.8}$$

where $\sigma_{RO} = 4.4 \times 10^{-16}\,\mathrm{cm}^2\,\mathrm{nm}^4$ for air. The Mie extinction coefficient, $\epsilon_M(\lambda)$, is given by:

$$\epsilon_M(\lambda) = \epsilon_{MO}\,\lambda^{-n} \tag{1.9}$$

where n is inversely related to the mean aerosol particle radius and ranges from 0.5 to 2.5. Taking Mie and Rayleigh scattering into consideration, the atmospheric absorption from a single absorbing trace species can be described by:

$$I(\lambda) = I_o(\lambda) e^{L(-\sigma(\lambda)c + \epsilon_R(\lambda) + \epsilon_M(\lambda))} \tag{1.10}$$

In order to account for the absorption of the various trace gases present in the atmosphere, Equation 1.10 must be extended, as shown below:

$$I(\lambda) = I_o(\lambda) e^{-L((\Sigma \sigma_i(\lambda) c_i) + \epsilon_R(\lambda) + \epsilon_M(\lambda))} \tag{1.11}$$

where i denotes the i^{th} absorbing species.

Determining the true light intensity transmitted in the absence of any absorbing species would be a difficult task; however, this issue is overcome by measuring the *differential absorption*, defined as the component of the total absorption of any molecule which rapidly varies as a function of wavelength (Platt and Stutz, 2008).

Based on this definition, the absorption cross section of a given trace gas can be separated into two components:

$$\sigma_i(\lambda) = \sigma_{i,0}(\lambda) + \sigma_i'(\lambda) \tag{1.12}$$

where $\sigma_{i,0}(\lambda)$ is the broadband component that varies slowly with wavelength while $\sigma_i'(\lambda)$ is the narrowband component which varies rapidly with wavelength, as illustrated in Figure 1.4.

Combining Equations 1.11 and 1.12 lead to the following result:

$$I(\lambda) = I_o(\lambda) e^{-L(\Sigma \sigma_i'(\lambda) c_i)} \, e^{-L(\Sigma \sigma_{i0}(\lambda) c_i + \epsilon_R(\lambda) + \epsilon_M(\lambda))} A(\lambda) \tag{1.13}$$

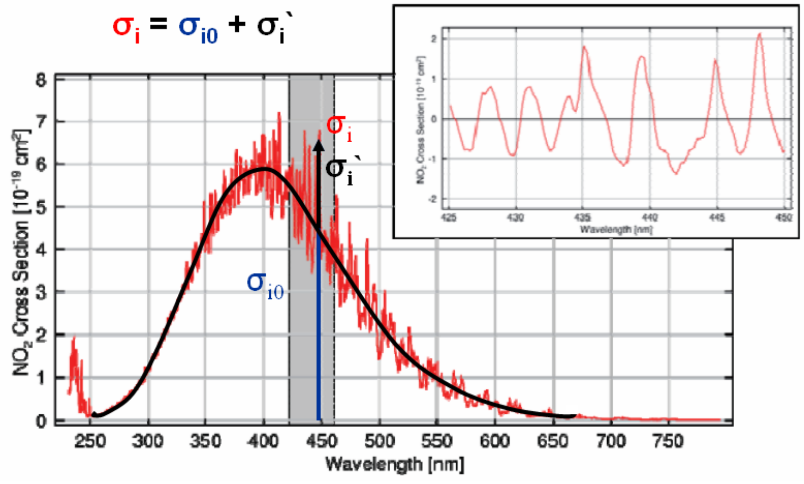

Figure 1.4: NO_2 absorption cross section spectrum illustrating of the broadband ($\sigma_{i,0}$) and narrowband (σ'_i) components. The resulting spectrum upon the removal of the slowly varying component is shown on the top right.

where the attenuation factor $A(\lambda)$ is a parameter describing the broadband wavelength dependent transmission of the optical system.

The corresponding differential absorption cross section $\sigma'(\lambda)$ can be substituted for $\sigma(\lambda)$ in Equation 1.11 and a differential optical density, D', is defined in analogy to Equation 1.4:

$$D' = \log\left(\frac{I'_o(\lambda)}{I(\lambda)}\right) = L\Sigma(\sigma'_i(\lambda)c_i) \tag{1.14}$$

Thus, the concentration of absorbent i is defined as:

$$c_i = \frac{D'}{\sigma'_i(\lambda)L} \tag{1.15}$$

The concentration of the species under analysis can be directly calculated by measuring $I(\lambda)$ and solving Equation 1.15. By computing a least squares fit of the structured absorptions, concentrations of trace absorbers can be calculated, provided that suitable absorption cross section reference spectra are available for the analyzed species.

One of the major advantages of the DOAS technique consists of the fact that simultaneous measurements of multiple trace gases can be obtained from a single ambient spectrum. The absorption cross sections of frequently measured atmospheric trace gases by DOAS are shown in Figure 1.5. Due to the nature of the technique, DOAS measurements provide a more representative concentration of pollutants in a given area, compared to single point measurements. DOAS measurements may be extended to acquire vertical profiles and column densities of various trace gases. Calibration of the DOAS system is not required since DOAS is an absolute measurement technique, providing that the absoption cross section of the molecule is known. The non-invasive nature of the technique also allows for the measurement of highly reactive radical species.

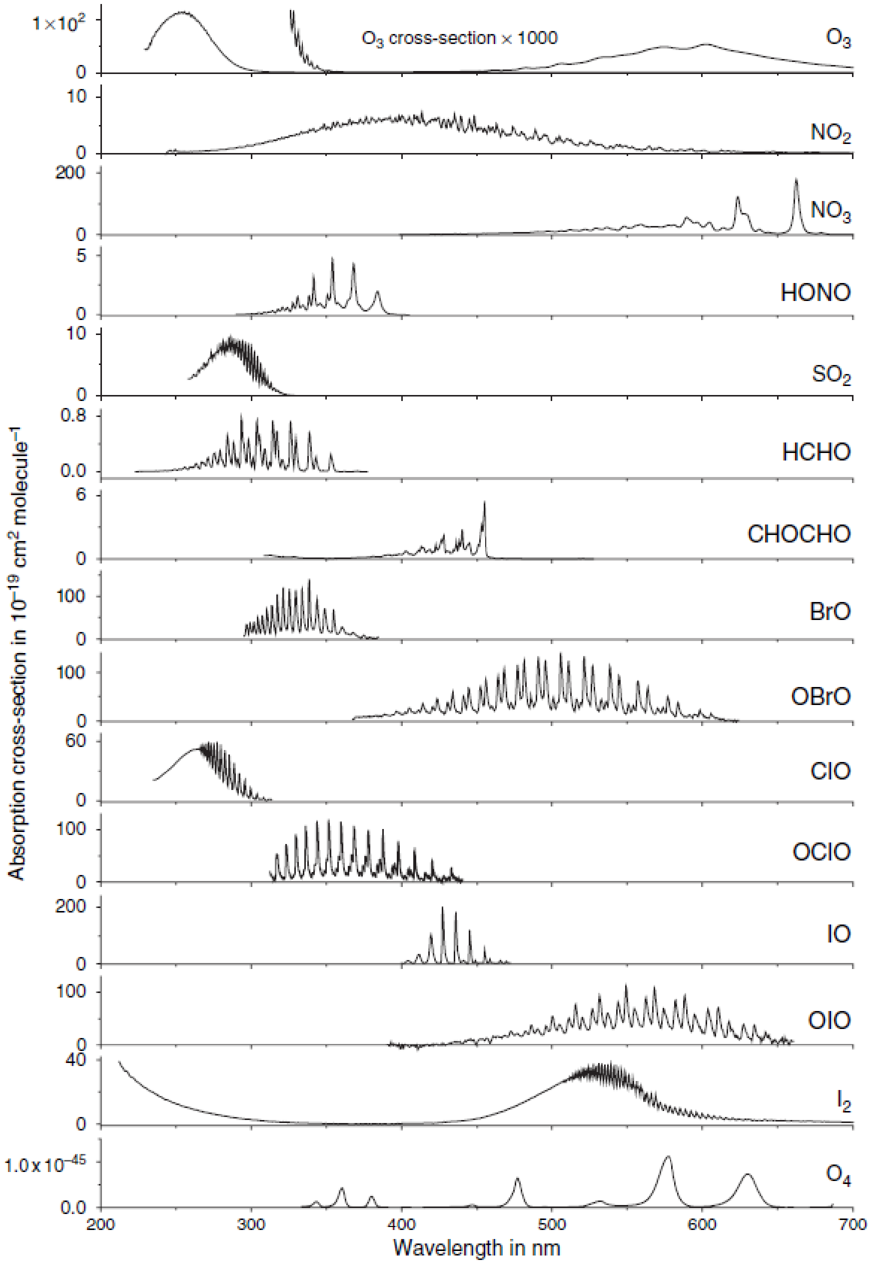

Figure 1.5: Absorption cross section structure for various atmospheric constituents in the 200 − 700 nm wavelength range commonly measured by the DOAS technique. Image taken from (Platt and Stutz, 2008).

2 Experimental

2.1 Instrumental Setup of Active-DOAS

Nocturnal active-DOAS measurements of NO_3, NO_2, HONO, and SO_2 were collected in polluted marine and urban environments. The active-DOAS system utilized consisted of a modified DOAS 2000 Instrument (TEI Inc.), as shown in Figure 2.1. The system is composed of a coaxial Cassegrain telescope with transmitting and receiving optics combined within the instrument. A 150 W high pressure xenon-arc lamp is employed as the light source and is placed in the focal plane of the 8" primary telescope mirror. The outgoing beam is collimated on the outer edges of the primary mirror and transverses through an open path in the atmosphere. A retroreflector, composed of 7×2" corner cubes, reflects the light beam back towards the telescope, resulting in total path lengths of 2−3.5 km. The returning light beam is focused onto a fiber optic cable by the inner portion of the primary mirror and is subsequently transmitted into a spectrometer, a device which separates the wavelength components of light and is optimized for the species of interest. Measurements of NO_3 and NO_2 were collected in the red region of the visible spectrum (550−840 nm) with a S2000 spectrometer controlled by OOIBase32 software. Spectra in the UV-visible region (295−492 nm) were collected with a USB2000 spectrometer controlled by Spectrasuite software, generating measurements of HONO, NO_2 and SO_2.

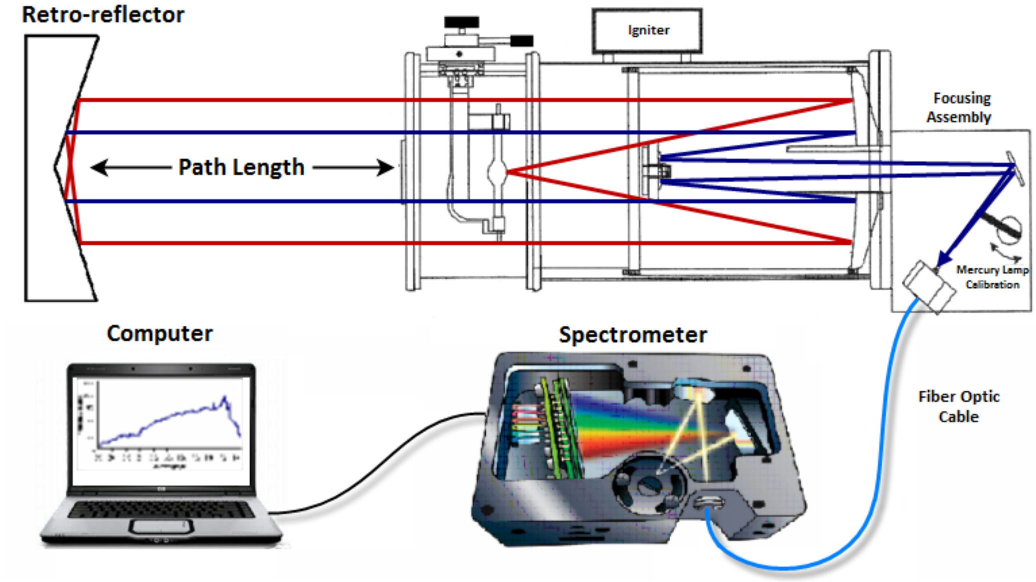

Figure 2.1: Schematic of the DOAS system instrumental setup. The paths for the outgoing and incoming beam are shown in red and blue, respectively.

2.1.1 Spectral Analysis Software

Due to strong interfering solar features present during the daytime, measurements were generally constrained to night-time periods with collection beginning several hours before sunset and lasting until after sunrise. The measured ambient spectra were corrected and analyzed using DOASIS software (Kraus, 2006), which uses the Levenberg-Marquardt algorithm to numerically solve non-linear systems (Levenberg, 1944). The algorithm uses an iterative approach to obtain a continuously improved estimate for the model parameters with each iteration until the optimal solution is found. The method consists of a least squares fit where a linear component is used for the retrieval of the trace gas absorptions in combination with a non-linear component, accounting for spectral shifts between the measured and chosen reference spectrum in attempt to minimize the residual of the fit.

In order to perform a fit, the software requires a predefined fit scenario, consisting of the spectra of the lamp and all species present in the light path with significant absorption features within the chosen wavelength range. Upon completing the algorithm, the software computes a slant column density and a fit error for each trace gas within the selected fit scenario. Subsequently, the mixing ratio for a given species is calculated given the path length of the light beam and the number density of the air mass for a specific temperature and pressure. However, before a fit can be performed, each spectra must be corrected and reference spectra must be convoluted, as discussed in greater detail in the following section.

2.1.2 Electronic Offset and Dark Current

An *offset* consists of the positive baseline signal produced during data sampling and depends exclusively on the detector electronics. Such a baseline is necessary in order to ensure that the signal intensity being fit is attributable to photons projected and received by the telescope.

Offset corrections are applied to the data prior to the fit procedure by subtracting the temperature specific offset spectrum from each collected ambient spectrum.

Offset spectra were collected with an integration time of 3 ms and 10,000 spectral averages. In addition, since the electronic offset reveals a negative dependence with temperature, it must be collected at the same detector temperature as the ambient data. An example of an offset spectrum obtained from the USB2000 spectrometer is shown in Figure 2.2, where the zoomed in baseline signal consists of about 4% of the maximum intensity for the spectrometer.

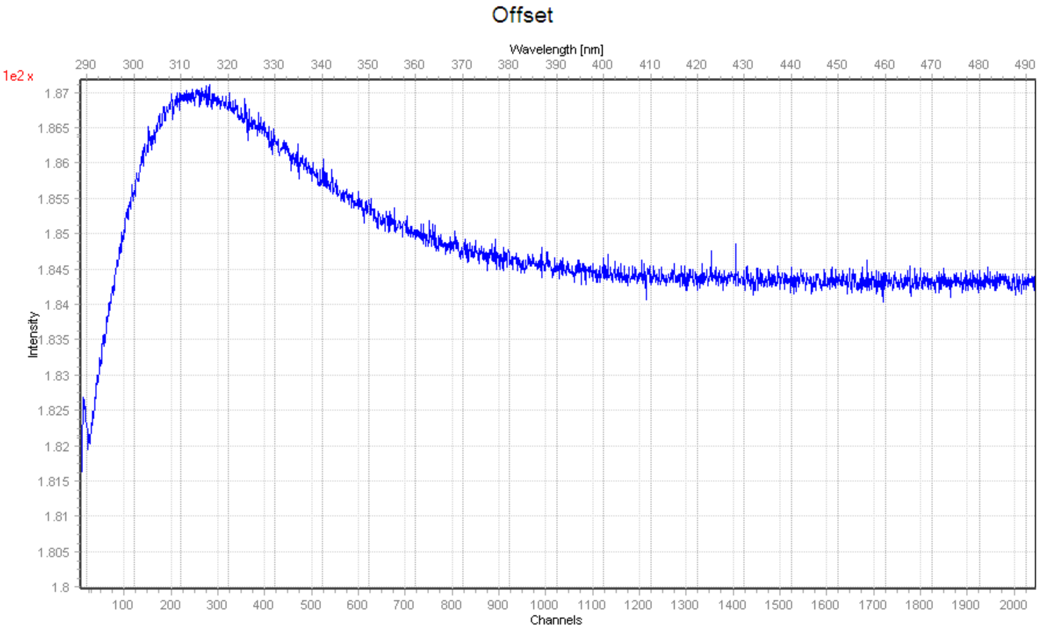

Figure 2.2: Sample offset spectrum collected on March 14, 2011 using the USB2000 spectrometer with integration time of 3 ms, 1000 averages and temperature control stabilized at 5°C.

The *dark current* is the constant response obtained by the detector in the absence of light, as exemplified in Figure 2.3. This pixel to pixel variation is caused by the thermal noise within the detector, and is positively correlated with temperature. The

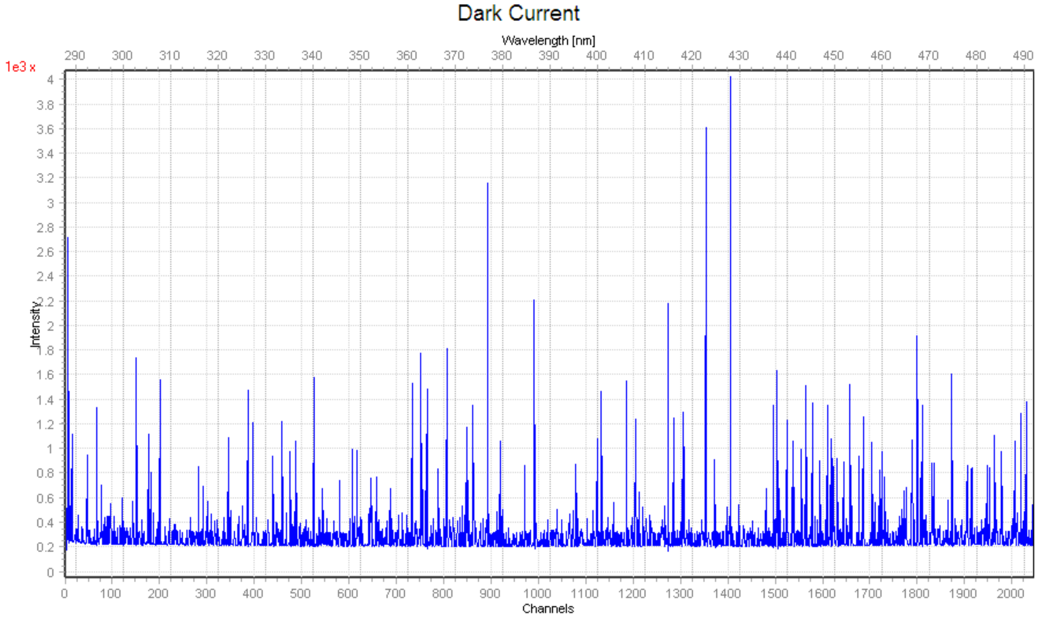

Figure 2.3: Sample dark current spectrum collected on March 14, 2011 using the USB2000 spectrometer with integration time of 25000 ms, 5 averages and temperature control stabilized at 5°C.

detector was generally kept near a relatively low temperature of 5°C in order to reduce the effects of dark current.

The measured dark current spectrum is subtracted from the lamp and measured ambient spectra prior to the fit procedure, correcting each spectrum for pixel hot spots. If temperature fluctuations are present over the course of measurements, the dark current spectrum can be included as an additional species in the fit scenario, effectively removing its features from collected spectra. Thus, dark current and offset spectra should be collected daily or at the beginning and end of each measurement period.

Unlike the offset, the dark current does increase with the exposure time of the measurement since increasing the exposure time increases the time available for hot electrons to be excited. Dark current spectra were measured with an integration time of 20,000 - 30,000 ms and 1 spectral average. Thus, it is important to note that the difference in integration times between the dark current spectrum and the ambient (or lamp) spectra must be accounted for. This task is achieved by multiplying the dark current by a ratio of the integration time used for its collection and the integration time used when obtaining the ambient spectrum to be corrected.

2.1.3 Mercury Lamp Spectrum and Spectral Convolution

A *mercury lamp* spectrum, as displayed in Figure 2.4, is required for wavelength calibration and spectral convolution of reference spectra. The mercury spectrum is collected by directing light from a mercury lamp into the fiber optic cable while blocking incoming light from all other external sources. An integration time of 300 ms and 1 spectral average was generally used.

The discrepancy between the actual and measured wavelength of the spectrometer is a function of temperature and wavelength. The wavelength calibration of ambient spectra was performed using the published values of mercury lines present at 334.15 nm, 365.02 nm, 404.66 nm, 407.78 nm, and 435.84 nm. The mercury lamp calibration function was determined using a 3rd order polynomial and applied to all spectra, correcting any wavelength drifts.

The wavelength shift of a spectrometer can also be determined by fitting a species present in high concentrations and conceding the fitting software unrestricted wave-

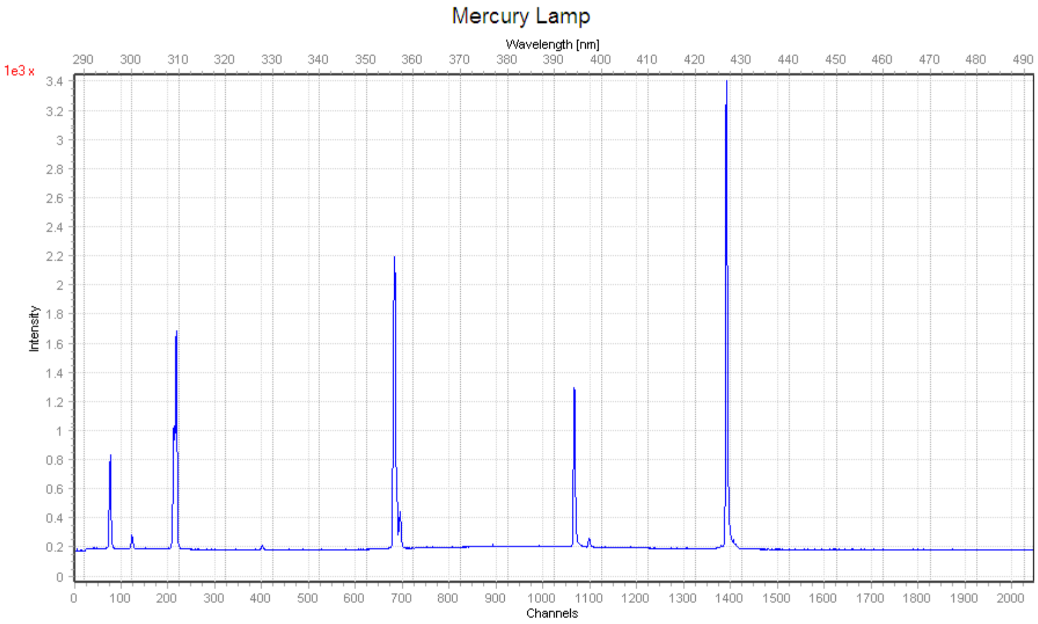

Figure 2.4: Sample mercury lamp spectrum taken on March 14, 2011 using the USB2000 spectrometer with integration time of a 25000 ms, 5 averages and temperature control stabilized at 5°C.

length shifts. The shift obtained from the fit of such species can be subsequently applied to all other species in the fit scenario within a similar wavelength range.

In most cases, absorption cross sections are available in higher resolution than that of the spectrometer. Through a process of *convolution*, the resolution of the reference spectra is tuned to match the spectrometer's. The resolution of the spectrometer is obtained from an emission line in the mercury lamp spectrum near the wavelength region where the fit is to be performed. The resolution of the USB2000 spectrometer was determined to be ∼0.5 nm at 5°C, determined by the full width half maximum (FWHM) of a mercury line near the NO_2 fit range.

2.1.4 Xenon-arc Lamp

A 150 W high-pressure xenon arc lamp was used for all active-DOAS measurements. A light arc is produced between the anode and cathode from a high voltage ignition discharge which ionizes the xenon gas. The small distance between the electrodes produces a short arc length and with the aid of the telescope primary mirror, a highly collimated light beam is emitted by the telescope. The lamp also generates a significant amount of electromagnetic radiation in the ultraviolet wavelength region allowing for measurements of SO_2 and O_3.

Xenon-arc lamp spectra were periodically collected throughout the measurement period. A sample spectrum is shown in Figure 2.5, with a integration time of 250 ms and 1500 averages using the USB2000 spectrometer at 5°C. The lamp spectrum consists of a sum of thermal emissions according to Planck's law with broadened emission lines due to pressure and temperature. The xenon lamp reference spectrum was collected by adjusting the optics of the DOAS system to direct the light emanating from the lamp directly into the fiber optic, without transversing through the open atmosphere. Typical integration times were between $100 - 300$ ms with $1000 - 2000$ averages.

2.1.5 Mode Mixer

A *mode mixer* consists of a modification to the fiber optic cable system implemented by introducing bends in the cable (Stutz and Platt, 1997). This alteration

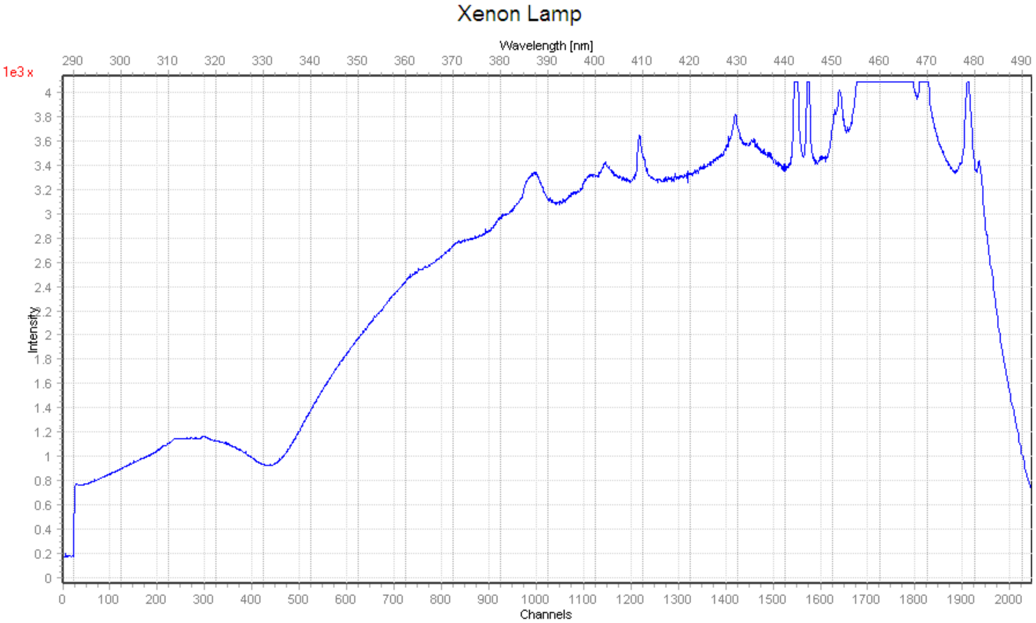

Figure 2.5: Sample xenon lamp spectrum taken on October 5, 2011 using the USB2000 spectrometer with integration time of 250 ms, 1500 averages and temperature control stabilized at 5°C.

results in a homogeneous illumination of the detector which is independent of the angular intensity distribution of the measured light, eliminating unwanted spectral structures.

The original mode mixer design contains bends in one of the directional planes along the fiber optic cable. The bends in the fiber optic were created by passing the fiber through a grating with metal rods approximately 2.5 cm apart with a total grating length of 30 cm. A novel alteration to the original design was created and tested, implementing additional bends along a secondary directional plane, perpendicular to the one in the original mode mixer design using a similar grating.

Absorbance noise (base e) is defined as the standard deviation of the natural logarithm of the ratio of two successive spectra, in a featureless wavelength region. The effect of a 2-dimensional mode mixer on absorbance noise was investigated by performing comparative tests on spectra obtained with 1- and 2-dimensional mode mixers, as well as with no mode mixer. The analysis was performed on the S2000 spectrometer using a path length of 3.44 km and a wavelength range of $600 - 700$ nm. The spectra were collected with 150 ms integration times and 1500 averages. The mode mixer results for absorbance noise, fit error and standard deviation of the fit residual, σ, are summarized in Table 2.1.

Table 2.1: Effects of 1- and 2-dimensional mode mixer on absorbance noise, fit error and residual standard deviation of NO_3 fit.

	No Mode Mixer	1-dimensional	2-dimensional
Aborbance Noise	1.35×10^{-3}	1.10×10^{-3}	8.76×10^{-4}
Fit Error	5.0 ppt	3.2 ppt	1.8 ppt
Fit Residual σ	3.09×10^{-3}	1.95×10^{-3}	1.10×10^{-3}

Thus, a significant reduction in overall noise is observed for spectra obtained with a mode mixer. However, a reduction of approximately 20 and 40% in the outgoing light intensity was observed for 1- and 2-dimensional mode mixers, respectively. For the majority of the measurements, a 1-D mode mixer was used in order to compromise between measurement time length and instrumental noise.

2.1.6 Spectral Fitting Procedure

Upon correcting the ambient spectra for the effects of dark current and offset, performing the necessary wavelength calibration and convoluting the high resolution absorption cross section references, the fit scenario must be specified within the DOASIS software. A fitting range is chosen for each species of interest, generally including the wavelength region where the species' most dominant absorption features are present. Ideally, the fitting range is chosen to be within a featureless region of the lamp spectrum, as well as a region where the absorption interference from other species is minimal. The fit scenario must include all species with significant absorption features contributing to the optical density in the wavelength fitting range, along with the lamp spectrum. In addition, a third or fourth order polynomial is incorporated into the fit, accounting for the slowly varying features present in ambient spectra due to Rayleigh scattering, Mie scattering and instrumental response features.

2.2 Saturna Field Study

Measurements of NO_3, NO_2, SO_2 and HONO were performed by DOAS and mixing ratios of N_2O_5 were calculated within the marine boundary layer for a 3 week period during the Saturna field study in the summer of 2005. The present chapter provides a description of the purpose, location, instrumental details and fitting procedures for the data set obtained at East Point, Saturna Island, which comprises a large focus of this thesis.

2.2.1 Location and Instrumentation

The Saturna field study took place on Saturna Island, within the Strait of Georgia, off the coast of British Colombia from July 23 to August 9, 2005. A map of the Lower Frazer Valley (LFV) is shown in Figure 2.6, displaying the location of the DOAS light path, which extended from the telescope position on East Point, Saturna Island (Latitude: 48°47.034'N and Longitude: 123°2.685'W) to the retro-reflector on Tumbo Island, yielding a total path length of 2.407 km.

Figure 2.6: Map of the Lower Frazer Valley, showing the DOAS path between the telescope located on East Point, Saturna Island and the retro-reflector placed on the tip of Tumbo Island.

The DOAS beam was set at an elevation of 15 m a.s.l. and traveled over the open ocean for the majority of the path length. Throughout the duration of the study, an Environment Canada weather station was set up at the same location as the DOAS telescope, providing meteorological observations at a height of 24 m a.s.l.. A Canadian Air and Precipitation Monitoring (CAPMon) network station was located at an elevation of 195 m a.s.l., 6 km west of the measurement site. The NO_2 levels on site were monitored via chemiluminescence measurements of NO_x, whereas O_3 was determined using a UV photometer which measured the attenuation of light due to O_3 at 254 nm.

Saturna Island is one of the Gulf Islands, positioned in close proximity to major international shipping lanes along the Strait of Georgia, which leads to the Strait of Juan de Fuca and to the open Pacific Ocean. With mainland $20 - 25$ km east across the Strait of Georgia, the closest major urban centers from the measurement site consist of Bellingham WA, 42 km east; Victoria BC, 46 km south-southwest; Vancouver BC 55 km north; and Seattle WA, 142 km south-southeast. Although Saturna Island has a relatively low population density and few anthropogenic sources, the measurement site is heavily affected by emissions from nearby marine vessel traffic. The surrounding region is influenced by a mix of urban, agricultural, marine, and biogenic emissions, leading to O_3 episodes and elevated pollution levels within the LFV.

The purpose of the Saturna field study was to investigate the chemical processing of polluted air masses over a marine environment and their effect on air quality.

It was previously proposed that due to the complex and unique air circulation patterns, polluted air masses can stagnate in the Strait of Georgia overnight and travel back into the Lower Frazer Valley during the following day due to sea breeze circulation. The stagnated air mass over the ocean undergoes nighttime processing of $\mathrm{NO_y}$ and halogenated species. Following the nocturnal accumulation of pollutants in the Straight of Georgia, sea breeze circulations lead to multiple days with elevated particulate matter with aerodynamic diameter up to 2.5 μm ($\mathrm{PM_{2.5}}$) and O_3 levels over the LFV.

The focus of the study consisted of obtaining spectroscopic measurements of nighttime NO_3 and NO_2, and calculations of N_2O_5, in order to determine whether the proposed stagnated pollution pools were indeed present and to study their evolution and impact in the LFV. Fortunately, due to the nature of the DOAS technique, HONO and SO_2 measurements were simultaneously retrieved due to their strong UV absorption features in the wavelength range of the spectrometer used to measure NO_2.

2.2.2 DOAS Fitting Procedure at the Saturna Field Study

Measurements of NO_3, NO_2, SO_2 and HONO were performed using a bifurcated quartz fiber optic cable (Ocean Optics) with dual 400 μm fibers; each leading to a different spectrometer. The dual fiber was optimized for a wavelength range of 250 − 800 nm and was used to simultaneously measure the ideal fit ranges of NO_3 (620 − 670 nm), HONO (335 − 360 nm), NO_2 (420 − 440 nm) and SO_2 (303 − 312 nm).

Measurements of NO_2 and HONO were made by a USB2000 spectrometer (295

$-$ 492 nm, Grating # 10, 1800 lines mm^{-1}, 2048 element CCD, 25 μm slit, UV2 upgrade, L2 lens, 0.5 nm resolution) and spectra were acquired using SpectraSuite software. NO_3 was measured using a S2000 spectrometer (550 $-$ 840 nm, $\lambda_{\text{blaze}} =$ 750 nm, 1200 lines mm^{-1}, 2048 element CCD, 25 μm slit, L2 lens, 0.6 nm resolution) and spectra were collected with the OOIBASE32 software. In this particular study, a diffuser, which accomplishes the same purpose as a mode mixer, was installed at the entrance of the fiber optic in order to lower atmospheric turbulence noise (Stutz and Platt, 1997). The spectrometers were cooled to -5°C in a portable freezer to diminish the effects of dark noise current.

2.2.2.1 NO_3 Fit Procedure

The concentration of NO_3 at the Saturna field study was quantified by performing a fit of the two strong absorption features present at 623 and 662 nm. In order to minimize the detection limits of NO_3 measurements, an early morning or late evening reference spectra substituted the xenon lamp reference spectrum in the fit scenario. Spectra collected in the early morning or evening contain the xenon lamp emission features and also includes absorption features of interfering trace gases such as water. The fitting procedure for such gases is complicated due to the temperature dependence of the absorption cross section. In the early morning or evening reference spectra, the concentration of NO_3 is assumed to be below the detection limit due to photolysis. This was tested and shown to be true by careful and judicious choice of successive ambient spectra in the evening or early morning spectra.

The fit scenario for NO_3 included all species that possess overlapping absorption features within the selected wavelength fit range of $617 - 673$ nm. The fit scenario contained convoluted reference spectra of NO_3 (Atkinson et al., 2004), H_2O (Coheur et al., 2002), $O_2 - O_2$ collision dimer (Hermans et al., 1999), a reference spectrum collected at early morning or evening, a Fraunhofer spectrum (Chance and Spurr, 1997) during daylight periods, and a 3rd order polynomial. A sample NO_3 fit result is shown in Figure 2.7, from which a NO_3 mixing ratio of 49.4 ± 3.3 ppt was determined.

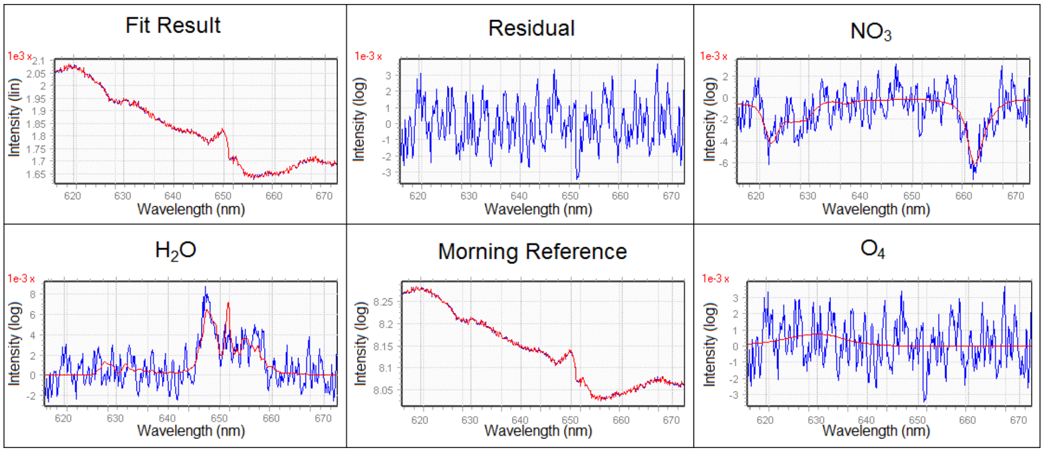

Figure 2.7: DOASIS NO_3 fit result measured on July 26, 2005 at 23:21 using the S2000 spectrometer. The NO_3 mixing ratio obtained from the fit consisted of 49.4 ± 3.3 ppt.

2.2.2.2 HONO and NO_2 Fit Procedure

An overlay of the absorption cross sections of HONO, NO_2 and O_4 is shown in Figure 2.8. The HONO and NO_2 fit regions appear highlighted in blue and red, respectively.

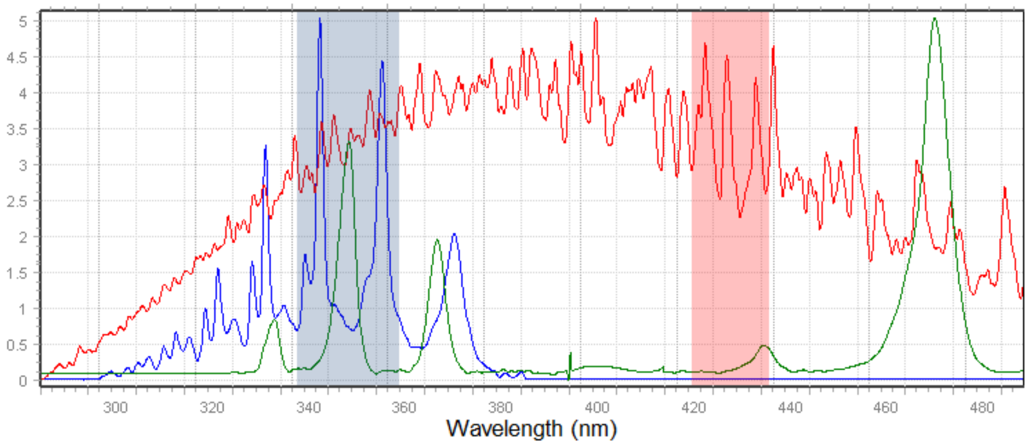

Figure 2.8: An overlay of the absorption cross section of HONO (blue), NO_2 (red) and O_4 (green) within the 295 − 490 nm wavelength range, convoluted to the USB2000 spectrometer. The HONO and NO_2 fit regions are highlighted in blue and red, respectively. The absorption cross sections are not shown to scale.

The fit of HONO was performed for the 337 − 358 nm wavelength region and the fit scenario contained reference spectra of HONO (Bongartz et al., 1994), NO_2 (Voigt et al., 2002), O_4 (Hermans et al., 1999), xenon lamp, Fraunhofer solar reference (if necessary during daylight hours) and a 3^{rd} order polynomial. A sample fit result for data collected on July 31, 2005 at 22:16 is shown in Figure 2.9, from which a HONO mixing ratio of 1.85 ± 0.31 ppb was obtained.

The fit of NO_2 was performed for the 422 − 437.5 nm wavelength region and the fit scenario included a convoluted absorption cross section spectrum of NO_2 (Vandaele et al., 1998), a xenon lamp spectrum, Fraunhofer solar reference (if necessary during daylight hours) and a 3^{rd} order polynomial. A sample fit result for data collected on July 24, 2005 at 21:09 is shown in Figure 2.10.

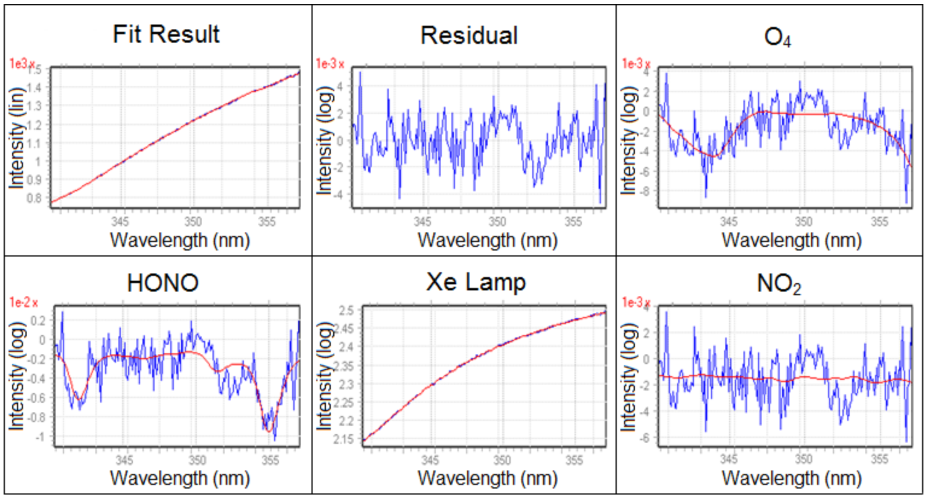

Figure 2.9: DOASIS HONO fit result measured on July 31, 2005 at 22:16 using the USB2000 spectrometer. The HONO mixing ratio obtained from the fit was 1.85 ± 0.31 ppb.

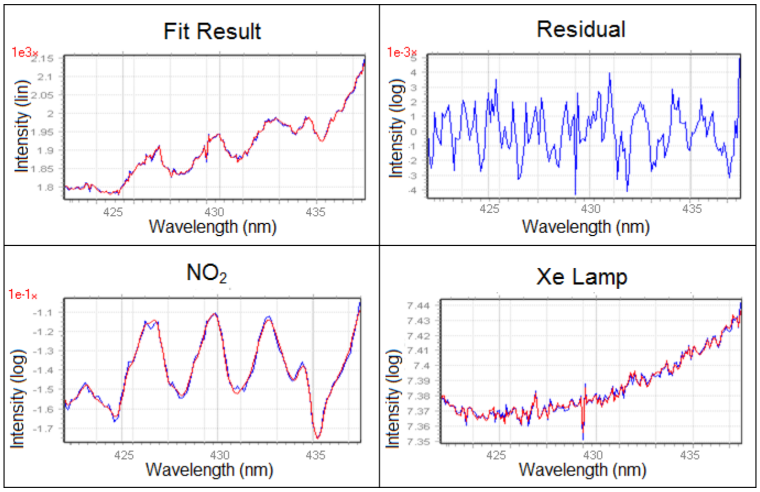

Figure 2.10: DOASIS NO_2 output measured on July 24, 2005 at 21:09 using the USB2000 spectrometer. The NO_2 mixing ratio obtained from the fit was 44.02 ± 0.40 ppb.

2.3 York University Measurements

Measurements of NO_3 and NO_2 were made at York University, Toronto from November to December, 2008 and from March to June, 2009. In addition, a year-long data set of HONO, NO_2 and SO_2 was collected between November 2010 to November 2011. These measurements were collected in order to augment the NO_3 analysis performed for the Saturna field study and to investigate the hypotheses regarding HONO formation proposed according to the findings obtained at Saturna.

2.3.1 Location and Instrumentation

Measurements of NO_3, HONO, NO_2, and SO_2 were collected using an active-DOAS system at York University, Toronto. The location of the DOAS light beam paths for the two data sets and a map of the surrounding greater Toronto area is shown in Figure 2.11.

York University is located within the northern region of the Toronto urban center and is greatly affected by anthropogenic emissions. The major source of NO_x emissions impacting the measurement site is vehicle traffic due to the proximity of major highways to the university. The three major highways which surround the measurement site are Highway 407 (1.7 km north), Highway 400 (2.3 km east) and Highway 401 (6 km south). Lake Ontario is located 16 km south of the site and the Toronto downtown core is approximately 17 km southeast. The southern wind sector is characterized by a mix of freshly emitted pollution from the Toronto downtown

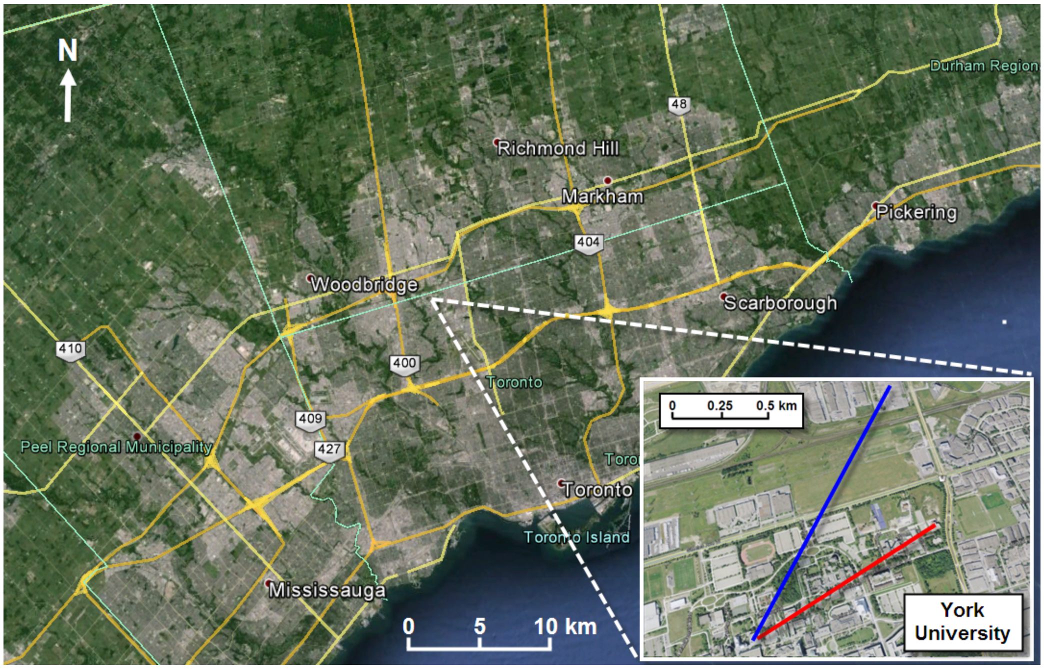

Figure 2.11: Site location for the NO_3 and HONO measurements collected at York University, Toronto. The active-DOAS light beam paths are shown in blue (NO_3 data set) and red (HONO data set), comprising path lengths of 3.4 km and 2.2 km, respectively.

core and aged polluted air mass from the USA. The northern wind sector is generally cleaner, consisting predominantly of biogenic emissions and very aged air masses (Liggio et al., 2010).

The DOAS telescope used to collect the NO_3 data set was housed at an elevation of 13 m a.g.l. and the DOAS retro-reflector was located on a rooftop at an elevation of 11 m a.g.l., yielding a total light path length of 3.44 km. The returning light beam was focused onto a 600 μm quartz fiber optic (Ocean Optics) equipped with a mode mixer. The spectrometer was cooled to 5°C to stabilize the temperature and reduce the effects of dark current. Spectra were collected using OOIBase32 software (Ocean Optics) and a S2000 spectrometer with integration times between $150 - 250$ ms and $1500 - 3000$ averages; yielding a time resolution of $4 - 13$ min. In total, data was collected and analyzed for 42 nights during the measurement period.

The DOAS instrumentation used to collect the HONO data set was located at an elevation of 16 m a.g.l. with the retro-reflector on a rooftop at a height of 17 m a.g.l., comprising a total light path length of 2.2 km. The distance weighted height of the light path above surfaces was calculated to be $\sim$12 m a.g.l. upon taking into account the height of trees and buildings below the beam path. The ground surface below the light beam path consisted approximately of 60% concrete and 40% vegetation. The returning beam was focused onto a 600 μm quartz fiber optic (Ocean Optics) equipped with a mode mixer. The spectrometer was cooled to 12°C using a custom built 2-stage Peltier Cooler (Resonance Inc.). Spectra were collected using SpectraSuite software (Ocean Optics) and a USB2000 spectrometer with integration times between $200 - 600$ ms and 1000 averages; yielding a time resolution of $3 - 10$ min. In total, data was collected and analyzed for 242 nights during the one-year period.

The longest day (summer solstice) in Toronto within the HONO measurement period was June 21, 2011, with sunrise and sunset times of 5:36 and 21:03, respectively. The shortest day (winter solstice) was December 21, 2010 with sunrise at 7:48 and sunset at 16:44. Significant amounts of snow ground cover were observed nearly continuously between December 6, 2010 to March 10, 2011.

2.3.2 DOAS Fitting Procedure at York University

The NO_3, HONO and NO_2 fits of spectra measured at York University were carried out in very similar fashion as for the data obtained at the Saturna field study, previously described in Chapter 2.2.2.2. The York University data sets were collected with an active-DOAS system and used a single fiber optic cable instead of the dual, as implemented for the measurements at Saturna Island. Besides performing the usual dark current correction, a dark current spectrum was also added to the fit scenario. This alteration ensures the removal of any left over noise due to dark current effects. Visually noticeable pixel hot spots unaccounted for by the dark current subtraction were also removed by including single pixel spectra within the fit scenario. The combinatory effect of these changes consisted of a significant increase in the quality of the NO_3, HONO and NO_2 fits at York University as compared to Saturna's, quantified by the magnitude of noise in the residuals.

2.3.2.1 NO_3 and NO_2 DOAS Fits

The fit scenarios and absorption cross section reference spectra utilized for the NO_3 fits were identical to those employed at Saturna Island. Detection limits (3σ) were calculated by repetitive assessment of a low concentration sample and were found to be approximately $2-4$ ppt. A sample DOASIS fit result of NO_3 is shown in Figure 2.12, corresponding to a mixing ratio of 31.1 ± 3.7 ppt.

The NO_2 fit was performed in the $560 - 605$ nm wavelength region and the fit

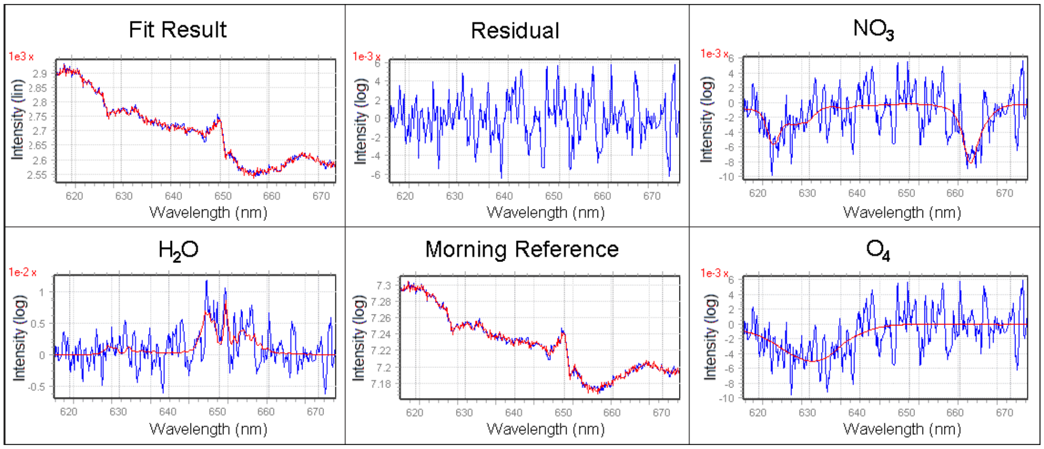

Figure 2.12: DOASIS NO_3 output measured on April 17, 2009 at 22:11 using the S2000 spectrometer. The NO_3 mixing ratio obtained from the fit was 31.1 ± 3.7 ppt.

scenario included a convoluted absorption cross section spectrum of NO_2 (Vandaele et al., 1998), H_2O (Coheur et al., 2002), O_4 (Hermans et al., 1999), a xenon lamp spectrum, Fraunhofer solar reference (if necessary during daylight hours) and a 3rd order polynomial. A sample fit result for data collected on April 16, 2009 at 21:31 is shown in Figure 2.13. Detection limits (3σ) were found to be 1 ppb.

2.3.2.2 HONO and NO_2 DOAS Fits

The fit scenarios and absorption cross section reference spectra utilized for the analysis of the HONO data set were identical to those employed at Saturna Island. Detection limits (3σ) were calculated by repetitive assessment of a low concentration sample and were found to be approximately 0.15 ppb and 0.3 ppb for HONO and NO_2, respectively. A sample DOASIS fit result of HONO is shown in Figure 2.14, from which a mixing ratio of 4.27 ± 0.21 ppb was obtained. A sample DOASIS fit result for NO_2, corresponding to a mixing ratio of 41.2 ± 0.2 ppb is shown in Figure 2.15.

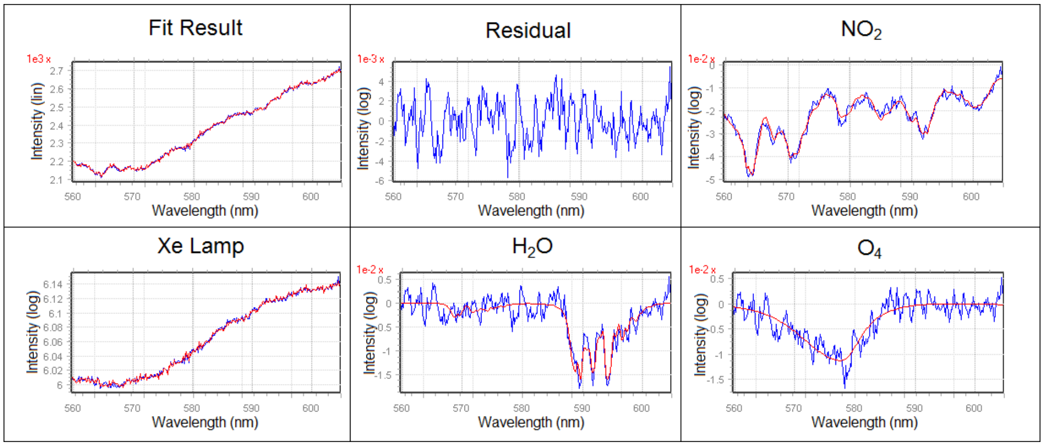

Figure 2.13: DOASIS NO_2 output measured on April 16, 2009 at 21:31 using the S2000 spectrometer. The NO_2 mixing ratio obtained from the fit was 46.3 ± 1.0 ppb.

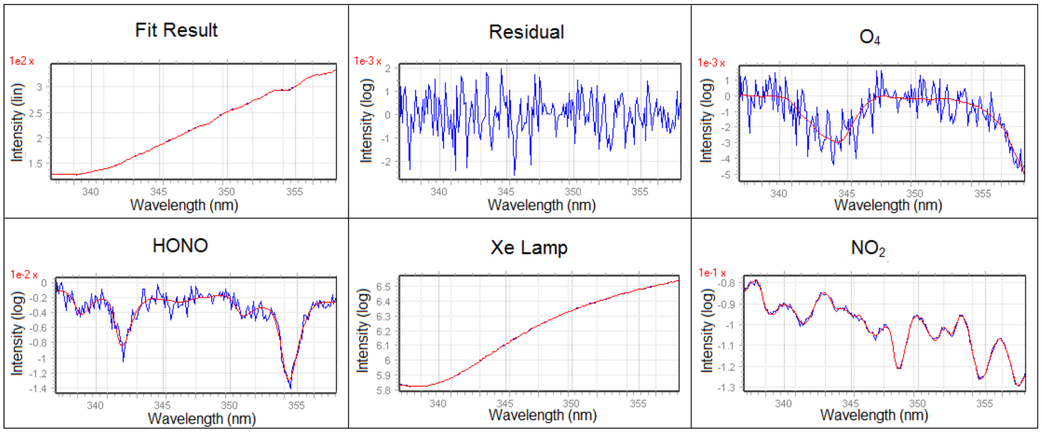

Figure 2.14: DOASIS HONO output measured on February 16, 2011 at 5:29 using the USB2000 spectrometer. The HONO mixing ratio obtained from the fit was 4.27 ± 0.21 ppb.

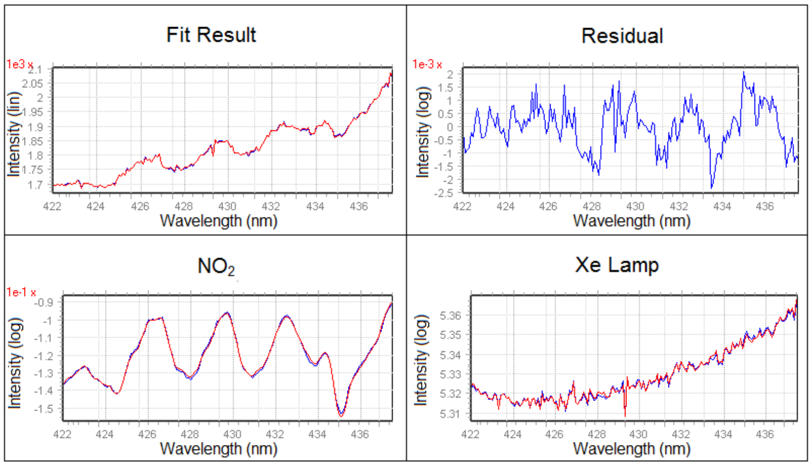

Figure 2.15: DOASIS NO_2 output measured on October 9, 2011 at 1:14 using the USB2000 spectrometer. The NO_2 mixing ratio obtained from the fit was 41.2 ± 0.2 ppb.

2.3.3 Ozone Measurements by UV Photometry

Ozone measurements were performed from December 2010 to November 2011 using a UV photometric ambient ozone analyzer (Thermo Environmental Instruments Inc., Model 49-003). The UV photometer determines the ozone concentration by measuring the attenuation of light due to ozone at a wavelength of 254 nm within an absorption cell. The system withdraws air from an inlet located 16 m a.g.l. within the same building as the DOAS telescope. The instrument contains two identical absorption cells with a shared light source, a low pressure mercury vapor lamp, and sample source. One of the cell measures a reference gas (ambient air flowing through a charcoal ozone scrubber) while the other cell simultaneously measures the sample. The sample and reference are subsequently swapped between the cells and measured once again, yielding an average signal for the sample and reference. By making use of the Beer-Lambert law, the instrument outputs the ozone mixing ratio with a time resolution of two minutes and a detection limit (3σ) of 0.4 ppb.

2.3.4 Meteorological Measurements at York University

Meteorological observations of air temperature, relative humidity, Δtemperature ($\mathrm{T_{9.5m}} - \mathrm{T_{1m}}$), corrected wind speed, wind direction, total precipitation, and downwelling shortwave radiation were collected at York University by the Earth and Space Science and Engineering Meteorological Observation Station (EMOS). The meteorological observations were performed 310 m northwest of the DOAS telescope. Daily snow depth measurements were available from the Environment Canada North York station which is located 2.7 km east from the measurement site and hourly $\mathrm{PM_{2.5}}$ and $\mathrm{O_3}$ data were available from the Ministry of the Environment Toronto North station, located 6.8 km east from the DOAS instrument.

2.3.5 DOAS Detection Limits Summary

A summary of the DOAS detection limits (3σ) for $\mathrm{NO_3}$, $\mathrm{NO_2}$ and HONO during the Saturna field study and for measurements made at York University is shown in Table 2.2. Detection limits of $\mathrm{NO_3}$, $\mathrm{NO_2}$ and HONO at the Saturna field study were 4 ppt, 0.2 ppb and 0.3 ppb, respectively. Detection limits of $\mathrm{NO_3}$, $\mathrm{NO_2}$ and HONO at York University were 2−4 ppt, 0.15 ppb and 0.2 ppb, respectively. The detection limits were calculated by repetitive determination of a low concentration sample.

Table 2.2: A summary of the DOAS detection limits (3σ) for NO_3, NO_2 and HONO during the Saturna field study and at York University.

Species	Saturna Island	YorkU
NO_3 (ppt)	4	2–4
NO_2 (ppb)	0.2	0.15
HONO (ppb)	0.3	0.2

3 Results and Discussion

Measurements and analysis of NO_3, NO_2, and HONO at the Saturna field study between July 23, 2005 and August 9, 2005 will be summarized. Observations of NO_3 and NO_2 between November 2008 and June 2009 at York University will be presented and discussed. Mixing ratios of HONO and NO_2, measured at York University from November 2010 to November 2011, will also be presented.

3.1 NO_3 during the Saturna Field Study

Measurements of NO_3 and NO_2 at the Saturna field study using an active-DOAS system will be summarized. The NO_3 and N_2O_5 data set and analysis presented in this section was published in Atmospheric Chemistry and Physics in May 2010 (McLaren et al., 2010). The data was collected at Saturna Island by Dr. Robert McLaren, Dr. Daniel Majonis, Joy McCourt and Dr. Jamie Halla. The spectral fitting of the data was done by Patryk Wojtal and the data set analysis was performed by Patryk Wojtal and Dr. Robert McLaren.

The procedure employed to calculate N_2O_5 mixing ratios will be discussed, along with a validation of the overall method. A theoretical and observational comparison between the steady-state and non steady-state lifetimes of NO_3 and N_2O_5 will be presented. Lastly, a rationale will be provided to explain the observed connection between enhancements of O_3 in the LFV and the chemistry occurring during the previous night within the Straight of Georgia.

3.1.1 Overview of NO_3, NO_2, N_2O_5 and O_3

An overview of the measurements of NO_3 and NO_2 at the Saturna field study, as well as the calculated N_2O_5 time series is shown in Figure 3.1 (see Chapter 3.1.2 for explanation of calculated N_2O_5). A statistical summary of the measurements is shown in Table 3.1, along with meteorological parameters and lifetimes which play a significant role in the analysis of the data. The analysis was performed for measurements taken between 20:00 and 8:00 PDT, henceforth called the dark period, yielding nighttime mean and median NO_3 mixing ratios of 13.1 ppt and 10.2 ppt, respectively. Mixing ratios larger than 20 ppt were observed every night, with maximum levels between $22 - 57$ ppt.

The temporal variation of NO_3, grouped into 30-minute time bins, is shown in Figure 3.2. Levels of NO_3 below detection limit were observed during the daytime due to photolysis, subsequently accompanied by a steady rise due to the reaction between NO_2 and O_3. As reflected by the 25th and 75th percentiles, overall NO_3 mixing ratios were highly variable throughout the night, presumably due to NO or other nighttime sinks, or variation in the air mass source of NO_2. Average NO_3 mixing ratios were highest for a ~2 hour period between 0:30 and 2:30, slowly decaying thereupon until levels below detection limit were reached shortly after sunrise.

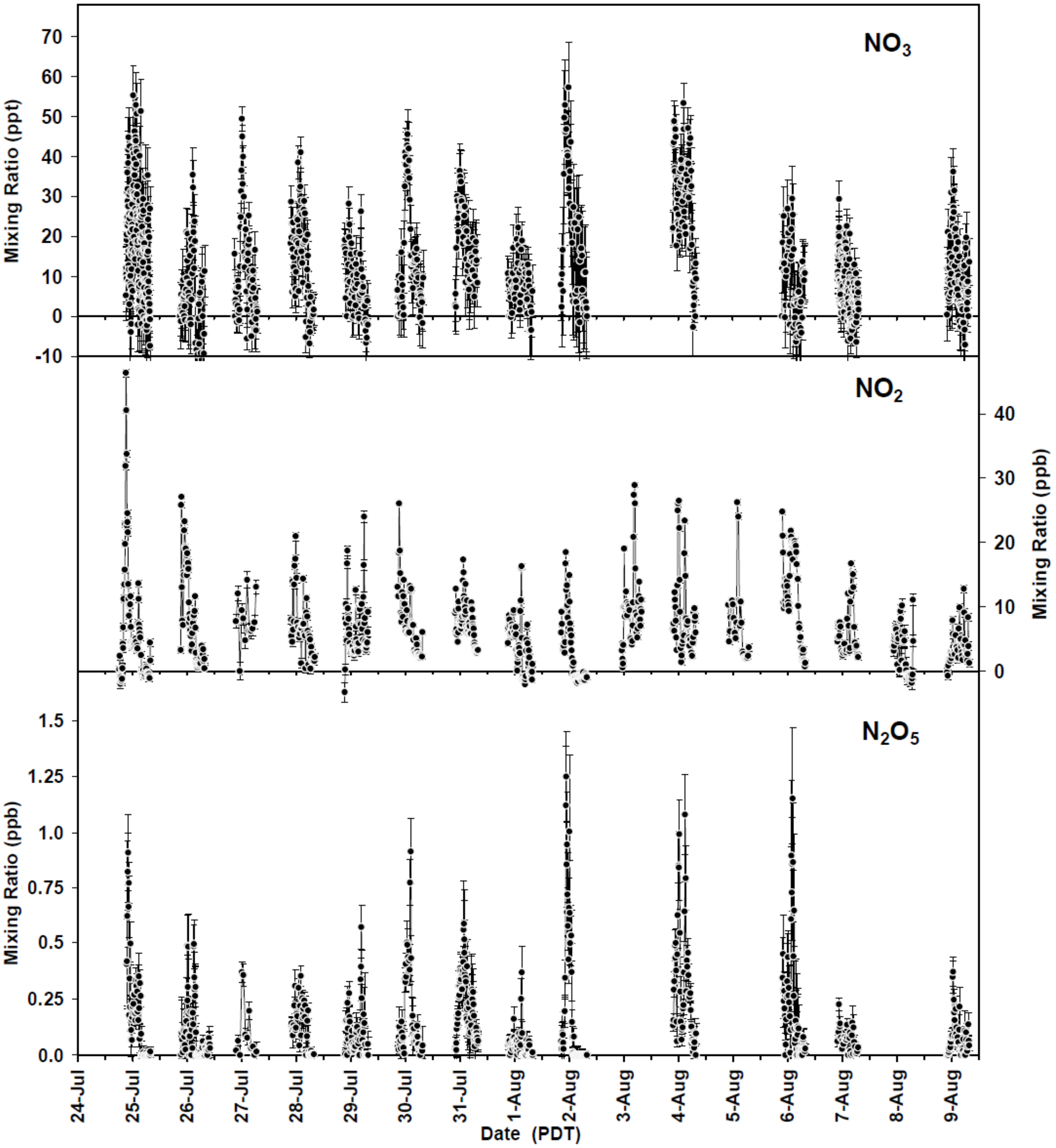

Figure 3.1: Overview of DOAS measurements of NO_3, NO_2 and calculated N_2O_5 at the Saturna field study.

Table 3.1: Overview of statistics for the Saturna field study; (^{a}) $\tau^*_{NO_3}$ (Equation 3.10), τ_{SS} (Equation 3.2) and F(NO_x) (Equation 3.1) calculated for NO_2>1.2 ppb and NO_3>4 ppt. (^{b}) $F(NO_x) = \frac{[NO_3]+2[N_2O_5]}{[NO_3]+[NO_2]+2[N_2O_5]}$. (^{c}) Hourly averages of MET parameters. The number of observations is represented by N.

	Max	95%	75%	Average	Median	25%	Min	N
NO_3 (ppt)	57.3	38.4	20.7	13.1	10.2	3.8	<DL	952
NO_2 (ppb)	45.9	19.0	9.0	6.4	5.2	2.2	<DL	810
N_2O_5 (ppt)	1253	565	205	139	76	14.4	<DL	678
O_3 (ppb)	84.6	60.3	37.5	29.2	24.9	18.8	<DL	528
$\tau^*_{NO_3}$ (sec)^a	4231	811	218	224	106	42	<DL	452
τ_{SS} (sec)^a NO_3	2592	594	258	208	136	63	10	452
F(NO_x)^{a,b}	0.203	0.123	0.076	0.057	0.050	0.030	0.009	452
T (°C)^c	24.6	22.1	19.8	18.3	18.0	16.5	14.4	192
RH (%)^c	90	86	82	76	79	71	50	192
H_2O (%)^c	1.94	1.82	1.66	1.56	1.56	1.47	1.21	192
WS ($km\,h^{-1}$)^c	30.0	20.9	17.0	11.1	11.0	6.0	0	192

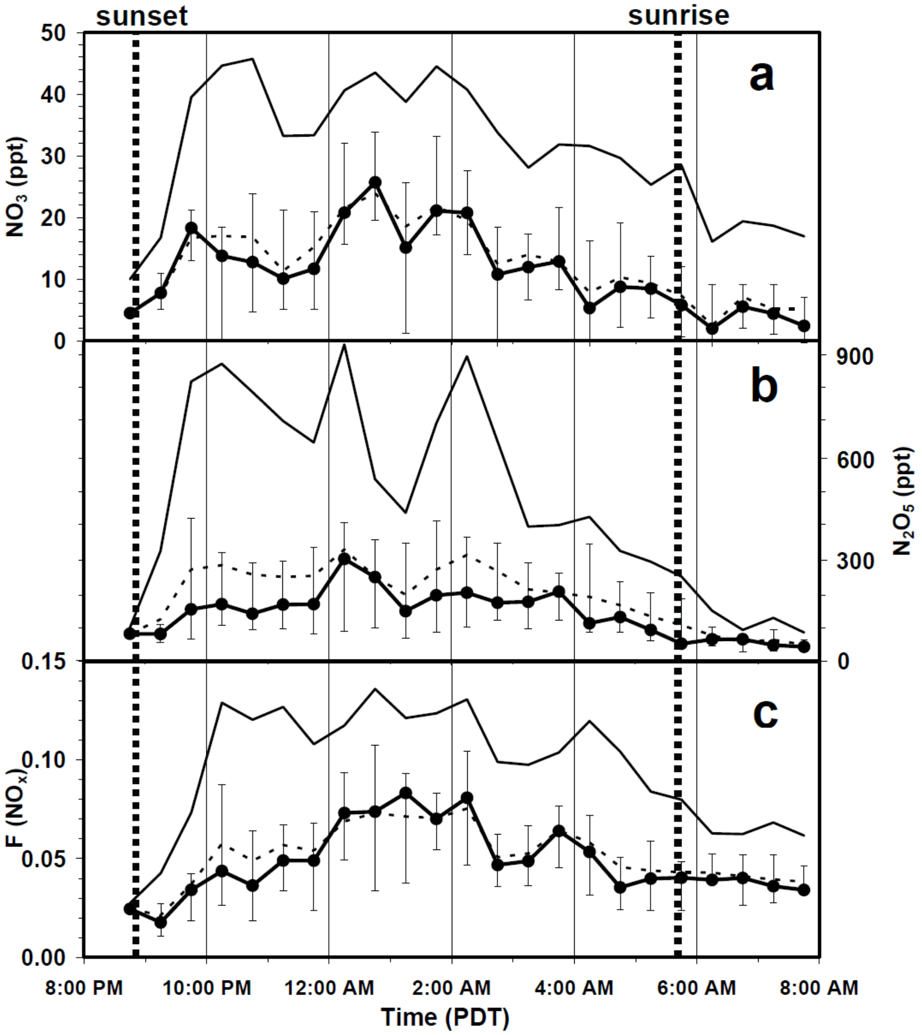

Figure 3.2: Measurement overview grouped into 30-minute time bins for (a) NO_3, (b) N_2O_5, and (c) $F(NO_x)$ - the nocturnal partitioning of nitrogen in nighttime reservoir species. The median (thick solid line) is shown along with the 25th and 75th percentiles (error bars), 95th percentiles (thin solid line) and the average mixing ratios (dashed line).

The median nighttime NO_2 mixing ratio measured at Saturna was 5.2 ppb with a maximum mixing ratio of 45.9 ppb, indicative of a polluted MBL. The observed levels of NO_2 were generally higher in the early evening and slowly decayed overnight, with sharp peaks from ship plumes impacting the site throughout the night. In comparison to recent studies of nighttime chemistry in a MBL (Allan et al., 2000; Martinez et al., 2000; Vrekoussis et al., 2004; Matsumoto et al., 2006; Vrekoussis et al., 2007), the mixing ratios observed at Saturna are relatively high. Such elevated background levels of NO_x can be attributed to a few factors, such as the close proximity of the measurement site to large cities, from which significant amounts NO_x are emitted. In addition, major shipping lanes are located in the Straight of Georgia and significant emissions of NO_x from marine vessels have been quantified (Metro-Vancouver, 2007). Due to the unique air circulation patterns in the Straight of Georgia, an overnight accumulation of air pollutants was proposed (Brook et al., 2004). These overnight stagnation events were shown to also occur from measurements taken at the Saturna field study (Halla, 2013).

A comparison between NO_2 diurnal profiles, averaged into 1-hour time bins, taken by the DOAS instrument at Saturna Island, Eastern Point (SAT-EP), and surrounding monitoring stations within the LFV is shown in Figure 3.3. Highest overall mixing ratios were observed at the north western region of the valley, with the highest levels reported at downtown Vancouver, station T01. Although significant amounts of NO_2 were observed with the DOAS system at Saturna Island, the measured levels are relatively low in comparison to inland monitoring stations.

Another monitoring station located within Saturna Island (SAT-CAP), positioned 6 km west of the DOAS instrument and at an elevation of 200±5 m, measured signifi-

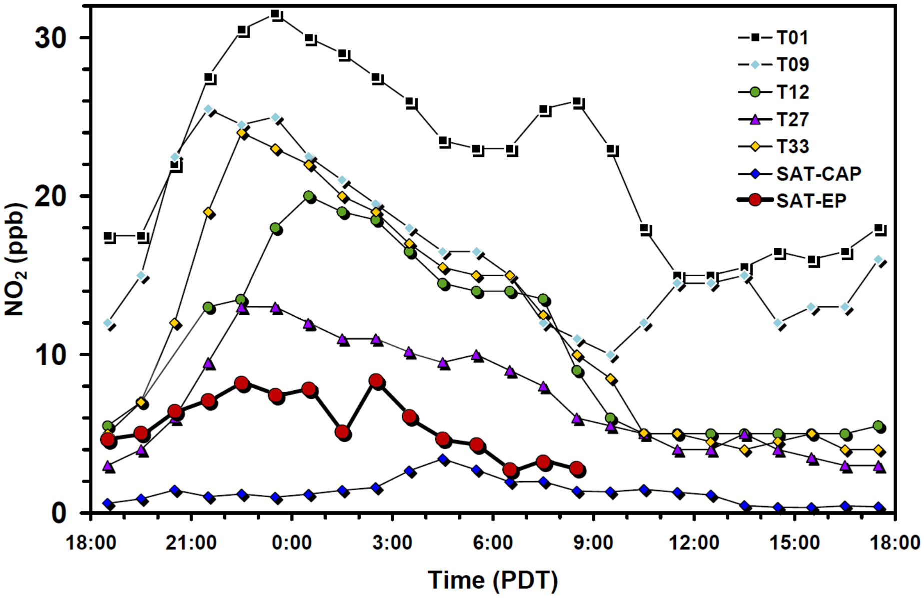

Figure 3.3: Observation of 1-hour averaged NO_2 diurnal profiles for various monitoring stations in the LFV for the study period. The DOAS instrument employed at Saturna island, East Point corresponds to the SAT-EP series, whereas the Canadian air and precipitation monitoring network is denoted as SAT-CAP, and was also located within the island.

cantly lower levels of NO_2 than the DOAS system at East Point. This observation can be explained by the difference in elevation between the two measurements. Since the DOAS instrument was positioned at an elevation of 15±9 m a.s.l., exposure to surface emissions within the MBL and surrounding area are presumed, while the SAT-CAP station was likely above the nocturnal MBL and decoupled from the pollution trapped within it. Another possible explanation for the observed discrepancy is attributed to the difference in wind patterns between the two locations. The DOAS measurement site was located at the north east tip of the island, in close proximity to major shipping lanes along the Straight of Georgia. Emissions from marine vessels within the Straight and land breezes from the LFV are presumably confined to the Straight of Georgia due to the Gulf Islands, which act as a physical barrier to surface emissions. Thus, the topography of the island may prevent the SAT-CAP station from being impacted, resulting in the observed discrepancy between measurements of NO_2 taken at the two sites.

The dependence of NO_3 and NO_2 on wind direction at East Point is shown in Figures 3.4a and 3.4b, respectively. The NO_3 mixing ratio shows little dependence on wind direction, suggesting the lack of direct point sources of NO_3 and alluding to a homogeneous air mass. Spatial inhomogeneities in the air mass probed by the

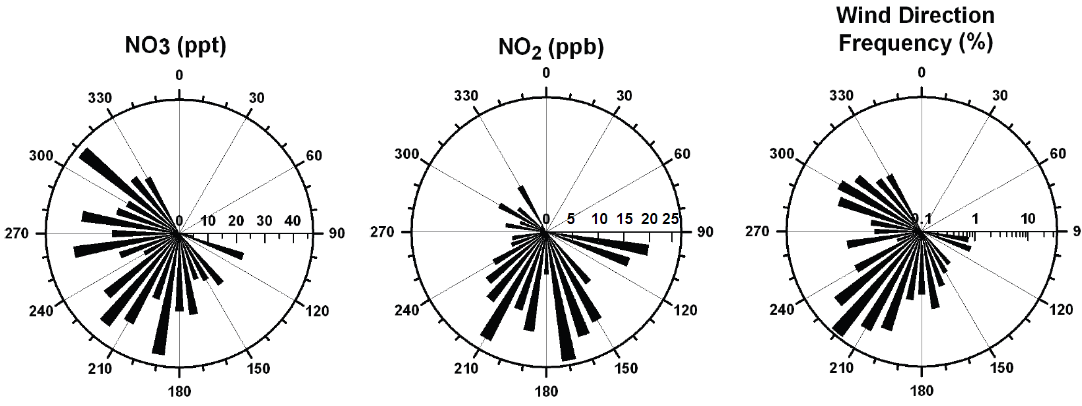

(a) (b) (c)

Figure 3.4: Wind rose plots of (a) NO_3, (b) NO_2 and (c) wind direction frequency. The plots only include measurements taken for wind speeds greater than $2\,\mathrm{km\,h^{-1}}$. The NO_3 and NO_2 mixing ratios displayed on the graphs consist of the 95th percentile of each 10° wind direction bin.

DOAS instrument may be present due to ship plume emissions impacting the site; however, these occurrences were not frequently observed and were easily identifiable. The highest levels of NO_2 were observed from the southeast and southwest sectors. Since the closest proximity of marine vessels to the measurement site occurs at the southeast region of the island, the high NO_2 mixing ratios observed from the southeast are expected. In addition, the southwest sector is aligned with a major shipping channel. It can be concluded that the high levels in both sectors arise from marine vessels, while the lower mixing ratios correspond to background emissions from the surrounding area.

The two main wind sectors which impact the measuring site at East Point can be deduced from Figure 3.4c, which displays the wind direction frequency. The first main sector is from the southwest (195−245°), accounting for 67% of all nighttime observations, while the second major sector is from the northwest (285−335°), accounting for 18% of the observations. Interestingly, the two wind sectors coincide with the direction of the major shipping channels within the Straight of Georgia. The northwest sector presumably contains outflow from Vancouver and the surrounding area (Hedley and Singleton, 1997), while the southwest sector likely comprises outflow from Victoria.

The median and average mixing ratios of O_3 at Saturna Island were 24.9 ppb and 29.2 ppb, respectively. These levels were significantly higher than those observed at all monitoring stations within the LFV, with mixing ratios ranging from 1.0−18.5 ppb among 19 stations. The observed discrepancy can be attributed to the frequent titration of O_3 at the mainland stations due to the close proximity of NO_x emissions and to the higher O_3 rate of deposition over land than water, due to the low solubility of O_3 in water (Walcek, 1987).

3.1.2 N_2O_5 Partitioning

The mixing ratios of N_2O_5 at Saturna were calculated based on the well understood temperature dependent equilibrium of the reaction $NO_2 + NO_3 \rightleftharpoons N_2O_5$. The ambient temperature was measured by the Environment Canada weather station and the equilibrium constant was determined using the forward and reverse rate constants, recommended by (Atkinson et al., 2004).

The value of the equilibrium rate constant was determined with 20% uncertainty and calculated as $K_{eq}{=}k_{(NO_2+NO_3)}/k_{(N_2O_5)}$ (Wängberg et al., 1997), with overall uncertainty for a single point of ±28% at the 95th percentile ($\sim$ 550 ppt). The calculation assumes a rapid formation of the equilibrium between NO_3, NO_2 and N_2O_5; generally a reasonable assumption for warm temperatures. The equilibrium may take up to several hours to form in colder environments (Osthoff et al., 2007). In order to verify if the equilibrium was achieved at the Saturna study, the lifetimes of NO_3 and N_2O_5 were calculated using the forward and reverse equilibrium rate constants. For a temperature of 18°C and a NO_2 mixing ratio of 5.2 ppb (study median), the rate constant for NO_2 + NO_3 is 1.3×10^{-12} cm^3 molec^{-1} s^{-1}, leading to a NO_3 lifetime of 6 seconds. Under identical conditions, the rate of the thermal decomposition of N_2O_5 is 1.9×10^{-2} s^{-1}, yielding a N_2O_5 lifetime of 53 seconds. Due to the high turnover times of NO_3 and N_2O_5, it is strongly believed that the assumption is valid and equilibrium is rapidly established.

The nighttime average and median levels of N_2O_5 were calculated to be 139 ppt and 76 ppt respectively, with a high of 1.3 ppb. The maximum mixing ratio on each night was > 229 ppt, with a median nighttime maximum of 575 ppt. An overview of the results grouped into 30-minute time bins is shown in Figure 3.2. The N_2O_5 mixing ratio generally remained between $120-310$ ppt, with slightly higher levels at dusk and a slow observable decrease throughout the night. Previous measurements in a moderately polluted MBL off the east coast of the USA reported average nighttime N_2O_5 levels of 84 ppt and highs of 1.0 ppb, with an average NO_2 mixing ratio of 4 ppb (Brown et al., 2004). N_2O_5 levels as high as 2 ppb were reported during pollution events on the edge of the Baltic Sea during summertime (Heintz et al., 1996). In addition, N_2O_5 was reported in excess of 700 ppt in the coastal area of Houston, for which levels of NO_y were $\sim$20 ppb (Osthoff et al., 2008). Thus, the calculated N_2O_5 mixing ratios at Saturna are consistent with the previous measurements for polluted air masses in the MBL.

The average and median values of the N_2O_5/NO_3 ratio for this study were 10.4 and 8.1, respectively. The calculated ratio is relatively large and can be attributed to the high levels of NO_2 present at Saturna. The N_2O_5/NO_3 ratio is a useful quantity which reflects the relative level of each species for a combined pool of $(NO_3 + N_2O_5)$. Due to the rapidly established equilibrium, an increase in the ratio signifies a larger loss of NO_3 into N_2O_5. The large value observed for the ratio leads to an increase in potential indirect losses of NO_3 via heterogeneous and homogeneous reactions of N_2O_5, which are discussed and quantified in Chapter 3.1.3.2. Previous studies found that the loss of NO_3 was mainly due to reaction with DMS in the remote marine air (Martinez et al., 2000), while indirect loss of NO_3 via N_2O_5 dominated in a moderately polluted MBL (Allan et al., 2000).

Another useful parameter consists of the molar partitioning of the nighttime reservoir species (NO_3 and N_2O_5) to the total oxidized nitrogen (NO_y) (Brown et al., 2003b; McLaren et al., 2004). Due to the lack of available measurements of other NO_y species at the site, the nocturnal partitioning, $F(NO_x)$, using the three species in the equilibrium between NO_3, NO_2 and N_2O_5 is defined as:

$$F(NO_x) = \frac{[NO_3] + 2[N_2O_5]}{[NO_3] + [NO_2] + 2[N_2O_5]} \tag{3.1}$$

$F(NO_x)$ measured the proportion of nitrogen oxide stored in the nocturnal reservoir of NO_3 and N_2O_5. Thus, high values of $F(NO_x)$ correspond to long lifetimes of NO_3 and N_2O_5. The temporal variation of $F(NO_x)$, averaged into 30-minute bins is shown in Figure 3.2, and an overview of the statistics is summarized in Table 3.1. From the observations, the average $F(NO_x)$ increased steadily throughout the night, starting at 2%, and stabilized ~7.5% between 00:30−2:30, before steadily declining to ~4% throughout the remainder of the night. The results suggest that the lifetime of the combined NO_3 and N_2O_5 is largest in the middle of the night; an observation which will be discussed in greater detail in Chapter 3.1.3.2. These results are consistent with another study performed in a moderately polluted MBL during summertime, which reported a F(NO_x) value of ~5% (Brown et al., 2004).

3.1.3 Lifetime and losses of NO_3 and N_2O_5

3.1.3.1 Theoretical Derivation

NO_3 is formed according to Reaction R 1.30 and through the thermal decomposition of N_2O_5. An equilibrium in the NO_2-NO_3-N_2O_5 system is reached when the forward and reverse reactions ($NO_2 + NO_3 \rightleftharpoons N_2O_5$) within the system occur at the same rate, leading to no net change in composition for the system $\left(\frac{[NO_2][NO_3]}{[N_2O_5]} = \text{constant}\right)$. A steady-state approximation for the NO_2-NO_3-N_2O_5 system can be used given that the rates of production and loss for each constituent of the system are approximately in balance, leading to roughly constant levels $\left(\frac{d[NO_3]}{dt} = \frac{d[N_2O_5]}{dt} = 0\right)$. In the steady-state scenario, the rate of change of the system's concentration is small in comparison to its rates of formation and removal (Brown et al., 2003a).

With knowledge of its sources and sinks, the NO_3 lifetime (τ_{NO_3}) can be calculated. Assuming that the system is in a steady-state balance between sources and sinks of NO_3 and N_2O_5 and that an equilibrium is rapidly established between the NO_3 and N_2O_5 forward and reverse reactions, the steady state lifetime of NO_3 is given by (Martinez et al., 2000):

$$\tau_{SS}(NO_3) = \frac{[NO_3]}{k_{(NO_2+O_3)}[NO_2][O_3]} \tag{3.2}$$

As shown by (Brown et al., 2003a), although an equilibrium can be rapidly established, a steady-state may take several hours to form. This consideration must be taken into account when performing lifetime calculations for NO_3, as biased results may be obtained if the steady-state condition is erroneously assumed.

For this study, it is assumed that an equilibrium is established between the NO_3 and N_2O_5 forward and reverse reactions, as previously demonstrated from the lifetimes of NO_3 and N_2O_5, although the steady-state assumption may not be valid. The steady-state assumption may not be applicable under conditions of moderate to high NO_2, colder temperatures or for very clean air masses for which the sinks of NO_3 and N_2O_5 are small (Brown et al., 2003a). For the presented analysis, substantial levels of NO_2 were observed, possibly slowing down the approach to steady-state. Thus, in order to derive an expression for the non steady-state lifetime of NO_3, a combined reservoir of NO_3 and N_2O_5 was considered. For a scenario where NO_3 and N_2O_5 are in equilibrium, the rate of change for the reservoir is solely dependent on chemical sources ($S_{(\mathrm{NO_3+N_2O_5})}$) and sinks ($L_{(\mathrm{NO_3+N_2O_5})}$), excluding fluxes:

$$\frac{d([\mathrm{NO_3}]+[\mathrm{N_2O_5}])}{dt} = S_{(\mathrm{NO_3+N_2O_5})} - L_{(\mathrm{NO_3+N_2O_5})} \tag{3.3}$$

The only significant source to the reservoir consists of the production of NO_3 through Reaction R 1.30. Thus, the expression for the sources to the reservoir takes the following form:

$$S_{(\mathrm{NO_3+N_2O_5})} = k_{(\mathrm{NO_2+O_3})}[\mathrm{NO_2}][\mathrm{O_3}] \tag{3.4}$$

The chemical sinks consist of the external losses of NO_3 and N_2O_5 and can be expressed as a pseudo first order loss:

$$L_{(\mathrm{NO_3+N_2O_5})} = L_{\mathrm{NO_3}} + L_{\mathrm{N_2O_5}} = k_{\mathrm{x}}[\mathrm{NO_3}] + k_{\mathrm{y}}[\mathrm{N_2O_5}] \tag{3.5}$$

where k_{x} and k_{y} are the overall pseudo first order rate constants for the loss of $\mathrm{NO_3}$ and $\mathrm{N_2O_5}$, respectively. By substituting the expressions for $S_{(\mathrm{NO_3+N_2O_5})}$ and $L_{(\mathrm{NO_3+N_2O_5})}$ into Equation 3.3, one obtains:

$$k_{(\mathrm{NO_2+O_3})}[\mathrm{NO_2}][\mathrm{O_3}] - \frac{d[\mathrm{NO_3}]}{dt} - \frac{d[\mathrm{N_2O_5}]}{dt} = k_{\mathrm{x}}[\mathrm{NO_3}] + k_y[\mathrm{N_2O_5}] \tag{3.6}$$

The lifetime of $\mathrm{NO_3}$ is defined as the ratio of the $\mathrm{NO_3}$ concentration to the losses of $\mathrm{NO_3}$, $L_{\mathrm{NO_3}}$:

$$\tau_{\mathrm{NO_3}} \equiv \frac{[\mathrm{NO_3}]}{L_{\mathrm{NO_3}}} \tag{3.7}$$

Similarly, the lifetime of $\mathrm{NO_3}$ from the combined reservoir ($\tau^*_{\mathrm{NO_3}}$), which also takes into account indirect losses of $\mathrm{NO_3}$ due to $\mathrm{N_2O_5}$ sinks, can be expressed as:

$$\tau^*_{\mathrm{NO_3}} = \frac{[\mathrm{NO_3}]}{L_{(\mathrm{NO_3+N_2O_5})}} \tag{3.8}$$

Analogously, the lifetime of $\mathrm{N_2O_5}$ from the combined reservoir ($\tau^*_{\mathrm{N_2O_5}}$) can also be determined:

$$\tau^*_{\mathrm{N_2O_5}} = \frac{[\mathrm{N_2O_5}]}{L_{(\mathrm{NO_3+N_2O_5})}} \tag{3.9}$$

By substituting Equations 3.5 and 3.6 into the expression for $\tau^*_{\mathrm{NO_3}}$, the non steady-state lifetime of $\mathrm{NO_3}$ can be obtained:

$$\tau^*_{\mathrm{NO_3}} = \frac{[\mathrm{NO_3}]}{k_{(\mathrm{NO_2+O_3})}[\mathrm{NO_2}][\mathrm{O_3}] - \frac{d[\mathrm{NO_3}]}{dt} - \frac{d[\mathrm{N_2O_5}]}{dt}} \tag{3.10}$$

As expected, the expressions obtained for the lifetimes at steady-state ($\tau_{\mathrm{SS}}(\mathrm{NO_3})$) and non steady-state ($\tau^*_{\mathrm{NO_3}}$) conditions are identical provided $d[\mathrm{NO_3}]/dt = d[\mathrm{N_2O_5}]/dt$ $= 0$. Furthermore, the non-steady state lifetime can be calculated if measurements of NO_3, NO_2, O_3 and N_2O_5 are available. For this study, the required species were measured using DOAS, in conjunction with N_2O_5 calculations. When using calculated N_2O_5 concentrations, the non steady-state lifetime calculation is presumably valid if an equilibrium is rapidly established for the NO_2-NO_3-N_2O_5 system; generally true for warmer temperatures. The rates of change of NO_3 and N_2O_5 were determined from the overnight time series of the two species, from which the quantities $d[\mathrm{NO_3}]/dt$ and $d[\mathrm{N_2O_5}]/dt$ were calculated using a 3 point running slope in the continuous data set. For this approach, it was assumed that changes in the concentration of both NO_3 and N_2O_5 were due to chemistry alone and not transportation.

From the definition of $\tau^*_{\mathrm{NO_3}}$ given by Equation 3.8 and the expression for the reservoir losses in Equation 3.5, the inverse non steady-state NO_3 lifetime can be obtained:

$$(\tau^*_{\mathrm{NO_3}})^{-1} = k_{\mathrm{x}} + k_{\mathrm{y}}\frac{[\mathrm{N_2O_5}]}{[\mathrm{NO_3}]} = k_{\mathrm{x}} + k_{\mathrm{y}}K_{\mathrm{eq}}[\mathrm{NO_2}] \tag{3.11}$$

Equation 3.11 is analogous to previously published equations by (Allan et al., 2000; Brown et al., 2003a), for which the steady-state lifetime was used instead of the non steady-state lifetime. Equation 3.11 is more general and can be applied to non-steady state conditions. This expression can be used to determine k_{x} and k_{y}, the overall first order loss rate constants for NO_3 and N_2O_5, respectively, by determining the slope and y-intercept of a plot of $(\tau^*_{\mathrm{NO_3}})^{-1}$ versus $K_{\mathrm{eq}}[\mathrm{NO_2}]$, or $(\tau^*_{\mathrm{NO_3}})^{-1}$ versus $[\mathrm{N_2O_5}]/[\mathrm{NO_3}]$. Note that this approach has been used frequently for the steady state lifetime case (Brown et al., 2003a, 2004, 2012).

3.1.3.2 Observations and Calculations

The NO_3 lifetime was calculated assuming both steady-state conditions (Equation 3.2) and non steady-state conditions (Equation 3.10) for comparison purposes. A time series of the calculated lifetimes, grouped into 30-minute time bins for the complete Saturna study, is shown in Figure 3.5.

The median lifetimes of NO_3 for both methods are fairly similar, ranging from 1−4 minutes overnight. These observations are consistent with other measurements

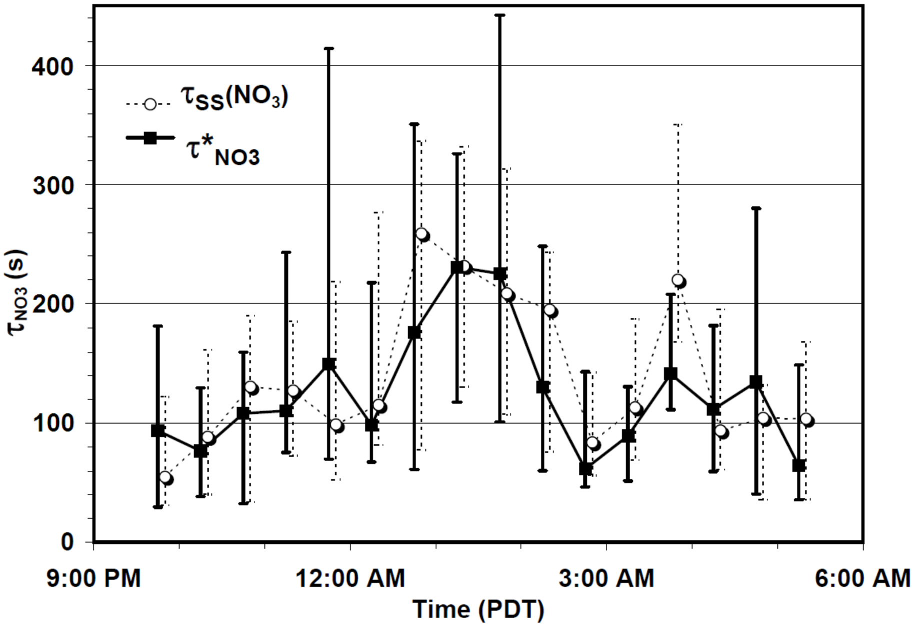

Figure 3.5: A comparison of the median steady-state NO_3 lifetime, $\tau_{SS}(NO_3)$, from Equation 3.2 (dashed line), and the median non steady-state NO_3 lifetime, $\tau^*_{NO_3}$, from Equation 3.10 (solid line), organized in 30-minute time bins. The 25th and 75th percentiles are shown as error bars. The steady-state lifetimes are offset by 5 minutes for clarity.

of the NO_3 lifetime in the marine boundary layer; within 0.2−17 minutes in a coastal German region (Martinez et al., 2000), ~3 minutes in the Mediterranean during summertime (Vrekoussis et al., 2004), ~4.2 minutes annual average in the Baltic sea (Heintz et al., 1996), between 1−20 minutes in the northeast and central Atlantic (Allan et al., 2000), and from a few seconds to 30 minutes in Southern Spain (Crowley et al., 2011). Generally, longest NO_3 lifetimes are obtained for cleaner marine air masses, as opposed to polluted environments. This trend is largely related to the relatively lower levels of NO_2 in cleaner air masses, resulting in a slower conversion of NO_3 to N_2O_5, which is subsequently lost as HNO_3 through hydrolysis. In addition, if the polluted marine environment contain alkenes or aromatics, the NO_3 lifetime can be significantly reduced.

In the early part of the evening, the combined NO_3 and N_2O_5 pool is expected to accumulate due to the decreasing and subsequent halt of NO_3 photolysis. As a result, positive values of $d[NO_3]/dt$ and $d[N_2O_5]/dt$ are obtained, and the steady-state lifetime equation is expected to predict values smaller than the true lifetime. The predicted effect is observed in the first time bin displayed in Figure 3.5. In addition, the average lifetime obtained for the non steady-state assumption is marginally longer before midnight and the 75th percentiles also show a similar trend for this time period. Such a trend may not be so obvious in the first few hours of the night due to the short timescale it may take the pool to accumulate. Furthermore, the NO_2 mixing ratio was generally highest in the earlier part of the night, leading a larger loss of NO_3 to N_2O_5 and subsequently HNO_3, ultimately shortening the lifetime of NO_3 and decreasing the values of $d[\mathrm{NO_3}]/dt$ and $d[\mathrm{N_2O_5}]/dt$.

Unlike the results obtained in at Saturna, significant differences between the steady-state and non steady-state lifetimes were found in a previous study (Brown et al., 2003a). Such a disparity is presumably the result of the temperature dependent decomposition of N_2O_5, in conjunction with the temperature difference between the two studies. An average temperature of 18°C was observed at Saturna, in comparison to 12°C in the Brown et al., study. The rate of the thermal decomposition of N_2O_5 becomes more than twice as large due to a 6 degree increase in temperature, which leads to a faster steady-state formation and minimizes the difference between the steady-state and non steady-state assumptions.

As previously mentioned, the overall first order rate constant for the losses of NO_3 (k_x) and N_2O_5 (k_y) can be determined by performing a regression of $(\tau^*_{\mathrm{NO_3}})^{-1}$ with $[\mathrm{N_2O_5}]/[\mathrm{NO_3}]$, as shown in Figure 3.6. The data appears fairly scattered, yielding a r^2 of only 0.10 and suggesting that only 10% of the observed variance is accounted for by the $[\mathrm{N_2O_5}]/[\mathrm{NO_3}]$ ratio. From the regression analysis, the y-intercept (k_x) was found to be $5.4(\pm1.2) \times 10^{-3}$ s^{-1}, with a slope (k_y) of $5.72(\pm0.81) \times 10^{-4}$ s^{-1}, where the errors are reported as the standard error of the fit coefficients. These results consist of study-wide averages and depend on many factors such as time of night, air mass origin, temperature, relative humidity, dilution effects and pollutant levels, among others.

The various NO_3 sinks can be separated into two categories; direct losses through oxidative reactions of NO_3 and indirect losses via hydrolysis of N_2O_5 and uptake

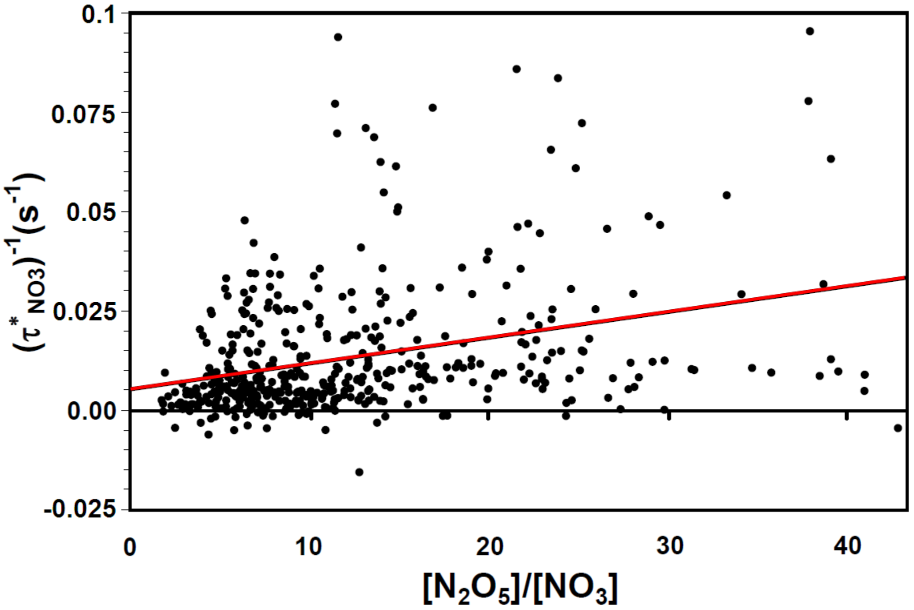

Figure 3.6: Plot of the inverse non steady-state lifetime of NO_3, $(\tau^*_{NO_3})^{-1}$, as a function of the $[N_2O_5]/[NO_3]$ ratio for study-wide observations. A line of best fit is shown (red line) in the graph, and is described by the equation: $(\tau^*_{NO_3})^{-1} = 5.72(\pm 0.81) \times 10^{-4}\,s^{-1}\ [N_2O_5]/[NO_3] + 5.4(\pm 1.2) \times 10^{-3}\,s^{-1}$. The plot only includes data collected between 20:00 − 8:00 PDT.

on aerosols. The relative significance of the two categories of NO_3 losses can be quantified based on the calculated values for the rate loss constants, by comparing k_x and $k_y[N_2O_5]/[NO_3]$. Using a value of $[N_2O_5]/[NO_3] = 9.3$ based on the median and average ratio, the direct loss of NO_3 was found to comprise 50.4 ± 13.2% of the total sinks, while the loss via N_2O_5 accounted for 49.6 ± 9.6% of the total. In a study performed in a polluted coastal marine boundary layer on Appledore Island, New England, the average loss of NO_3 via N_2O_5 was determined to be 51 − 54% (Ambrose et al., 2007), in agreement with the presented results.

In order to reduce the variance of the data from parameters which may be correlated with the time of night (i.e. temperature, relative humidity, wind speed, pollutant levels, etc), the approach for the calculation of direct and indirect losses of NO_3 was applied for data binned within 1-hour periods. The relationship between the inverse non steady-state lifetime of NO_3 and $[N_2O_5]/[NO_3]$ for each 1-hour time interval for the entire study is shown in Figures 3.7 and 3.8, for which the y-intercept and slope of each line of best fit corresponds to the k_x and k_y values for the particular hour bin, respectively, as summarized in Table 3.2. The uncertainties reported correspond to the standard error of the fit coefficients.

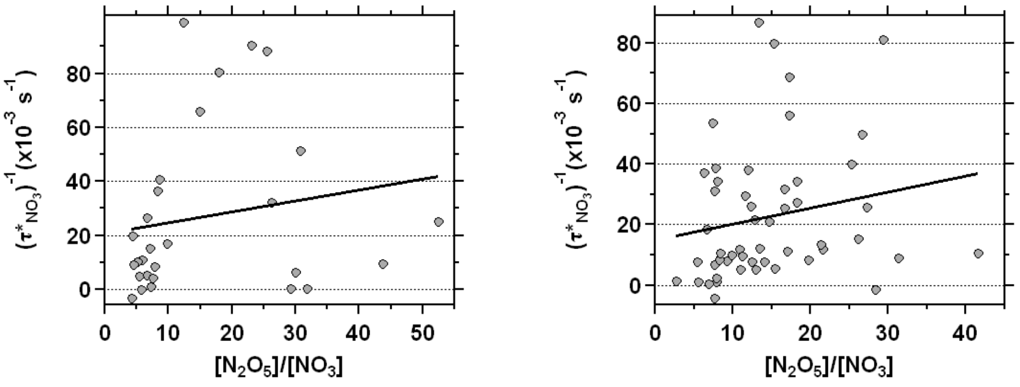

(a) 9:00 PM − 10:00 PM

(b) 10:00 PM − 11:00 PM

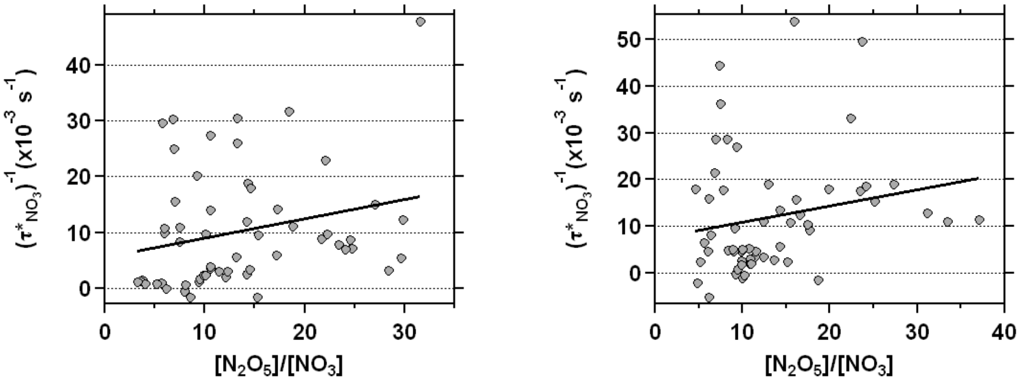

(c) 11:00 PM − 12:00 AM

(d) 12:00 AM − 1:00 AM

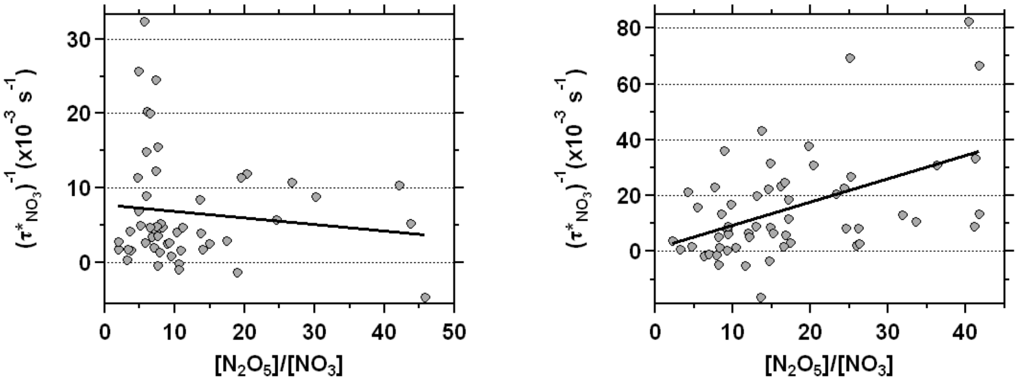

(e) 1:00 AM − 2:00 AM

(f) 2:00 AM − 3:00 AM

Figure 3.7: Linear regression between the inverse non steady-state NO_3 lifetime and $[N_2O_5]/[NO_3]$ for each hour interval between 9:00 PM−3:00 AM over the entire study.

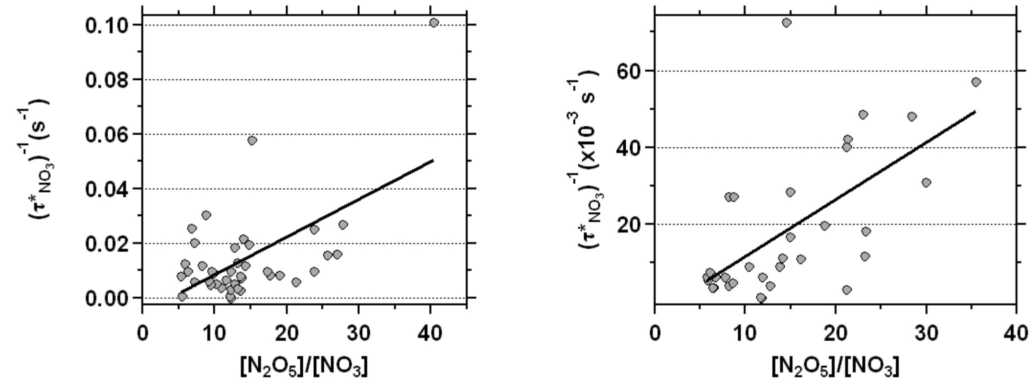

(a) 3:00 AM – 4:00 AM (b) 4:00 AM – 5:00 AM

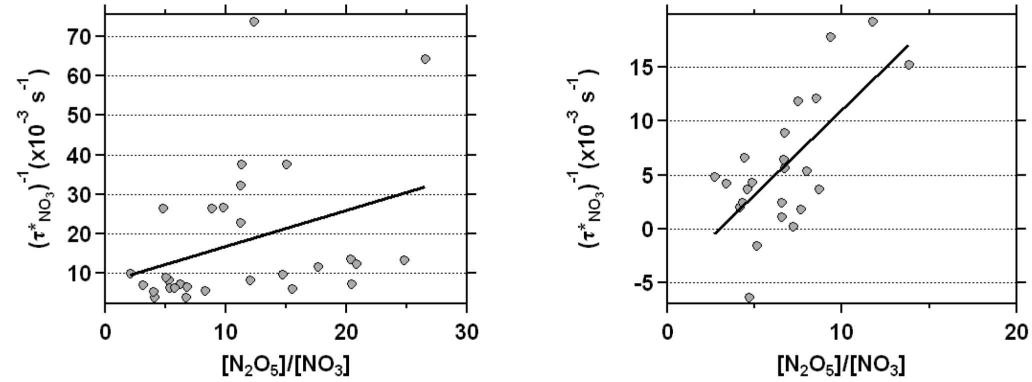

(c) 5:00 AM – 6:00 AM (d) 6:00 AM – 7:00 AM

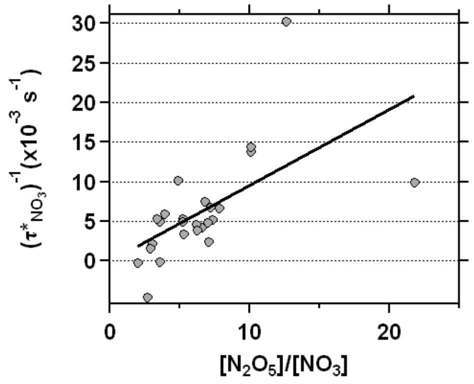

(e) 7:00 AM – 8:00 AM

Figure 3.8: Linear regression between the inverse non steady-state NO_3 lifetime and $[N_2O_5]/[NO_3]$ for each hour interval between 3:00 AM–8:00 AM over the entire study.

Table 3.2: Calculated k_x (y-intercept) and k_y (slope) values obtained for each hour interval from each line of best fit from Figures 3.7 and 3.8 for the entire study.

Time Interval (Local)	k_x (s^{-1})	k_y (s^{-1})
9:00 PM – 10:00 PM	$2.1(\pm0.8) \times 10^{-2}$	$5.1(\pm0.2) \times 10^{-5}$
10:00 PM – 11:00 PM	$1.5(\pm0.5) \times 10^{-3}$	$1.9(\pm2.1) \times 10^{-4}$
11:00 PM – 12:00 AM	$4.8(\pm2.6) \times 10^{-3}$	$2.4(\pm1.1) \times 10^{-4}$
12:00 AM – 1:00 AM	$5.5(\pm3.1) \times 10^{-3}$	$2.5(\pm1.4) \times 10^{-4}$
1:00 AM – 2:00 AM	$6.6(\pm1.4) \times 10^{-3}$	$-4.4(\pm6.3) \times 10^{-5}$
2:00 AM – 3:00 AM	$3.9(\pm0.4) \times 10^{-4}$	$5.0(\pm1.2) \times 10^{-4}$
3:00 AM – 4:00 AM	$-5.2(\pm4.3) \times 10^{-3}$	$8.5(\pm1.9) \times 10^{-4}$
4:00 AM – 5:00 AM	$-3.0(\pm5.3) \times 10^{-3}$	$9.2(\pm2.1) \times 10^{-4}$
5:00 AM – 6:00 AM	$7.1(\pm5.6) \times 10^{-3}$	$5.7(\pm2.9) \times 10^{-4}$
6:00 AM – 7:00 AM	$-4.4(\pm2.5) \times 10^{-3}$	$9.8(\pm2.3) \times 10^{-4}$
7:00 AM – 8:00 AM	$-3.91(\pm0.02) \times 10^{-5}$	$6.0(\pm1.6) \times 10^{-4}$

The k_x and k_y values obtained from the analysis are shown in Figure 3.9, from which the direct loss of NO_3 (k_x) is evidently dominant in the early evening, rapidly decreasing until 2:00, at which point it remains $\sim$0 within statistical error for the remainder of the night. The decay of k_x was investigated by examining the temporal evolution of known reactive sinks of NO_3 within the polluted marine boundary layer. The observed decrease for the direct loss rate is consistent with the expected overnight decline of species readily oxidized by NO_3 such as NO, dimethyl sulfide (DMS), α-pinene, isoprene and other unsaturated hydrocarbons. Although no direct measure-

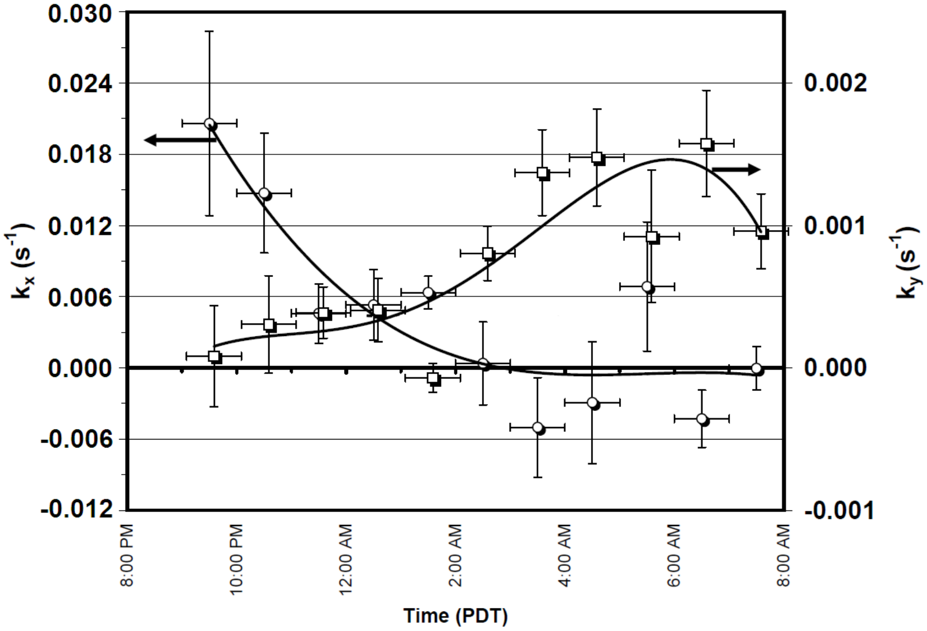

Figure 3.9: Plot of the first-order rate constants for direct losses of NO_3 (k_x) and indirect losses via N_2O_5 (k_y, averaged into 1-hour time bins. k_y is the heterogeneous losses of N_2O_5, which consists of N_2O_5 uptake on aerosols and hydrolysis. The k_x and k_y data points were fit to a 4th order polynomial to outline the general trends, with the standard error of the fit coefficients shown by the vertical error bars and the size of the time bins delineated by the horizontal error bars.

ments of VOCs or NO were available at the site during the Saturna field study, levels were estimated based on previous studies within the area. The region was previously shown to be impacted by NO_x emissions from ship plumes (Lu et al., 2006), large fluxes of DMS from marine phytoplankton (Sharma et al., 2003), α-pinene emissions from the surrounding forested area (McLaren et al., 2004), isoprene and a large range of anthropogenic VOCs (Jiang et al., 1997). In marine environments, rapid depletion of DMS (Vrekoussis et al., 2004), monoterpenes, isoprene (Geyer et al., 2001) and reactive anthropocentric hydrocarbons (Dimitroulopoulou and Marsh, 1997) through the oxidation of NO_3 was measured within the first few hours after sunset, consistent with the observed nocturnal variation of the first order loss rate of NO_3 at Saturna.

Excluding NO_3 losses due to photolysis and slow heterogeneous reactions, the direct loss rate of NO_3 is given by:

$$k_{\mathrm{x}} = k_{(\mathrm{NO_3+NO})}[\mathrm{NO}] + \sum_{\mathrm{i}} k_{(\mathrm{i,NO_3+VOC})}[\mathrm{VOC}]_i \tag{3.12}$$

where $k_{(\mathrm{NO_3+NO})}$ is the rate constant for Reaction R 1.32 and $k_{(i,\mathrm{NO_3+VOC})}$ is the loss rate of NO_3 to the i^{th} species of VOC. Using the calculated value for the direct loss rate of NO_3 at the beginning of the night ($k_{\mathrm{x}} = 0.021\ \mathrm{s}^{-1}$), the mixing ratio of each species oxidized by NO_3 was individually determined. A summary of the relevant rate constants taken from (Atkinson et al., 2004)(Atkinson et al., 2006)(Finlayson-Pitts and Pitts Jr, 1999) is summarized in Table 3.3, along with the individual mixing ratio of species which are dominant sinks of NO_3 in the MBL required to account for the observed NO_3 direct losses.

It is important to note that the mixing ratios outlined in Table 3.3 represent the maximum mixing ratio required for individual species to account for the observed NO_3 direct losses, in the absence of any additional direct sinks. Although a mixed scenario is a more realistic assumption, the analysis provides valuable results. From the mixing ratios displayed in Table 3.3, the low NO mixing ratio required to account for k_{x} suggests that any fresh NO_{x} plume impacting the site would be the dominant sink of NO_3, if NO in the plume is not completely titrated by O_3. In order to quantify

Table 3.3: Relevant reactions of NO_3 with various pollutants commonly found in the MBL at night. The rate of each reaction is shown along with the mixing ratio of each pollutant required to individually account for the observed NO_3 direct loss rate at the beginning of the night ($k_x = 0.021$ s^{-1}).

Reaction ($NO_3 +$)	k(cm^3 molec^{-1} s^{-1})	Mixing ratio
$NO \rightarrow 2NO_2$	2.6×10^{-11}	32 ppt
$CH_3SCH_3 \rightarrow HNO_3 + CH_3SCH_2$	1.1×10^{-12}	744 ppt
isoprene → products	7.0×10^{-13}	1.2 ppb
α-pinene → products	6.2×10^{-12}	136 ppt
isobutene → products	3.3×10^{-13}	2.5 ppb
cresol → products	1.4×10^{-11}	62 ppt

the VOC contribution to depleting NO_3 in the nocturnal MBL, measurements of these and other VOCs would be required. However, it can be said that all of the VOC present in Table 3.3 have been seen in the LFV at the mixing ratios given, apart from the 2.5 ppb of isobutene which is excessively high.

As seen from Figure 3.9, the loss of NO_3 through indirect sources (k_y) is initially low at the beginning of the night and steadily increases, exhibiting a trend opposite to that of k_x. The sinks of N_2O_5 consist of its homogeneous reaction with gas phase water (minor and still not in agreement) and heterogeneous uptake on aerosols (major) producing HNO_3, $ClNO_2$, and Cl_2.

As seen in Figure 3.9, the curve corresponding to k_{y} becomes significant at around 12:00 am, indicating that the contribution from the heterogeneous sink becomes significant at that point of the night. However, since aerosol properties were not measured at the site, the magnitude of the heterogeneous loss rate, k_{het}, is unknown. Nevertheless, the observed rise in k_{het} may be attributed to an increase in relative humidity beyond the deliquescence relative humidity point (DRH); the relative humidity required for aerosols to become liquid due to water absorption from the air, for sea salt aerosols at $70 - 75\%$ (Tang et al., 1997). For this process to occur, dry aerosols which have the potential to absorb water must be present within the MBL. Dry aerosols are not expected to originate from the MBL since their efflorscence relative humidity (ERH), the relative humidity at which aerosols lose their water content, occurs at $42 - 48\%$ (Tang et al., 1997), while relative humidity >50% was observed during the nighttime. However, aqueous marine aerosols may be brought inland via sea breezes and exposed to a relative humidity below the ERH point, being subsequently transported back to the MBL as dry aerosols (Hedley and Singleton, 1997). In addition, dry anthropogenic aerosols produced inland or emitted by ships would become aqueous in the MBL once the relative humidity goes beyond the DRH point.

Overnight outflow from the LFV to the Straight of Georgia was modeled by A Unified Regional Air-quality Modeling System (AURAMS) with a 4 km resolution (Halla, 2013). The model used CO as an air mass tracer to determine the location of polluted air masses within the Straight, providing evidence that the land / sea breeze circulation constitutes a possible process by which dry aerosols from land may reach the site.

Previous studies have determined a total loss rate of N_2O_5 of $2.0 \times 10^{-3} - 1.0 \times 10^{-4}\,s^{-1}$ from calculated N_2O_5 levels in the MBL (Heintz et al., 1996)(Martinez et al., 2000), in agreement with k_y values obtained in this work. Observations of NO_x, NO_3, N_2O_5, $ClNO_2$ and O_3 were modeled in a polluted MBL and loss rates of N_2O_5 were found to be between $1.0 - 3.0 \times 10^{-3}\,s^{-1}$ (Osthoff et al., 2008), also in agreement with the calculated N_2O_5 loss rate at Saturna. It is useful to note that in the last study, it was found that heterogeneous loss of N_2O_5 accounted for significant levels of $ClNO_2$, up to ∼1ppb.

3.1.4 Relationship between N_2O_5 and O_3 in the Lower Fraser Valley

A semi-observational analysis was performed to determine the relationship between nighttime chemistry within the MBL of the Straight of Georgia and O_3 formation in the LFV. The correlation between O_3 mixing ratios observed at inland monitoring stations and integrated mixing ratios of N_2O_5 from Saturna Island was investigated. N_2O_5 was used as a surrogate for chlorine containing photolabile species which are expected to accumulate overnight in the Straight of Georgia and enhance O_3 production within the LFV valley when transported inland via a sea breeze throughout the following day. The chemistry that can give rise to enhanced O_3 formation via early morning photolysis of photolabile chlorine species is given by Reactions R 1.46, R 1.47 and R 1.48 in the introduction. The following analysis does not provide definite proof of the relationship between N_2O_5 and O_3 in the LFV, simply indicating a possible scenario/explanation. Other possible causes for the relationship are discussed at the end of the section.

$\mathbf{ClNO_2}$ Production from $\mathbf{N_2O_5}$ in the MBL

N_2O_5 is known to undergo heterogeneous reactions in the MBL, producing:

$$\mathrm{N_2O_5} \xrightarrow{\text{sea salt aerosols}} \mathrm{HNO_3,\ ClNO_2,\ Cl_2,\ others} \tag{R 3.1}$$

The production rate for each individual product, p_i, is defined as:

$$\frac{dp_{\mathrm{i}}}{dt} = k_{\mathrm{het},i}[\mathrm{N_2O_5}] \tag{3.13}$$

where $k_{\mathrm{het},i}$ is the N_2O_5 heterogeneous pseudo first-order rate constants. At present, estimates for $k_{\mathrm{het},i}$ are uncertain and under investigation. Nevertheless, the heterogeneous rate constant for $ClNO_2$ production from N_2O_5 uptake on sea salt aerosols was previously determined along the southeast coastline of the United States near Houston, Texas, from which an estimate of $1 \times 10^{-4} - 3 \times 10^{-3}\ \mathrm{s}^{-1}$ was obtained (Osthoff et al., 2008).

For a species with no known significant nighttime sinks, such as $ClNO_2$, ClNO and Cl_2, the concentration is expected to accumulate overnight and reach levels of:

$$P_i = \int_0^t k_{\mathrm{het},i}[\mathrm{N_2O_5}]\,dt = k_{\mathrm{het},i}\int_0^t [\mathrm{N_2O_5}]\,dt \tag{3.14}$$

where P_i is the total accumulated concentration for species without nighttime sinks and the integral over time accounts solely for overnight periods. Assuming that the calculated N_2O_5 levels at Saturna are representative of the concentration in the Straight of Georgia, the integral can be rewritten as:

$$\int_0^t [\mathrm{N_2O_5}]\mathrm{d}t = \sum_{j=1}^{\mathrm{N}} [\mathrm{N_2O_5}]_\mathrm{j}\,\Delta_\mathrm{j} \tag{3.15}$$

where N consists of the number of overnight observations between 20:00 − 8:00 and $\Delta_j \equiv t_{\mathrm{end},j} - t_{\mathrm{start},j}$, where $t_{\mathrm{end},j}$ and $t_{\mathrm{start},j}$ are the end and start times for the j^{th} observation, respectively. Overnight N_2O_5 integrals ranging from $4.2 \times 10^{13} - 3.0 \times 10^{14}\,\mathrm{molec\,cm^{-3}\,s}$ or 0.038−0.275 ppb · night were calculated from the Saturna observations.

Using the lower limit $ClNO_2$ production rate of $1.0 \times 10^{-4}\,\mathrm{s^{-1}}$ (Osthoff et al., 2008) and the calculated overnight N_2O_5 integral, $ClNO_2$ accumulations of 0.16 − 1.2 ppb were calculated for the 13 nights for which N_2O_5 data was available, with a median of 0.45 ppb. This results are consistent in comparison to (Osthoff et al., 2008), where mixing ratios of $ClNO_2$ as high as 1.2 ppb were measured and correlated with the uptake of N_2O_5 on aerosols in the MBL.

An alternative method used to determine the overnight accumulation of $ClNO_2$ is based on modeling studies by (Simon et al., 2009). The model uses the result that 11 − 61% of a pool of NO_2 + O_3 would ultimately be converted to $ClNO_2$, based on observations made by (Osthoff et al., 2008). Using the lower estimate of this conversion frequency, the overnight accumulated $ClNO_2$ can also be calculated as:

$$\mathrm{ClNO_2} = 0.11 \int_0^t k_{(\mathrm{NO_2+O_3})}[\mathrm{NO_2}][\mathrm{O_3}]\,dt \tag{3.16}$$

Using NO_2 and O_3 observations from the study at Saturna, the levels of $ClNO_2$

accumulated overnight were estimated with Equation 3.16 to be 0.19 − 0.99 ppb with a median of 0.48 ppb. This alternative method does not take into account strong direct losses of NO_3 in the MBL other than that to N_2O_5, posing a significant drawback. Nevertheless, good agreement was obtained using the two methods.

Transportation of Pollutants into the LFV

In order to determine a possible link between the overnight integrated concentration of N_2O_5 (and hence production of Cl atoms the next day) and the formation of O_3 in the LFV on the following day, the transportation of pollutants from the Straight of Georgia into the LFV was investigated. Since the transport of air masses towards the land is associated with sea breezes (airflow from sea to land), a wind sector analysis was performed using data from inland meteorological stations in the valley, in order to determine the days on which significant sea breezes were observed. Using a similar approach as previously shown in (Snyder and Strawbridge, 2004), sea and land breezes were identified with wind direction vectors between 180−330° and 0−120°, respectively, which were sustained for several hours at wind speeds above 5 $\mathrm{km\,h^{-1}}$. As summarized in Table 3.4, sea breezes were observed on 9 out of 13 days.

Evidence for the transportation of sea salt aerosols into the LFV was also provided by previous studies for which aerosols exhibiting Cl^- deficiency compared to Na^+ were observed. This can be attributed to the heterogeneous reaction with N_2O_5 at night and/or HNO_3 displacement during the day (McLaren et al., 2004; Anlauf et al., 2006).

Table 3.4: Summary of average wind sectors for the 9 days identified with a clear sea breeze between 12:00−16:00. The 9 nights identified and analyzed were July 24/25, 25/26, 26/27, 27/28, 31/August 1, 1/2, 3/4, 5/6 and 6/7.

MET Station	Wind Direction (°)	Wind Speed ($\mathrm{km\,h^{-1}}$)
Vancouver International	286	17.6
Sandheads	287	17.3
Pitt Meadows	258	7.8
White Rock	228	6.8
Abbotsford	229	11.6
Hope	290	19.9

Correlation Between O_3 levels and Overnight Accumulated N_2O_5

A positive correlation between overnight integrated N_2O_5 mixing ratios and 1-hour maximum O_3 levels during the following day is expected from chlorine atom chemistry, as previously discussed in Chapter 1.2.3. A plot of the daily 1-hour maximum O_3 mixing ratio measured during the day within the LFV and the integrated N_2O_5 concentration from the previous night ($d\,O_3/d\int[N_2O_5]\,dt$) is shown in Figure 3.10 for various monitoring stations. As seen from Figure 3.10, weak correlations were obtained from the regression analysis. In general, the r^2 for the regression ranged from 0.0015 for T01 to 0.28 for T33. The only station which observed a slope significantly

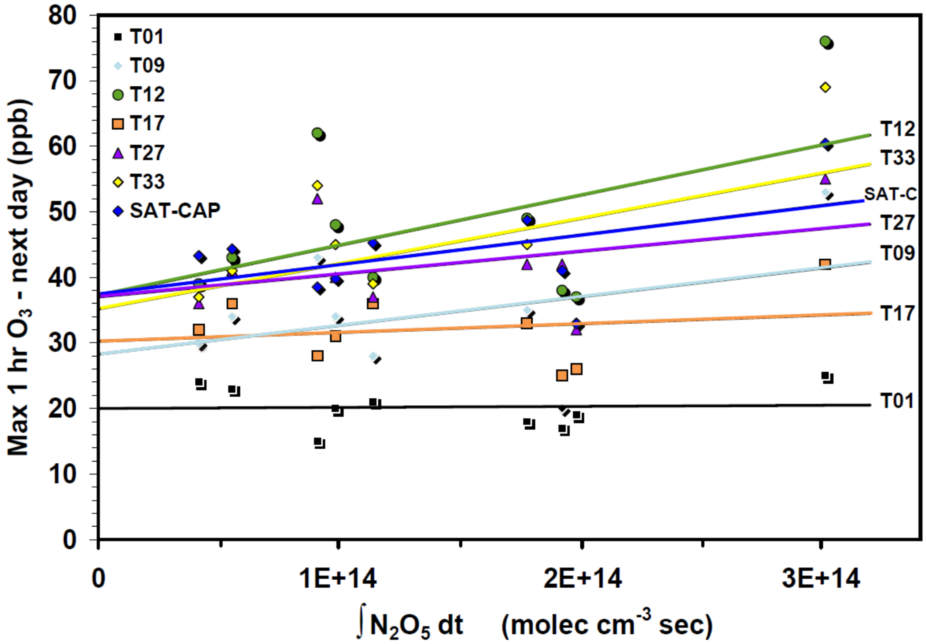

Figure 3.10: Correlation between the overnight integrated N_2O_5 concentration in the Straight of Georgia and daily 1-hour maximum O_3 mixing ratios measured the following day at various monitoring stations within the LFV. Measurements are shown exclusively for cases where a significant sea breeze was observed during the following day.

different than 0 at the 90% confidence interval was station T33. Thus, only 28% of the observed variance in the daily maximum of O_3 can be attributed to the nighttime N_2O_5 chemistry at the T33 station. Despite the weak correlation, as later shown in Table 3.5, measurements from 18 out of 20 stations showed positive correlation with an average slope of $d\,\mathrm{O_3}/d\int[\mathrm{N_2O_5}]\,dt = (2.77 \pm 0.69) \times 10^{-14}\,\mathrm{ppb\,O_3\,cm^3\,molec^{-1}\,s^{-1}}$, or $30.3 \pm 7.7\,\mathrm{ppb\,O_3\,ppb\,N_2O_5}^{-1}\,\mathrm{night}^{-1}$, statistically significant at the 95% confidence interval.

Table 3.5: Summary of the correlation between overnight integrated N_2O_5 concentration and daily 1-hour maximum O_3 levels measured the next day (Day +0.5) and the next day after (Day +1.5).

	Day+0.5		Day+1.5	
Station	$d[O_3]/d\int[N_2O_5]dt$ ppbO_3 ppb$N_2O_5^{-1}$night^{-1}	r^2	$d[O_3]/d\int[N_2O_5]dt$ ppbO_3 ppb$N_2O_5^{-1}$night^{-1}	r^2
T01	+1.8±16	0.002	+46.9±16	0.551
T02	+24.5±24	0.131	+4.8±16	0.013
T04	+32.1±26	0.178	−2.4±13	0.005
T06	+0.5±21	0.000	+28.2±14	0.375
T09	+47.9±42	0.153	+15.0±23	0.057
T12	+83.7±56	0.235	+44.3±37	0.164
T13	+0.6±29	0.000	−3.2±23	0.003
T14	+48.9±29	0.280	+35.2±18	0.352
T15	+14.5±29	0.033	+41.6±27	0.257
T17	+14.5±26	0.041	+42.9±21	0.388
T18	−3.5±15	0.009	+4.2±13	0.014
T20	+19.8±29	0.059	+46.0±23	0.368
T26	+3.7±21	0.004	+37.4±27	0.213
T27	+38.1±34	0.153	+21.9±31	0.066
T29	+49.3±60	0.088	+53.4±55	0.116
T30	+50.0±37	0.201	+61.0±29	0.369
T31	−3.7±23	0.004	+52.2±29	0.311
T32	+59.3±44	0.209	+18.2±23	0.085
T33	+75.5±45	0.281	+31.6±31	0.130
CAPMon	+49.3±34	0.236	+15.3±42	0.019

The amount of O_3 generated the following day, ΔO_3, can be estimated from the slope in Figure 3.10 as:

$$\Delta O_3 = d\,O_3/d\int[N_2O_5]\,dt \times d\int[N_2O_5]\,dt \qquad (3.17)$$

Using the previously determined range for the overnight N_2O_5 integral of $0.038 - 0.275$ ppb $\cdot$ night, a hourly average maximum increase in O_3 was calculated to range from +1.1 to +8.3 ppb.

Levels of O_3 produced from fluxes of Cl atoms in coastal areas were recently modeled by various groups. Enhancements of O_3 were estimated from +1 to +9 ppb from $ClNO_2$ in Houston (Osthoff et al., 2008)(Simon et al., 2009), from +4 to +12 ppb from Cl_2 in the South Coast Air Basin, California (Knipping and Dabdub, 2003) and up to +40 ppb in a 1-hour average from ClNO in regions downwind of Los Angeles (Raff et al., 2009).

In order to confirm whether the elevated O_3 levels in the LFV were indeed due to nighttime chemistry within the Straight of Georgia, the analysis was further extended to 2 days prior and 2 days after the nighttime N_2O_5 accumulation. The value of $d\,O_3/d\int[N_2O_5]\,dt$, averaged for all the stations, was plotted and is shown in Figure 3.11. The previous and following days relative to the observed N_2O_5 accumulation are referred to as Day -1.5, -0.5, +0.5, +1.5, and +2.5. From the graph, a rise in O_3 levels is observed for two days past the accumulation night (Day +0.5 and +1.5), dissipating before the third day. A detailed summary of each station is presented in Table 3.5. The magnitude of the O_3 enhancement between Days +1.5 and +0.5

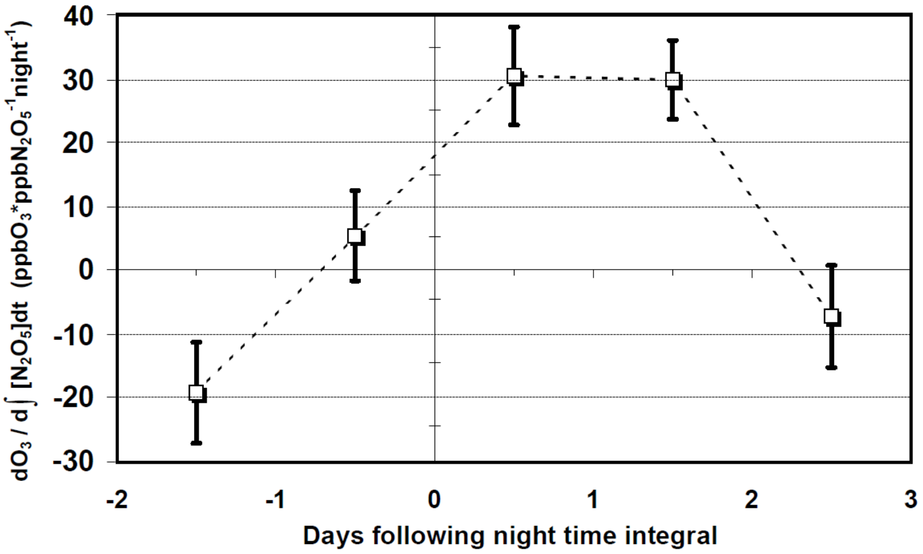

Figure 3.11: The average change of 1-hour maximum O_3 with respect to integrated N_2O_5 concentration for all the stations as a function of days before and after the overnight N_2O_5 accumulation. Only nights with a significant sea breeze on Day +0.5 are included in the plot. Error bars represent the standard error (1σ) arising from the regression analysis.

is quite comparable; however, data from Day +1.5 shows a stronger correlation, as suggested by the calculated r^2. The negligible and/or negative enhancement levels on Days -1.5, -0.5 and +2.5 provide additional evidence that the enhancement of the O_3 mixing ratios in the LFV is correlated with nighttime chemistry in the Straight of Georgia.

The spatial variation among the enhancements of O_3 between Days +0.5 and +1.5 was further examined and is shown in Figure 3.12. On Day +0.5, the strongest correlations are observed for stations further inland, such as stations T33 and T12 with

$d\,\mathrm{O_3}/d\int[\mathrm{N_2O_5}]\,dt > 75$ ppb $\mathrm{O_3}$ ppb $\mathrm{N_2O_5}^{-1}$ night^{-1}. Stations near the coastal region and downtown Vancouver area, on the other hand, show much weaker correlation. A noticeable increase is also seen northeast of Vancouver, an area which contains a concentrated industrial sector with large VOC emissions; possibly contributing to the observed $\mathrm{O_3}$ increase.

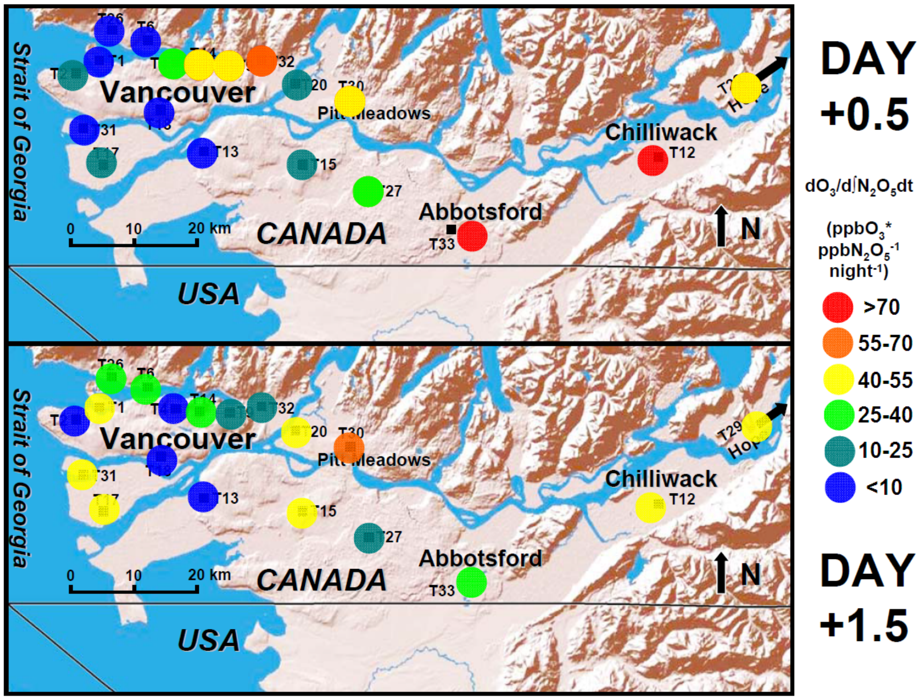

Figure 3.12: Spatial variation of $\mathrm{O_3}$ enhancement at various monitoring stations within the LFV for Day +0.5 (top panel) and +1.5 (bottom panel), potentially due to overnight $\mathrm{N_2O_5}$ chemistry in the Straight of Georgia.

It is possible that the furthest sites experience a chemical amplification due to the longer transport times, estimated to range between 5 and 10 hours from the coast to Abbotsford and Chilliwack. The lower levels seen at coastal regions may be due to the high $\mathrm{NO_x}$ levels encountered at these sites, causing these regions to be VOC limited and reducing/titrating O_3 levels. These lower O_3 levels may also be attributed to the catalytic destruction of O_3 from chlorine atoms, which is expected to be present in large amounts at the coastal sites as compared to the further downwind locations. As previously discussed, chlorine atoms may undergo reaction with methane to initiate O_3 production; however, chlorine may also catalytically destroy O_3 through the following reaction mechanism:

$$\mathrm{Cl^{\cdot} + O_3 \longrightarrow ClO^{\cdot} + O_2} \qquad \text{(R 3.2)}$$

$$\mathrm{ClO^{\cdot} + HO_2{}^{\cdot} \longrightarrow HOCl + O_2} \qquad \text{(R 3.3)}$$

$$\mathrm{HOCl} + h\nu \longrightarrow \mathrm{Cl^{\cdot} + OH^{\cdot}} \qquad \text{(R 3.4)}$$

$$\mathrm{OH^{\cdot} + CO \xrightarrow{O_2} HO_2{}^{\cdot} + CO_2} \qquad \text{(R 3.5)}$$

This mechanism is expected to occur at locations with low or moderate halogen oxide levels such as coastal regions coastal regions, notably reducing the $[HO_2]/[OH]$ ratio.

In the presence of high halogen levels, the halogen oxide radicals may self-react, creating another pathway for the catalytic destruction of O_3:

$$\mathrm{X^{\cdot} + O_3 \longrightarrow XO^{\cdot} + O_2} \qquad \text{(R 3.6)}$$

$$\mathrm{XO^{\cdot} + YO^{\cdot} \longrightarrow X^{\cdot} + Y^{\cdot} + O_2} \qquad \text{(R 3.7a)}$$

$$\mathrm{\longrightarrow XY + O_2} \qquad \text{(R 3.7b)}$$

$$\mathrm{Y^{\cdot} + O_3 \longrightarrow YO^{\cdot} + O_2} \qquad \text{(R 3.8)}$$

where X and Y are Br, Cl or I atoms. This mechanism yields a net reaction:

$$\mathrm{O_3 + O_3 \longrightarrow 3\,O_2} \qquad \text{(R 3.9)}$$

The chlorine atom reaction rates with CH_4 and O_3 are $9.95 \times 10^{-14}\,\mathrm{cm^3\,molec^{-1}\,s^{-1}}$ and $1.18 \times 10^{-11}\,\mathrm{cm^3\,molec^{-1}\,s^{-1}}$, respectively, at 298 K (Sander et al., 2006). Assuming a CH_4 mixing ratio of 1.8 ppm and a O_3 mixing ratio of 30 ppb, the reaction of the chlorine atom with O_3 is approximately 2 times faster than that with CH_4, leading to a net loss of O_3 for very high Cl concentrations.

The spatial variation trends observed on Day +1.5 are significantly different when compared to Day +0.5. The stations surrounding the Vancouver area show greater and more statistically significant O_3 enhancements, while the effect is less pronounced for the downwind stations. The seven strongest correlations are observed for western stations, with r^2 ranging from $0.31 - 0.55$. This can be attributed to the possible recirculation of air originally transported into the valley, which is expected to move back towards the coast in the event of a land breeze occurrence. It is also possible for O_3 and other products to be present in a residual layer above, which experiences downward mixing upon the inversion breakup during the following day, contributing to the O_3 enhancement at the coastal sites.

In conclusion, the presented results provide substantial evidence for a possible link between O_3 formation in the LFV to the nighttime chemistry in the Straight of Georgia. However, a correlation between accumulated N_2O_5 at night and enhanced ozone the next day *still* does not prove cause and effect; it simply indicates that it is possible. There are other reasons why enhanced ozone could be seen on these days that would show a casual correlation. Other possible explanations for the observed enhancements of O_3 consist of HONO transportation into the valley. An accumulation of HONO overnight was observed, as discussed in Chapter 3.2, and may be transported into the LFV during the following day due to a sea breeze, releasing OH-radicals upon photolysis. As a result, an increase in O_3 is expected. Alternatively, it is also possible that meteorologically induced stagnation events can lead to higher levels of NO_3 and N_2O_5 in the MBL while simultaneously increasing the O_3 concentration in the valley (Valente et al., 1998). In order to further verify the proposed findings from this analysis and link O_3 formation in the valley to nighttime chemistry in the Straight of Georgia, measurements of chlorine containing photolabile species are required in combination with modeling studies. Alternatively, it is also possible that correlation between N_2O_5 and O_3 is due to transport of O_3 from the LFV to the Straight of Georgia.

3.2 HONO during the Saturna Field Study

The measurements of HONO and NO_2 taken at East Point, Saturna Island, are the first reported observations of HONO in a polluted marine environment, providing a unique scenario in which to study the chemistry of HONO. An overview of the data set is presented along with the observed dependence of HONO on NO_2, temperature, and relative humidity. The hypothesis of a potential aqueous reservoir for HONO in the MBL is discussed and a conceptual model of HONO formation on aqueous surfaces is presented. Furthermore, the implications of a reservoir of HONO on atmospheric chemistry are discussed. The HONO data set and analysis presented in this section were published in Atmospheric Chemistry and Physics in April 2011 (Wojtal et al., 2011). The data was collected at Saturna Island by Dr. Robert McLaren, Dr. Daniel Majonis, Joy McCourt and Dr. Jamie Halla. The analysis of the data set was performed by Patryk Wojtal and Dr. Robert McLaren.

3.2.1 Overview of Measurements

The temporal profile of HONO, NO_2 and SO_2 measured at Saturna using active-DOAS are shown in Figure 3.13, along with the various meteorological parameters measured by the Environment Canada weather station. Measurements of aerosol optical properties and vertical column densities of NO_2 were also performed at the site using MAX-DOAS (Halla et al., 2011). As observed from the data set, the HONO mixing ratio rapidly increases during sunset (21:51±11 min PDT), reaching a steady-state value between $0.5 - 1.5$ ppb, dependent on the night. HONO levels remained generally constant throughout each night until after sunrise (05:46±11 min PDT), when it rapidly undergoes photolysis.

The NO_2 mixing ratio was typically higher early in the evening and steadily declined overnight. Short spikes observed in the NO_2 mixing ratio may be attributed to ship plume emissions impacting the measurement site. Mixing ratios as high as 46 ppb were measured with median levels at 7.8 ppb and minimum mixing ratios below detection limit ($3\sigma = 0.31$ppb). The SO_2 to NO_2 ratio was used to identify ship plume events impacting the site and are published in (McLaren et al., 2012). The temperature and relative humidity measurements exhibited a typical diurnal variation, with decreasing temperatures overnight ranging from 25 to 14°C, and increasing relative humidity ranging from 60 to 90%.

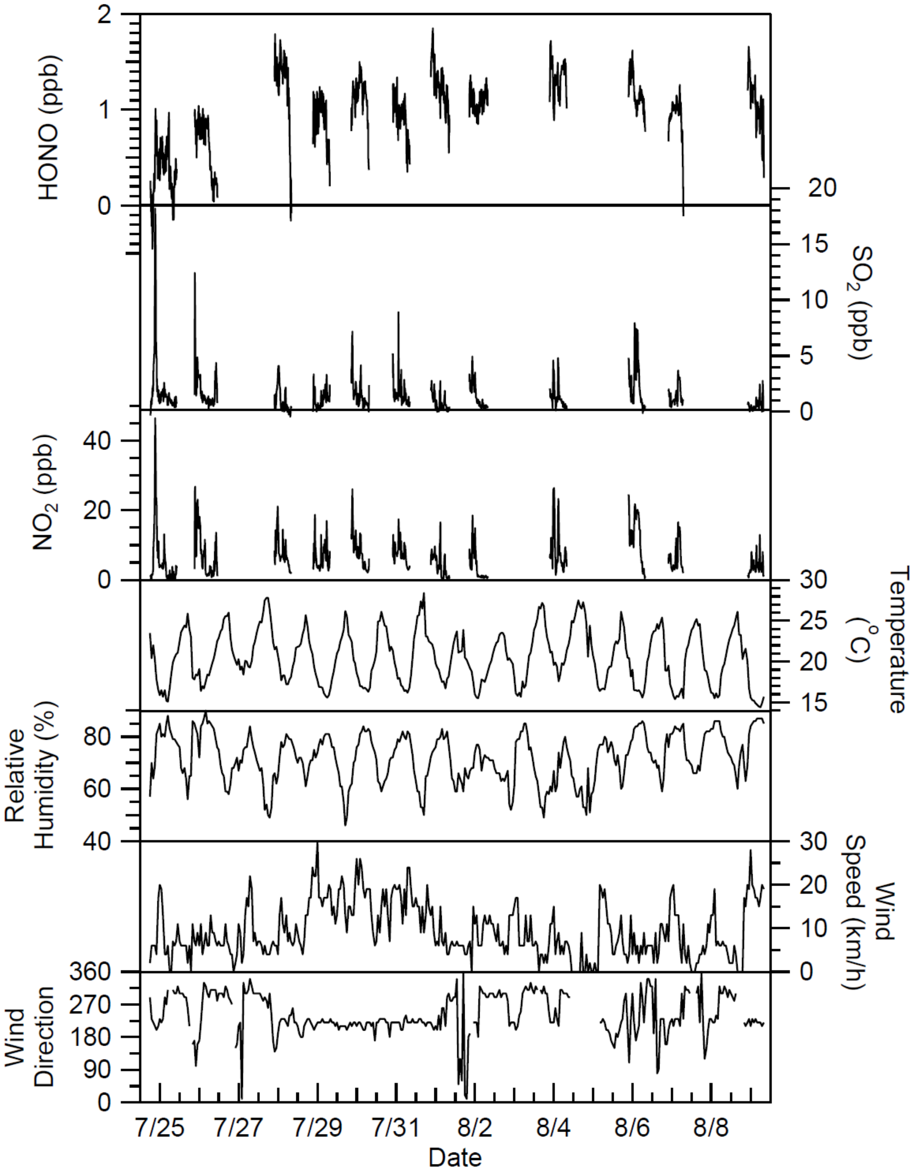

Figure 3.13: Overview of the two-week measurements of HONO, NO_2 and SO_2, along with the various meteorological measurements at East Point, Saturna Island.

3.2.2 Case Study Observations of HONO

July 24/25, 2005

In order to investigate the general HONO trends observed during the Saturna field study, two case studies were chosen and analyzed in detail. Observations from the night of July 24/25 are shown in Figure 3.14. Before sunset, HONO mixing ratios were below detection limit due to photolysis and rapidly increased to nearly 1.0 ppb shortly after sunset. The HONO levels remained relatively constant throughout the night (average = 0.5 ppb), before dropping below detection limit once again after sunrise.

A concentrated ship plume impacted the measurement site shortly after sunset on this evening, identified by the sharp spike of the NO_2 and SO_2 mixing ratios. The NO_2 mixing ratio declined after the ship plume event and stabilized at $\sim$4 ppb for several hours. A second ship plume impacted the site at 2:30, following a drop in the NO_2 mixing ratio below the detection limit for the remainder of the night. The HONO/NO_2 ratio was quite low at the beginning of the night and varied greatly over the course of the night, ranging from 0.05 to >1, but gradually increased as the night progressed.

Two periods of meteorological and chemical stability took place during this case study. The first period occurred between 23:30−2:00, lasting 2.5 hours, with winds dominantly from the southwest direction at $\sim$18 $\mathrm{km\,h^{-1}}$. The air mass passed over mostly open ocean for more than 2 hours prior to arrival at the measurement site and

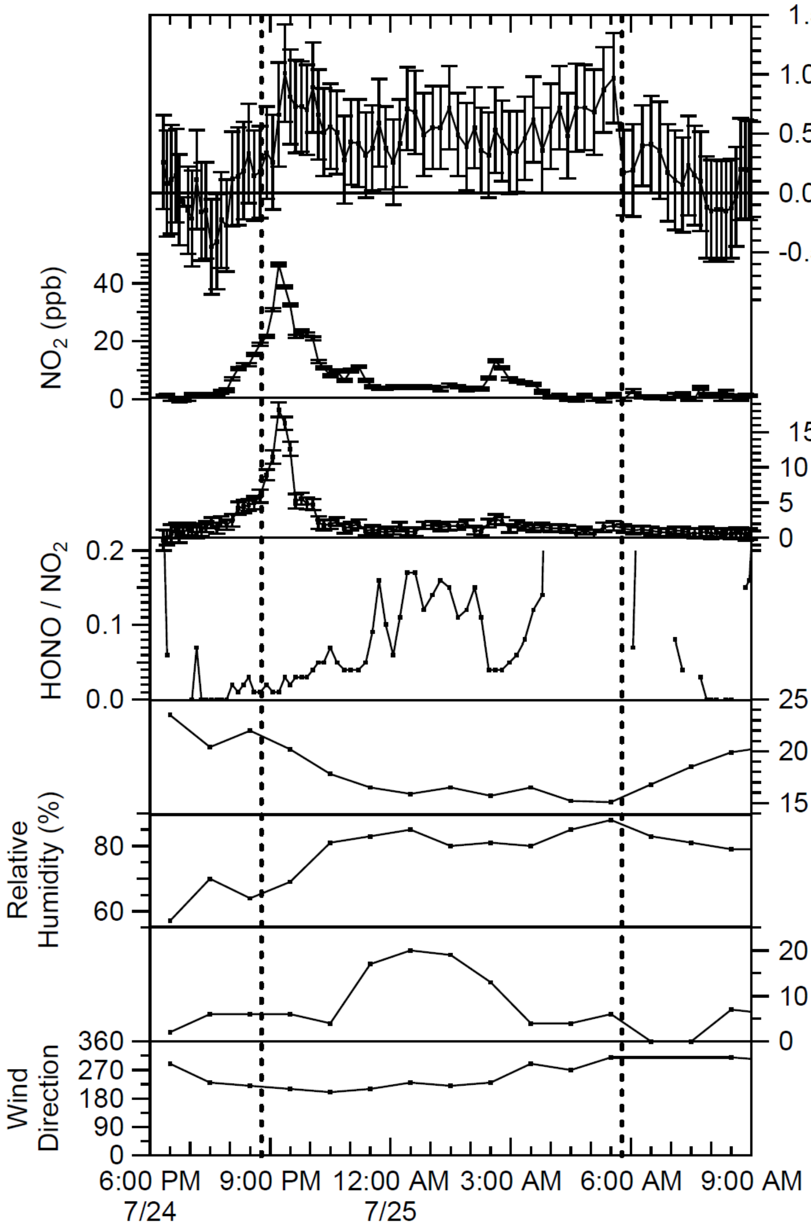

Figure 3.14: Overview of the measurements made on the night of July 24/25 at East Point, Saturna Island. The dashed vertical lines represent sunset and sunrise.

the pollutant levels were relatively constant during this time. The average HONO, NO_2 and HONO/NO_2 ratio were 0.51 ppb, 3.9 ppb and 0.13, respectively. The second stable period lasted for 2 hours, between 3:30−5:30, with winds from the northwest at ~5 $\mathrm{km\,h^{-1}}$. This wind sector brought a cleaner air mass to the site, with an average NO_2 mixing ratio of 0.40 ppb, near the detection limit of the instrument. The average HONO mixing ratio was 0.67 ppb and the HONO/NO_2 ratio was highly variable, reaching even >1.0 due to the uncertainty on the NO_2 measurements near the detection limits of the instrument. Despite the change in air mass and large variability in the NO_2 mixing ratio, the HONO mixing ratio remained relatively constant overnight and was uncorrelated with NO_2.

July 29/30, 2005

An overview of the second case study is shown in Figure 3.15. Large HONO mixing ratios were measured at sunset and levels remained relatively constant throughout the night at ~1.2 ppb. The NO_2 mixing ratio was 14 ppb early in the night and slowly decreased to 2 ppb by the morning, with several NO_2 peaks occurring from ship emissions. The HONO/NO_2 ratio was ~0.05 early in the evening, increasing to 0.4 by the morning. Short duration decreases in the ratio were observed during ship plume events with emissions of NO_2 from nearby vessels. The winds were consistently from the southwest, with wind speeds fairly high overnight. The HONO mixing ratio during this case study also appeared to be independent of the NO_2 concentration, a consistent pattern which was observed every night during the two-week long field study.

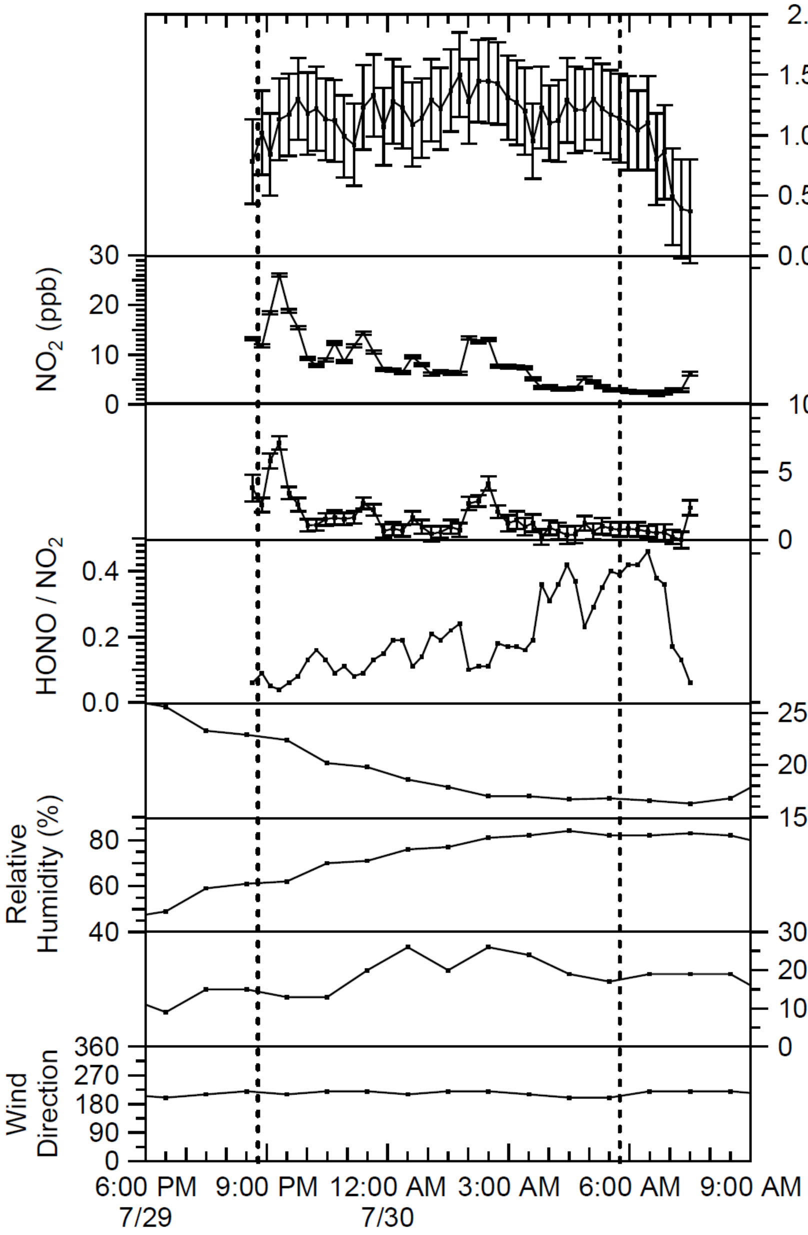

Figure 3.15: Overview of the measurements made on the night of July 29/30 at East Point, Saturna Island. The dashed vertical lines represent sunset and sunrise.

3.2.3 Study Wide Observations of HONO

An overview of the 30-minute time binned profiles of HONO, NO_2, HONO/NO_2, temperature and relative humidity is summarized in Table 3.6 and presented in Figure 3.16. The HONO mixing ratio was found to rapidly increase after sunset and stabilize at median and average overnight mixing ratios of 1.1 ppb within an hour after sunset, with the 5th and 95th percentiles at 0.5 and 1.5 ppb, respectively. The HONO mixing ratio remained generally constant overnight until the onset of photolysis at sunrise, when the levels dropped significantly.

The observed steady-state of HONO implies a balance between production and losses of HONO and is not unique to the presented data set. Other studies at terres-

Table 3.6: Statistical summary of observations during the dark period of the night, defined as 22:00−5:00.

	95th percentile	75th percentile	Average	Median	25th percentile	5th percentile
HONO (ppb)	1.54	1.26	1.08	1.08	0.93	0.52
NO_2 (ppb)	19.1	10.6	7.8	6.7	3.7	0.90
SO_2 (ppb)	4.1	1.92	1.52	1.14	0.64	0.19
HONO/NO_2	1.17	0.30	–	0.155	0.093	0.048
Temp (K)	294.6	292.3	291.0	290.8	289.6	288.4
RH (%)	86	83	77.4	79	74	62
WS ($\mathrm{km\,h^{-1}}$)	24	19	12.7	13	6	4

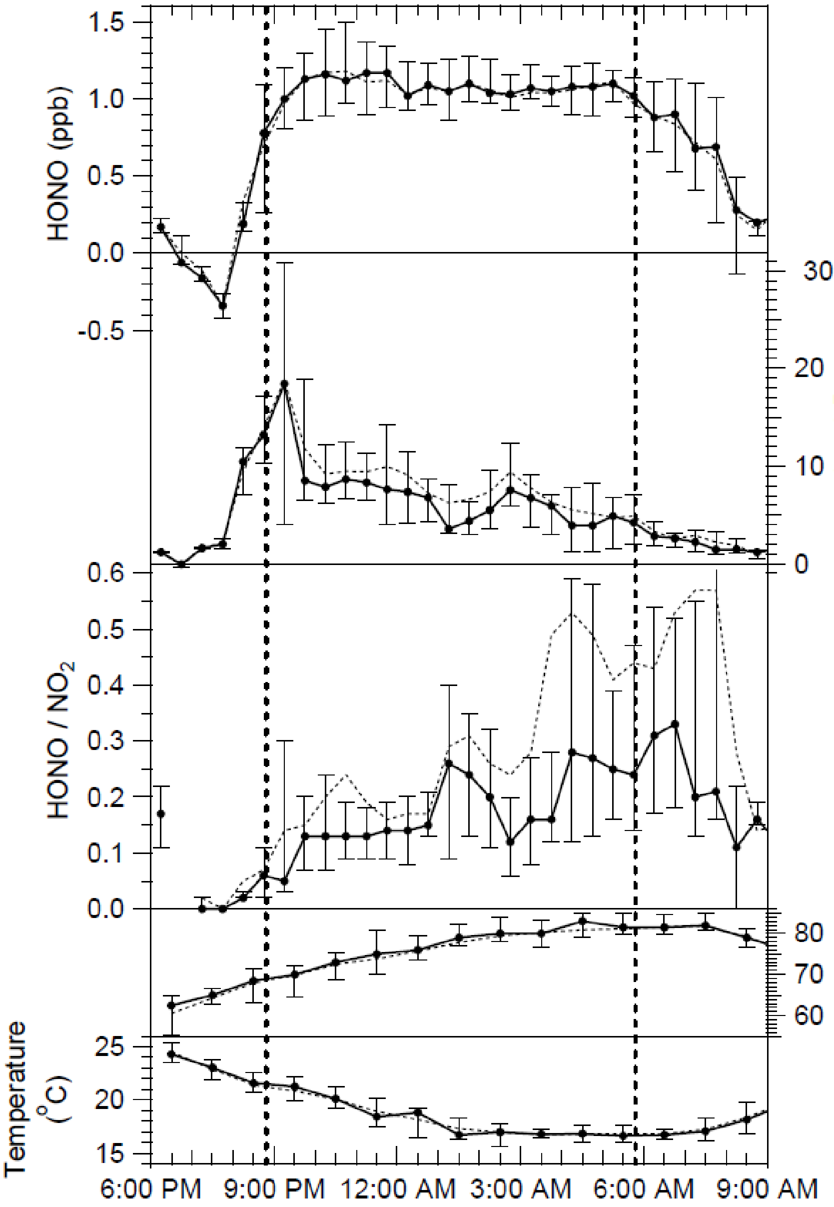

Figure 3.16: Nocturnal profiles for the period of July 24 to August 9, 2005. Medians (solid line), 25th and 75th percentiles (error bars), and average values (dashed line) are shown within each 30-minute time bin. The vertical dashed lines represent the average sunset and sunrise times during the study period.

trial locations have also observed a steady-state of HONO during the night; however, the HONO steady-state formation for these studies occurred later in the night, as compared to the observations over the open ocean (typically <1 hour). Previous measurements of HONO in urban areas with relative humidity between $60 - 100\%$ found a leveling off of HONO occurring and persisting after 00:00 in Nashville, 2:30 in Houston with NO_2 increasing by more than 60% afterwards and ~1:00 in Phoenix (Stutz et al., 2004), taking several hours longer to form than at Saturna Island. Table 3.7 summarizes the data set from additional studies which observed steady-state of HONO. Such frequently observed overnight steady-state is likely not unique to the MBL and an underlying mechanism is presumably responsible in both terrestrial and marine environments.

The steady-state of HONO was previously described using a simple box model in which the heterogeneous HONO formation reaction of NO_2 on surfaces was balanced by the irreversible first-order deposition of HONO (Stutz et al., 2004). Assuming a constant level of NO_2, a steady-state expression for HONO and the HONO/NO_2 ratio was derived as:

$$[\mathrm{HONO}] = \frac{\gamma_{\mathrm{NO_2 \to HONO}}(\mathrm{RH})}{\gamma_{\mathrm{HONO}}(\mathrm{RH})}[\mathrm{NO_2}] \tag{3.18}$$

where $\gamma_{\mathrm{NO_2 \to HONO}}(\mathrm{RH})$ is the conversion probability of NO_2 to HONO and γ_{HONO} (RH) is the uptake coefficient of HONO on surfaces, both dependent on relative humidity. The time constant associated with the approach to the steady-state is defined as:

$$\tau = \frac{S}{V} \times \frac{\upsilon_{\mathrm{HONO}}}{4} \times \gamma_{\mathrm{HONO}}(\mathrm{RH}) \tag{3.19}$$

Table 3.7: Summary of nocturnal steady-state observations of HONO from previous studies in terrestrial locations.

Reference	Location	Date	Time (local)	HONO (ppb)	NO_2 (ppb)	T (°C)	RH (%)
Stutz (2004)	Houston, USA	5 Sep 2000	2.5−5.0	0.9−1.1	11−24	–	88−93
Stutz (2004)	Nashville, USA	13 Jul 1999	0.0−5.0	0.6−0.9	16−22	–	90−100
Stutz (2004)	Phoenix, USA	26 Jun 2001	0.0−5.7	1.2−1.7	15−33	–	65−75
Acker (2004)	Melpitz, Germany	10−12 Apr 2000	1.0−6.0	0.1−0.2	1.1−2.2	−1−1	70−90
Kleffman (2007)	Wuppertal, Germany	3 Sep 2004	22.5−5.5	1.0−1.2	–	–	–
Yu (2009)	Kathmandu, Nepal	3 Feb 2003	0.0−3.0	0.8−1.4	3−15	4−11	70−100
Yu (2009)	Kathmandu, Nepal	4 Feb 2003	1.0−4.0	0.8 −1.2	5−9	3−10	80−100
Yu (2009)	Kathmandu, Nepal	5 Feb 2003	1.0−4.0	0.9−1.7	8−15	3−10	80−100
Yu (2009)	Kathmandu, Nepal	6 Feb 2003	1.0−4.0	1.1−1.7	7−15	3−10	80−100
This work	Saturna Is, Canada	24 Jul−9 Aug 2005	22−5.0	0.5−1.5	4−19	15−21	74−86
This work	Toronto, Canada	Nov 2010−Nov 2011	20−7	0.6−1.4	5−15	-5−10	65−80

where υ_{HONO} is the mean molecular velocity of HONO. From Equation 3.19, the time constant to reach a steady-state is essentially described as the inverse of the first-order loss constant due to deposition of HONO to the surface, τ_{dep}. The steady-state of HONO observed at Saturna Island was rapidly established each night, with a time constant generally <1 hour. From Equation 3.18, the HONO concentration is predicted to be proportional to the levels of NO_2 during the steady-state period, and the HONO/NO_2 ratio is expected to remain constant. However, observations at Saturna Island show that the HONO/NO_2 ratio was not constant during the steady-state period, the HONO steady-state level was not proportional to the concentration of NO_2, and the HONO steady-state did not respond to changes in the NO_2 concentration with a time constant of τ_{dep}. The HONO steady-state observed at Saturna was relatively undisturbed and independent of the NO_2 concentration and source of the air mass.

The major sink of HONO during the nighttime is believed to be its deposition to surfaces. Although the lifetime of HONO from the steady-state was shown to be <1 hour based on Equation 3.19, the steady-state was observed to last for ~7 hours each night. The observations of HONO at Saturna Island can not be explained by the model described by Equation 3.18, which assumes a dependence of HONO on NO_2 and the irreversible deposition of HONO. Given that HONO is independent of NO_2 during the steady-state period, a reservoir of nitrogen that is significantly larger than the gas phase reservoir of HONO in the MBL must exist and/or HONO must be deposited back into the source after deposition. Thus, the observations suggest that HONO deposition to the ocean surface may not be an irreversible process. Both of these points will be explored in greater detail in Chapter 3.2.5.

The NO_2 temporal profile, previously presented and discussed in Chapter 3.1.1, exhibits a sharp increase during sunset which may be attributed to frequent ship emissions impacting the site, followed by a steady decrease overnight. The overnight decline can be attributed to several factors including a drop in anthropogenic emissions, losses to the NO_3/N_2O_5 reservoir and subsequent hydrolysis to HNO_3, dissolution into the ocean, heterogeneous formation of HONO, and meteorological dilution effects, among others.

The $HONO/NO_2$ ratio is frequently used as an indicator of the efficiency of the first-order dependent heterogeneous conversion of NO_2 to HONO. During the study, the $HONO/NO_2$ ratio was relatively low before sunset and stabilized at $\sim$0.13 in the early part of the night. The ratio reached median levels of 0.3 with the 95th percentile $>$1.0 by morning. Since the HONO remained at a steady-state mixing ratio of $\sim$1.1 ppb, the observed trends for the $HONO/NO_2$ ratio were mainly governed by the decreasing mixing ratio of NO_2 overnight, frequently $<$2 ppb by early morning.

The study wide relationship between HONO and NO_2 is shown in Figure 3.17, with the entire data set shown in Figure 3.17a. A large amount of scatter is observed in the data and the $HONO/NO_2$ ratio is bounded by a lower limit of 0.0084. This observation is consistent with tunnel experiments which determined the direct emissions of HONO from diesel vehicles, and reported values of $HONO/NO_x = 0.008 \pm 0.001$ (Kurtenbach et al., 2001). Aside from emissions from nearby ships, it is expected that negligible amounts of NO will be present at the measuring location at night due to long distance of direct NO_x emissions, strongly suggesting that $[NO_x]=[NO_2]$ at the site.

From a recent study in Nepal, a similar lower limit was found, with a zero forced regression slope of $HONO/NO_2 = 0.083 \pm 0.03$ (Yu et al., 2009). An interesting observation arising from the relationship between HONO and NO_2 consists of the apparent lack of an upper limit for the $HONO/NO_2$ ratio. This matter was also

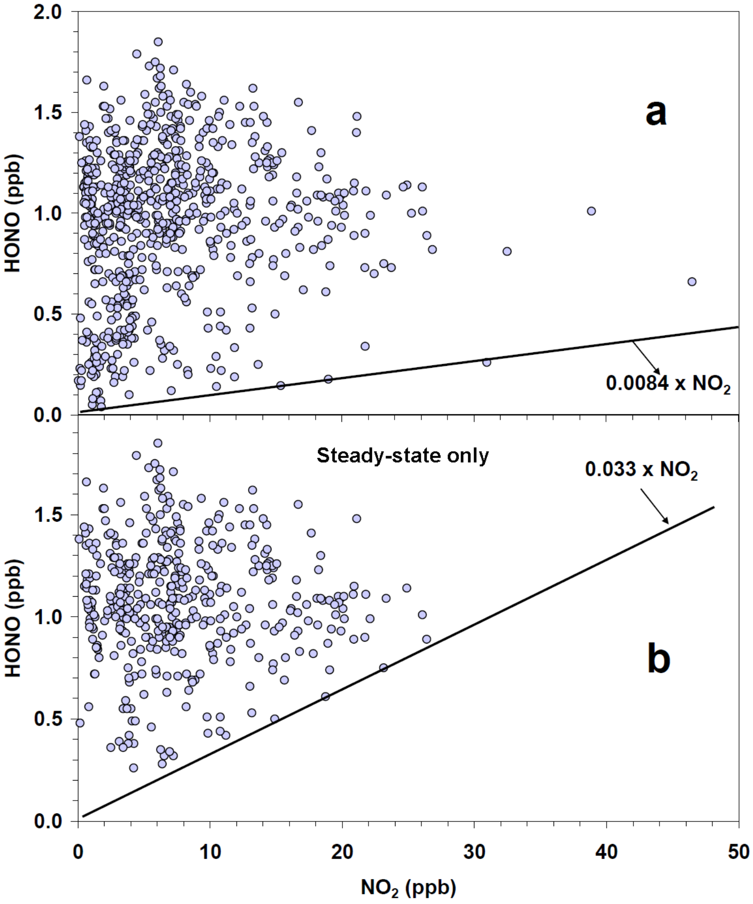

Figure 3.17: Relationship between HONO and NO_2 for (a) entire data set and (b) nighttime data only, between 20:00−5:00. A lower limit line is shown with a value of $HONO/NO_2 = 0.0084$ in (a) and $HONO/NO_2 = 0.033$ in (b).

examined using exclusively nighttime data (between 22:00−5:00), in order to remove any effects from photolysis and buildup/decay of HONO during sunset and sunrise, as shown in Figure 3.17b. During the nighttime, an upper bound remains unapparent, however, a new lower limit of $HONO/NO_2 = 0.033$ is observed. From the statistical summary shown in Table 3.6, the HONO mixing ratio over the open ocean was restricted to a relatively small range of $0.5 - 1.5$ ppb, accounting for 90% of all nighttime observations, while the NO_2 mixing ratio varied by nearly 20 ppb over the same percentile range. This clearly demonstrates the lack of a dependence of HONO on NO_2 and will be further explored in this work.

The nocturnal $HONO/NO_2$ ratios at Saturna Island are significantly larger as compared to previously reported values from rural, semi-urban and urban environments. Nighttime $HONO/NO_2$ ratios were found to rarely exceed 0.04 in urban Birmingham, England (Harrison et al., 1996), 0.035 in Milan, Italy after vehicle emission correction (Stutz et al., 2002), 0.02−0.06 in a semi-urban site in Kwangju, South Korea (Park et al., 2004), 0.075 at two rural sites in England (Harrison et al., 1996), 0.09 in Los Angeles, USA (Harris et al., 1982), 0.02−0.1 in the urban center of Beijing, China (Qin et al., 2006), 0.03−0.10 at various urban locations in the USA, increasing with an increase in RH (Stutz et al., 2004), 0.125 in South East England (Kitto and Harrison, 1992) and 0.13 at various locations in Europe (Lammel and Cape, 1996). The previously mentioned study in Nepal observed $HONO/NO_2$ ratios as large as 0.30 in the mountainous region of Kathmandu (Yu et al., 2009). The authors attributed the high conversion frequency of NO_2 to HONO during the nighttime to the high levels of relative humidity, low inversion layer, and high aerosol loading at their measurement site. Thus, as also suggested from observations from other studies, it is plausible that surface water may be a limiting reagent in the HONO formation reaction, hindering the conversion frequency of NO_2 to HONO when insufficient surface water is available.

3.2.4 Relative Humidity and Temperature Dependence of HONO during Steady-State Periods

HONO measurements during the dark period of the night were plotted as a function of relative humidity and are shown in Figure 3.18. A significant amount of scatter is observed, along with a weak, however statistically significant, negative dependence at the 95% confidence interval. The equation for the line of best fit was found to be:

$$\text{HONO ppb} = \text{-}0.0182\ (\pm 0.0049)\times\text{RH\%} + 2.47(\pm 0.35)\ \text{ppb}$$

with a r^2=0.17 over a relative humidity range of $59 - 90\%$. The dependence was also determined to be statistically significant at the 95% confidence interval for two separate regressions of the data, $RH<75\%$ and $RH\geq75\%$. An additional regression was performed for each 1-hour time bin during the dark period to determine whether HONO was coincidentally correlated with relative humidity. The binned HONO data showed a slight decrease of HONO throughout the night and may be coincidentally correlated with a temporal change in other parameters. Upon the removal of any temporal dependence, HONO was still found to have a statistically significant negative dependence on relative humidity in all seven 1-hour time bins, although the results are not shown.

Studies have suggested that a positive dependence between HONO and surface adsorbed water exists (Finlayson-Pitts et al., 2003b). In addition, the amount of surface adsorbed water is expected to be proportional to the relative humidity; hence, the HONO levels would also exhibit a correlation with relative humidity. These findings may be tied to results from previous studies, which determined the number of water mono-layers on glass in accordance with a Brunauer, Emmett, and Teller (BET)

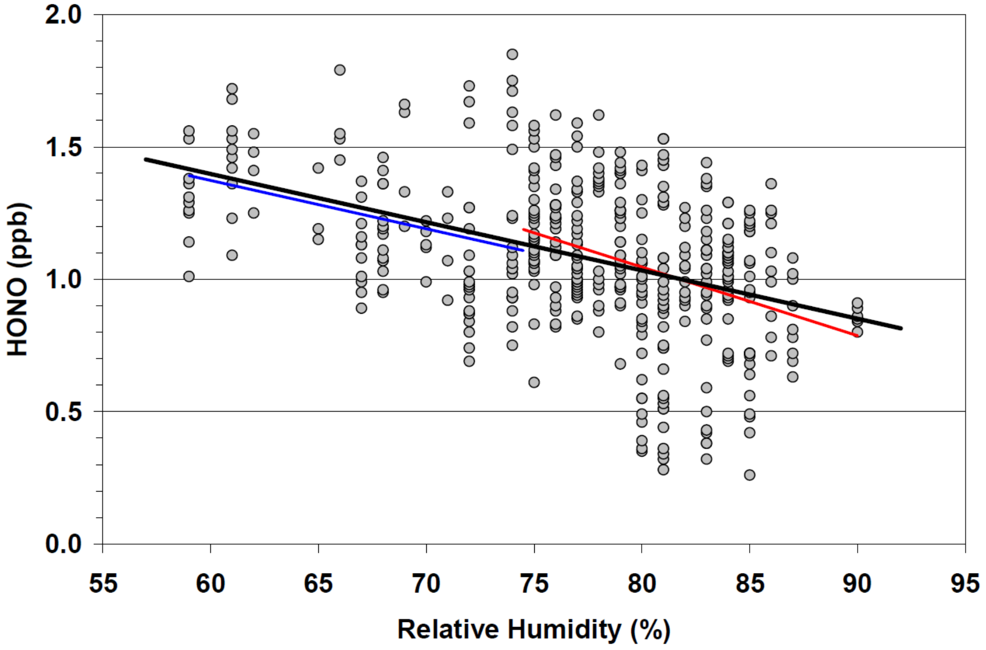

Figure 3.18: Relationship between HONO and relative humidity during the steady-state period. The black line shows a line of best fit all data points yielding HONO ppb = -0.0182 (±0.0049)×RH% + 2.47(±0.35) ppb with a r^2=0.17. Two separate linear fits are shown for relative humidity <75% (blue) and relative humidity ≥75% (red).

isotherm (Saliba et al., 2001) and showed that the water coverage of various materials, expressed as number of mono-layers of water, increases steadily with relative humidity (Lammel, 1999). It was estimated that 1 mono-layer of water was present on stone surfaces at $10-45\%$ RH, for soil at $\sim$20% RH and for vegetation at $50-90\%$ RH. It is possible that surface water was a limiting reagent in the formation of HONO for previous studies in urban and rural environments, leading to a positive dependence between HONO and relative humidity. Figure 3.18 shows a clear contrast to observations made at terrestrial locations and is discussed below.

During periods of steady-state, two possible scenarios may account for the constant levels of HONO; 1) the production and loss mechanisms of HONO are not active or 2) there is an ongoing balance between the sources and sinks of HONO. Assuming that HONO production and losses are active throughout the night, a positive(negative) relative humidity dependence implies an increase in the HONO production(loss) rate. The HONO measurements at Saturna Island are unique due to the constant availability of surface water on the surface of the ocean in this unique environment; different from previous studies. It is extremely unlikely that surface water could comprise a limiting reagent over the ocean; thus, a positive dependence is not expected between HONO in the MBL and relative humidity.

Furthermore, an increase in relative humidity could potentially increase the amount of water available on marine aerosols. As marine aerosols uptake water, the loss rate of HONO on aerosols may become significant, explaining the observed negative dependence between HONO and relative humidity. The increase in the HONO loss rate with relative humidity on marine aerosols may only be considered significant if the surface and/or volume densities of marine aerosols is considerably larger than the ocean's. Since direct measurements of the surface and volume densities of sea salt aerosols, anthropogenic aerosols and the ocean surface were not available, these quantities were estimated. Using a deliquesced sea salt aerosol concentration of 10 μg m^{-3}, the total sea salt aerosol surface and volume densities at 96% RH were calculated to be $4.3 \times 10^{-5}\,\mathrm{m}^2\,\mathrm{m}^{-3}$ ($43\,\mu\mathrm{m}^2\,\mathrm{cm}^{-3}$) and $1.47 \times 10^{-10}\,\mathrm{m}^3\,\mathrm{m}^{-3}$ ($147\,\mu\mathrm{m}^3\,\mathrm{cm}^{-3}$), respectively (Chameides and Stelson, 1992). The surface and volume densities of anthropocentric aerosols were estimated assuming a moderately polluted MBL with an anthropocentric aerosol concentration of 10 μg m^{-3}, containing 50% H_2O with d_p=0.2 μm and were found to be $5.5 \times 10^{-4}\,\mathrm{m}^2\,\mathrm{m}^{-3}$ ($550\,\mu\mathrm{m}^2\,\mathrm{cm}^{-3}$) and $9.1 \times 10^{-12}\,\mathrm{m}^3\,\mathrm{m}^{-3}$ ($9.1\,\mu\mathrm{m}^3\,\mathrm{cm}^{-3}$), respectively. Combining sea salt and anthropogenic aerosols, the total surface and volume densities of water in marine aerosols was estimated to be $5.9 \times 10^{-4}\,\mathrm{m}^2\,\mathrm{m}^{-3}$ and $1.6 \times 10^{-10}\,\mathrm{m}^3\,\mathrm{m}^{-3}$, respectively.

The ocean's surface and volume densities of water were estimated by dividing the height of the nocturnal MBL, h_{MBL}, by the thickness of the aqueous layer in the sea surface micro-layer (SML), t_{SML}. Assuming a well mixed MBL height of $h_{\mathrm{MBL}} = 100$ m (Brown et al., 2004) and a SML depth of $t_{\mathrm{SML}} = 50\,\mu$m (Zhang et al., 1998), the surface and volume densities of water were estimated to be $0.01\,\mathrm{m}^2\,\mathrm{m}^{-3}$ and $5.0 \times 10^{-7}\,\mathrm{m}^3\,\mathrm{m}^{-3}$, respectively[3]. These calculations indicate that the surface

---

[3] It is important to note that the nocturnal MBL may not be well mixed at night (Stutz et al., 2002) and the calculated surface and volume densities of water over the ocean are lower estimates.

and volume densities of water over the ocean are, respectively, 17 and 3×10^3 times greater than for marine aerosols. These results suggest that an increase in the surface and/or volume density of marine aerosols with relative humidity is insignificant when compared to the ocean's surface, producing a negligible effect on the HONO deposition.

An alternative explanation for the negative dependence of HONO with relative humility consists of the overnight temperature profile. Over the course of the night, the amount of water in the atmosphere stays relatively constant, while the temperature generally decreases. Due to the cooling of the atmosphere overnight, the water capacity of air decreases, leading to an increase in the relative humidity for a constant amount of water vapor. Therefore, it is possible that the observed negative dependence of HONO on relative humidity is actually just a positive dependence of HONO on temperature.

The relationship between HONO and inverse temperature during the dark period of the night is shown by the logarithmic plot in Figure 3.19. The temperature coefficient of HONO for the temperature dependent evaporation is given by:

$$\frac{1}{P_{\mathrm{HONO}}}\frac{dP_{\mathrm{HONO}}}{dT} = \frac{\Delta H_{\mathrm{vap}}}{R}\frac{1}{T^2} \tag{3.20}$$

from which the following expressions are obtained:

$$P_{\mathrm{HONO}} = P^{\circ}_{\mathrm{HONO}} e^{\frac{\Delta H_{\mathrm{vap}}}{R}\left(\frac{1}{T^{\circ}} - \frac{1}{T}\right)} \tag{3.21}$$

$$\ln(P_{\mathrm{HONO}}) = \ln(P^{\circ}_{\mathrm{HONO}}) + \frac{\Delta H_{\mathrm{vap}}}{R}\frac{1}{T^{\circ}} - \frac{\Delta H_{\mathrm{vap}}}{R}\frac{1}{T} \tag{3.22}$$

where P_{HONO} and $P^{\circ}_{\mathrm{HONO}}$ are the partial pressures of HONO at temperatures T and T°, ΔH_{vap} is the enthalpy of vaporization of $\mathrm{HONO_{(aq)}}$ and R is the gas constant. By performing a linear fit to the data, the HONO concentration may be expressed as:

$$\ln(\mathrm{HONO}) = 24.1(\pm 2.4) - 6.98(\pm 0.69) \times 10^{3}\,\mathrm{K}^{-1} \times \frac{1}{T}$$

with a $r^2 = 0.2$. Using the slope of the line of best fit, the temperature coefficient of HONO at the center of the temperature range of 288−296 K was found to be $(1/\mathrm{HONO_{(292K)}}) \times d\mathrm{HONO}/dT = +8.2(\pm 0.8)\%\,\mathrm{K}^{-1}$. By performing a regression on each 1-hour time bin in order to remove any temporal dependent processes, a positive correlation significant at the 95% confidence interval was also obtained at each time

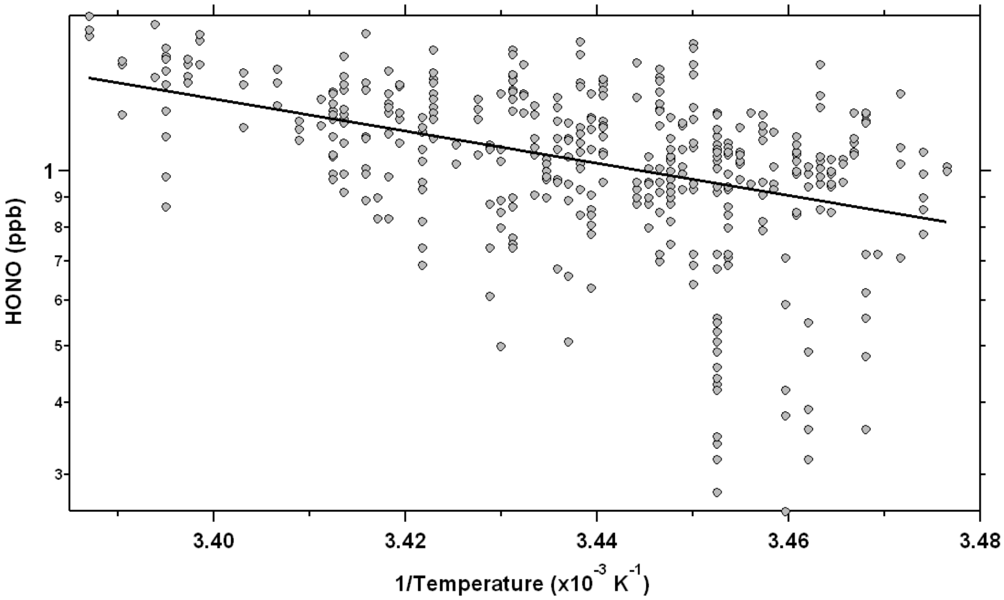

Figure 3.19: Logarithmic plot of HONO as a function of inverse temperature during the steady-state period. The best fit (black line) yields $\ln(\mathrm{HONO}) = 24.1(\pm 2.4) - 6.98(\pm 0.69) \times 10^{3}\,\mathrm{K}^{-1} \times \frac{1}{T}$, with $r^2 = 0.2$.

interval. Therefore, the previously discussed HONO dependence on relative humidity may indeed consist of a reflection of the HONO temperature dependence.

A possible explanation for the observed positive correlation between HONO and temperature consists of the gas/aqueous phase equilibrium defined by the Henry's Law coefficient, $H(T)$, for the solubility of HONO in water:

$$H(T) = \frac{[\text{HONO}]_{(\text{aq})}}{P_{\text{HONO}}} = H^{\circ}\text{exp}\left(\frac{\Delta H_{\text{vap}}}{R}\left(\frac{1}{T} - \frac{1}{T^{\circ}}\right)\right) \tag{3.23}$$

where H° is the Henry's Law constant at a reference temperature T°.

Using the literature values of $H^{\circ} = 49 \pm 1$ mol L^{-1} atm^{-1} (298 K) (Park and Lee, 1988), $\Delta H_{\text{vap}}/R = 4900 \pm 150$ K in water (Becker et al., 1996), and an overnight average ocean temperature in the Straight of Georgia of 285.7 K, the temperature coefficient of HONO is predicted by Equation 3.20 to be $+6.0 \pm 0.2\%\,\text{K}^{-1}$. Despite the potential differences in Henry's Law constant between sea and fresh water and the air mass in the MBL not being in thermal equilibrium with the ocean, the calculated value is comparable to the result of $+8.2(\pm0.8)\%\,\text{K}^{-1}$ from Figure 3.19.

The enthalpy of vaporization, ΔH_{vap} of $\text{HONO}_{(\text{aq})}$, can also be determined from the least squares regression previously performed with $-\Delta H_{\text{vap}}/R$ as the slope. The value of ΔH_{vap} for HONO was found to be 58.1 ± 5.8 kJ mol^{-1}, similar to the literature value of $\Delta H_{\text{vap}} = 40.7 \pm 1.2$ kJ mol^{-1}. Although these results do not provide concrete evidence, they are consistent with a temperature dependent equilibrium process, releasing HONO from the ocean surface.

3.2.5 Potential Aqueous Reservoir for HONO

As previously discussed, the observed temporal profile of HONO in the polluted MBL at Saturna Island may be the result of an aqueous HONO reservoir. Previous literature reports have suggested that an aqueous surface reservoir of HONO or NO_2^- could be photolytically activated, leading to a daytime source of HONO (Zhou et al., 2002; Acker et al., 2004; He et al., 2006). It is also possible that an aqueous reservoir of HONO or its precursors exists in the MBL during both the day and night periods. The reservoir would be significantly larger than the gas phase reservoir and/or can also be driven by the deposition of HONO, which would remain in the reservoir. Within the MBL, an aqueous reservoir may exist in the sea surface micro-layer, on or within aerosols, or at the air-sea surface interface. The possibility of each potential reservoir is discussed below.

Sea Surface Micro-Layer

The fate of surface deposited HONO was previously studied in laboratory experiments, for which NO was found to be released during long reaction times and high NO_2 concentration (Finlayson-Pitts et al., 2003b). Deposited HONO was also shown to dissolve on aqueous surfaces as shown below (Mertes and Wahner, 1995):

$$\mathrm{HONO_{(g)}} \longrightarrow \mathrm{HONO_{(aq)}} \qquad \text{(R 3.10)}$$

The heterogeneous HONO formation reaction produces dissolved $HNO_{3(aq)}$, which further acidifies the aqueous surface and $HONO_{(aq)}$ which ionizes:

$$HONO_{(aq)} + H_2O_{(1)} \longrightarrow H_3O^+_{(aq)} + NO^-_{2\ (aq)} \qquad (R\,3.11)$$

The dissociation reaction depends on the acid dissociation constant of $HONO_{(aq)}$, $K_{a,HONO}$, and the pH of the aqueous surface. The aqueous reservoir can accumulate total nitrite ($[N(III)] = [HONO]_{(aq)} + [NO_2^-]_{(aq)}$) and continue to acidify until it becomes a source of gas phase HONO;

$$HONO_{(aq)} \longrightarrow HONO_{(g)} \qquad (R\,3.12)$$

A dynamic equilibrium, based on Henry's Law constant (Equation 3.23), is established when the rate of R 3.10 equals that of R 3.12. At equilibrium, the concentration of N(III) in the aqueous reservoir is described by:

$$[N(III)] = P_{HONO} H \left(1 + \frac{K_{a,HONO}}{[H^+]}\right) \qquad (3.24)$$

In order to accumulate a significant amount of N(III), capable of reaching an equilibrium in the ocean, the N(III) must be concentrated within the top of the ocean SML. This SML layer is $\sim 50\mu$m thick and is relatively isolated from the ocean and can have different physical and chemical properties than the ocean beneath (Hardy, 1982). Previous studies in Daya Bay, China, have determined that the chemical and physical parameters of the SML were indeed different than those of the underlying ocean, such as enhanced concentrations of organic matter, nutrients, dissolved trace metals, biochemical oxygen demand, chemical oxygen demand, chlorophyll-a, surface tensions, and pH (Zhang et al., 2001, 2006).

The molar fraction of N(III) stored in the SML aqueous reservoir at equilibrium, f_{SML}, would be given by:

$$f_{\mathrm{SML}} = \frac{N_{\mathrm{N(III),SML}}}{N_{\mathrm{N(III),SML}} + N_{\mathrm{HONO,MBL}}} = \frac{1}{1 + \frac{h_{\mathrm{MBL}}}{RT\,Ht_{\mathrm{SML}} \times \left(1 + \frac{K_{\mathrm{a}}}{[\mathrm{H}^{+}]}\right)}} \tag{3.25}$$

where $N_{\mathrm{N(III),SML}}$ is the number of moles of N(III) in the SML, t_{SML} is the thickness of the SML, $N_{\mathrm{HONO,MBL}}$ is the number of moles of HONO in the MBL and h_{MBL} is the MBL height. The concentration of N(III) in the SML reservoir depends on the temperature, pH and thickness of the SML. From Equation 3.25, an estimate of the fraction of HONO between the gas and aqueous phases in the SML was calculated for the following conditions; ocean pH=8.1 in the SML, t_{SML}=50μm, h_{MBL}=100 m, T=290 K, K_{a}=5.1×10^{-4}, and $H(T)$=76 M atm^{-1}. Under these conditions, it is expected that 98% of the N(III) partitions into the SML, independent of gas phase HONO. It is expected that HONO and HNO_3 would cause a change in the pH of the SML, however, this effect is presumably minor.

As a result, the SML at equilibrium with the ocean can potentially comprise a significant reservoir of N(III). Using Equation 3.24 and assuming a gas phase HONO mixing ratio of 1.0 ppb, the concentration of N(III) in the SML at equilibrium is 4.9×10^{-3} M, several orders of magnitude larger than previous reports of N(III)<2 μM (Zafiriou and True, 1979; Zhang et al., 2001, 2006) and of the highest N(III)=9 μM in the SML (Grasshoff, 1975). Previous studies observed minor enhancements of N(III) and N(V) in the SML in a polluted MBL (Zhang et al., 2001), and an acidification of only -0.2 pH of the SML compared to the underlying ocean (Zhang et al., 2006).

The low concentrations of N(III) in the SML, previously reported from other studies, suggest that the bulk alkaline ocean consists of a net sink of HONO. From these observations and estimates, the bulk ocean, represented by the SML appears to be significantly understaturated with N(III), greatly reducing the likelihood that a bulk aqueous reservoir of N(III) is the source of steady-state nighttime HONO observed in the MBL.

Marine Aerosols

Alternatively, an aqueous reservoir in the MBL may also exist within or on the surface of marine aerosols. The amount of HONO that can be dissolved in aerosols was calculated along with the fraction of HONO present in the aerosol reservoir, f_{aerosol}, compared to the total amount of HONO in the combined gas phase and aerosol reservoir. Assuming alkaline aerosols with pH=8.5 for sea salt aerosols (Chameides and Stelson, 1992) and using the previously calculated aerosol volume density of 1.56 $\times 10^{-10}\,\mathrm{m}^3\,\mathrm{m}^{-3}$, along with the previous choices of H, T and K_{a} used for the SML reservoir calculation, f_{aerosol} was found to be 0.038, with a gas phase equivalent of 40 ppt of N(III) existing in the aerosol.[4] These results suggest that aerosols comprise a minor reservoir of N(III) in comparison to the gas phase. These findings are in agreement with previous studies (Lammel and Cape, 1996), indicating that aerosols cannot support the aqueous reservoir required to account for the observed HONO in the MBL.

---

[4] This value is expected to decrease with a decline in pH.

Air-water Interface

The last potential reservoir is located at the air-water interface of any aqueous surface, such as the surface of the ocean, deliquesced aerosols, or terrestrial surfaces with adsorbed water. It is generally accepted that the nocturnal heterogeneous formation of HONO requires surfaces with at least one mono-layer of water. Earlier studies suggested that the heterogeneous reaction is initiated with a gas-phase molecule of NO_2 which adsorbs to a molecule of H_2O adsorbed to a surface ($S{-}OH_2$), which may consist of another molecule of H_2O ($S{-}OH_2{\cdot}H_2O$) (Lammel, 1999):

$$S{-}OH_2 + NO_2 \longrightarrow S{-}OH_2{\cdot}NO_2 \tag{R 3.13}$$

$$S{-}OH_2{\cdot}H_2O + NO_2 \longrightarrow S{-}OH_2{\cdot}H_2O{\cdot}NO_2 \tag{R 3.14}$$

An alteration to this mechanism was suggested by (Finlayson-Pitts et al., 2003b). The reaction was proposed to be initiated by the NO_2 dimer, N_2O_4, due to the preferred stability of N_2O_4 with two molecules of H_2O, over NO_2 with a single H_2O molecule. In a model similar to a previous work presented by (Mertes and Wahner, 1995), we suggest that the heterogeneous reaction of NO_2/N_2O_4 can also occur on the surface of bulk aqueous water, $((H_2O)_\infty{\cdot}H_2O)$ as follows:

$$(H_2O)_\infty{\cdot}H_2O + NO_2 \longrightarrow (H_2O)_\infty{\cdot}H_2O{\cdot}NO_2 \tag{R 3.15}$$

$$(H_2O)_\infty{\cdot}2\,H_2O + N_2O_4 \longrightarrow (H_2O)_\infty{\cdot}2\,H_2O{\cdot}N_2O_4 \tag{R 3.16}$$

The amount of NO_2 required to completely saturate the surface of the ocean at the air-water interface (S_{NO_2}) can be estimated, assuming a flat geometry of water on the surface. For R 3.15 and R 3.16, the maximum density of NO_2 that can be adsorbed to the surface is equal to the maximum density of water molecules at the surface. The radius and the cross sectional area of a H_2O molecule were calculated to be $r_{H_2O} = 1.9 \times 10^{-10}$ m and $A_{H_2O} = 1.2 \times 10^{-19}$ m^2, respectively. The surface density of water was estimated as, $S_{H_2O} = 1/A_{H_2O} = 8.6 \times 10^{18}$ molec m^{-2}. The amount of NO_2 required to saturate the aqueous surface is equal to the surface density of water at the surface, $S_{NO_2} = S_{H_2O}$.

The equivalent surface density of NO_2 required to saturate the surface if all the gas phase NO_2 in the MBL is brought down to the surface ($S^*_{NO_2}$) is described by:

$$S^*_{NO_2} \equiv \frac{P}{RT} C_{NO_2} h_{\mathrm{MBL}} \tag{3.26}$$

where C_{NO_2} is the gas phase mixing ratio of NO_2. By assuming a MBL height of $h_{\mathrm{MBL}} = 100$ m and a standard temperature and pressure, the gas phase NO_2 mixing ratio required to completely saturate the surface was found by equating $S^*_{NO_2}$ and S_{NO_2}, yielding $C_{NO_2} = 3.4$ ppb. Thus, given a fully saturated surface at the air-water interface, the reservoir would contain the equivalent of ∼3 ppb of NO_2 brought down to the surface. It is important to note that the surface density calculation above is an upper limit estimate for the surface saturation of NO_2 and the density of nitrogen precursors required to carry out the reactions as presented in the conceptual model is uncertain. It is possible that only a small percentage of the layer calculated above is in fact needed. Experimental confirmation for the presence of a nitrogen reservoir at the air-water interface is required. Based on observations, approximately 1 ppb of

HONO was measured in the gas phase. Under these conditions and ignoring excess NO_2 in the gas phase, the maximum mole fraction stored on the surface would be

$$f_{\text{surface}} = \frac{N_{\text{N(III),surface}}}{(N_{\text{N(III),surface}} + N_{\text{HONO,MBL}})} = 0.77 \tag{3.27}$$

Therefore, among the three potential reservoirs explored, the air-water interface appears to be the most probable since the NO_2 mixing ratios required to saturate the surface overnight are readily available, assuming that the mechanism proceeds as suggested. It should be noted that the amount of NO_2 to saturate a surface is currently unknown since there are no means to measure the saturation, but the estimation is useful as a potential upper limit.

Since the mechanism predicts the depletion of NO_2 on the surface reservoir, the lifetime of the reservoir can be estimated with a time constant of $\tau_{\text{surface}} = \tau_{\text{dep}}$ / (1 $-$ f), where f is the fraction of nitrogen in the surface reservoir compared to the combined gas and surface nitrogen reservoir and assuming a gas-phase mixing ratio of $NO_2 = 0$ ppb. Using a HONO lifetime with respect to deposition over the ocean of $\tau_{\text{dep}} = 1$ hour, the lifetime of the surface reservoir is found to be $\tau_{\text{surface}} = 4.4$ h, as an upper limit. On the night of August 2, HONO levels remained constant for a 6 hour period while NO_2 declined from 15 to <1.0 ppb. Assuming a balance between sources and sinks of HONO during the steady-state period, in order for the constant levels of HONO to be maintained over such a long period of time with low NO_2, deposited HONO must be recycled back into the reservoir.

The previous analysis demonstrates that the air-water interface on the surface of the ocean can potentially operate as a reservoir of NO_2 and HONO precursors. The surface reservoir would be confined to the top mono-layer of surface water with a potential thickness of $\sim$0.4 nm. We refer to this surface as the sea surface nano-layer (SNL). A recent published study showed that anions catalyze the hydrolysis of NO_2 at the air/water interface on micro-droplets, presumably forming HONO in the process (Yabushita et al., 2009). It was proposed that an anion within an aqueous layer can share its electron density with the empty orbital of a molecule of NO_2 in the gas phase, binding it to the surface until reaction with another NO_2 molecule, producing HONO. Another recent study determined the intermolecular $NO_2{-}H_2O$ potential using high-level ab initio calculations and found it to be two times stronger than previously calculated (Murfachaew et al., 2013). This study also used scattering simulations of an NO_2 molecule interacting with a water slab and observed that the majority of the scattering events resulted in the NO_2 molecule becoming trapped at the surface or in the interior of the water slab. It was suggested that the residence times of NO_2 on an aqueous surface may be increased by the interaction with other species in the aqueous phase such as Cl^-, HNO_3, NO_3 and other surfactants.

These more recent studies support the existence of a surface reservoir containing nitrogen dioxide and/or other nitrogen precursors. Therefore, the observations and analysis of this work provide compelling evidence for the existence of an aqueous reservoir at the air-water interface, which supports the steady-state concentrations of HONO. Furthermore, recent literature provides possible mechanisms of the interaction of NO_2 on water surfaces which would help to stabilize this reservoir.

3.2.6 A Conceptual Model of HONO Formation on Aqueous Surfaces

A summary of the observations and conclusions on the steady-state of HONO in the MBL at Saturna Island are as follows:

1. The steady-state of HONO is characterized by $d[\mathrm{HONO}]/dt \approx 0$ for an extended period of time during the night. The steady-state is formed within an hour after sunset and persists throughout entire night, until photolysis in the morning. The HONO mixing ratio during the steady-state period was between 0.5−1.5 ppb, varying nightly.

2. The NO_2 mixing ratio was high early in the evening (median $[NO_2] = 15$ ppb) and slowly decreased over the course of the night. This is indicative of a well mixed NBL with a relatively short lifetime of NO_2.

3. During the steady-state period, the HONO concentration was independent of the NO_2 concentration, suggesting a zero-order dependence of HONO on NO_2. The median HONO/NO_2 ratio during the steady-state period increased from $0.03 - 0.30$, with an upper limit >1.0.

4. The concentration of HONO was independent of air mass and wind direction, suggesting a source of HONO which is constant throughout the region, such as the surface of the ocean.

5. The concentration of HONO was negatively correlated with relative humidity over a range of $60 - 90\%$ RH.

6. HONO was positively correlated with temperature over the range of 15−23 °C during the steady-state period. The correlation has a temperature coefficient of $(1/P_{\mathrm{HONO}})(dP_{\mathrm{HONO}}/dT) = +8.2 \pm 0.8\,\%\,\mathrm{K}^{-1}$. Based on the temperature dependence, the calculated enthalpy of vaporization of HONO from the SNL is $\Delta H_{\mathrm{vap,SNL}} = 58.1 \pm 5.8\,\mathrm{kJ\,mol^{-1}}$, roughly consistent with HONO vaporization from pure water $\Delta H_{\mathrm{vap}} = 40.7 \pm 1.2\,\mathrm{kJ\,mol^{-1}}$.

7. The maximum amount of N(III) stored in a bulk ocean SML or aerosol aqueous reservoir is likely unable to support the steady-state observations of HONO in the MBL.

8. The top mono-layer of H_2O at the air-water interface of the ocean surface can sustain a sufficient reservoir to support the observed HONO steady-state. The air-water interface is potentially saturated with NO_2 and/or nitrogen precursors and products such as N_2O_4, $ONONO_2$, $NO^+NO_3^-$, HONO, HNO_3 etc. It is also likely that deposited HONO is recycled back into the reservoir.

Several studies have parameterized the heterogeneous production of HONO via hydrolysis of NO_2. The uptake of gas-phase NO_2 and HONO on aqueous surfaces was studied using a liquid jet technique by (Mertes and Wahner, 1995). The study proposed a model for NO_2 hydrolysis on an aqueous surface and suggested a surface layer, separate from the bulk liquid phase, to explain their results. Another study by (Lammel, 1999) suggested a surface based mechanism and parameterized HONO formation on dry (containing one mono-layer of water), wet (humid), and aqueous/bulk water surfaces as:

$$\frac{d[\mathrm{HONO}]}{dt} = a\,[\mathrm{NO_2}]\left\{\left[\left(\frac{S}{V}\right)_{\mathrm{dry}} + \left(\frac{S}{V}\right)_{\mathrm{aqueous}}\right]k_{\mathrm{het},1} + \left(\frac{S}{V}\right)_{\mathrm{wet}} k_{\mathrm{het},2}[\mathrm{H_2O}]\right\} \tag{3.28}$$

where $a = 0.5$, and $k_{\mathrm{het},1}$, $k_{\mathrm{het},2}$ are different heterogeneous conversion rates of NO_2 hydrolysis to HONO, depending on surface water coverage. This equation predicts that HONO formation is zero-order with respect to H_2O for dry and aqueous surfaces, first-order with respect to H_2O for humid/aqueous surfaces and first-order with respect to NO_2 for all surface types. After adsorption of a NO_2 molecule to the surface water, (Lammel, 1999) hypothesized the following process as the main reaction step to produce HONO:

$$\mathrm{S{-}OH_2{\cdot}H_2ONO_2 + NO_2 \longrightarrow S{-}OH_2{\cdot}HNO_3 + HONO} \tag{R 3.17}$$

An alternative formation mechanism based on laboratory and field study observations was recently proposed by (Finlayson-Pitts et al., 2003b) and was previously summarized in Chapter 1.2.4.

Building upon the work from previous field and laboratory studies, a conceptual model of HONO formation on aqueous surfaces is proposed based on the steady-state observations of HONO at Saturna Island and the other observations summarized above. The conceptual model, shown in Figure 3.20, assumes that a single mechanism is responsible for the observed zero-order dependence of HONO on NO_2 in the MBL. In addition, the model was also extended to describe the frequently observed first-order dependence of HONO on NO_2 and is illustrated by Figure 3.21.

A key aspect of the model is the assumption of the sea surface nano-layer saturated with nitrogen precursors upon exposure to NO_2. The SNL is considered to be the reservoir of HONO located at the air-water interface on the ocean surface, supporting the observed steady-state of HONO. The SNL is potentially $1 - n$ mono-layers of water thick, where each mono-layer has a thickness of ≈0.38 nm. The SNL could be no more than a layer of surface adsorbed NO_2 or equivalent precursors on top of the water that is stabilized by a high adhesive force of attraction between the precursor molecule and water, which is less than the cohesive force of attraction between water molecules. Although the SNL may be occasionally disturbed by wave action, the SML has been reported as a stable phenomenon, persisting for extended periods of time (Zhang et al., 2006). Rapid formation of surface layers of adsorbed NO_2 have been shown in previous glass experiments (George et al., 2005), while recent studies have shown NO_2 adsorption on an aqueous surface stabilized by interaction with anions in the aqueous phase (Yabushita et al., 2009; Murfachaew et al., 2013), as previously discussed.

The conceptual model shown in Figure 3.20 predicts the saturation of the ocean's surface with HONO precursors (NO_2, N_2O_4, $ONONO_2$, $NO^+NO_3^-$, HONO, HNO_3 etc.), given that sufficient gas-phase NO_2 is present over the course of the night. Upon surface saturation, HONO takes part in a dynamic equilibrium between production from the reservoir and dry deposition into the reservoir, possibly governed by Henry's Law constant. The surface saturation is maintained by the reversible deposition of HONO, which comprises the dominant sink for HONO during the steady-state period.

The surface saturation inhibits NO_2 from further depositing on the surface, leading to the zero-order dependence of HONO with respect to NO_2.

As shown in the diagram, the heterogeneous formation of HONO results in the production of HNO_3, which increases the acidity of the surface. The HNO_3 can be

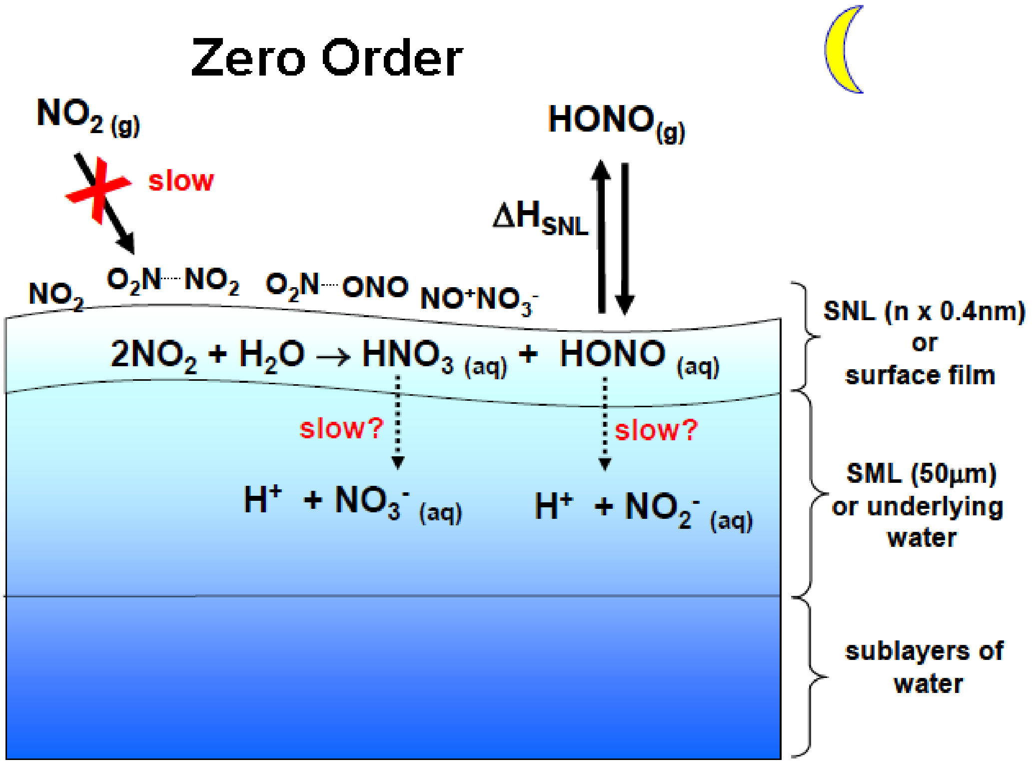

Figure 3.20: Conceptual model of HONO formation over an aqueous surface operating under zero-order with respect to NO_2 during the nighttime. The surface becomes saturated with HONO precursors if sufficient gas-phase NO_2 is present. The saturated surface inhibits NO_2 from further reacting on the surface, leading to a zero-order dependence. HONO is in a dynamic equilibrium between deposition and production from the reservoir and remains in a steady-state for the duration of the night as long as the reservoir is not depleted.

transported into the sub-layers of the underlying ocean via diffusion, turbulence, wave breaking and bubble bursting in the ocean at an uncertain rate. The water sub-layers may allow for the diffusion of HNO_3, H_3O^+ and NO_3^- away from the SNL, preventing the SNL from becoming too acidic. This possibility for surface deacidification may provide a key difference between the SNL on the ocean and terrestrial humid surfaces.

It is interesting to explore what may occur in this model system during the daytime. During the daytime, when HONO is irreversibly lost from the system via photolysis, the surface would become under-saturated in oxides of nitrogen, as shown in Figure 3.21. Gas-phase NO_2 would once again deposits to the surface, replenishing the reservoir and forming HONO; at which point the system returns to first-order kinetics. Several hours after sunrise, the photolysis of HONO is expected to become the major sink of gas-phase HONO, depleting the surface reservoir. Thus, this mechanism may provide insight into the missing daytime source of HONO.

By combining the mechanisms proposed in Figures 3.20 and 3.21 with those previously published by (Lammel, 1999; Finlayson-Pitts et al., 2003b), the final HONO production reaction is shown below:

$$\mathrm{NO^+NO_3^-} + \mathrm{H_2O} \longrightarrow \mathrm{HONO_{(SNL)}} + \mathrm{HNO_{3\,(SNL)}} \tag{R 3.18}$$

where the products are equivalent to those in Reactions R 3.17 and R 1.52. The HNO_3 produced at the SNL acidifies the surface and supports reversible partitioning of HONO to the atmosphere:

$$\mathrm{HONO_{(SNL)}} \rightleftharpoons \mathrm{HONO_{(g)}} \tag{R 3.19}$$

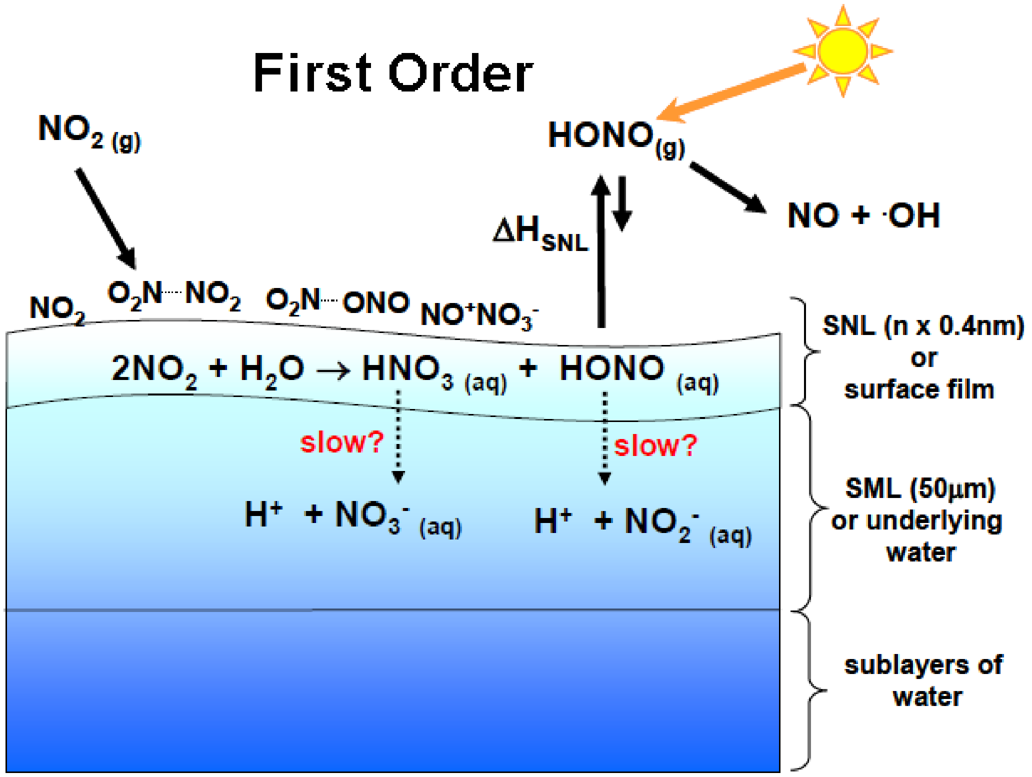

Figure 3.21: Conceptual model of HONO formation over an aqueous surface, operating under first-order with respect to NO_2 during the daytime. HONO is permanently lost from the system via photolysis and gas-phase NO_2 replenishes the reservoir, leading to the first-order dependence.

where the enthaply of R 3.19 is largely responsible for the observed temperature dependence. This dynamic equilibrium is presumably the dominant source of HONO during the steady-state period, leading to the observed zero-order dependence of HONO on NO_2.

It is important to note that some experiments did not observe HONO production from NO_2 exposure on distilled H_2O surfaces. As reported by (Cheung et al., 2000), heterogeneous reaction of NO_2 was not observed over a distilled aqueous surface using droplet train and bubble train flow reactors. The disappearance of NO_2 was instead attributed to the bulk phase solubility and reaction. In turn, the previously mentioned studies by (Yabushita et al., 2009; Murfachaew et al., 2013), indicate that NO_2 adsorption and HONO production may be enhanced/catalyzed by anions in the water surface. Such anions certainly exist in the ocean, and are presumably present in sufficient levels in urban areas due to ubiquitous HCl, or NaCl. This suggests that the presented conceptual model may need to be modified by adding Cl^- and/or NO_3^- catalysts to the surface.

It is also important to mention that the conceptual model proposed is merely a hypothetical model which explains the observations gathered at Saturna Island, against which future theories can be tested. The model describes one possible HONO reservoir theory, which is currently unproven. Alternate reservoirs have been proposed, providing additional HONO or NO_2^- sources in soil (Su et al., 2011) and minerals (VandenBoer, 2012).

3.2.7 Implications for Atmospheric Chemistry

The conceptual model described in Figures 3.20 and 3.21 was initially proposed to explain observations in the polluted MBL (Wojtal et al., 2011), but can be extended to include other environments where sufficient NO_2 is present along with an aqueous surface. This mechanism can potentially occur on freshwater lakes, surfaces of deliquesced aerosols, or any terrestrial surface with condensed water, generally occurring late in the night when the relative humidity is $\gtrsim$80%. On terrestrial surfaces, the transition from a dry/humid HONO production mechanism to an aqueous production would be marked by the time at which rising HONO concentrations level off, generating a period with $d[\mathrm{HONO}]/dt = 0$, with conditions similar to that in the polluted MBL.

In regions within the remote marine boundary layer, the formation of a HONO steady-state is not expected due to insufficient levels of NO_2. Previous shipboard measurements of HONO were made in the remote MBL within the Eastern Mediterranean Sea (Večeřa et al., 2008). The authors observed HONO mixing ratios below 50 ppt and NO_2 mixing ratios between 4−6 ppb for the majority of the study, with peaks of HONO as high as 2.7 ppb during episodes correlated with ship plume emissions. As predicted, due to the low mixing ratios of NO_2, high levels of HONO were not observed, likely due to insufficient amounts of NO_2 present to saturate the ocean surface in the remote MBL.

The proposed model may also have important implications in coastal areas with high NO_x emissions. With the onset of HONO photolysis in the morning, the mechanism is expected to convert to first-order kinetics, producing significant amounts of OH-radicals. The reactions expected to occur during the daytime are as follows:

$$2\,\mathrm{NO}_{2\,(g)} \longrightarrow 2\,\mathrm{NO}_{2\,(SNL)} \tag{R 3.20}$$

$$2\,\mathrm{NO}_{2\,(SNL)} + \mathrm{H_2O} \longrightarrow \mathrm{HONO}_{(SNL)} + \mathrm{HNO}_{3\,(SNL)} \tag{R 3.21}$$

$$\mathrm{HNO}_{3\,(SNL)} \longrightarrow \mathrm{HNO}_{3\,(SML)} \tag{R 3.22}$$

$$\mathrm{HONO}_{(SNL)} \rightleftharpoons \mathrm{HONO}_{(g)} \tag{R 3.23}$$

$$\mathrm{HONO}_{(g)} + h\nu \longrightarrow \mathrm{NO}_{(g)} + \mathrm{OH}_{(g)} \tag{R 3.24}$$

$$\mathrm{NO}_{(g)} + \mathrm{O}_{3\,(g)} \longrightarrow \mathrm{NO}_{2\,(g)} + \mathrm{O}_{2\,(g)} \tag{R 3.25}$$

Assuming that the O_3 concentration is not completely titrated by NO and a sufficient amount of NO_2 is present to saturate the surface, the overall net reaction would be:

$$\mathrm{NO}_{2\,(g)} + \mathrm{O}_{3\,(g)} + \mathrm{H_2O} + h\nu \longrightarrow \mathrm{HNO}_{3\,(SML)} + \mathrm{OH}_{(g)} + \mathrm{O}_{2(\,g)} \tag{R 3.26}$$

where a loss of odd oxygen (O_3 + NO_2) is predicted, along with the generation of HNO_3 in the SML and OH-radicals in the boundary layer. If this reaction indeed occurs, positive vertical gradients of odd oxygen ($d[\mathrm{NO_2} + \mathrm{O_3}]/dz > 0$) and negative gradients of OH ($d[\mathrm{OH}]/dz > 0$) would be expected, given that significant levels of odd oxygen are present in the boundary layer.

In order to further investigate the formation of a steady-state of HONO in a terrestrial environment, a year-long data set of HONO and NO_2 was collected at York University. A better understanding of the causes and implications of the HONO steady-state comprised a strong motivation for the research performed at York University, discussed in details in Chapter 3.4.

3.3 NO_3 at York University

Active-DOAS measurements of NO_3 and NO_2 were collected from November 13, 2008 to December 18, 2008 and from March 17, 2009 to June 14, 2009. In total, 42 nights of data were collected and analyzed in the polluted urban environment at York

University. The purpose of these measurements was to augment the NO_3 analysis performed for the Saturna data set. A summary of the NO_3 and NO_2 measurements will be presented, exploring the dependence of NO_3 on temperature and atmospheric stability. In addition, a comparison between the steady-state and non steady-state lifetimes of NO_3 will be shown.

3.3.1 Overview of Measurements

An overview of the observations of NO_3 and NO_2 is shown in Figure 3.22 and a statistical summary is shown in Table 3.8. The analysis was mostly restricted to measurements during the dark period of the night, defined as all observations 1 hour after sunset and 1 hour before sunrise. The nighttime average and median NO_3 mixing

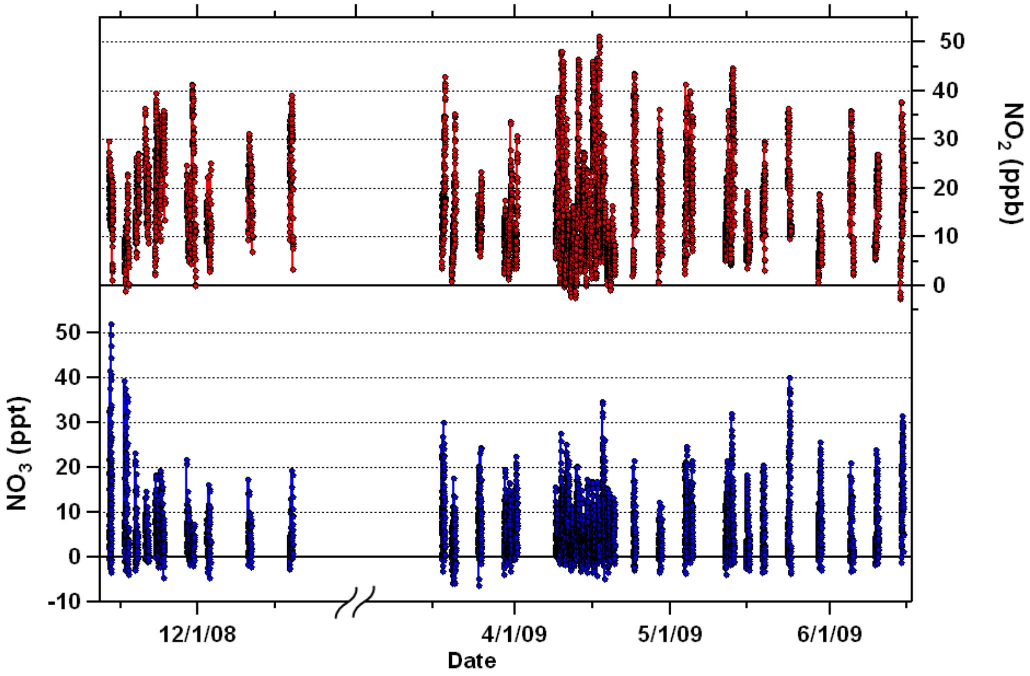

Figure 3.22: Observations of NO_3 and NO_2 at York University.

Table 3.8: Statistics of NO_3 and NO_2 measurements made at York University during the dark period of the night, along with statistics of 5 minute MET parameters from the York University EMOS station.

	Max	95%	75%	Average	Median	25%	Min	N
NO_3 (ppt)	51.9	20.9	11.1	7.7	6.0	<DL	<DL	3238
NO_2 (ppb)	48.1	36.2	24.2	18.1	16.6	10.4	<DL	3286
T (°C)	24.2	15.6	10.1	5.4	6.0	0.51	-11.0	5892
RH (%)	91	87	75	59	59	44	18	5892
WS ($\mathrm{m\,s^{-1}}$)	8.3	5.3	3.7	2.5	2.4	1.4	0	5892

ratios were 7.7 ppt and 6.0 ppt, respectively. The mixing ratio of NO_3 was below the detection limit of the instrument for 36% of all nocturnal measurements while the maximum observed mixing ratio was 51.9 ppt. The average and median mixing ratios of NO_2 were 18.1 ppb and 16.6 ppb, respectively, with an observed maximum mixing ratio of 48.1 ppb. For comparison, the average NO_3 and NO_2 mixing ratios measured at Saturna Island were 13.1 ppt and 6.4 ppb, respectively. Thus, the average NO_3 mixing ratio observed at Saturna Island was almost twice as high as the average mixing ratio of NO_3 at York University in the presence of nearly 3 times less NO_2. This difference will be explored later in this Chapter.

The temporal variation of NO_3 and NO_2, grouped into 30-minute time bins, is shown in Figure 3.23. Contrary to the NO_3 measurements at Saturna Island, there does not appear to be any significant trend between the NO_3 mixing ratio with time of night. Median mixing ratios of NO_3 are ~5 ppt throughout the night with the 95th percentile >20 ppt, 1.5 hours after sunset. The NO_2 temporal profile shows an increase in the beginning of the night and median levels remain constant with time at ~18 ppb overnight.

Figure 3.24 displays a case study from which the typical nocturnal behavior of NO_3 may be observed. The NO_3 mixing ratio is below detection limit during the daytime

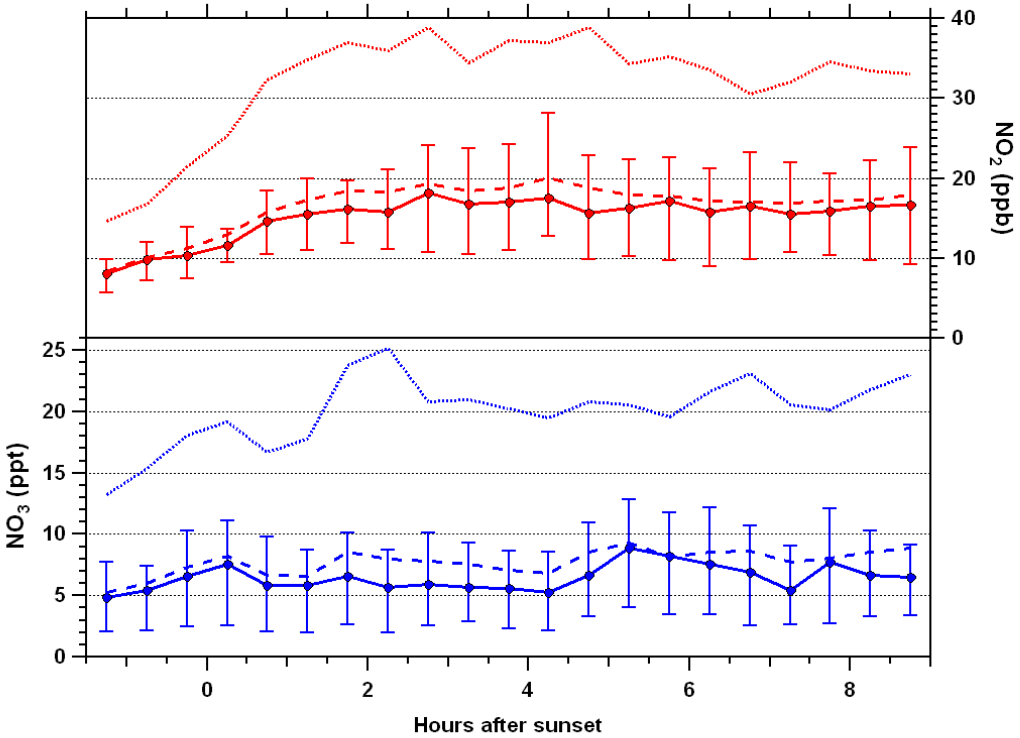

Figure 3.23: Nocturnal temporal profile of NO_3 and NO_2 grouped into 30-minute time bins. The average (dashed line), median (solid line), 25th, 75th (error bars) and 95th percentiles (dotted line) are shown.

and sporadically rises to ∼10 ppt multiple times overnight. Before sunrise, the NO_3 mixing ratio once again falls below detection limit and there remains after sunrise. Sufficient concentrations of NO_2 and O_3 were present throughout the night, leading to production of NO_3. The sporadic temporal profile of NO_3 is likely explained by the availability and abundance of NO from surrounding sources, rapidly destroying NO_3 and preventing an overnight buildup. This is presumably the largest cause of

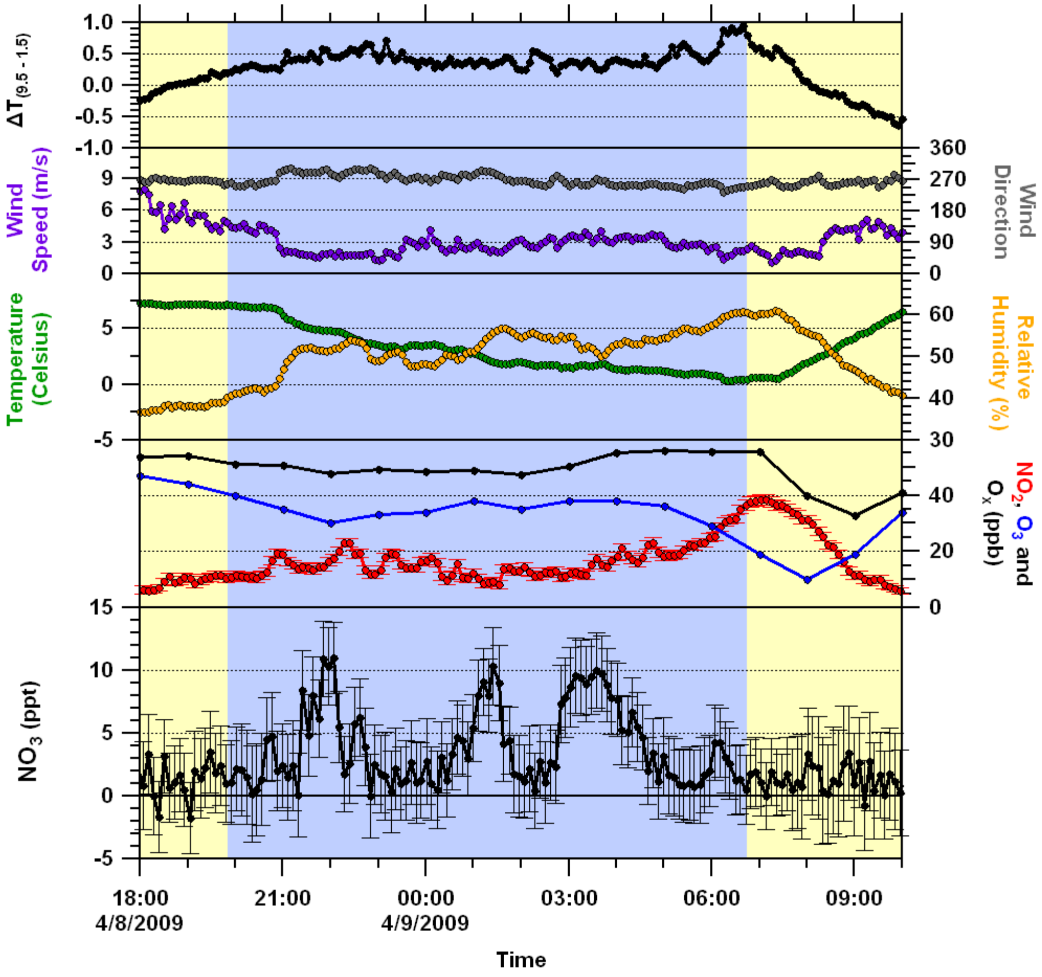

Figure 3.24: Nocturnal measurements on April 8/9, 2009. The yellow and blue background represent daytime and nighttime, respectively.

the difference between the NO_3 mixing ratios observed at Saturna Island and York University.

3.3.2 NO_3 Temperature Dependence

The temperature dependence of NO_3 is shown in Figure 3.25 for 3°C temperature bins during the dark period of the night. The NO_3 mixing ratio is observed to strongly correlate with temperature, leading to higher levels of NO_3 for warmer overnight temperatures. This observation is likely linked with the temperature dependent equilibrium of the NO_2-NO_3-N_2O_5 system, with colder temperatures favoring the stability of N_2O_5. The equilibrium constant for this system, $K_{\mathrm{eq}} = [\mathrm{N_2O_5}]/[\mathrm{NO_3}][\mathrm{NO_2}]$, varies from $4.24 \times 10^{-11}\,\mathrm{cm^3\,molec^{-1}\,s^{-1}}$ at 20°C to $1.28 \times 10^{-9}\,\mathrm{cm^3\,molec^{-1}\,s^{-1}}$ at -5°C (Wängberg et al., 1997). The lifetime of N_2O_5 with respect to thermal decomposition at 20°C and -5°C is 41 seconds and 20.8 minutes, with rate constants of $k_{(\mathrm{N_2O_5})} = 2.46 \times 10^{-2}\ \mathrm{s^{-1}}$ and $8.02 \times 10^{-4}\ \mathrm{s^{-1}}$, respectively. The rate constant for the formation of NO_3 from the reaction between NO_2 and O_3 is also temperature dependent. The rate constant varies from $1.29\ \times 10^{-17}\,\mathrm{cm^3\,molec^{-1}\,s^{-1}}$ at -5 °C to $2.82\ \times 10^{-17}\,\mathrm{cm^3\,molec^{-1}\,s^{-1}}$ at 20 °C, signifying a slower production of NO_3 for colder temperatures. Therefore, since the increase of $k_{(\mathrm{N_2O_5})}$ with temperature is about ∼15 times as large as for the formation rate of NO_3, the observed temperature dependence is expected be mostly governed by K_{eq}.

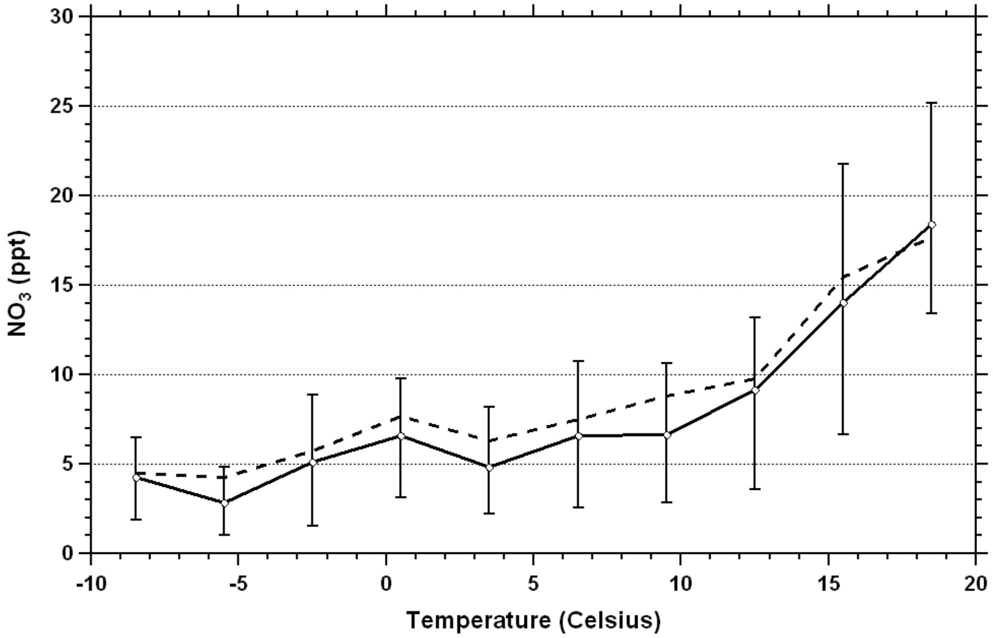

Figure 3.25: Nocturnal statistics for the NO_3 mixing ratio as a function of temperature. The median (solid line), 25th, and 75th percentiles (error bars) along with the average (dashed line) are shown for 3°C temperature bins.

3.3.3 NO_3 and Atmospheric Stability

Δ Temperature ($\Delta T_{9.5-1}$) is a measure of the temperature difference between the vertical elevations of 9.5 and 1.0 meters and is an indicator of atmospheric stability. For a well mixed atmosphere, the temperature in the troposphere decreases at an average lapse rate of 6.5 °C/km, lower than the adiabatic lapse rate (9.8 °C/km). Negative or near 0 values of Δ temperature are indicative of a well mixed surface layer. Vertical mixing is restricted when $\Delta T_{9.5-1}$ is positive, leading to stable and low nocturnal inversions (Schnell et al., 2009).

A case study of an atmospherically stable night is shown in Figure 3.26, determined by the high $\Delta T_{9.5-1}$ values and low wind speeds overnight. The formation of a low nocturnal inversion was accompanied by the decline of O_3, likely due to reaction of O_3 with NO, as shown by the constant odd oxygen ($NO_2 + O_3$) throughout the beginning of the night. The NO_3 mixing ratio remains below detection limit for the duration of the night due to the absence of O_3, preventing the production of N_2O_5. These conditions favor longer nocturnal lifetimes of NO_2, by removing the N_2O_5 and HNO_3 loss pathways.

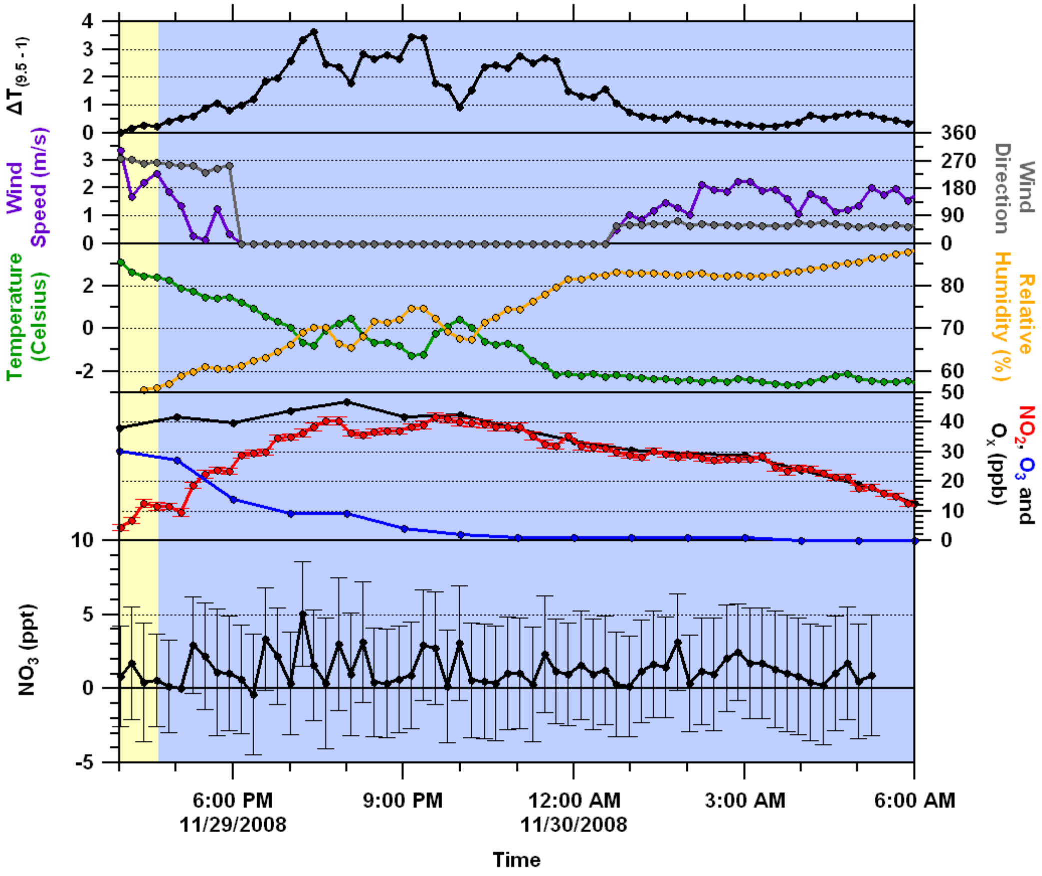

Figure 3.26: Nocturnal observations of NO_3, NO_2 and O_3 during an atmospherically stable night on November 29/30, 2008.

A case study of an atmospherically unstable night is shown in Figure 3.27, determined by $\Delta T_{9.5-1} \simeq 0°C$ and high wind speeds. Contrary to the previous case study, the overnight mixing ratios of NO_2 and O_3 remained at ~10 ppb and 35 ppb, respectively, with odd oxygen steady at ~45 ppb overnight. The NO_3 mixing ratio was highly variable throughout the night, reaching peaks of 20 ppt. During an unstable night, formation of N_2O_5 and subsequently HNO_3 is expected to occur, leading to significantly different nighttime nitrogen chemistry compared to the stable night.

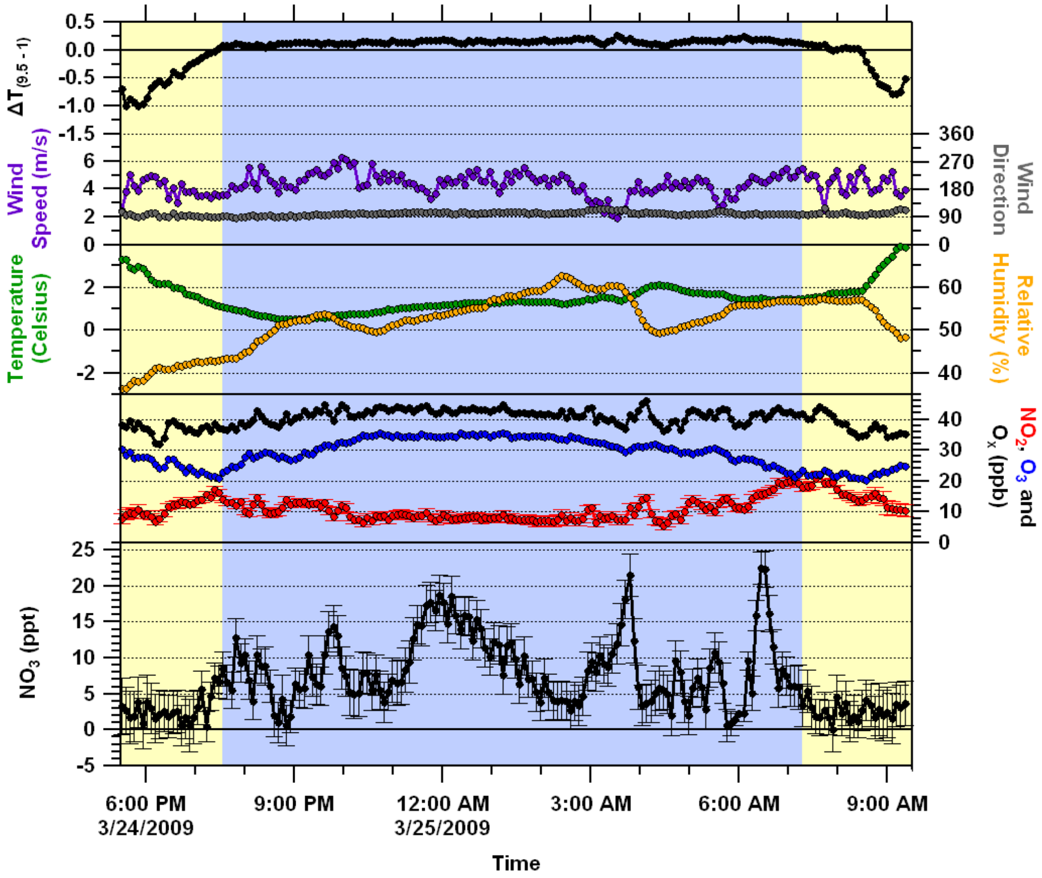

Figure 3.27: Nocturnal observations of NO_3, NO_2 and O_3 during an atmospherically unstable night on March 24/25, 2009.

3.3.4 Lifetime of NO_3

The NO_3 lifetime was calculated under steady-state and non steady-state assumptions for two case studies. The approach used to determine the lifetimes is nearly identical to that previously discussed in Chapter 3.1.3 using Equations 3.2 and 3.10 respectively, with the exception that a 9 point running slope was used in the continuous data set to calculate $d[NO_3]/dt$ and $d[N_2O_5]/dt$ instead of a 3 point running slope, in order to reduce noise. In order to investigate the lifetimes of NO_3, two case studies with different overnight temperatures were chosen, for which elevated levels of NO_3 were observed for extended periods of time.

The first case study was June 14/15, 2009 and is shown in Figure 3.28. This case study has a similar overnight NO_3 temporal profile to the observations at Saturna Island, along with similar overnight temperatures. As shown for the Saturna field study (T_{avg} = 18.3°C), the equilibrium for the NO_2-NO_3-N_2O_5 system is expected to be rapidly achieved as a consequence of high turnover times of the forward and reverse reactions due to warmer temperatures. Early in the evening, the NO_2 mixing ratio rapidly rose as the O_3 mixing ratio decreased, likely due to NO emissions and to the formation of a stable NBL. During this time, the NO_3 mixing ratio rapidly rose from below detection limit to ∼30 ppt.

The calculated N_2O_5 mixing ratio along with steady-state and non steady-state lifetimes of NO_3 are shown in Figure 3.29 for the time period between 22:00−5:00. Due to similar temperatures between this case study and the observations at Saturna

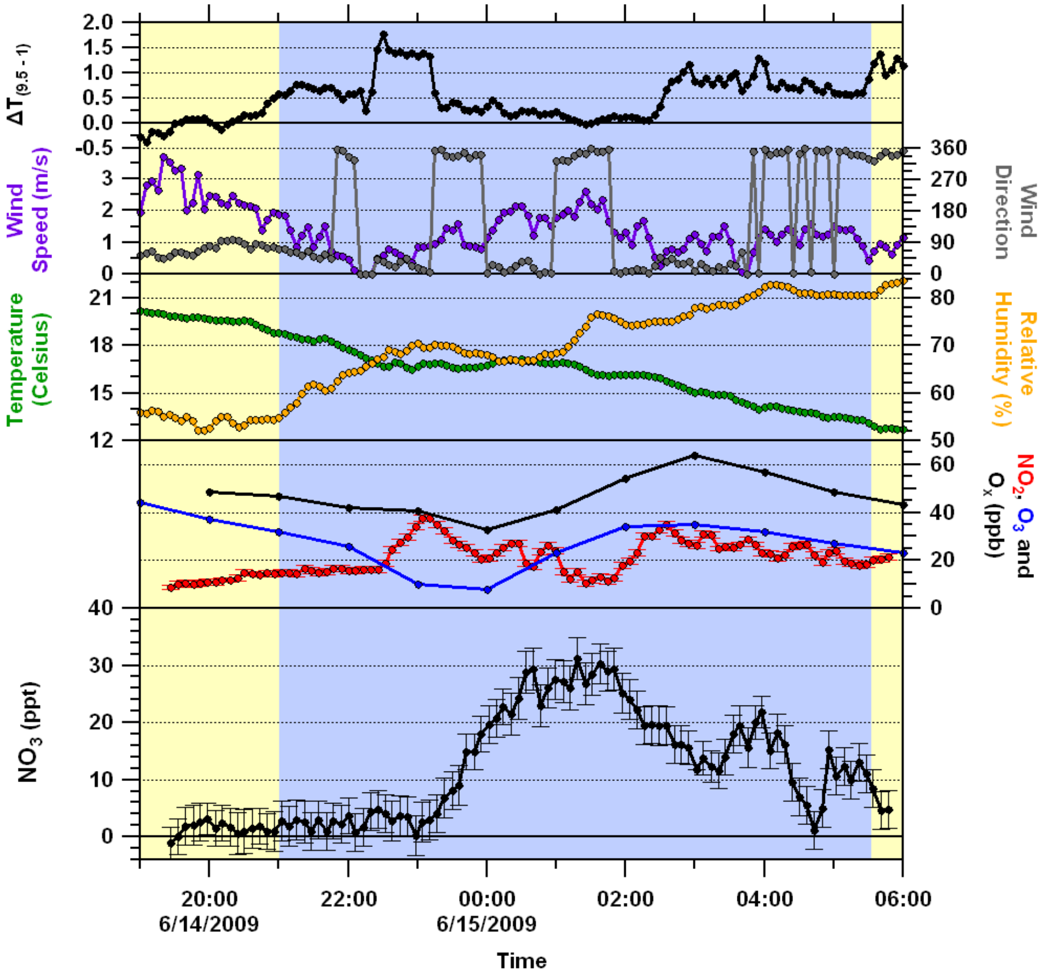

Figure 3.28: Nocturnal observations on June 14/15, 2009.

Island, an equilibrium is expected to be established between the NO_2-NO_3-N_2O_5 system, as previously discussed in Chapter 3.1.2. The calculated N_2O_5 mixing ratio was low in the beginning of the night and remained between 0.5 and 1.0 ppb overnight after the NO_3 rise. The steady-state lifetime of NO_3 varied from ∼20 seconds to 3 minutes overnight, similar to lifetimes encountered at Saturna Island. Aside from the period between 23:30−0:30 where the non steady-state lifetime was highly variable, the two calculated lifetimes are in very good agreement and the steady-state

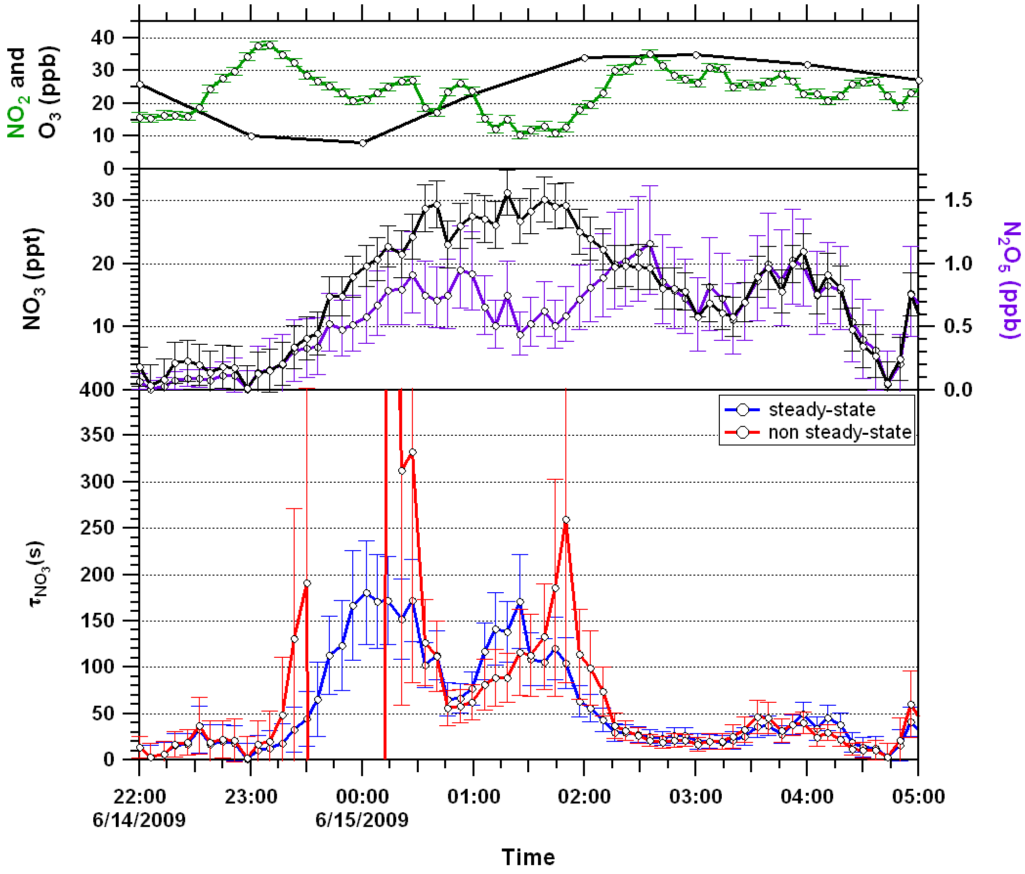

Figure 3.29: Comparison of steady-state and non steady-state lifetimes for the June 14/15, 2009 case study.

assumptions appears to be valid.

The November 28/29, 2008 case study is shown in Figure 3.30. Contrary to the previous case study, the overnight temperatures ranged between 0 − 1°C. Winds from the west were observed for the entire case study, reducing the possibility that a change in air mass occurred overnight. Rainy conditions were observed before sunset and peaks in the NO$_3$ mixing ratio were detected early in the evening. The NO$_3$ mixing ratio was highly variable throughout the night, remaining above detection

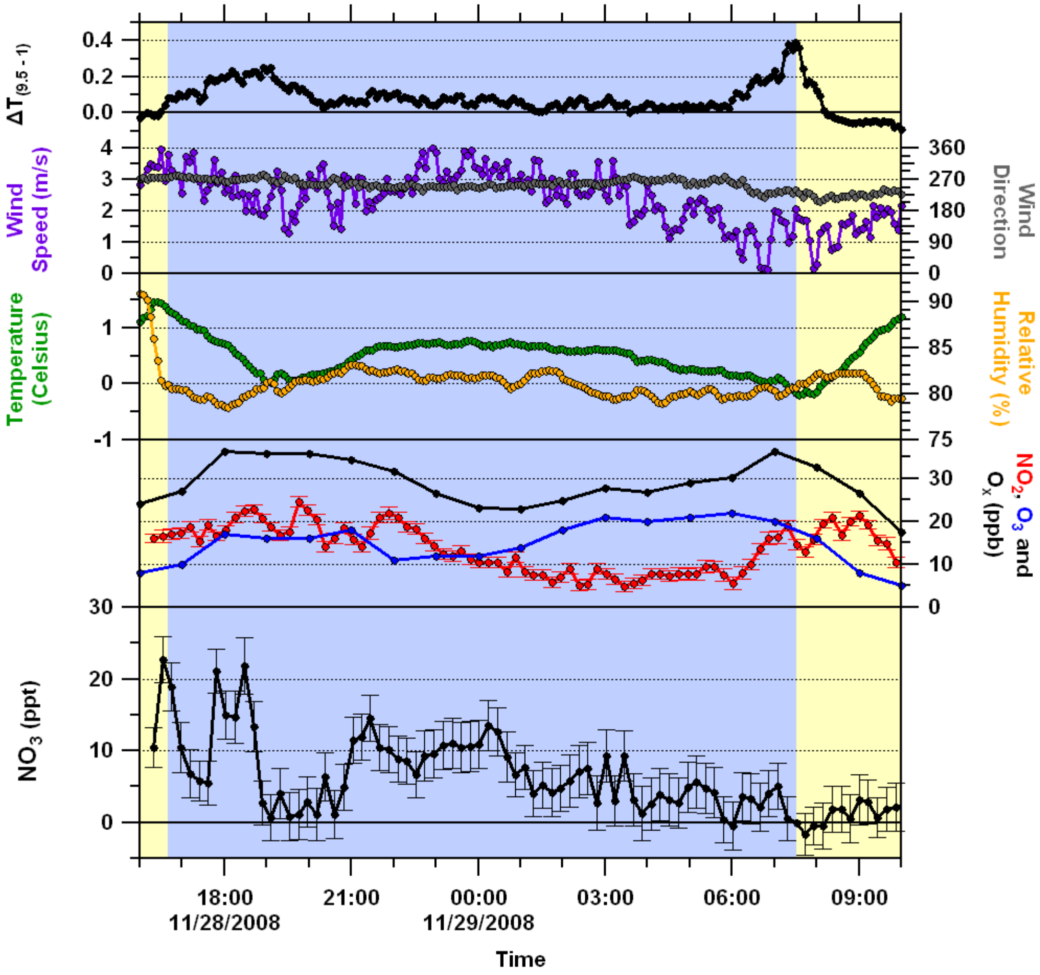

Figure 3.30: Nocturnal observations on November 28/29, 2008.

limit for an extended period of time after 21:00. The mixing ratio of NO_3 was ∼10 ppt between 21:00 − 1:00 and slowly decayed overnight while the NO_2 and O_3 mixing ratios were measured between 5 ppb and 25 ppb.

The calculated N_2O_5 mixing ratio along with the steady-state and non steady-state lifetimes are shown in Figure 3.31 for the time period between 21:30 − 5:30. The lifetime of N_2O_5 with respect to thermal decomposition at 1°C is 9.3 minutes and the lifetime of NO_3 for the reaction with NO_2 to form N_2O_5 is 2 seconds. The

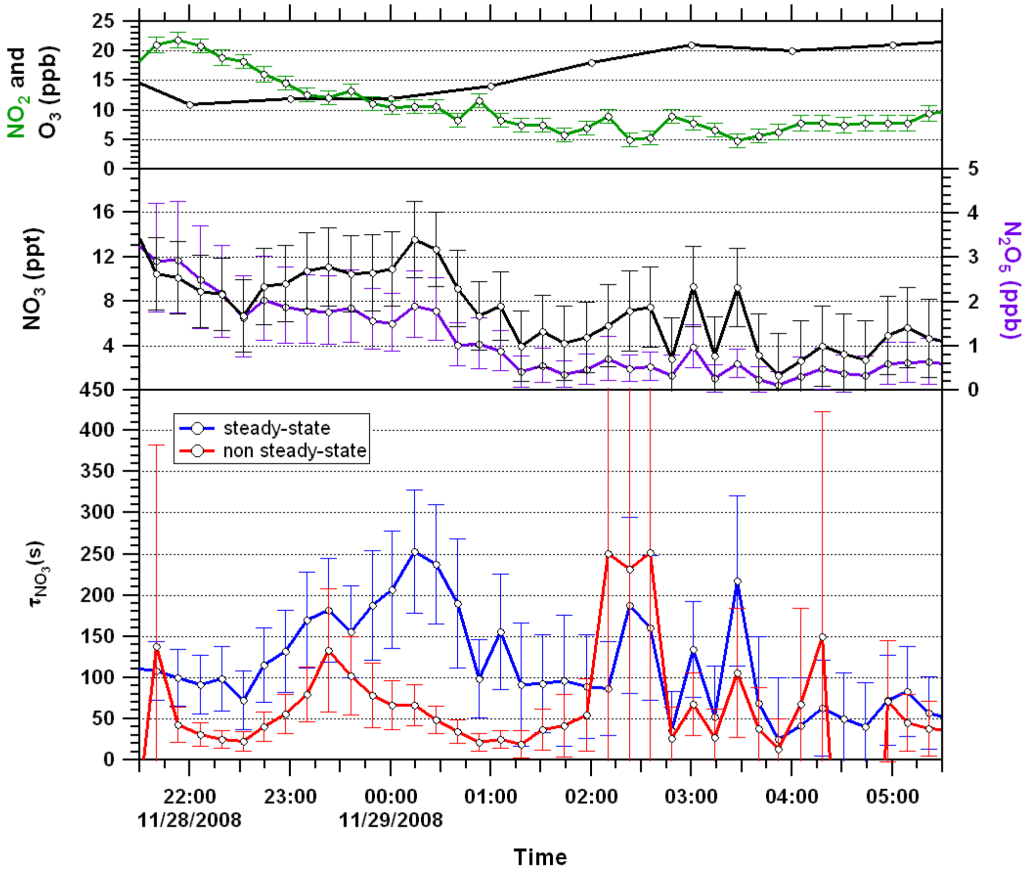

Figure 3.31: Comparison of steady-state and non steady-state lifetimes for the November 28/29, 2008 case study.

time required for N_2O_5 to reach equilibrium is uncertain, although likely on a 1 hour timescale. The calculated N_2O_5 mixing ratio decreased from 3 ppb to 0.5 ppb overnight. As seen in Figure 3.31, the steady-state lifetimes of NO_3 ranged from 1.5 minutes to 4 minutes. The non steady-state assumption NO_3 lifetimes were much lower in the early portion of the night, ranging from 20 seconds to 2 minutes, and agree with the steady-state lifetimes in the later part of the night. The colder temperatures increase the lifetime of N_2O_5 and greatly slow the approach of the system to steady-state as previously described by (Brown et al., 2003a), causing the steady-state assumption to overestimate the lifetime of NO_3. This emphasizes the fact that the steady-state assumption is not always valid when calculating lifetimes of NO_3, and that non-steady state lifetimes of NO_3 should be used when appropriate.

It is important to emphasize that due to the colder temperatures encountered during this case study, the equilibrium assumption of the NO_2-NO_3-N_2O_5 system is uncertain. In the occasion that equilibrium is not established for this case study, the non steady-state lifetimes calculated in this analysis are not definitive. In order to explore the differences between steady-state and non steady-state assumption lifetimes under non equilibrium conditions, other data sets with experimentally determined NO_2, NO_3, N_2O_5 and O_3 concentrations should be utilized.

3.4 HONO at York University

Active-DOAS measurements of HONO and NO_2 were collected in the nocturnal urban atmosphere at York University, Toronto over a 1-year period. The purpose of these measurements in a terrestrial urban environment was to augment the analysis of HONO at Saturna Island, with a view towards further understanding the nocturnal HONO formation mechanism and to test several hypotheses:

1. A HONO steady-state can exist during certain periods at night in an urban area. The HONO concentration during the steady-state period is independent of NO_2, given that the surface contains sufficient water coverage and is saturated

with nitrogen containing precursors;

2. A HONO steady-state can exist over a snow covered surface, similar to that over the ocean, as one expects that a quasi liquid layer will exist at the air/snow surface layer;
3. The concentration of HONO is positively correlated with temperature during periods where a steady-state exists, similar to that observed over the ocean;
4. Different conversion efficiencies of NO_2 to HONO exist on dry, wet and snow covered surfaces;
5. HONO formation has a NO_2 dependence between zero-order and first-order, dependent on the NO_2 concentration, relative humidity, etc;

In addition, the measurements at York University were aimed to determine whether the proposed conceptual model of HONO formation in the MBL could support observations of HONO in a polluted terrestrial environment.

An overview of the trends and statistics of the year-long measurements of HONO, NO_2, and O_3 will be presented and discussed. The relationship between HONO, NO_2 and the HONO/NO_2 ratio with various meteorological parameters such as relative humidity, temperature, wind speed, wind direction, and atmospheric stability will be explored. The photolysis of HONO during sunrise was modeled and a comparison to observations will be presented in order to determine if an active source of HONO production exists in the morning. A transition between two types of HONO nighttime behaviors was identified; this phenomenon will be discussed along with its connection to atmospheric stability. Modeling studies were performed to reproduce the observed behaviors and will be presented, along with estimates of HONO production rates, loss rates, deposition velocities, and lifetimes. Based on the model results, a new view of HONO production and loss kinetics is hypothesized and tested.

3.4.1 General Observations of HONO and NO_2

3.4.1.1 Overview of Measurements

HONO and NO_2 were measured using active-DOAS from November 1, 2010 to November 7, 2011. Measurements were collected for 242 nights during the year-long period, comprising a total of ~16,500 data points with an average time resolution of 10.2 minutes. These measurements form a comprehensive HONO data set, including a large range of temperatures, relative humidity, surface conditions (snow, water, dry, etc.) and NO_2 mixing ratios. An overview of the year-long measurements of HONO is shown in Figure 3.32, with daily measurements of snow ground cover shown in the top panel. In total, 89 days had more than trace amounts of snow ground cover.

A summary of the statistics for HONO, NO_2, O_3 and various meteorological parameters is shown in Table 3.9. The statistics were determined for the dark period of the night, defined as the time period one-hour after sunset to one-hour prior to sunrise. Nocturnal HONO mixing ratios were typically greater than 0.4 ppb, with a maximum of 4.3 ppb. The 25th, 50th, and 75th percentiles of HONO during the dark

Table 3.9: Statistical summary of observations of various species and meteorological parameters measured at York University for the year-long data set. Statistics are restricted to the dark period of the night, defined as the time period one-hour after sunset to one-hour before sunrise.

	5th percentile	25th percentile	Median	Average	75th percentile	95th percentile
HONO (ppb)	0.46	0.77	1.02	1.05	1.27	1.78
NO_2 (ppb)	3.79	8.67	15.76	18.15	25.54	41.15
$HONO/NO_2$	0.031	0.046	0.063	0.080	0.097	0.184
O_3 (ppb)	1.42	8.93	16.19	16.16	22.95	31.17
Temp (°C)	-11.12	-2.00	5.72	5.58	14.13	20.95
RH (%)	50.52	65.27	73.70	71.91	80.20	87.5
WS ($\mathrm{m\,s^{-1}}$)	0.41	1.26	2.03	2.32	3.13	5.11
$\Delta T_{9.5-1}$ (°C)	-0.06	0.08 0	0.32	0.57	0.84	2.05

period of the night were 0.77 ppb, 1.02 ppb and 1.27 ppb, respectively. The median and lower range of HONO mixing ratios are very similar to those measured over the open ocean at Saturna Island (median = 1.08 ppb), although higher maximum HONO mixing ratios were observed at York University.

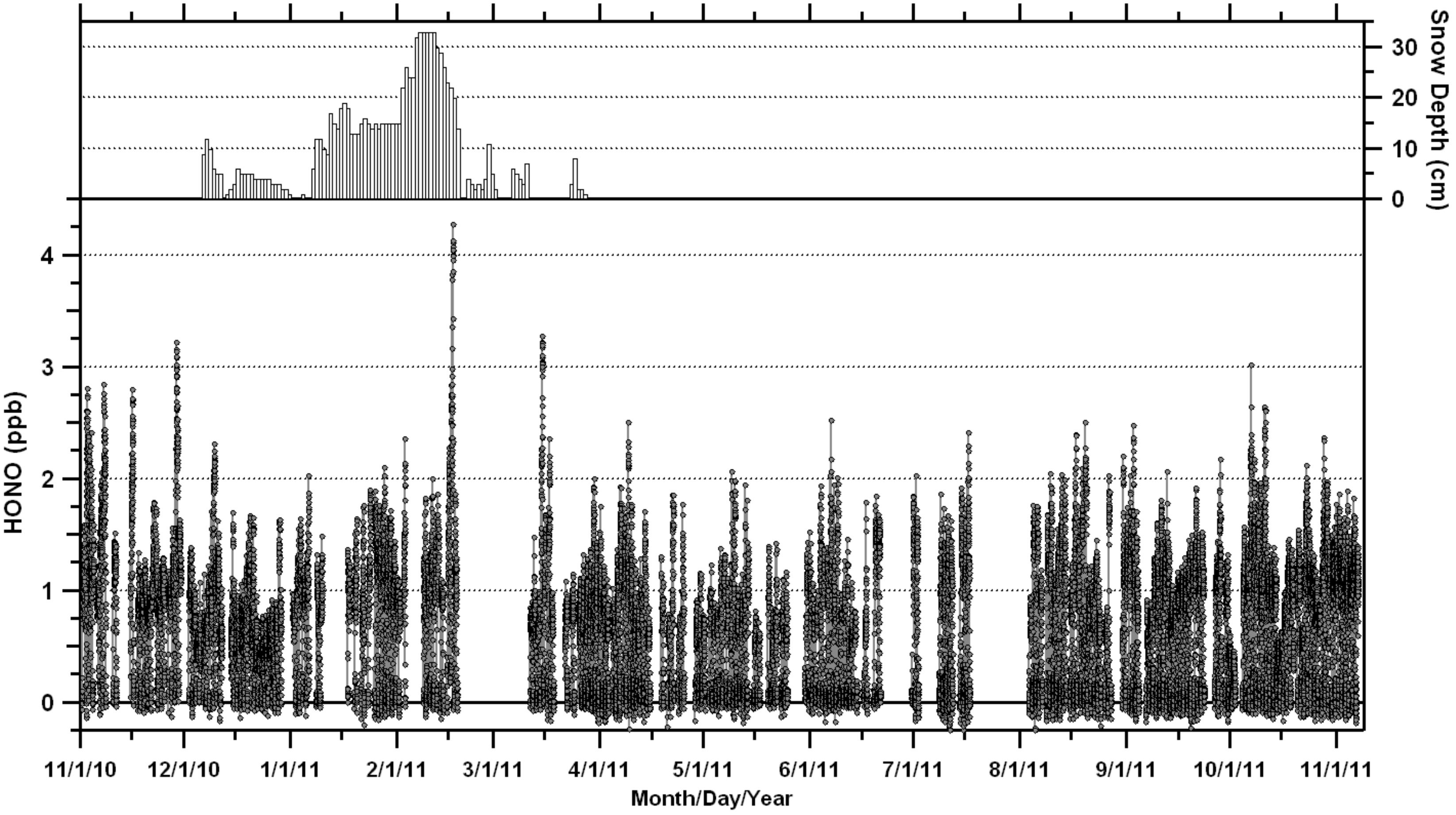

Figure 3.32: Overview of the one-year measurements of HONO at York University. Daily measurements of snow ground cover are shown in the top panel.

The diurnal variation of HONO for all observations is shown in Figure 3.33. The mixing ratio of HONO was generally below detection limit during the daytime and rapidly increased during sunset. The HONO mixing ratio remained between 0.5 and 1.5 ppb for the majority of the night, with the highest observed values occurring late in the night. The HONO mixing ratio rapidly decreased after sunrise with the onset

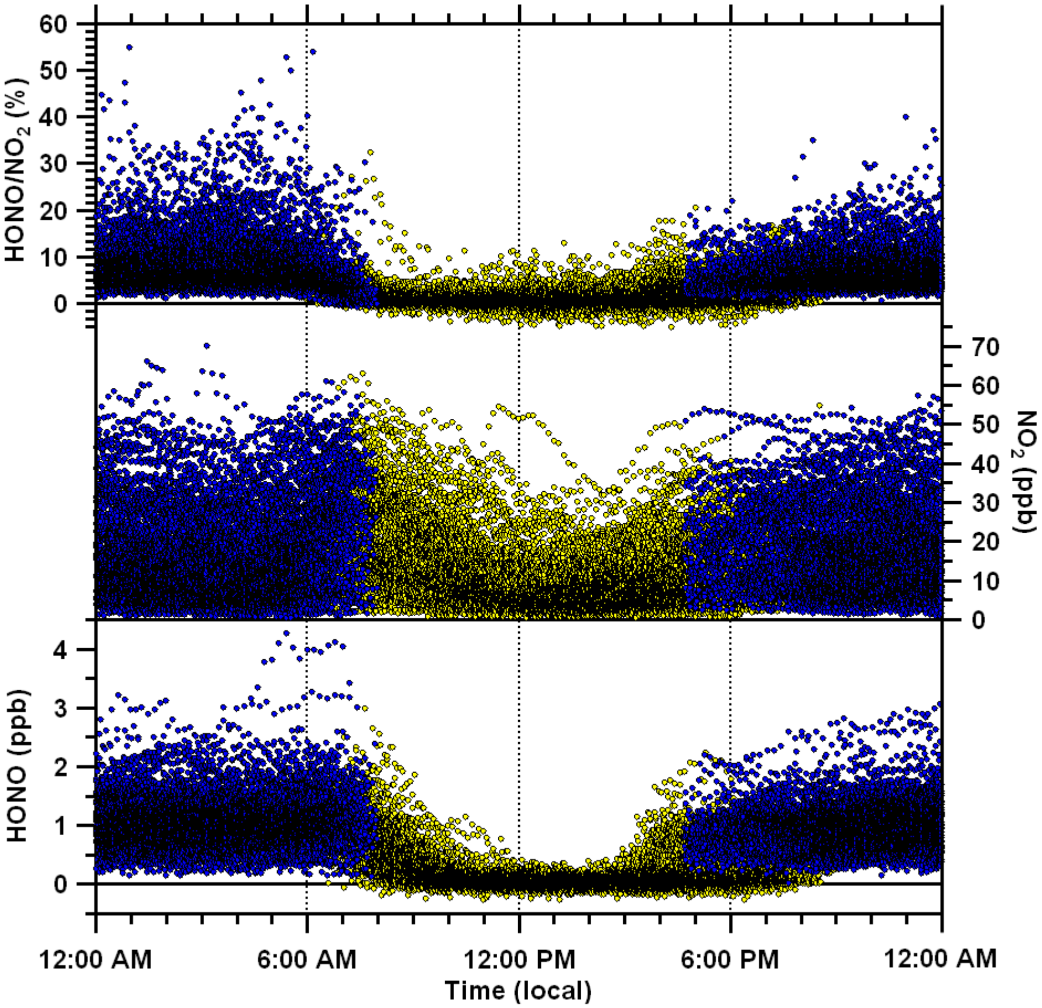

Figure 3.33: Diurnal variation of HONO, NO_2 and the HONO/NO_2 ratio. In total, 242 days are shown with a total of ∼16,500 data points. Daytime observations are shown in yellow while nighttime observations are in blue.

of photolysis and was generally below detection limit approximately $3 - 4$ hours after sunrise, or at times longer due to cloudy conditions.

The 25th, 50th, and 75th percentiles of NO_2 during the dark period of the night were 8.7 ppb, 15.8 ppb and 25.5 ppb, respectively, indicative of a polluted atmosphere at York University. The highest observed NO_2 mixing ratio during the night was 70.2 ppb and the lowest 0.7 ppb. The mixing ratios of NO_2 are significantly higher than those observed at Saturna Island (median = 6.7 ppb) and likely the reason for the higher observed HONO mixing ratios. The diurnal variation of NO_2 for all observations is shown in Figure 3.33. The NO_2 mixing ratio was generally higher during the nighttime due to photolysis during the daytime, with large peaks typically observed during the morning and evening rush hour.

The diurnal variation of the HONO/NO_2 for all observations is also shown in Figure 3.33. The 25th, 50th, and 75th percentiles of the HONO/NO_2 ratio during the dark period of the night were 4.6%, 6.3% and 9.7%, respectively. The maximum observed HONO/NO_2 ratio was 55.0% while the minimum was 0.47% during the dark period of the night. The HONO/NO_2 ratio was low during the daytime due to photolysis of HONO and began to increase $1 - 2$ hours prior to sunset. Lower values were generally observed in the early part of the evening, with the highest observed ratios occurring after midnight, similar to observations at Saturna Island. The highest ratios were observed on nights which the mixing ratio of NO_2 continuously decreased overnight. Stable overnight ratios between $4 - 6\%$ were observed when the NO_2 mixing ratio was relatively high overnight. The ratio also rapidly decreased after sunrise, attributed to the photolysis of HONO.

The relationship between HONO and NO_2 for all data points during the dark period of the night is shown in Figure 3.34. The nocturnal observations at York University are restricted to an upper and lower limit, in contrast to the observations at Saturna Island which had no apparent upper limit. The limits consist of the line of best fit for the eight highest and lowest $HONO/NO_2$ ratios, which comprise 0.1% of all nocturnal observations. The lower and upper limit lines were determined to be $HONO/NO_2 = 0.010(\pm0.001)$ and $HONO/NO_2 = 0.49(\pm0.02)$, respec-

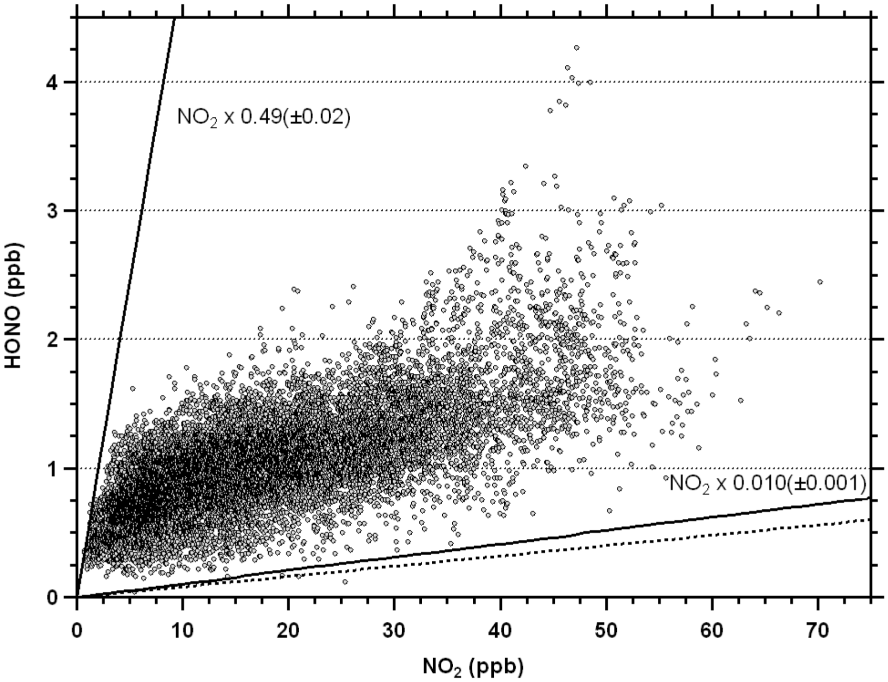

Figure 3.34: Relationship between HONO and NO_2 during the dark period of the night. A lower limit line is shown corresponding to $HONO/NO_2 = 0.010(\pm0.001)$ and upper limit corresponding to $HONO/NO_2 = 0.49(\pm0.02)$. The dashed line ($HONO/NO_2 = 0.008$) corresponds to the direct vehicle emission of HONO.

tively, where the uncertainties correspond to the standard error of the fit. A dashed line ($HONO/NO_2 = 0.008$) corresponding to the direct vehicle emission of HONO (Kurtenbach et al., 2001) is also shown in the plot for comparison. The upper limit of the $HONO/NO_2$ ratio is only reached when the NO_2 mixing ratio is <4 ppb. For NO_2 mixing ratios between 5 − 30 ppb, HONO was generally below 2 ppb and only rose above 2 ppb when NO_2>30 ppb. A large amount of scatter exists in the HONO mixing ratio during periods with high NO_2, ranging from ∼0.5 ppb − 4.3 ppb. The large scatter indicates that other variables besides the NO_2 concentration govern the nocturnal HONO concentration.

3.4.1.2 HONO and NO_2 Relationship with MET Parameters

Relative Humidity

The correlation of HONO, NO_2 and the $HONO/NO_2$ ratio with relative humidity during the dark period of the night was investigated, as shown in Figure 3.35, with statistics calculated for 5% relative humidity bins. The median and average mixing ratios of HONO are both ∼1.0 ppb over the relative humidity range of 35 − 95%. The 25th and 75th percentiles also show a similar relationship over the same relative humidity range, with the HONO mixing ratio ranging from ∼0.75 − 1.25 ppb. A slight decrease in the HONO mixing ratio is observed when relative humidity is <35%, implying that water may be a limiting reagent during dry conditions. The maximum HONO mixing ratio increases with increasing relative humidity, with the highest

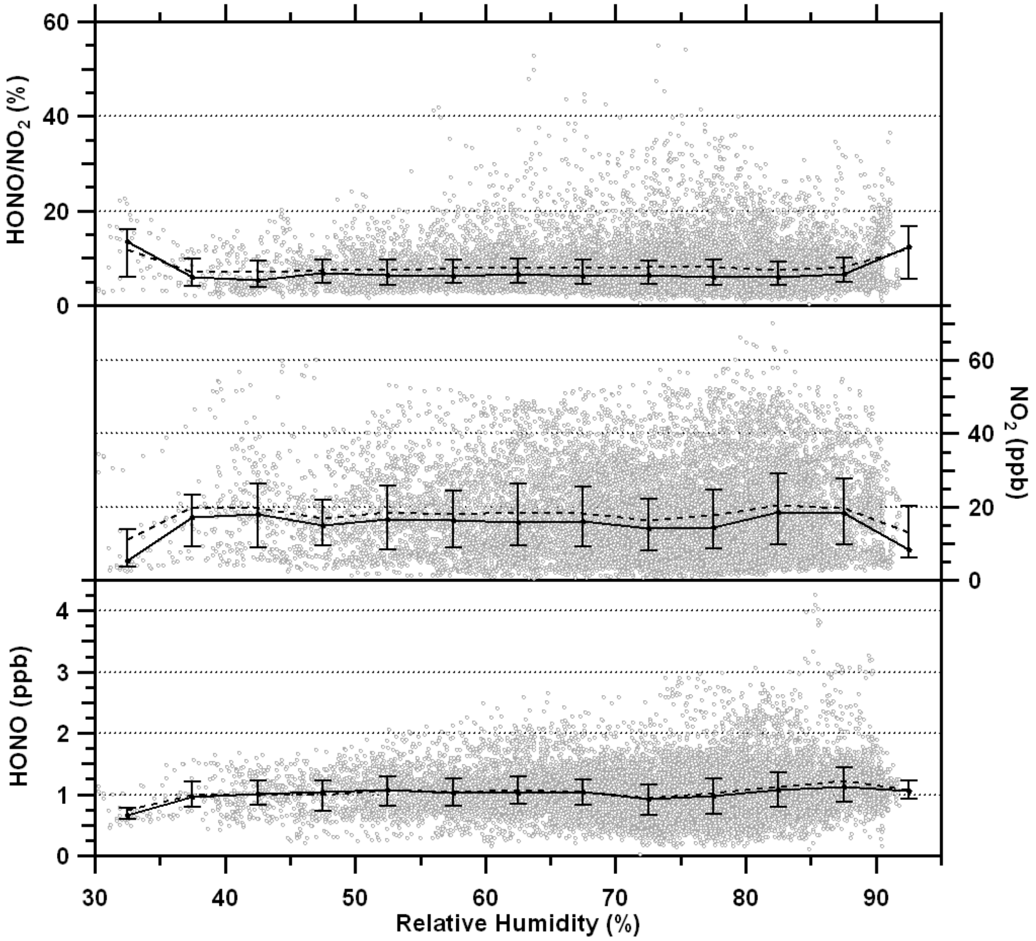

Figure 3.35: Relationship of HONO, NO_2 and the HONO/NO_2 ratio with relative humidity. Each data point for the year-long measurement during the dark period of the night is shown as grey circles. The median (solid line), 25^{th} and 75^{th} percentiles (error bars) along with the averages (dashed line) are shown for 5% relative humidity bins.

levels of HONO observed when RH>85%. The 25^{th}, 50^{th} and 75^{th} percentiles of NO_2 and the HONO/NO_2 ratio do not appear to correlate with relative humidity over the range of 35 − 95% RH. Slightly higher ratios are observed between 55 −

85% relative humidity, although only a few measurements display this trend. Based on the observations, it does not appear that relative humidity is a major factor in controlling the HONO concentration overnight, as its dependence may be masked by other factors in the large data set.

Temperature

The relationship between HONO, NO_2 and HONO/NO_2 with temperature during the dark period of the night is shown in Figure 3.36 with statistics calculated for 2 °C temperature bins. Similar to the relative humidity observations, the 25^{th}, 50^{th} and 75^{th} percentiles of the HONO mixing ratio are $\sim$0.75 ppb, $\sim$1.0 ppb, and $\sim$1.25 ppb, respectively, across all temperature bins. Nearly all observations of HONO >2.5 ppb occurred when temperatures were between -4 to 5 °C. A surface transition occurs from aqueous to ice/frost at temperatures $\leq$ 0°C, potentially causing an increase in the surface to volume ratio (S/V). Previous studies observed more efficient conversions of NO_2 to HONO with an increase in the S/V ratio and a strong dependence on surface properties (Kleffmann et al., 1998; Svensson et al., 1987). Mixing ratios of HONO on steady-state nights (discussed later) did not correlate with temperature in contrast to that seen at Saturna Island, suggesting that those observations may be unique to the MBL or the temperature dependence at Saturna Island was simply a result of statistical fluctuations.

Similarly, the NO_2 mixing ratio and HONO/NO_2 ratio did not exhibit a significant correlation with temperature. Higher median levels of NO_2 were observed for the few

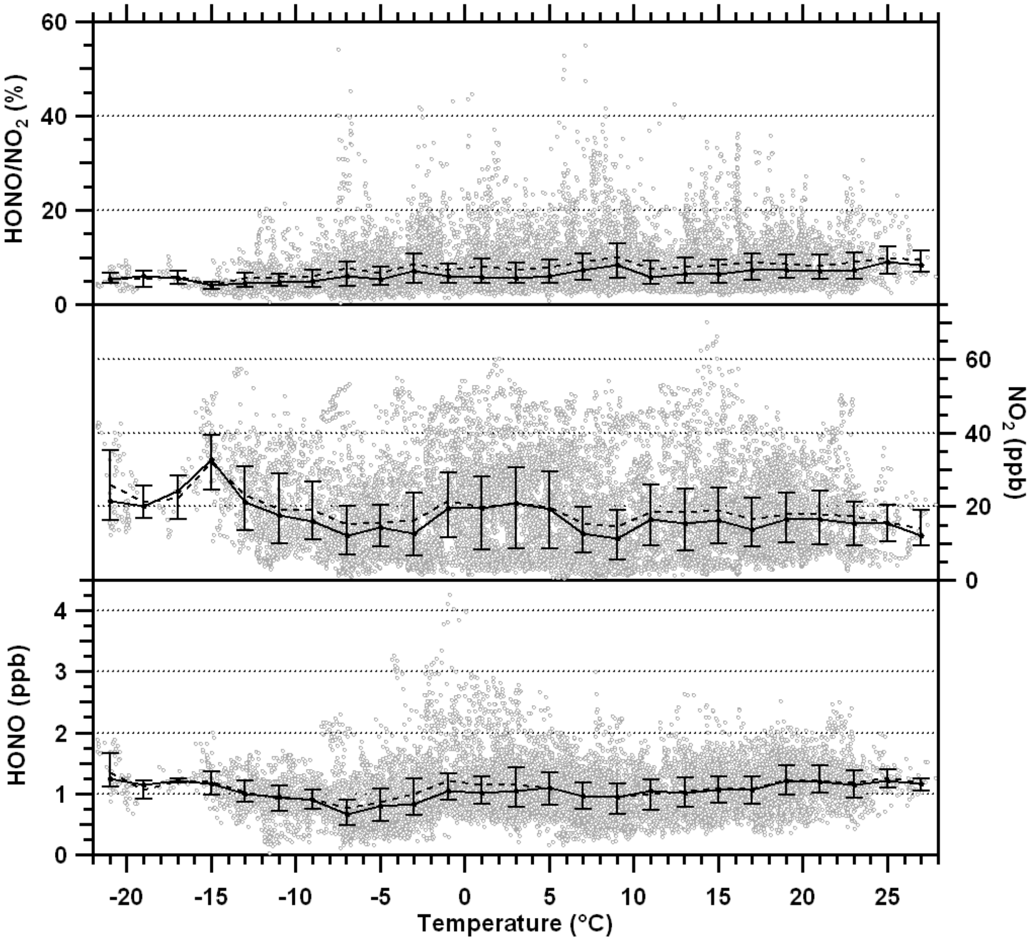

Figure 3.36: Relationship of HONO, NO_2 and the HONO/NO_2 ratio with temperature. Each data point for the year-long measurement during the dark period of the night is shown as grey circles. The median (solid line), 25th and 75th percentiles (error bars) along with the averages (dashed line) are shown for 2 °C temperature bins.

overnight measurements made at temperatures below -15 °C, while the ratio was below 10% for this temperature range.

Wind Speed

The relationship between HONO, NO_2 and the HONO/NO_2 ratio with wind speed during the dark period of the night is shown in Figure 3.37, with statistics calculated for 1 m/s wind speed bins. The HONO and NO_2 mixing ratios are found to negatively

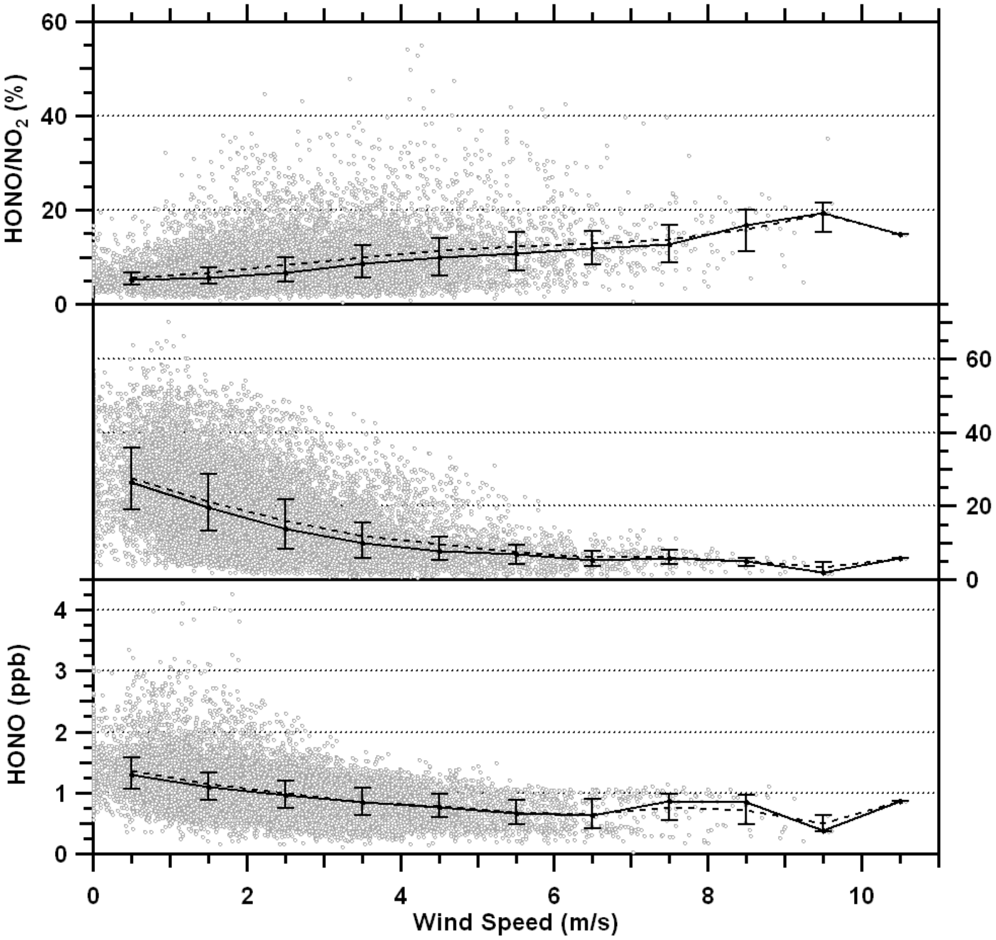

Figure 3.37: Relationship of HONO, NO_2 and the HONO/NO_2 ratio with wind speed. Each data point for the year-long measurement during the dark period of the night is shown as grey circles. The median (solid line), 25th and 75th percentiles (error bars) along with the averages (dashed line) are shown for 1 m/s wind speed bins.

correlate with wind speed, while the HONO/NO_2 ratio exhibits a positive correlation. These observations suggest that conversion of NO_2 to HONO becomes more efficient as wind speed increases. The observed trends are likely a meteorological effect, for which an increase in the NO_2 concentration results from a more stable nocturnal atmosphere concurring with lower wind speeds. The negative dependence of HONO with wind speed is also presumably due to a combination of meteorological effects of a lower NBL and due to the first order dependence of HONO on NO_2 (Finlayson-Pitts, 2003a), with larger NO_2 mixing ratios observed during nights with low wind speeds, leading to higher amounts of HONO.

Wind Direction

Figure 3.38 shows the dependence between the HONO, NO_2 and HONO/NO_2 ratio with wind direction during the dark period of the night. The largest enhancements of HONO are observed when there were low wind speeds from the east north-east sector, as more clearly observed from the wind rose diagram in Figure 3.39(a), associated with air from a long stretch of a nearby highway (Hwy 407). A minor enhancement is also observed for winds from the southern direction, corresponding to transport of air from the downtown urban center of Toronto. As also observed in Figure 3.39(b), the highest HONO and NO_2 mixing ratios observed were generally from the south while the lowest mixing ratios were typically from the northern sector. The NO_2 concentration is strongly correlated with population density and is likely responsible for the observed HONO trend. Northern winds transport a cleaner air mass to the measure-

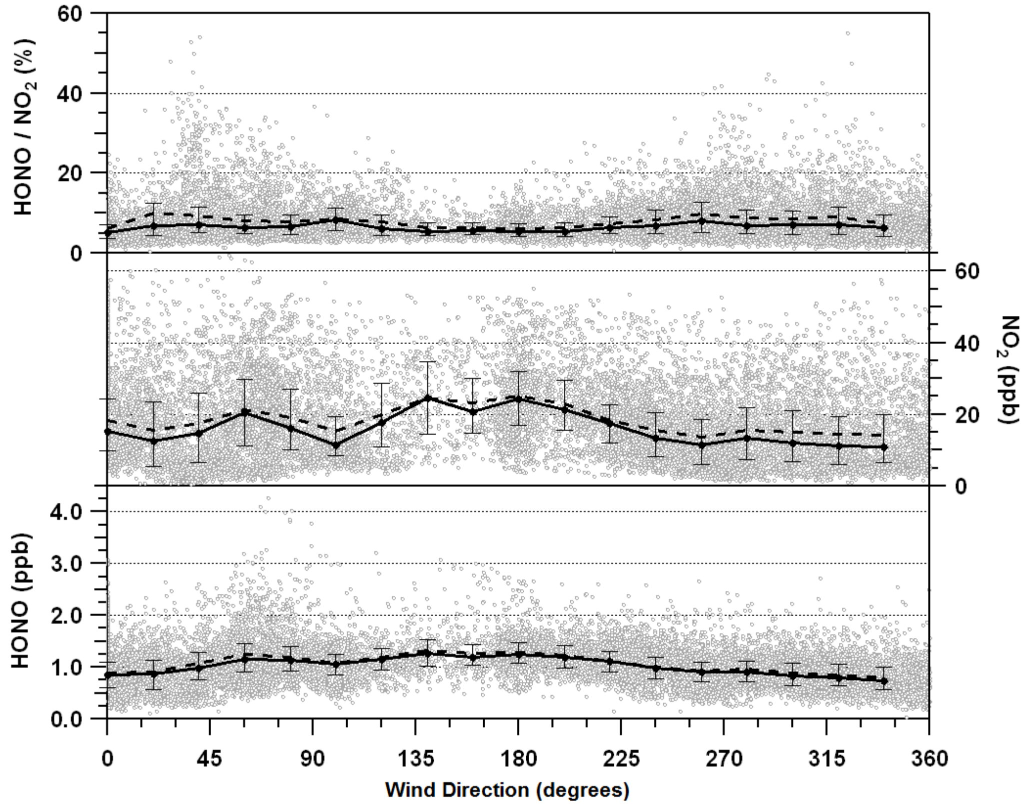

Figure 3.38: Relationship of HONO, NO_2 and the HONO/NO_2 ratio with wind direction. Each data point for the year-long measurement during the dark period of the night is shown as grey circles. The median (solid line), 25th and 75th percentiles (error bars) along with the averages (dashed line) are shown for 20 degrees wind direction bins.

ment site while southern winds bring higher pollutant levels (Liggio et al., 2010). The highest HONO/NO_2 ratios (Figure 3.39(c)) are generally observed from the northern sector when the NO_2 concentration is the lowest, corresponding to periods with high wind speeds.

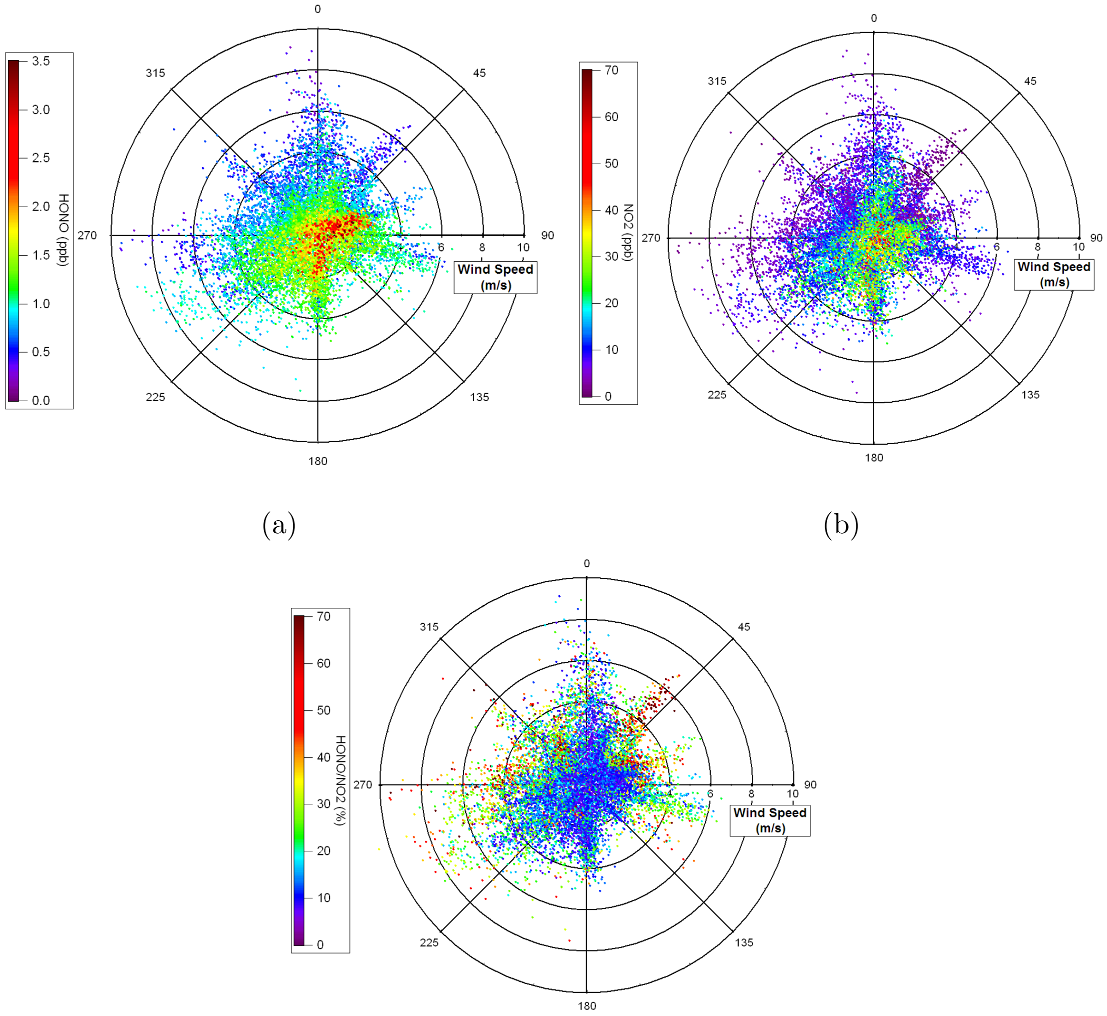

(a) (b)

(c)

Figure 3.39: Wind rose plot for (a) HONO, (b) NO_2 and (c) the HONO/NO_2 ratio during the dark period of the night. The radial direction shows the wind speed and the color scale corresponds to the mixing ratio for (a) and (b), and percentage of the ratio for (c).

ΔTemperature

The relationship between HONO, NO_2 and HONO/NO_2 with $\Delta T_{9.5-1}$ during the dark period of the night is shown in Figure 3.40, with statistics calculated for 0.25°C $\Delta T_{9.5-1}$ bins. Both HONO and NO_2 show a pronounced positive correlation

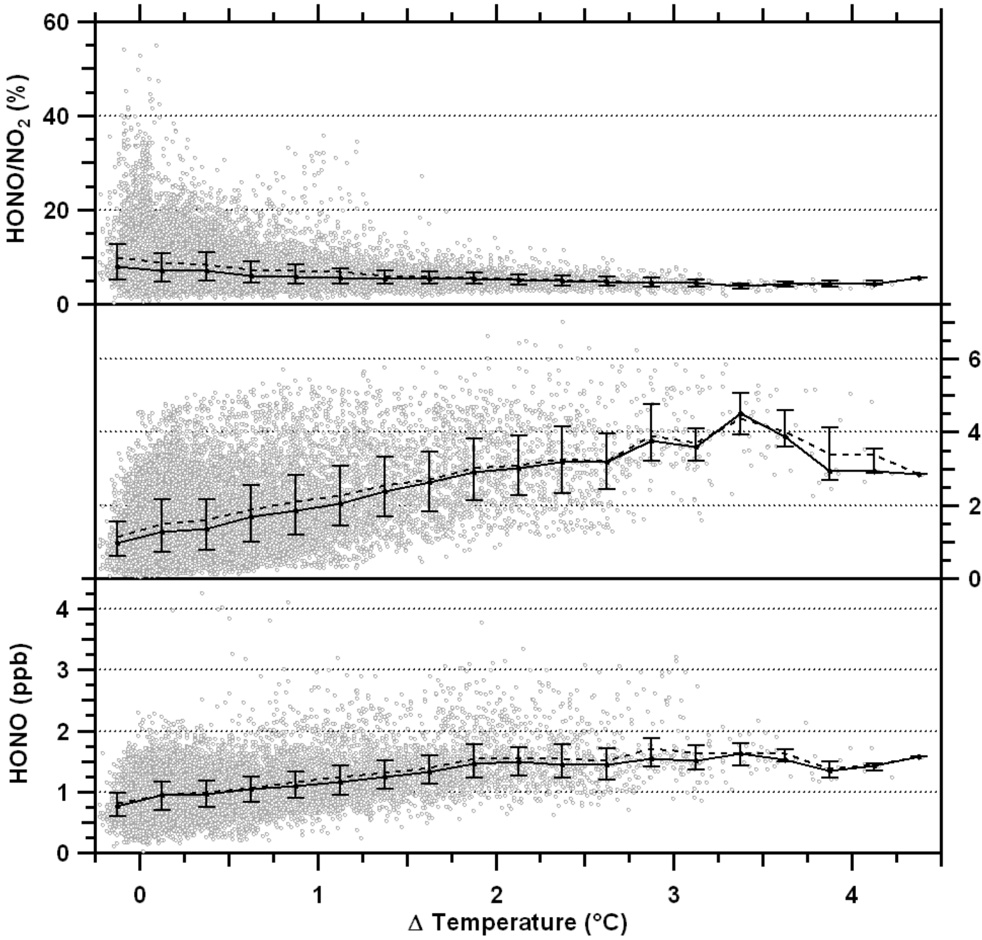

Figure 3.40: Relationship of HONO, NO_2 and the HONO/NO_2 ratio with $\Delta T_{9.5-1}$. Each measurement during the dark period of the night for the year-long data set is shown as grey circles. The median (solid line), 25th and 75th percentiles (error bars) along with the averages (dashed line) are shown for 0.25 °C $\Delta T_{9.5-1}$ bins.

with $\Delta T_{9.5-1}$. As the nocturnal atmosphere becomes more stable ($\Delta T_{9.5-1} > 0$), the HONO and NO_2 mixing ratio increases. For the case of NO_2, the correlation can be partially attributed to meteorological effects that would result from a shallower NBL with an increase in $\Delta T_{9.5-1}$, also giving rise to the observed increase of HONO. The HONO/NO_2 ratio shows an interesting relationship with $\Delta T_{9.5-1}$. The average and median ratio slightly decreases with increasing $\Delta T_{9.5-1}$. The highest ratios are observed when the atmosphere is well mixed while the ratio converges between $4 - 6\%$ as the nocturnal atmosphere becomes increasingly stable.

It is important to note that certain meteorological parameters are interdependent, such as the overnight relationship between temperature and relative humidity, previously discussed in Chapter 3.2.4. The relationship between $\Delta T_{9.5-1}$ and wind speed observed is shown in Figure 3.41 for 0.25°C $\Delta T_{9.5-1}$ bins. Low values of $\Delta T_{9.5-1}$ were coincident with high wind speeds, signifying a well mixed NBL. In turn, low wind speeds were observed with high values of $\Delta T_{9.5-1}$, corresponding to a shallow NBL. The strong negative correlation is expected since both parameters are associated with atmospheric stability.

These observations indicate that the nocturnal NO_2 concentration is strongly driven by atmospheric stability (in addition to the emission rate of NO_x). The highest NO_2 mixing ratios were observed when the nocturnal atmosphere was stable and a low inversion formed. From the dependence of HONO on NO_2, it appears that the NO_2 concentration strongly governs the overnight HONO concentration, leading to the observed HONO dependence on atmospheric stability. The HONO/NO_2 ratio

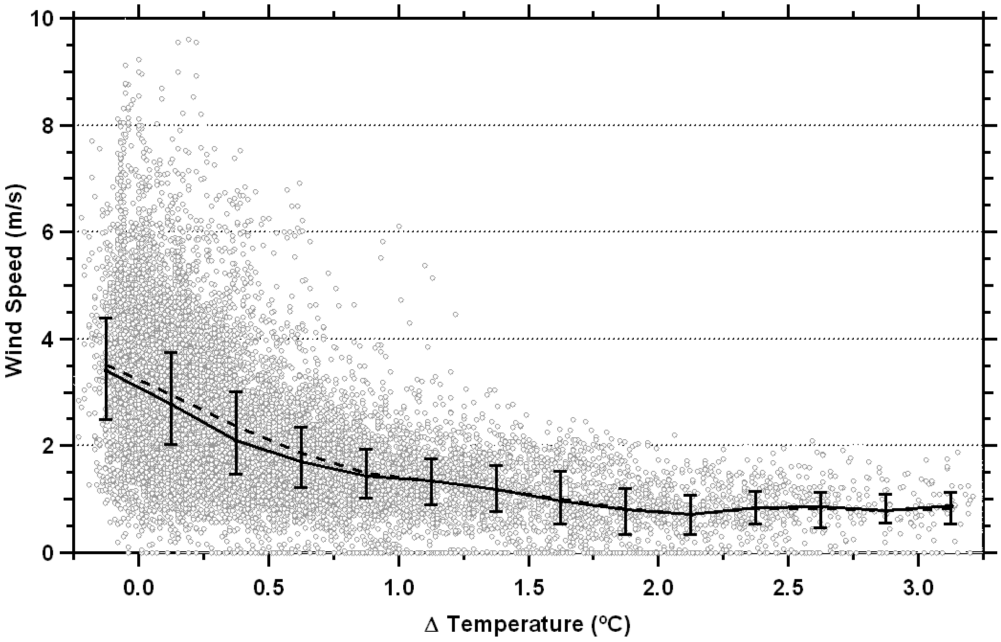

Figure 3.41: Relationship between wind speed and $\Delta T_{9.5-1}$. Measurements from the year-long data set during the dark period of the night are shown as grey circles. The median (solid line), 25th and 75th percentiles (error bars) along with the averages (dashed line) are shown for 0.25°C $\Delta T_{9.5-1}$ bins.

also suggests variable conversion efficiencies of NO_2 to HONO and different HONO dependencies during stable and unstable conditions. Case studies of the dependence of HONO and NO_2 on atmospheric stability are discussed in Chapter 3.4.2.

3.4.1.3 Snow Dependence

The nature of the surface has been shown to be of significant importance for the heterogeneous conversion of NO_2 to HONO, from previous studies by (Lammel, 1999; Finlayson-Pitts, 2003a; Stutz et al., 2004; Wojtal et al., 2011). A surface covered with snow may behave similarly to the surface of the ocean, with constant water availability for the heterogeneous HONO formation reaction, as a quasi liquid layer is expected to exist at the air/snow surface layer. As a continuation of the work from Saturna, differences between HONO formation over the ocean's surface at Saturna and snow surfaces at York University are explored with a focus on overnight HONO formation in polluted aqueous environments. The focus of previous studies measuring HONO production over snow surfaces were limited either to the daytime in arctic regions or to very low NO_x conditions (Simpson et al., 2002; Liao et al., 2006; Beine et al., 2006), under which a steady-state is not expected to occur.

A statistical comparison between NO_2, HONO, HONO/NO_2 and O_3 during nighttime periods with and without snow ground cover is shown in Figure 3.42. Only minor statistical differences between the two ground covers were observed for NO_2 and O_3, with slightly higher median mixing ratios during nights with snow. The HONO concentration and the HONO/NO_2 ratio were higher for nearly all percentiles during nights without snow ground cover. Given that the NO_2 mixing ratios were nearly identical for both periods, these observations suggest that either heterogeneous conversion of NO_2 to HONO is more efficient during nights without snow cover, or that meteorological differences are responsible. Meteorological differences between these two types of ground cover are explored next.

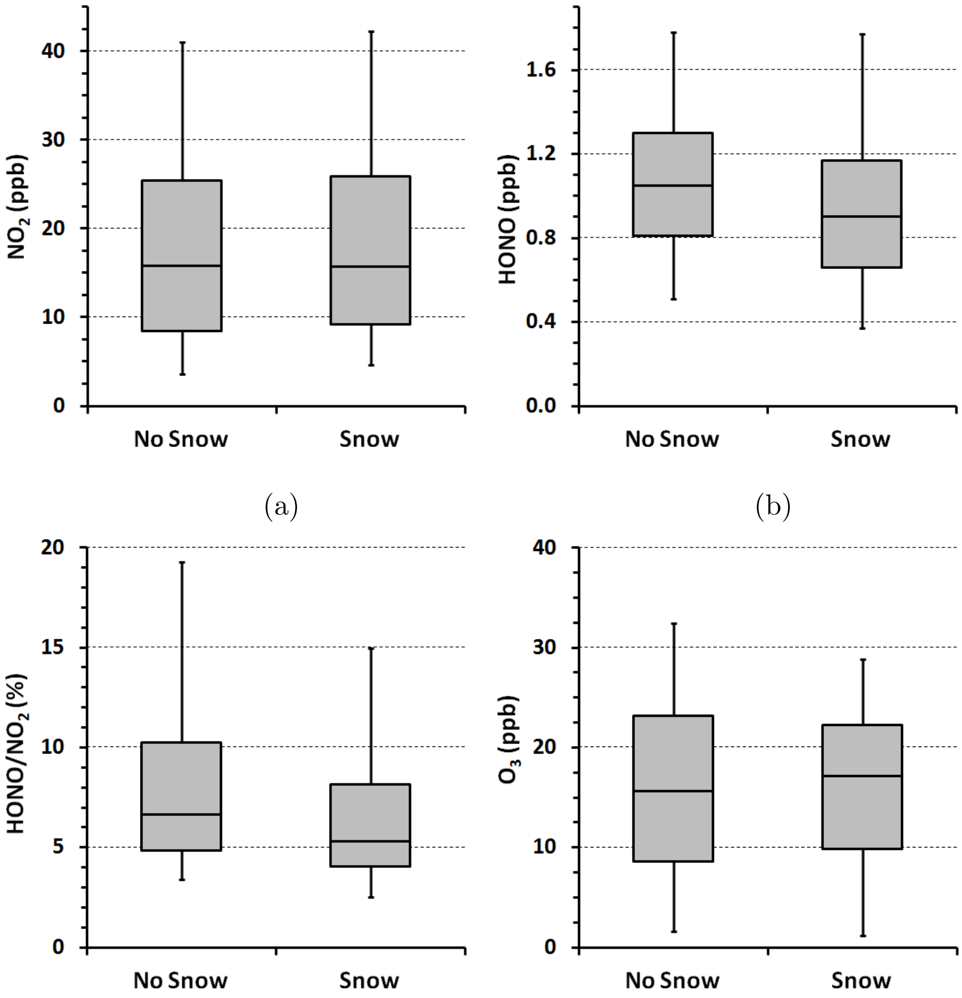

(a) (b)

(c) (d)

Figure 3.42: Box whisker plots of (a) NO$_2$, (b) HONO, (c) HONO/NO$_2$ ratio and (d) O$_3$ representing the 5th, 25th, 50th, 75th, and 95th percentiles of nocturnal measurements with and without snow ground cover. For cases with snow ground cover, 84 nights were selected with >1 cm of snow.

A statistical comparison of meteorological parameters with and without snow is shown in Figure 3.43. Warmer temperatures are encountered during periods with no snow while periods with snow ground cover are limited to near 0 °C or below. The

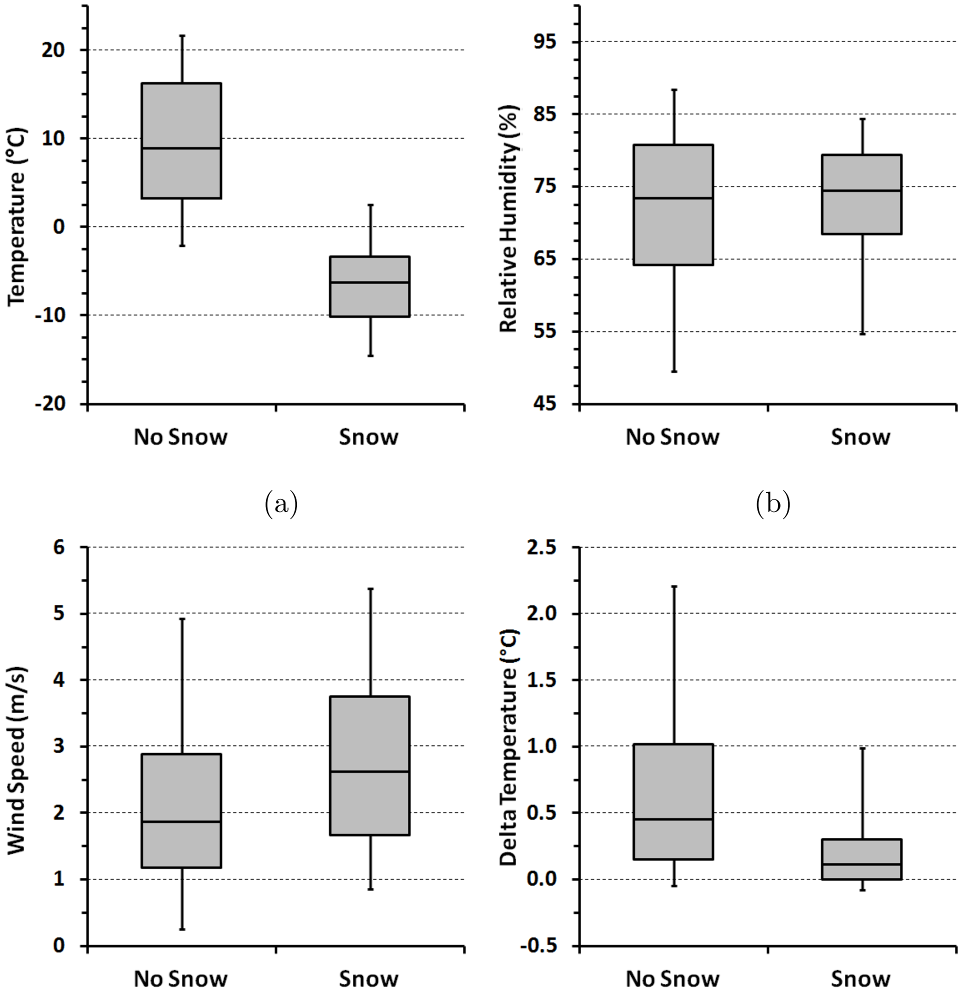

(a) (b)

(c) (d)

Figure 3.43: Box whisker plots of (a) temperature, (b) relative humidity, (c) wind speed and (d) $\Delta T_{9.5-1}$ representing the 5th, 25th, 50th, 75th, and 95th percentiles of nocturnal measurements with and without snow ground cover. For cases with snow ground cover, 84 nights were selected with >1 cm of snow.

overnight relative humidity range is smaller during periods with snow ground cover, however, the median levels are very similar. The wind speed and $\Delta T_{9.5-1}$ observations indicate that unstable well mixed air masses occur more frequently with overnight snow ground cover, while air masses are generally more stable during periods without snow. It is interesting to note that these large differences in atmospheric stability between the two ground covers are not reflected in the NO_2 statistics, but are in HONO and the HONO/NO_2 ratio. The snow vs. no snow measurements suggest once again a relationship between the nocturnal HONO behavior and atmospheric stability, explored in detail in Chapter 3.4.2.

3.4.2 Relationship Between HONO and Atmospheric Stability

3.4.2.1 Stable Night Case Study (No Snow)

A case study where the HONO and NO_2 mixing ratios were strongly correlated is shown in Figure 3.44. The overnight HONO mixing ratio increased from 0.7 ppb at sunset to 2.2 ppb after midnight and slowly decreased to ~1.0 ppb before sunrise. The NO_2 mixing ratio followed a similar trend as HONO with levels as high as 55 ppb, while the HONO/NO_2 ratio remained between ~$3-4\%$ for the entire night. The wind speed dropped below 2 m/s after 23:00 and $\Delta T_{9.5-1}$ was as high as 4°C, indicating the formation of a very stable nocturnal inversion at that time. The combination of a shallow NBL with overnight NO_x emissions led to the depletion of O_3, likely by titration with NO. Low overnight mixing ratios of O_3 suppress the formation of

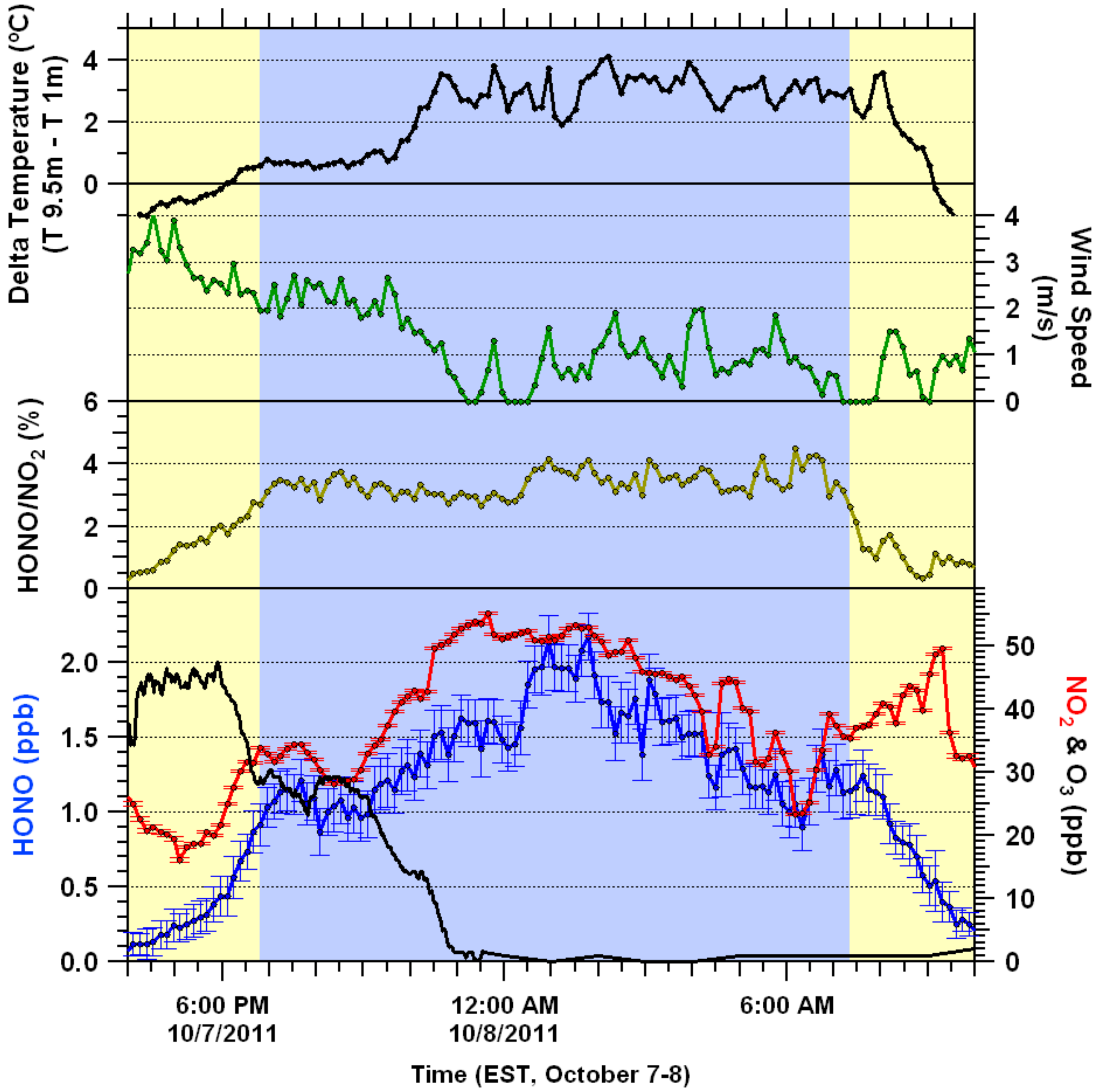

Figure 3.44: Measurements of HONO, NO_2, HONO/NO_2, O_3, wind speed and $\Delta T_{9.5-1}$ on October 7/8, 2011 are shown. This night is characterized by the formation of a stable NBL where the mixing ratios of HONO and NO_2 are strongly correlated and the O_3 mixing ratio is titrated to 0 ppb. The yellow and blue background represent day and nighttime, respectively.

NO_3 and N_2O_5, greatly increasing the nocturnal lifetime of NO_2, as was shown in a previous study (Brown et al., 2012). The NO_3 temporal profile at York University during a stable night was previously shown in Chapter 3.3.3, Figure 3.26.

This case study displays a rapidly established first-order dependence between HONO and NO_2. As will be later explored in detail, the ratio between the production rate of HONO from NO_2 and the deposition rate of HONO remains constant throughout the entire night. The defining feature of this type of night consists of the rapidly established first-order dependence between HONO and NO_2, where $d([\mathrm{HONO}]/[\mathrm{NO_2}])/dt \approx 0$ overnight, which occurs in the presence of a stable NBL.

3.4.2.2 Unstable Night Case Study (Snow)

A case study of a rapidly established steady-state of HONO with 15 cm of snow ground cover at York University is shown in Figure 3.45. The levels of HONO exhibited an initial increase at a rate of $\sim$1.4 ppb h^{-1} during sunset and a steady-state was rapidly established, persisting throughout the entire night until after sunrise. The HONO concentration during the steady-state period was independent of the NO_2 concentration, similar to the observations made during the Saturna field study. The wind speed was higher than the previous case study, ranging from 2 to 4 m/s and the $\Delta T_{9.5-1}$ was 0 °C, indicative of a well mixed NBL.

The NO_2 mixing ratio steadily decreased overnight due to the combination of effects, including the decline in anthropogenic NO_x emissions, dilution in a well mixed boundary layer, and loss to the NO_3/N_2O_5 reservoir. The overnight NO_2 temporal

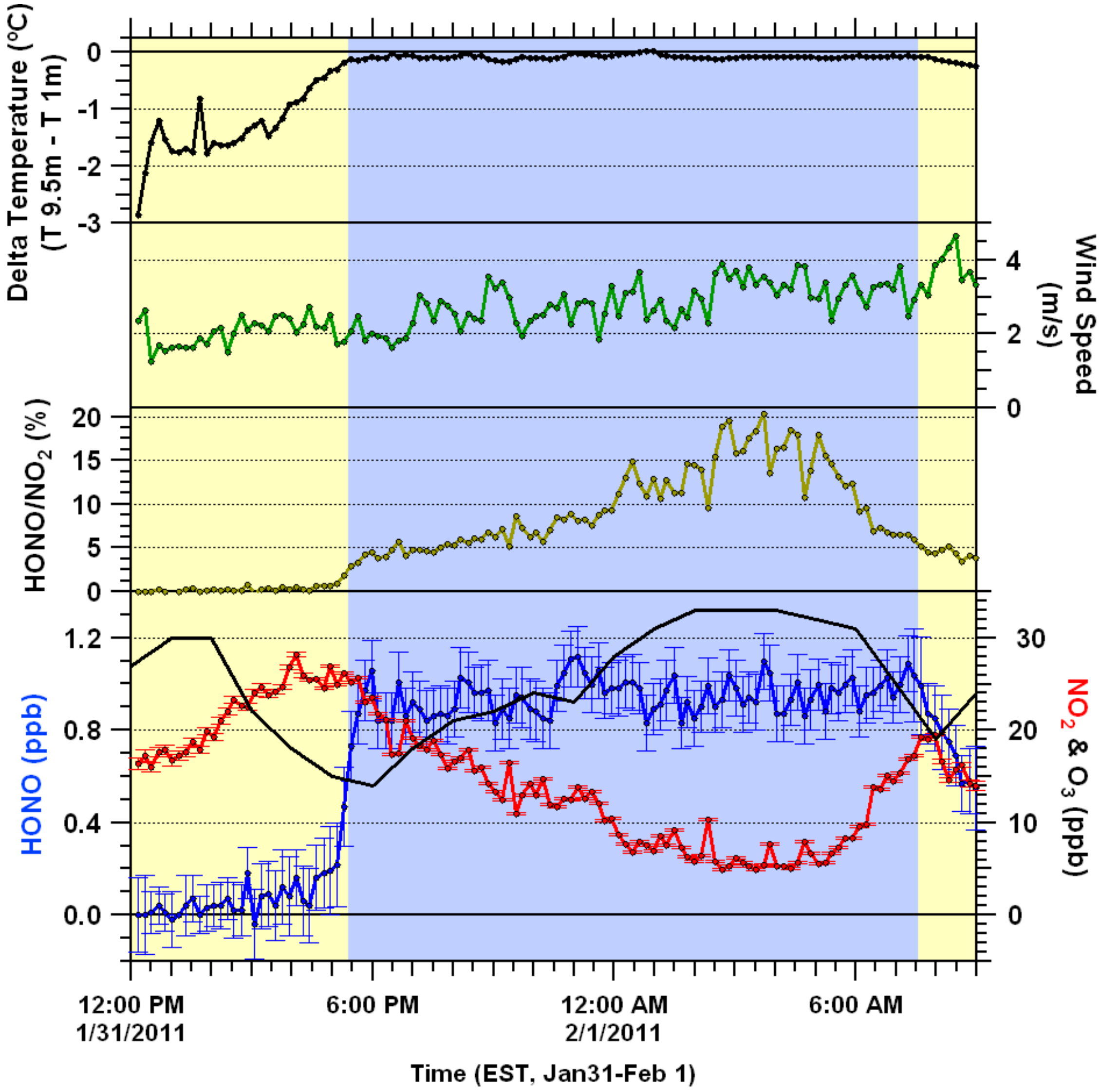

Figure 3.45: Measurements of HONO, NO_2, O_3, HONO/NO_2, wind speed and $\Delta T_{9.5-1}$ on January 31/February 1, 2011 are shown. The conditions for this evening consisted of an unstable nocturnal boundary layer, 15 cm of snow ground cover and a HONO increase during sunset of ~1.4 ppb h^{-1}. The yellow and blue background represent day and nighttime, respectively.

profile closely resembles the observations of NO_2 at Saturna Island over the open ocean; high NO_2 mixing ratio early in the evening and decreasing throughout the night. The O_3 mixing ratio was between 15 and 35 ppb, not depleted as in the previous case, leading to the production of NO_3 and subsequently N_2O_5, while simultaneously reducing the lifetime of NO_2. The NO_3 temporal profile at York University during an unstable night was previously shown in Chapter 3.3.3, Figure 3.27. N_2O_5 hydrolyzes heterogeneously and homogeneously to produce HNO_3 which is lost via dry deposition. The deposited HNO_3 can potentially play a key role in the observed steady-state of HONO by enhancing the acidification of the surface.

Steady-states of HONO such as those typified in this case study, were observed numerous times throughout the year-long data set, supporting the previous premise that such steady-state scenarios are not limited to marine environments. These observed steady-states of HONO at York University are also not predicted by the model proposed by Stutz, previously described by Equation 3.18. As previously mentioned, it is likely that deposited HONO is not irreversibly lost to the surface at York University, and is recycled into the atmosphere after deposition. From these observations, it appears that atmospheric stability plays a key role in the formation of a steady-state, given sufficient amounts of NO_2 and surface adsorbed water. The defining feature of this type of night consists of the rapidly established steady-state of HONO, $d[\text{HONO}]/dt = 0$, which occurs in the presence of a unstable and well mixed NBL and is accompanied by a decrease of NO_2 overnight. For increasingly stable atmospheric conditions, in which the NO_2 concentration increased throughout the night, steady-states of HONO were not observed. However, for nights with constant and generally high amounts of NO_2, constant levels of HONO and HONO/NO_2 were also observed due to the presumable first-order dependence between HONO and NO_2, as previously reported by Stutz (Stutz et al., 2004).

3.4.2.3 Comparison Between Stable and Unstable Nights

The previously discussed case studies illustrate the link between atmospheric stability and overnight HONO behavior. To summarize, a steady-state of HONO ($d[\mathrm{HONO}]/dt = 0$) was rapidly established during well mixed and atmospherically unstable nights. In turn, the formation of a stable and low nocturnal inversion results in a strong correlation between the HONO and NO_2 mixing ratios ($d([\mathrm{HONO}]/[\mathrm{NO_2}])/dt \approx 0$). These two types of HONO behaviors were observed numerous times throughout the year-long data set.

A statistical analysis was performed on nights which clearly demonstrated one of these behaviors and is shown in Figure 3.46. The determination of whether the HONO mixing ratio remained constant throughout each night was performed based on two simultaneous requirements; the slope of the HONO mixing ratio ($d[\mathrm{HONO}]/dt < 0.1$ ppt min^{-1}) and the standard deviation (std. < 0.1 ppb) during the dark period of the night (Figure 3.46a). In total, there were 19 nights (5 of which had snow ground cover) which met these criteria. These nights were distinctly identifiable as having low $\Delta T_{9.5-1}$, high wind speeds and decreasing NO_2 mixing ratios, indicative of an unstable nocturnal boundary layer, as shown in Figures 3.46e,d,b, respectively.

The median HONO/NO_2 ratio (Figure 3.46c) continuously increased throughout the night and is a reflection of the decreasing NO_2 concentration.

The nights for which HONO and NO_2 were strongly correlated were selected based

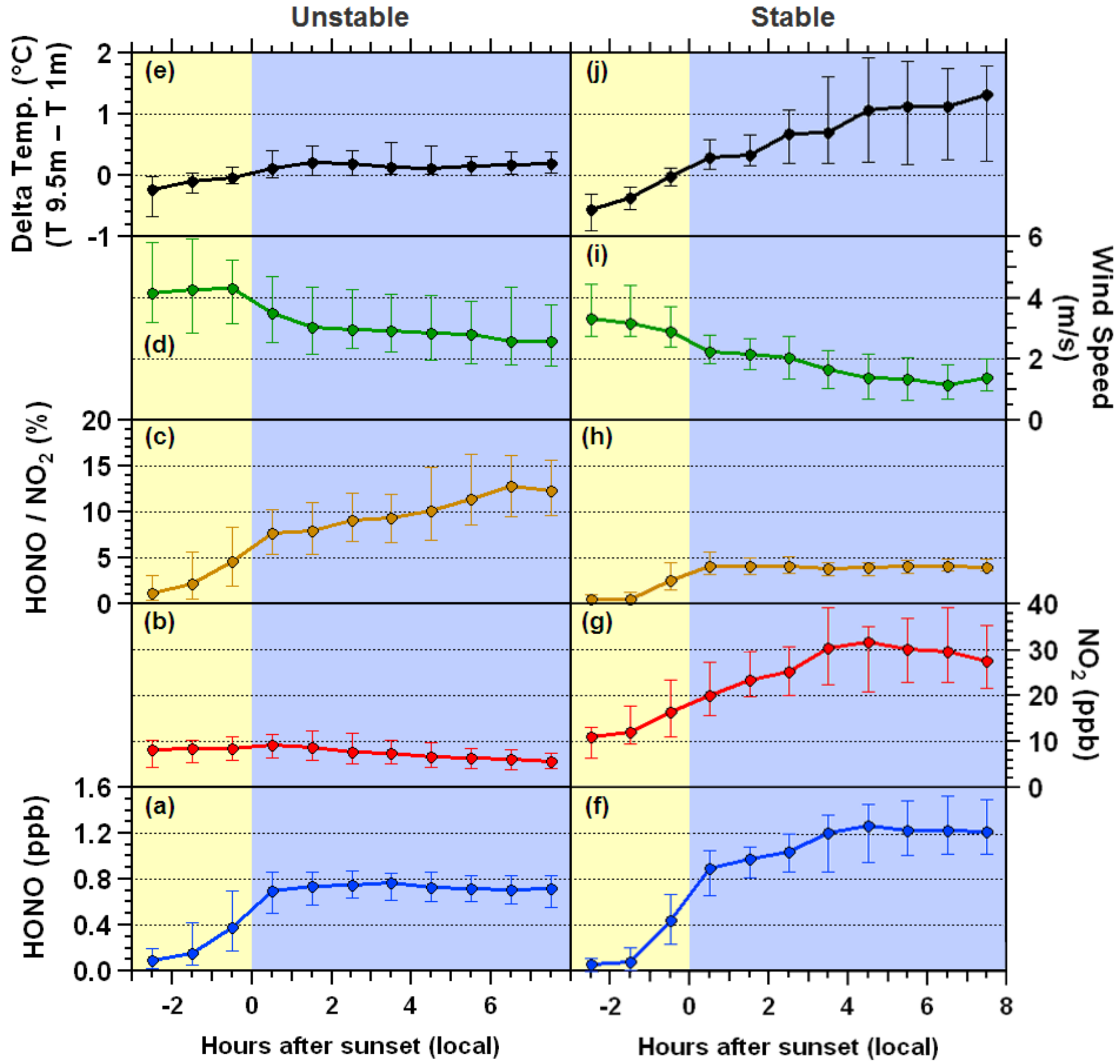

Figure 3.46: Hourly time bins of the median (solid line), 25th and 75th percentiles (error bars) for unstable nights (6 of 22 with snow, selected based on a steady-state overnight HONO temporal profile) and stable nights (5 of 19 with snow, selected based on the linearity of the overnight HONO/NO_2 ratio).

on the r^2 for the HONO vs. NO_2 data ($r^2 > 0.4$) and standard deviation of the HONO/NO_2 ratio (std. < 1 ppb ppb^{-1}) during the dark period of the night. In total, 22 nights met the set criteria, 6 of which had snow ground cover. These nights had a very stable nocturnal boundary layer forming within a few hours after sunset, indicated by the low wind speeds (Figure 3.46i) and increasing $\Delta T_{9.5-1}$ (Figure 3.46j). The HONO mixing ratio (Figure 3.46f) increased along with the NO_2 mixing ratio (Figure 3.46g) and the HONO/NO_2 ratio (Figure 3.46h) remained steady between $3 - 5\%$. This comparison provides further evidence that atmospheric stability and the NO_2 concentration appear to determining factors for the type of HONO behavior observed.

The previous analysis utilized the HONO and NO_2 mixing ratios to categorize the two types of HONO behavior and atmospheric stability was determined as the distinguishing factor. In order to confirm whether atmospheric stability is the determining factor, an alternative analysis was performed by choosing meteorological based criteria, comprising of two parameters associated with atmospheric stability; $\Delta T_{9.5-1}$ and wind speed. Hourly time bins summarizing the trends of HONO, NO_2 and the HONO/NO_2 ratio based on $\Delta T_{9.5-1}$ and wind speed criteria for unstable and stable nights are shown in Figure 3.47. Atmospherically unstable nights were selected based on overnight averages of $\Delta T_{9.5-1}$ <0.2 °C and wind speed >3 m/s. In total, 39 nights met this criteria with 21 containing snow ground cover. For the unstable nights, the HONO mixing ratio (Figure 3.47a) clearly exhibits a steady-state behavior with median levels stabilizing at ~0.75 ppb and 25th and 75th percentiles ranging from 0.6

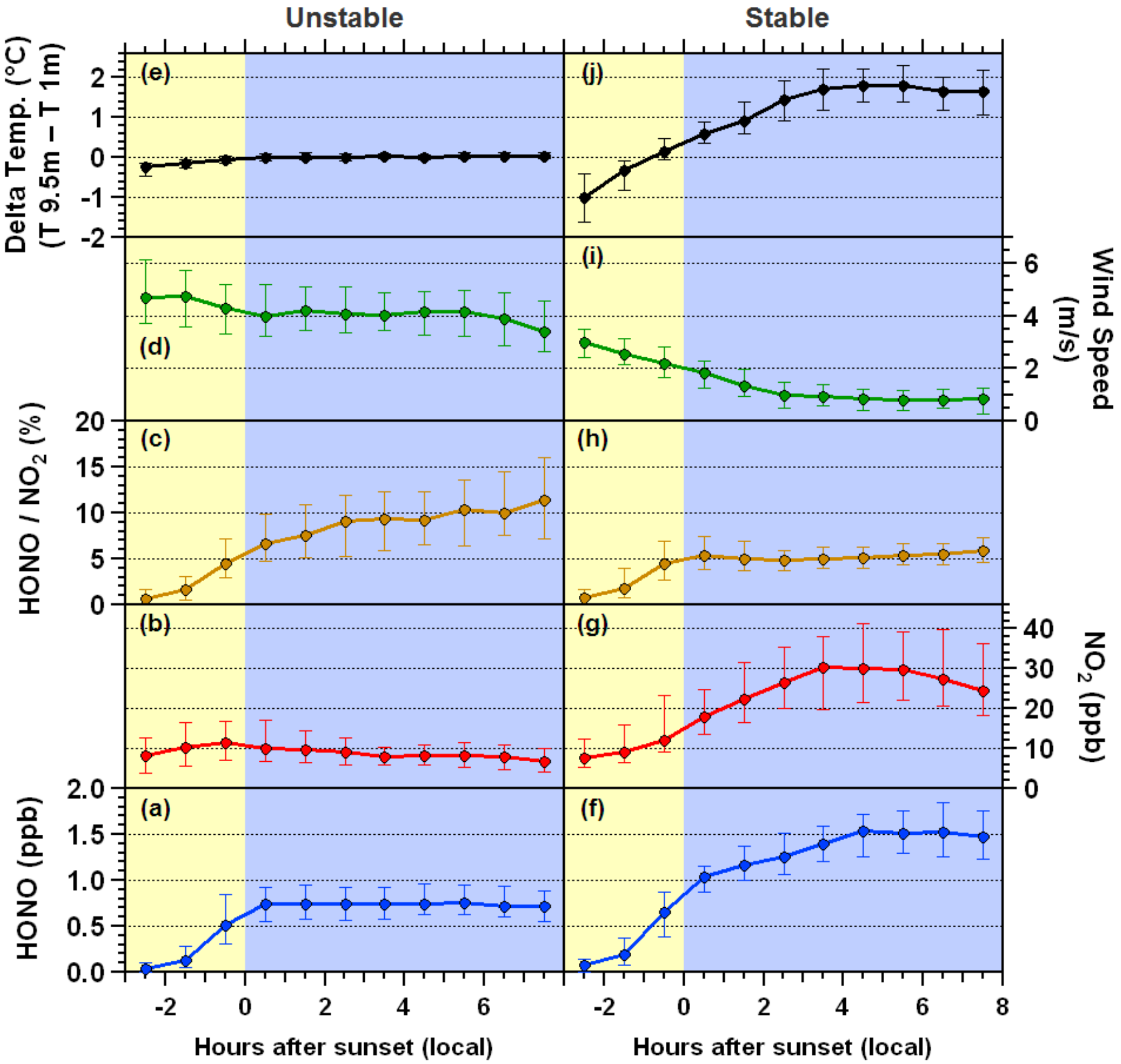

Figure 3.47: Hourly time bins of the median (solid line), 25th and 75th percentiles (error bars) for unstable nights (21 of 39 with snow, selected based on overnight averages $\Delta T_{9.5-1}$ <0.2 °C and wind speed >3 m/s) and stable nights (2 of 41 with snow, selected based on overnight averages $\Delta T_{9.5-1}$ >1 °C and wind speed <1.5 m/s).

– 0.9 ppb. The NO_2 mixing ratio (Figure 3.47b) slightly peaks during sunset and steadily decreases overnight with median levels ≤12 ppb. The overnight decrease of NO_2 is reflected in the steady overnight rise of the HONO/NO_2 ratio (Figure 3.47c), with median levels increasing from 5% at sunset to 12% late into the night. The wind speed (Figure 3.47d) and $\Delta T_{9.5-1}$ (Figure 3.47e) emulate the chosen criteria for unstable nights.

A very different behavior is seen on the stable nights. The HONO and NO_2 mixing ratios rapidly increase shortly before sunrise (Figure 3.47f/g), reaching median mixing ratios of 1.5 ppb and 30 ppb, respectively. The HONO/NO_2 ratio (Figure 3.47h) levels off within ~2 hours during sunset and the 25^{th} and 75^{th} percentiles range from $4 - 7\%$ for the entire night. A slight increase in the HONO/NO_2 ratio is observed late into the night. The wind speed and $\Delta T_{9.5-1}$ (Figure 3.47i/j) emulate the chosen criteria for stable nights.

In total, the 39 most unstable and 41 most stable nights account for 33% of all observations. By examining these nights, it is clear that stable nights occur more frequently during the summertime and unstable nights are more common during the wintertime with snow ground cover. These results are in agreement with the comparison of data with and without snow ground cover, previously shown in Chapter 3.4.1.3, and explain the observed HONO and HONO/NO_2 trends.

To gain further insight into the differences between stable and unstable nights and to better understand the role of atmospheric stability in the observed HONO behaviors, the temporal variation of O_3, temperature and relative humidity for stable and unstable nights was analyzed and is shown in Figure 3.48. For unstable nights, the median relative humidity increases marginally from 70% at sunset to 75% by morning. These nights would likely have significant amounts of surface adsorbed

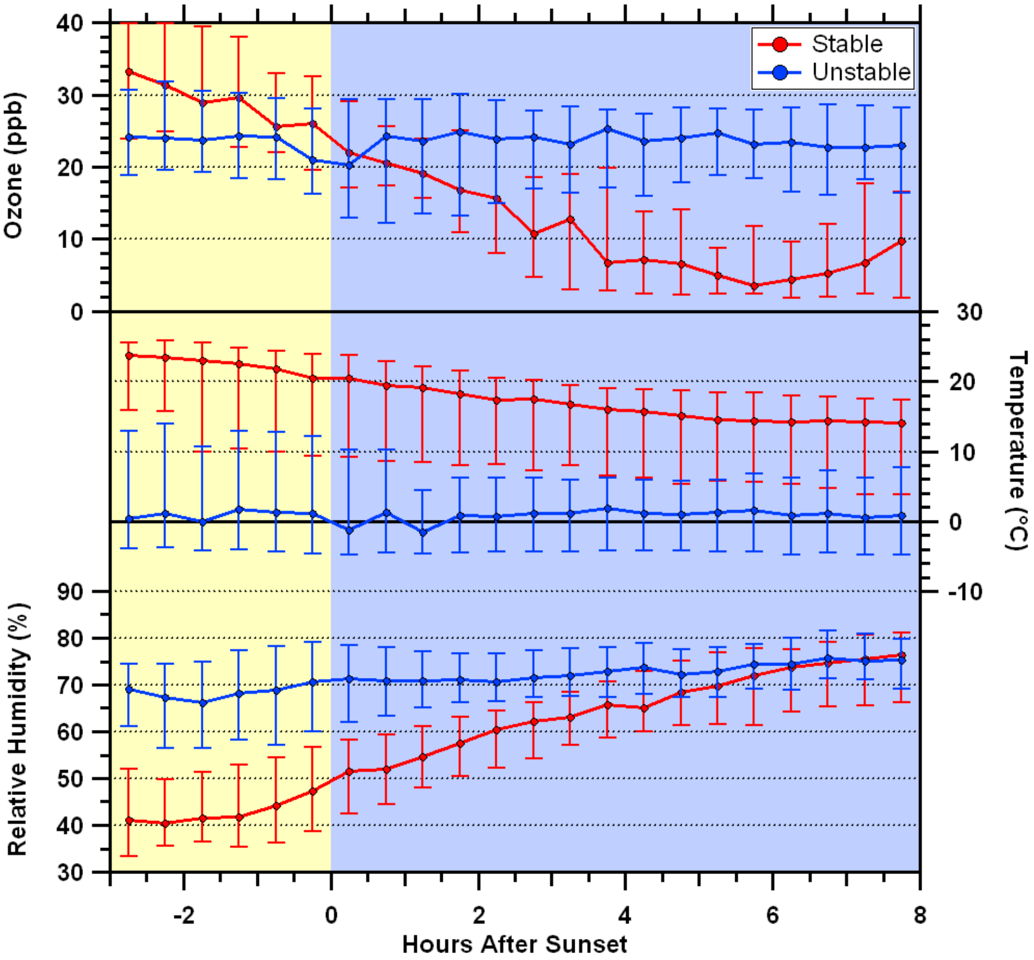

Figure 3.48: 30-minute time bins of the median (solid line), 25^{th} and 75^{th} percentiles (error bars) for (red) stable nights (41 nights selected based on overnight averages $\Delta T_{9.5-1}$ >1 °C and wind speed <1.5 m/s) and (blue) unstable nights (39 nights selected based on overnight averages $\Delta T_{9.5-1}$ <0.2 °C and wind speed >3 m/s).

water at the beginning of the night due to the high relative humidity and/or snow cover, which may enhance the heterogeneous formation of HONO. The nonfluctuating relative humidity throughout the night is linked with the roughly constant overnight temperature profile for unstable nights, with an overnight median level of ∼0 °C.

The O_3 mixing ratio remained at a steady level between $20 - 30$ ppb throughout the nights. The long lifetime of O_3 on unstable nights could be attributed to the low concentration and overnight decrease of NO_x, causing minimal titration of O_3. It is also possible that deposition rates of O_3 over water is reduced on these nights (Walcek, 1987).

During stable nights, the relative humidity climbs steadily throughout the night from 40% two hours before sunset to 70% by early morning. The temperature profile shows a steady decrease over the course of the night, reflecting the increase in relative humidity for a constant amount of water vapor. The O_3 concentration is strongly titrated by NO a few hours after sunset. As seen before, the low O_3 concentration greatly increases the lifetime of NO_2 by removing the formation pathway of NO_3 and N_2O_5.

In order to distinguish the effects of atmospheric stability from any possible artifacts arising due to snow ground cover, the same analysis was performed for stable and unstable nights excluding nights with snow (not shown). As expected, the average temperature for unstable nights was higher once the snow nights were removed, with the same overall trend. Most importantly, the ozone and relative humidity temporal profiles remained unchanged, strongly suggesting that a correlation of relative humidity and ozone levels with snow ground cover does not exist.

Since a positive temperature dependence was observed for HONO during the steady-state period at Saturna Island, a similar analysis was performed for the York University data set, including stable nights for comparison. The relationship between

HONO and temperature for stable and unstable nights is shown in Figure 3.49. For stable nights, a minor negative correlation was observed, with the majority of observations occurring during warmer temperatures. An enhancement at ~273 K was also observed, corresponding to a single night with significant amounts of snow ground cover. For unstable nights, a slight positive correlation was observed, with a large amount of scattering. A line of best fit was determined from a linear regression analysis for stable and unstable conditions, yielding HONO (ppb) = -0.014(±0.001)

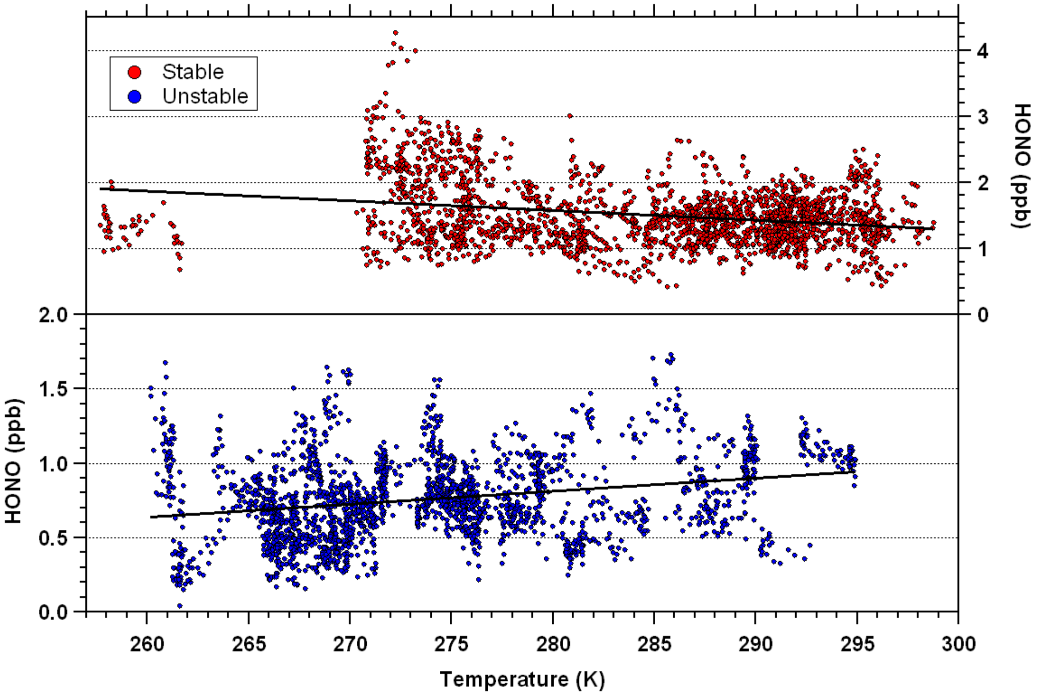

Figure 3.49: Relationship between HONO and temperature for (blue) unstable nights (39 nights selected based on overnight averages $\Delta T_{9.5-1}$ <0.2 °C and wind speed >3 m/s) and (red) stable nights (41 nights selected based on overnight averages $\Delta T_{9.5-1}$ >1 °C and wind speed <1.5 m/s). Only measurements during the dark period of the night are shown.

ppb K$^{-1}\times$ T + 5.6($\pm$0.3) ppb and HONO (ppb) = -0.0087($\pm$0.0007) ppb K$^{-1}\times$ T - 1.6($\pm$0.2) ppb, respectively, with r^2 = 0.065 for both fits. At the 95% confidence level, the slopes for stable and unstable nights were found not to be statistically different from one another, suggesting no evident temperature dependence for the HONO measurements at York University. However, these results are not fully conclusive, as a possible temperature dependence may be masked by other variables.

The relationship between HONO and NO$_2$ for the 41 unstable and 39 stable nights

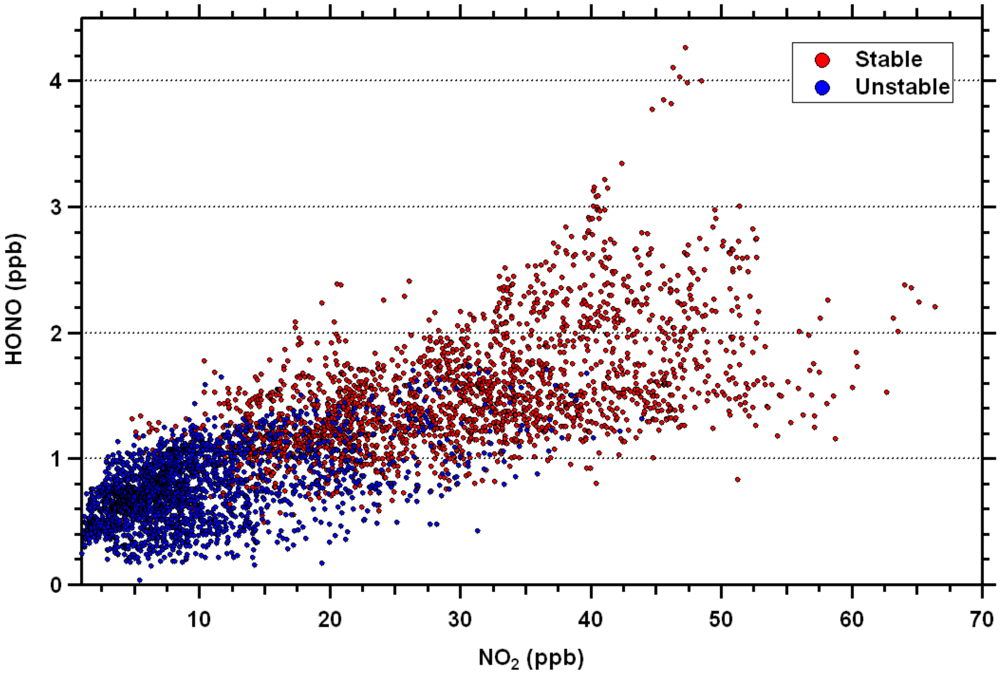

Figure 3.50: Relationship between HONO and NO$_2$ for (blue) unstable nights (39 nights selected based on overnight averages $\Delta T_{9.5-1}$ <0.2 °C and wind speed >3 m/s) and (red) stable nights (41 nights selected based on overnight averages $\Delta T_{9.5-1}$ >1 °C and wind speed <1.5 m/s). Only measurements during the dark period of the night are shown.

is shown in Figure 3.50. These two types of nights cover the low and high ends of the observed NO_2 concentration. A transition occurs between stable and unstable nights at a NO_2 mixing ratio of ~20 ppb, indicating a turning point from one type of HONO behavior to the other. From the graph, the transition between the two types of night is smooth, and atmospheric stability alone may define the type of observed HONO behavior in polluted environments.

Although the previous analysis provided useful insight into the behavior of HONO on stable and unstable nights, only 33% of the measured nights fall into these two meteorological extremes. In order to include a greater portion of the data set, an additional investigation was performed including a wider range of overnight wind speeds and $\Delta T_{9.5-1}$. Nights were classified as either very stable, stable, very unstable or unstable, with each category containing 41, 39, 41, and 39 nights, respectively. In total, the analysis included 66% of all observations. The median mixing ratios of HONO and NO_2 for 1-hour time bins, along with the criteria for the classification of the nights are shown in Figure 3.51. An increase in atmospheric stability results in an increase in the HONO and NO_2 mixing ratios. There appears to be a gradual transition from steady-state nights of HONO to the nights of highly correlated HONO to NO_2, depending on atmospheric stability.

As shown in Figure 3.52, the night of September 22/23 consists of a case study during which an overnight transition in atmospheric stability occurred. During this night, high values of $\Delta T_{9.5-1}$ and low wind speeds were initially encountered, characteristic of the presence of a very stable NBL. The HONO and NO_2 mixing ratios

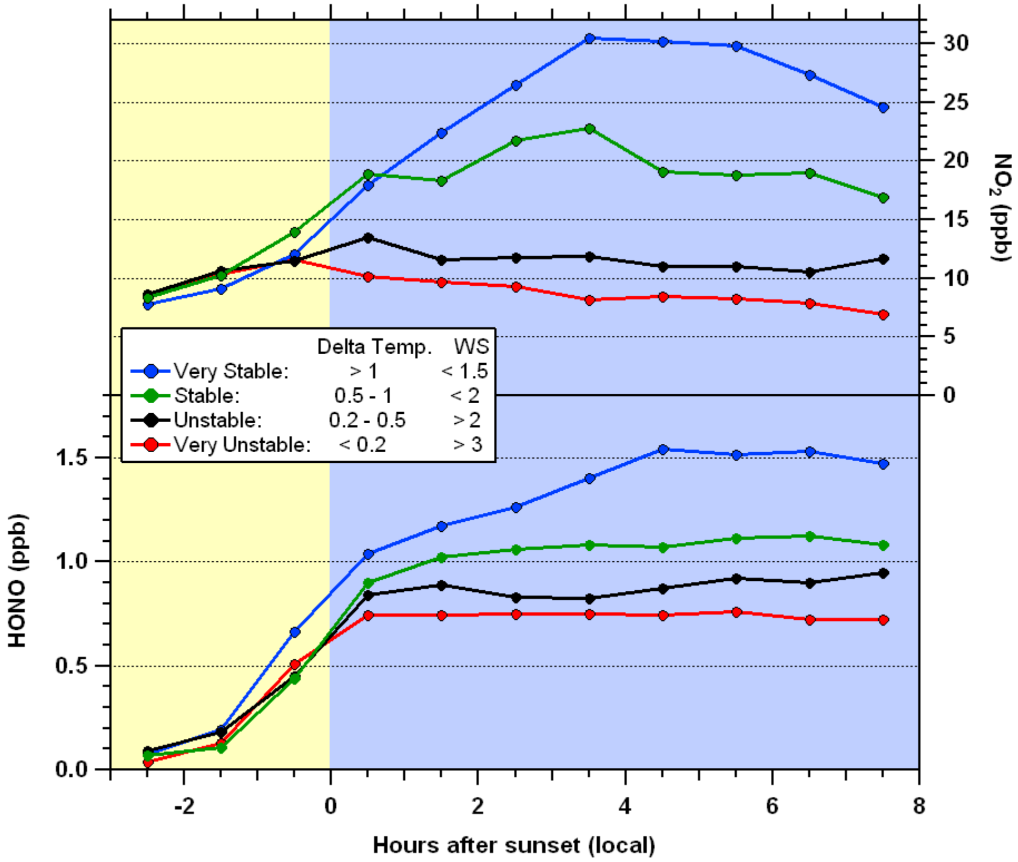

Figure 3.51: Median mixing ratios of HONO and NO_2 binned by nights with various atmospheric stability based on overnight averages of wind speed and $\Delta T_{9.5-1}$ during the dark period of the night. In total, the atmospheric classifications of very stable, stable, very unstable and unstable included 41, 39, 41, and 39 nights respectively.

are observed to strongly correlate, with a constant HONO/NO_2 ratio ~4% for the entire stable period. Between 2:00–3:00, the $\Delta T_{9.5-1}$ is observed to decrease to 0°C, coincident with a rise in the wind speeds, signifying the transition from a stable to unstable nocturnal atmosphere. At this time, the NO_2 mixing ratio decreased while the HONO mixing ratio remained constant at a level of ~1.1 ppb, resulting in an increase of the HONO/NO_2 ratio to 12%. This case study also shows the timescale at

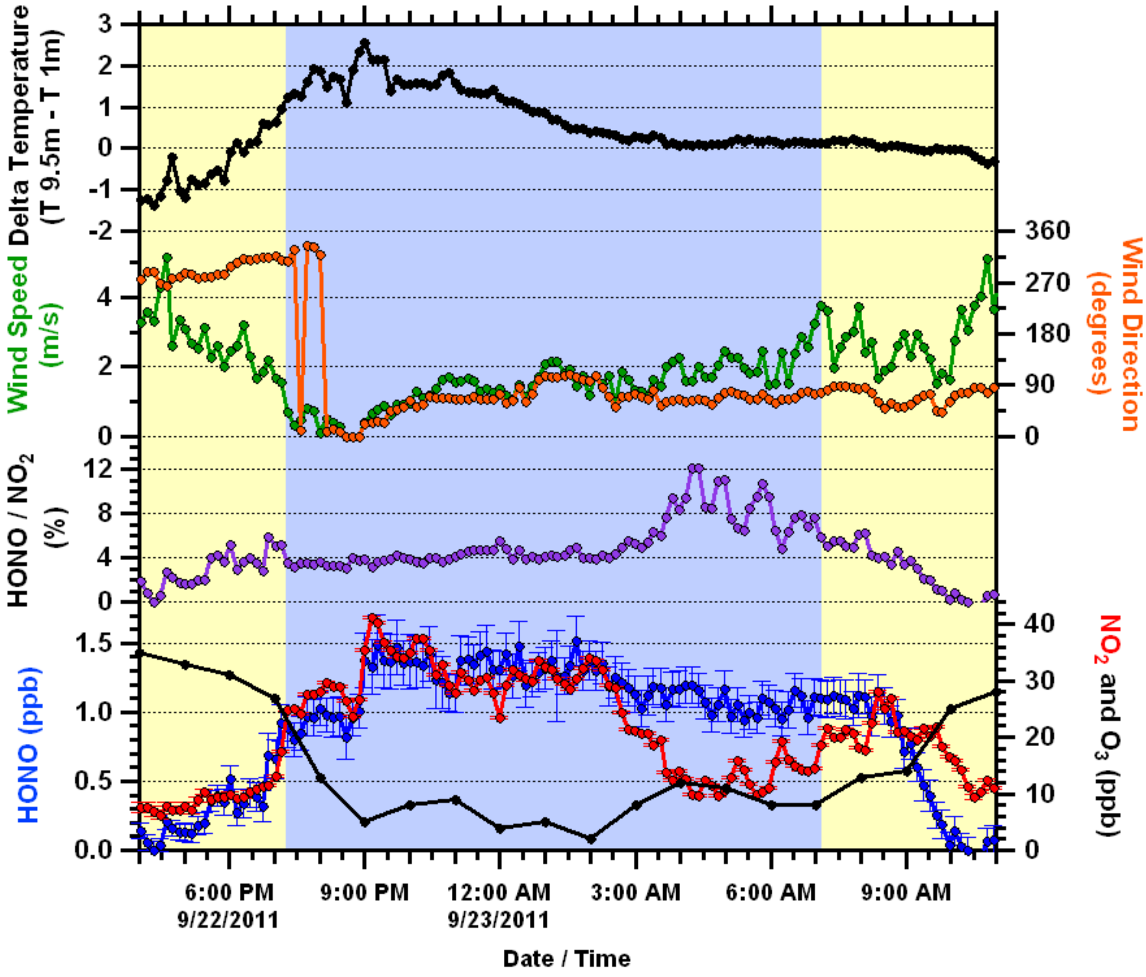

Figure 3.52: Nocturnal measurements on September 22/23, 2011. A transition occurs during the night from a stable to an unstable atmosphere, determined from the wind speed and $\Delta T_{9.5-1}$ profile.

which the HONO dependence on NO_2 can transition from a first-order relationship to zero-order.

In summary, a smooth transition was observed between the two types of HONO behaviors. During well mixed and unstable nights, the NO_2 mixing ratio steadily decreased while the HONO mixing ratio remained constant overnight. The relative humidity was ∼70% at the beginning of the night, and slowly increased over the course of the night. Unstable nights are observed to occur frequently during the wintertime, with the average temperature relatively constant throughout the night. The O_3 mixing ratio remains between $20 - 30$ ppb throughout the night, which led to significant overnight formation of NO_3 and N_2O_5. The combination of high relative humidity and high O_3 concentration greatly reduce the nocturnal lifetime of NO_2. The defining feature of this night is the formation of a rapidly established steady-state of HONO, where $d[\mathrm{HONO}]/dt = 0$.

The formation of a stable and low nocturnal inversion early in the night is accompanied by high levels of NO_2. The HONO and NO_2 mixing ratios correlate very closely, as reflected by the HONO/NO_2 ratio, which ranges from $3 - 6\%$. The relative humidity during these nights is observed to continuously rise, with median levels at ∼50% at sunset, rising to 75% by early morning. It is perhaps not coincidental that as the relative humidity reaches ∼70-75% several hours after sunset on these nights, that HONO mixing ratios tend to level off as would occur on a steady state night (see Figures 3.47f and 3.51). Stable nights occur more frequently during the summertime with the temperature steadily decreasing overnight. The O_3 mixing ratio decreased throughout the night, often to negligible levels, most likely due to reaction with NO. On such nights, it is very likely that suppression of NO_3 and N_2O_5 formation increases the lifetime of NO_2. The defining feature of this night is the rapid formation of a first-order dependence of HONO with NO_2, where $d([\mathrm{HONO}]/[\mathrm{NO_2}])/dt \approx 0$.

The conceptual model previously presented in Chapter 3.2.6 describing steady-states of HONO at Saturna Island can be extended to explain the observed steady-states of HONO at York University. Steady-states of HONO were observed in both atmospheres during unstable conditions, with average overnight wind speeds of 3.1 m/s during the Saturna field study and 4.0 m/s for unstable nights at York University. An abundance of surface water due to the high relative humidity during unstable nights at York University may mimic the ocean surface at Saturna, supporting steady-states of HONO over terrestrial environments. The atmospheric stability and persistent aqueous surface may be the key feature linking the steady-state observations from the two studies. However, the conceptual model cannot be extended to explain HONO observations during stable nights, where the HONO and NO_2 concentrations were strongly correlated. The model would only predict a correlation between the HONO and NO_2 concentrations given a continuous depletion of the surface reservoir, analogous to the daytime conceptual model (Figure 3.21). Furthermore, surface acidity may play a key role in HONO formation and/or additional mechanisms may be active overnight, however, these suggestions are beyond the scope of this work.

3.4.3 HONO Production Normalized to NO_2

A parameter used to investigate the average nighttime conversion frequency of NO_2 to HONO, $\overline{\mathrm{F}}_{\mathrm{HONO,night}}$, is given by the following equation:

$$\overline{\mathrm{F}}_{\mathrm{HONO,night}} \equiv \frac{[\mathrm{HONO}](t_2) - \mathrm{HONO}](t_1)}{(t_2 - t_1)[\mathrm{NO_2}]_{\mathrm{avg}}} \times 100\% \tag{3.29}$$

where the formation of HONO is determined by assuming a linear increase of the HONO concentration over the time period $(t_2 - t_1)$. The HONO formation is assumed to be first-order with respect to NO_2 and is therefore normalized to the average NO_2 concentration over the time period. The conversion frequency has in the past been assumed to be independent on the gas phase water concentration (Kleffmann et al., 1998) or the amount of surface adsorbed water.

When examining linear increases of HONO, it is difficult to distinguish whether the increase of HONO arises due to chemical reactions or changes in air mass. Meteorological measurements made at York University were used to ensure that the air mass was unchanging, singling out variations of HONO due to chemical reactions.

A case study analysis of the conversion frequency is shown in Figure 3.53. For the majority of the night of March 14−15, 2011 (between 20:06 − 3:34), HONO increased linearly and is accompanied by a steady increase in NO_2. During this time, the wind direction was dominantly from the south with wind speeds decreasing over the course of the night. The $\Delta T_{9.5-1}$ data indicates the formation of a stable nocturnal boundary layer at 11:30 pm, persisting until morning. A change in wind direction from south to east at 4:30 indicates a likely change in air mass. The HONO/NO_2 ratio remains constant at 4% during for the first half of the night and steadily rises with the formation of a more stable atmosphere. A sharp rise in the HONO mixing ratio is observed between 3:08 − 3:59 and occurred as $\Delta T_{9.5-1} > 2°C$. The rapid increase of HONO may possibly be due to a change in air mass or may be related to the formation of a very stable NBL and was not included in the calculation. $\overline{F}_{HONO,night}$

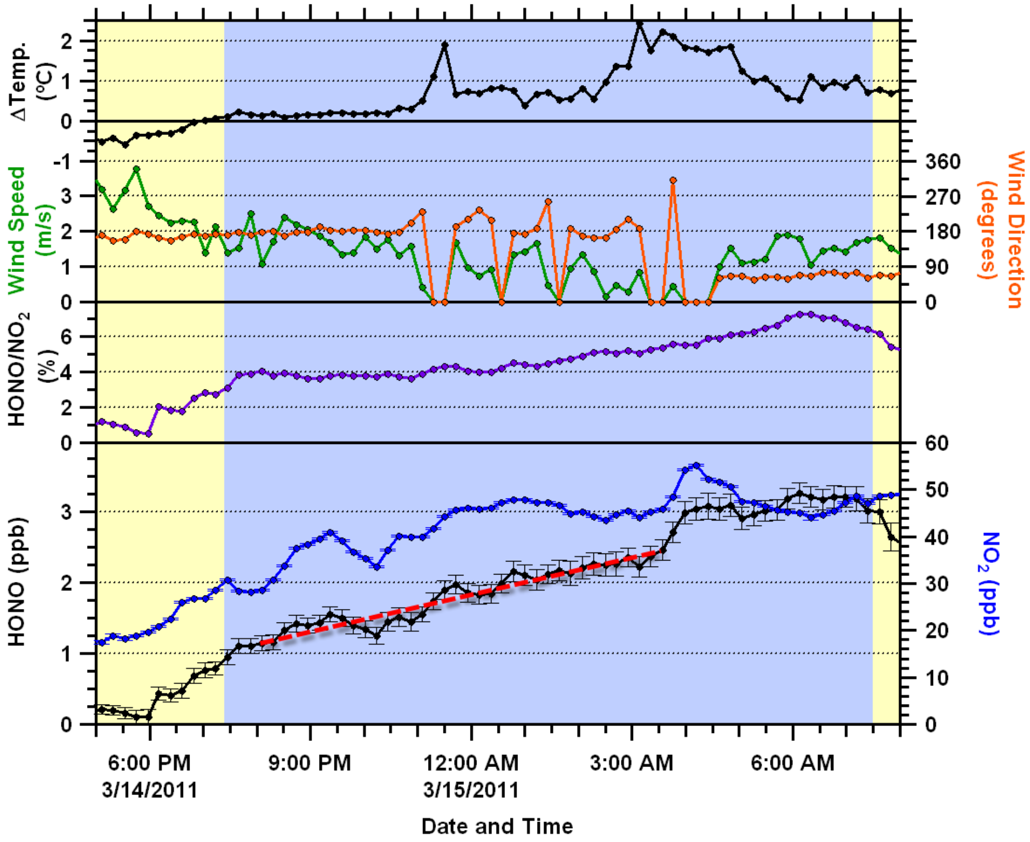

Figure 3.53: Measurements during March 14/15, 2011 with the dashed red line representing the calculated conversion frequency time period. The yellow and blue background represent day and night time respectively.

was calculated to be 0.42 $\% \, h^{-1}$ for the steady rise of HONO overnight.

A summary of various conversion frequencies of HONO to NO$_2$ during the year-long study period at York University is shown in Table 3.10. The nights selected for this analysis exhibited linear increases of HONO and constant meteorological parameters, in order to eliminate variations in the HONO mixing ratio due to changes in the air mass. Steady rises of HONO generally occurred in conjunction with high NO$_2$ mixing ratios ($[NO_2]_{avg}$ >20 ppb), and the length of the HONO increase ranged

Table 3.10: Observed nocturnal conversion frequencies for various nights. The date, time period, Δ HONO, average NO_2 and conversion frequency ($\overline{\mathrm{F}}_{\mathrm{HONO,night}}$) for the time period is shown.

Date	Time (local)	[HONO](t_1) − [HONO](t_2) (ppb)	$[\mathrm{NO_2}]_{\mathrm{avg}}$ (ppb)	$\overline{\mathrm{F}}_{\mathrm{HONO,night}}$ ($\%\,\mathrm{h}^{-1}$)
11/7	20:10 − 21:01	1.47 − 2.00	34.8	1.79
11/15	18:10 − 19:18	1.17 − 1.75	42.0	1.22
3/14-15	20:06 − 3:34	1.15 − 2.46	41.9	0.42
4/8	19:06 − 23:42	0.40 − 1.57	29.6	0.86
5/5	1:06 − 4:56	0.81 − 1.27	27.0	0.45
6/3-4	21:58 − 2:01	1.14 −1.77	34.2	0.45
8/13-14	21:01 − 2:08	1.07 − 1.93	20.9	0.81
9/10	19:24 − 23:50	0.36 − 1.69	22.1	1.36
10/7	19:57 − 23:47	0.91 − 1.60	41.0	0.44
10/8	20:41 − 23:57	1.25 − 1.66	30.1	0.42

from ∼1−5 hours. The observed $\overline{\mathrm{F}}_{\mathrm{HONO,night}}$ at York University ranged from 0.42 − 1.79 $\%\,\mathrm{h}^{-1}$ for the 10 selected nights, chosen as a representative sample of the data set.

Previous studies calculated conversion frequencies of 1.59 $\%\,\mathrm{h}^{-1}$ at a non-urban site in Xinken, China (Su et al., 2008), 0.44 $\%\,\mathrm{h}^{-1}$ in Mainz Germany (Lammel, 1999), 0.49 $\%\,\mathrm{h}^{-1}$ in Milan, Italy (Lammel, 1999), 0.90 $\%\,\mathrm{h}^{-1}$ at a site 30 km north of the urban environment of Marseille, France (Acker et al., 2005), 0.43 $\%\,\mathrm{h}^{-1}$ inside the urban center in Karlsruhe, Germany (Kleffmann et al., 2003), 1.2 $\%\,\mathrm{h}^{-1}$ within an urban area in Milan, Italy (Alicke et al., 2002), and 1.8 $\%\,\mathrm{h}^{-1}$ at a rural site in Pabstthum near Berlin, Germany (Alicke et al., 2003). The observed $\overline{\mathrm{F}}_{\mathrm{HONO,night}}$ at York University matches the range observed at other rural and urban sites, suggesting the occurrence of a common mechanism between the various sites.

The nights were also analyzed to determine whether there exists a relationship between $\overline{\mathrm{F}}_{\mathrm{HONO,night}}$ and $\Delta\mathrm{T}_{9.5-1}$ or relative humidity (not shown). Each of the selected nights exhibited stable atmospheric boundary layers, making it difficult to determine possible relationships between conversion frequency and atmospheric stability. Although no significant correlation was found between $\overline{\mathrm{F}}_{\mathrm{HONO,night}}$ and the average $\Delta\mathrm{T}_{9.5-1}$, atmospheric stability may have significant effects for the conversion frequency. In addition, no correlation was found between $\overline{\mathrm{F}}_{\mathrm{HONO,night}}$ and relative humidity, likely due to the complexity of simultaneously varying chemistry and meteorology.

It is worth mentioning that the conversion frequencies during steady-state HONO nights would be 0, since $d[\mathrm{HONO}]/dt = 0$. Also, the conversion frequency does not take deposition of HONO into account and is therefore not a true conversion frequency, only a lower limit.

3.4.4 Modeling Studies of HONO

The modeling studies presented in this chapter were performed numerically using a simple box model in Microsoft Office Excel with a 1-second time step. The reactions utilized in the study are shown in Table 3.11. Reaction (a) is the photolysis of HONO, Reaction (b) corresponds to the surface reaction $2NO_2 + H_2O \rightarrow HONO + HNO_3$, and Reaction (c) is the irreversible deposition of HONO. Chapter 3.4.4.1 summarizes the model results for the photolysis of HONO during sunrise for a case study on April 2, 2011, including Reaction (a) exclusively. Chapter 3.4.4.2 describes the simulated dark first-order production and loss rate constants of HONO during stable conditions, only taking into account the production and deposition reactions, Reactions (b) and (c). This analysis was performed in order to provide initial insight into the kinetic rates required to reproduce observations of HONO during stable nights. Chapter 3.4.4.3 summarizes the modeled HONO concentration during sunset for two case studies and includes all 3 reactions in Table 3.11. Chapter 3.4.4.4 summarizes the simulated dark

Table 3.11: A summary of the reactions used in the modeling studies.

	Reaction	Rate
(a)	$HONO + h\nu \rightarrow NO + OH$	k_{p}
(b)	$NO_2 \rightarrow HONO$	k_{prod}
(c)	$HONO \rightarrow$	k_{dep}

HONO steady-state during unstable conditions, taking into account Reaction (c).

The photolysis of HONO during sunset and sunrise was determined by calculating the photolysis rate (k_p) of HONO as a function of solar zenith angle (SZA), given by:

$$k_p = \int F(\lambda)\,\sigma(\lambda)\,\phi(\lambda)\,d\lambda \tag{3.30}$$

where $F(\lambda)$ is the actinic flux (photons $\mathrm{cm^{-2}\,s^{-1}\,nm^{-1}}$) for a given SZA, $\sigma(\lambda)$ is the absorption cross section of HONO ($\mathrm{cm^2\,molecule^{-1}}$) and $\phi(\lambda)$ is the quantum yield of HONO for a given wavelength range of λ. The actinic flux was calculated using the Tropospheric Ultraviolet and Visible (TUV) radiative transfer column model version 4.1 provided by National Center for Atmospheric Research (NCAR). The absorption cross section and quantum yield of HONO were obtained from Jet Propulsion Laboratory (JPL) Chemical Kinetics and Photochemical Data for Use in Atmospheric Studies Evaluation Number 15 (Sander et al., 2006).

3.4.4.1 Case Study - HONO Photolysis During Sunrise

The photolysis rate of HONO was calculated as a function of the SZA for a range of 0 to 100 degrees. The HONO photolysis was determined using first-order kinetics according to the following differential equation by assuming an initial HONO mixing ratio equal to the average measured HONO just before sunrise.

$$\frac{d[\mathrm{HONO}]}{dt} = -k_{\mathrm{p}}[\mathrm{HONO}](\mathrm{t}) \tag{3.31}$$

A summary of the photolysis of HONO for a case study on Saturday, April 2, 2011, as a function of time of day and SZA is shown in Table 3.12. The photolysis of

HONO during sunrise was modeled for the case study and the temporal profiles of HONO, NO_2 and NO are shown in Figure 3.54. The hourly measurements of NO from Environment Canada North York site were interpolated to match the time resolution of the DOAS measurements. Clear sky conditions and no visible rush hour NO peak was observed during the morning. After sunrise at 6:58 (local time), HONO decreased at a steady rate for 3 hours before falling below detection limit.

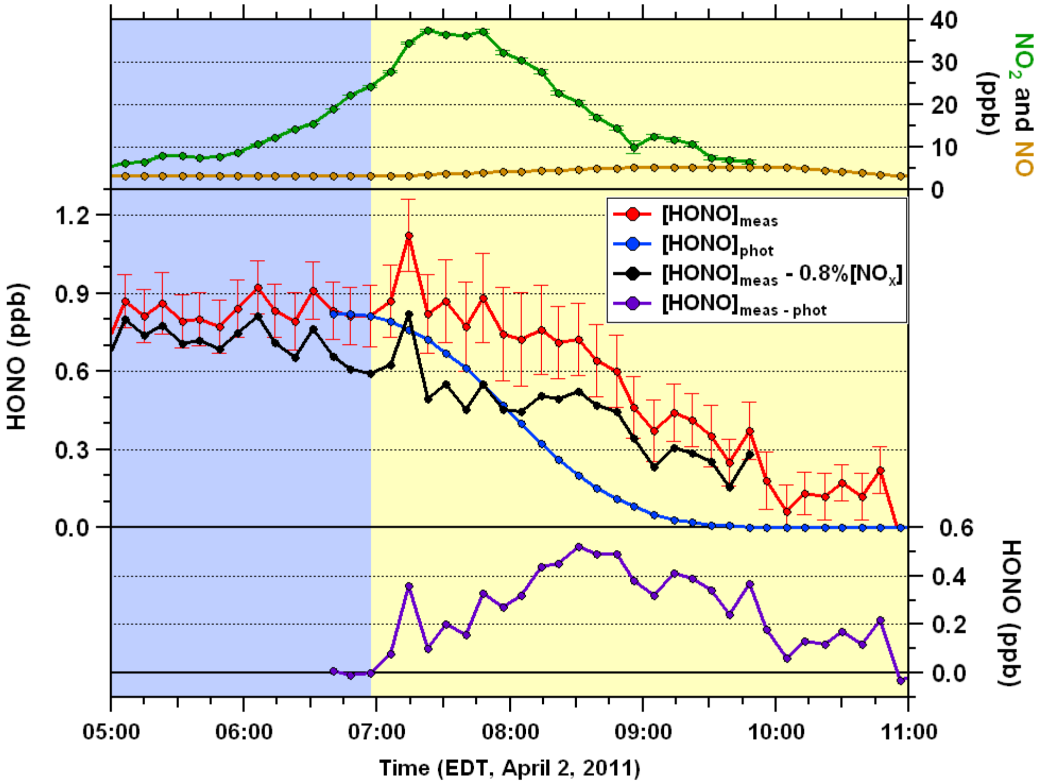

Figure 3.54: A case study comparing the measured (red) and calculated (blue) photolysis of HONO on April 2nd, 2011 at York University. The mixing ratios of NO_2 (green) and NO (gold) along with the measured HONO - $0.008 \times NO_x$ (black) and the difference between measured and modeled HONO (purple) are shown.

Table 3.12: Calculations of the SZA, photolysis rate of HONO (k_p), lifetime of HONO with respect to photolysis (τ_{phot}), modeled HONO mixing ratio from only photolysis loss and percentage of HONO lost for the case study on April 2, 2011 during sunrise.

Time (am) (Local, EDT)	Solar Zenith Angle (degrees)	k_p (s^{-1})	τ_{phot} (hour)	$[\text{HONO}]_{\text{phot}}$ (ppb)	Percent Photolyzed
6:40	92.3	5.96×10^{-6}	46.6	1.14	0 %
6:50	90.4	2.08×10^{-5}	13.4	1.12	1.8 %
7:00	88.6	4.52×10^{-5}	6.15	1.10	3.6 %
7:20	85.2	1.17×10^{-4}	2.37	0.98	14.2 %
7:40	81.9	2.16×10^{-4}	1.29	0.78	31.6 %
8:00	78.7	3.41×10^{-4}	0.81	0.54	52.7 %
8:20	75.5	4.79×10^{-4}	0.58	0.32	72.2 %
8:40	72.3	6.25×10^{-4}	0.44	0.16	86.3 %
9:00	69.1	7.76×10^{-4}	0.36	0.06	94.3 %
9:20	65.9	9.25×10^{-4}	0.30	0.02	98.1 %
9:50	61.1	1.14×10^{-3}	0.24	0.00	100 %

From the calculation of HONO photolysis based on a clear sky actinic flux, HONO is expected to be completely photolyzed within ∼2 hours after sunrise. The difference between measured and modeled HONO, shown in the bottom panel of Figure 3.54, was as high as 0.5 ppb nearly 2 hours after sunrise, and slowly decreased with time. The maximum amount of HONO from direct vehicle emissions ($0.008\times NO_x$) was calculated and subtracted from measured HONO time series, as seen in Figure 3.54 as the black line. This direct source of HONO was found to be insufficient to explain the difference between the measured and modeled HONO mixing ratio shortly after sunrise, indicating the presence of an active source of HONO during this time period. An excess of HONO with respect to the modeled photolysis was frequently observed in the year-long data set. This result is in agreement with previous literature reports (VandenBoer, 2012; Wojtal et al., 2011; Harrison and Kitto, 1994), indicating that a reservoir source of HONO may be present, continuously emitting to the atmosphere in the early morning. The source may potentially consist of a surface reservoir and/or evaporation of water, as well as the heterogeneous conversion of NO_2 to HONO. The production rate of the heterogeneous reaction was investigated for stable and unstable night conditions and is shown in Chapters 3.4.4.2, 3.4.4.3 and 3.4.4.4.

3.4.4.2 HONO Production and Loss Rates During Stable Nights

A few assumptions are made for the following numerical model studies presented. Firstly, it is assumed that the only source of HONO during the modeled period is the first-order heterogeneous reaction of NO_2 with surface adsorbed water. The first-order assumption is justified based on the results reported by various laboratory and field studies (Lammel and Cape, 1996; Stutz et al., 2002; Finlayson-Pitts, 2003a). A reservoir and/or additional sources of HONO may be present, but were not included in the model because of the uncertainties associated with these parameters. The reaction between NO and OH to produce HONO was not included in the modeling studies due to the low concentrations of OH in the early evening. Secondly, the only losses of HONO are taken to be the irreversible deposition and photolysis (if applicable). Recent literature (VandenBoer, 2012) and the results previously presented from Saturna Island suggest that reversible deposition of HONO may be occurring, but was not included in the modeling due to insufficient knowledge. In addition, the HONO production and loss rate constants for stable nights were assumed to reflect the observed HONO/NO_2 ratio. The ratio of $k_{\mathrm{prod}}/k_{\mathrm{dep}} = 3 - 6\%$ was based upon the observed HONO/NO_2 ratio for the chosen case study night. It is further assumed that for stable conditions, the particular HONO/NO_2 and $k_{\mathrm{prod}}/k_{\mathrm{dep}}$ ratios persist throughout the entire night, including periods during sunrise and sunset. It is also assumed that transport is not responsible for a change in HONO concentration during the modeling period, by only including nights during which meteorological conditions were relatively constant. Direct emissions of HONO from vehicles have not been taken into consideration in the model since NO measurements were not available at York University.

As previously discussed, the HONO concentration was strongly correlated to the NO_2 concentration during atmospherically stable nights. The HONO/NO_2 ratio was generally less than 0.5% 1−2 hours before sunset, rising to a stable ratio of 3 − 6% within 0.5−1 hour after sunset. The box model was implemented as a preliminary step to simulate the dark HONO temporal profile for stable conditions and determine the magnitude of HONO production and loss rates required to match the observed timescales and mixing ratios, excluding photolysis effects. The model assumes that the ratio of the first order rate constants corresponding to HONO heterogeneous formation and loss from deposition is 4% as shown below:

$$\frac{k_{\mathrm{prod}}}{k_{\mathrm{dep}}} = 0.04 \tag{3.32}$$

where k_{prod} is the HONO production rate constant for the first-order heterogeneous conversion of NO_2 to HONO and k_{dep} is the first order rate constant for HONO deposition. The mixing ratio of HONO in the model is determined by the following equation:

$$\frac{d[\mathrm{HONO}]}{dt} = k_{\mathrm{prod}}[\mathrm{NO_2}](\mathrm{t}) - k_{\mathrm{dep}}[\mathrm{HONO}](\mathrm{t}) \tag{3.33}$$

The timescales required for the system to reach a constant HONO/NO_2 ratio of 4% under dark conditions, using the relationships from Equations 3.33 and 3.32, are shown in Figure 3.55 for various choices of HONO production rates. The model assumed a constant NO_2 mixing ratio of 25 ppb, typical at York on a stable night, and an initial HONO mixing ratio of 0 ppb. These results provide a minimum estimate of the production rate required to reproduce the general observations of HONO during stable conditions.

The timescale required to reach a HONO/NO_2 ratio of 4% for each production

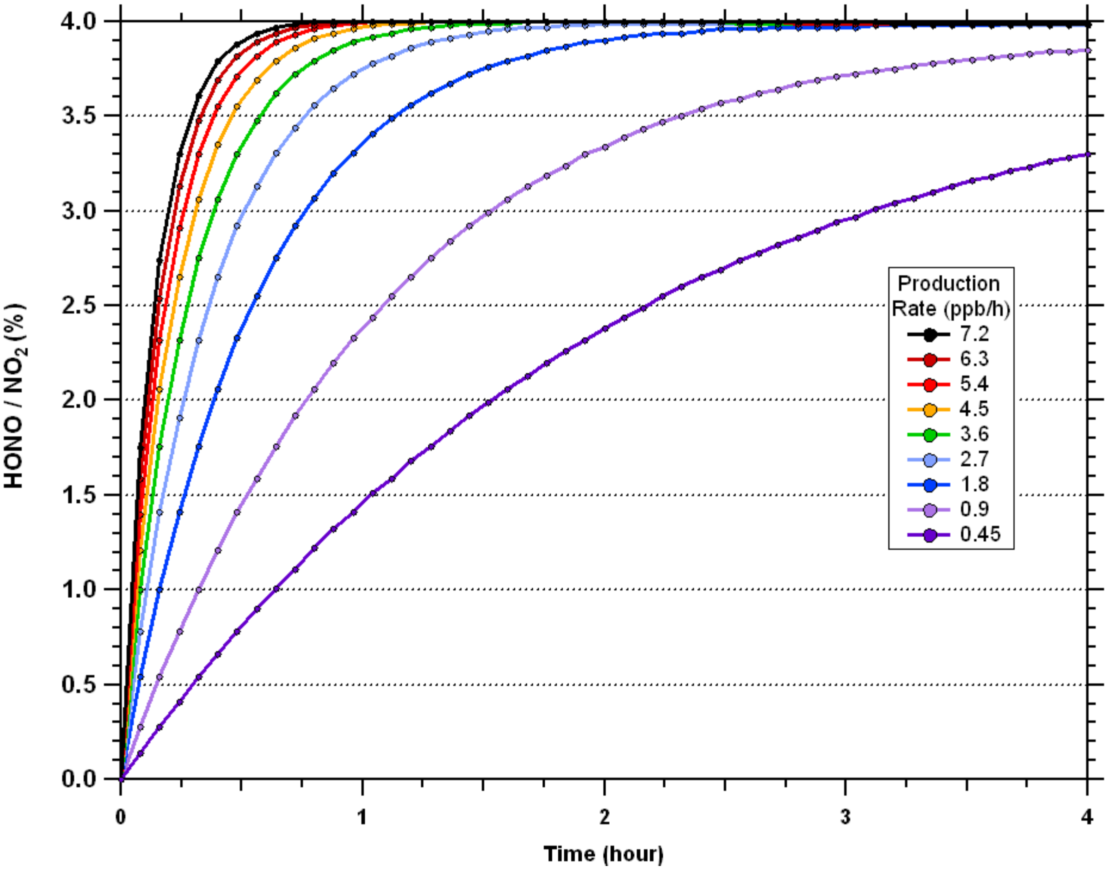

Figure 3.55: Box model results showing the resulting HONO/NO_2 ratio for different HONO first order production rates, ranging from 0.45 to 7.2 ppb h^{-1}.

rate was summarized in Figure 3.56. From observations, the timescale required to reach a steady HONO/NO_2 ratio was generally ∼1.5 hours in the early evening, corresponding to a modeled production rate of ∼3.0 ppb h^{-1} according to Figure 3.56. Since photolysis during sunset comprises an additional sink for HONO, a stable HONO/NO_2 ratio is expected to be reached more slowly in the presence of photolysis. Thus, from the simple box model results, a HONO production rate $\gtrsim$3.0 ppb h^{-1} is required to reproduce observations during stable nights for a typical NO_2 mixing ratio

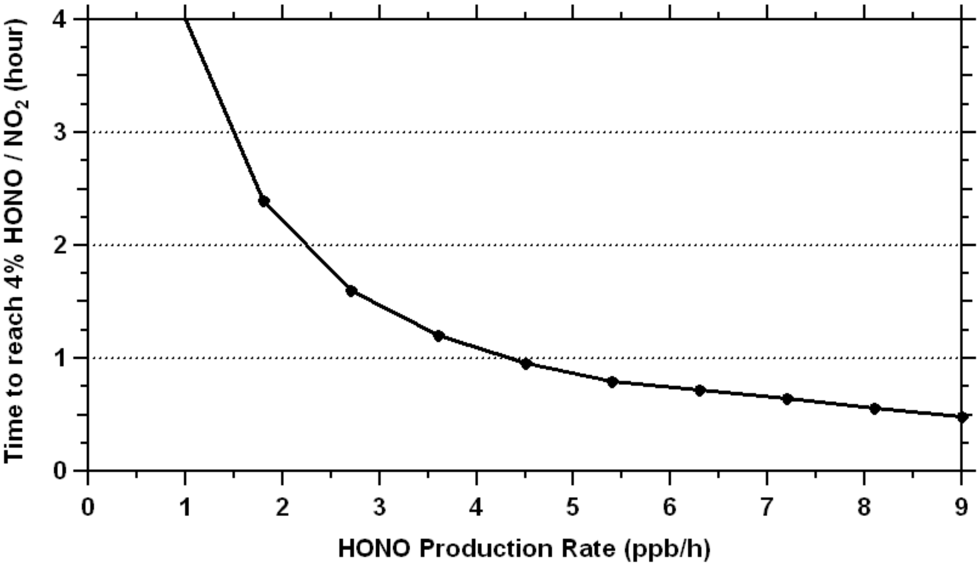

Figure 3.56: Timescale required to reach a HONO/NO$_2$ ratio of 4% for various first order production rates of HONO for the simple box model, based on the results from Figure 3.55.

of 25 ppb.

3.4.4.3 Modeling Case Studies during Sunset for Stable Nights

This chapter summarizes the modeled HONO concentration during sunset for two stable night case studies, with and without snow ground cover. The model includes the photolysis, first-order production from NO$_2$ and deposition of HONO, described by the three reactions previously shown in Table 3.11. The differential equation describing the change of the HONO concentration with time as calculated in the model is as follows:

$$\frac{d[\mathrm{HONO}]}{dt} = k_{\mathrm{prod}}[\mathrm{NO_2}](\mathrm{t}) - (k_{\mathrm{p}} + k_{\mathrm{dep}})[\mathrm{HONO}](\mathrm{t}) \qquad (3.34)$$

where the time dependent NO_2 concentration was determined from a fit of the observed NO_2 over several time intervals.

Stable Night without Snow - Case Study on October 7, 2011

The evening of Friday, October 7$^{\text{th}}$, 2011 was chosen as a stable night case study without snow ground cover. The measured HONO temporal profile was modeled for a 5-hour interval during sunset to determine the production and loss rates of HONO. From the MET data, clear sky conditions, low wind speeds and large $\Delta T_{9.5-1}$ were observed $3-4$ hours after sunset, indicating the formation of a stable nocturnal inversion, as previously presented in Figure 3.44. The temperature during the modeled period decreased from 22°C to 18°C while the relative humidity increased from 45% to 60%. This particular evening was chosen due to the quick approach to a steady $HONO/NO_2$ ratio early in the evening along with clear sky conditions, which allow for the modeling of HONO photolysis without additional complications due to cloud cover.

The initial HONO mixing ratio was set to the measured mixing ratio 4 hours prior to sunset, while the NO_2 mixing ratio was fit to match the observations. The $k_{\text{prod}}/k_{\text{dep}}$ ratio was set to 3.5%, based on the average observed $HONO/NO_2$ ratio overnight for this particular case study. The production and loss rates of HONO were subsequently optimized to obtain the greatest agreement between the model and observations using the calculated weighted averaged variance and mean error, described below. The weighted averaged variance reflects the quality of the model results and is defined as:

$$\text{Variance} = \sum_{i=1}^{n} \frac{w_i(y_i - \hat{y}_i)^2}{n} \tag{3.35}$$

where y_i is the i^{th} measured data point, $\hat{y}_i$ is the i^{th} model data point, n is the number of data points and w_i is the weight of the measured data point based on the measurement error defined by:

$$w_i = \frac{1}{\Delta y_i^2} \tag{3.36}$$

where Δy_i is the measurement error for the i^{th} data point. The error of the model was determined by calculating the mean squared error defined as:

$$\text{Mean Error} = \sqrt{\sum_{i=1}^{n} \frac{(y_i - \hat{y}_i)^2}{n}} \tag{3.37}$$

The measured and modeled temporal profiles of HONO, NO_2 and the HONO/NO_2 ratio are shown in Figure 3.57. Unexpectedly, in order to obtain agreement between the modeled and measured HONO, time dependent production and loss rate constants were required 1−4 hours before sunset. An initial first order HONO production rate constant of $k_{\text{prod,initial}} = (4.66 \pm 0.39) \times 10^{-6}\,\text{s}^{-1}$ followed by a linear increase at a rate of $k'_{\text{prod,rise}} = (3.98 \pm 0.33) \times 10^{-13}\,\text{s}^{-2}$ for 2.75 hours with a rate constant upper limit of $k_{\text{prod,upper}} = (2.45 \pm 0.20) \times 10^{-5}\,\text{s}^{-1}$ was determined to best match the measured HONO temporal profile. In other words, the model required an increasing HONO production rate constant for nearly 3 hours, after which the rate constant reached an upper limit and plateaued, as later shown in Figure 3.58. A variance of 0.108 and a mean error of 0.033 ppb were obtained for the model, implying very good agreement

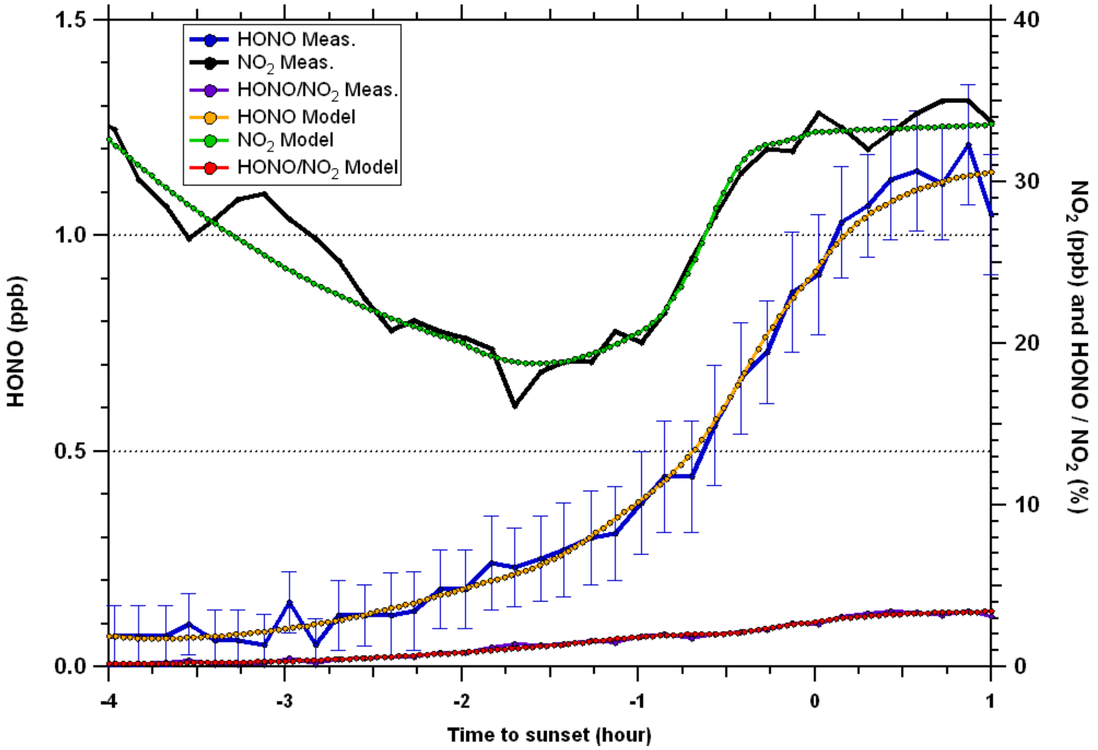

Figure 3.57: Comparison between modeled (yellow) and measured (blue) HONO during sunset on October 7th, 2011. The measured (black) and fit (green) NO_2 mixing ratios are shown, along with the modeled (red) and measured (purple) $HONO/NO_2$ ratios.

between the modeled and measured HONO. The rate constant errors were determined using the mean error and median HONO mixing ratio for the modeled period.

The temporal profiles of the production and loss rates (ppb/h) of HONO along with the production and deposition rate constants obtained from the model are shown in Figure 3.58. Four hours before sunset, the HONO production rate was ~0.5 ppb/h, steadily increasing to 2.8 ppb/h over a 3 hour period. The modeled system reaches a stable $HONO/NO_2$ ratio of 3.5% within ~1 hour after sunset, matching observations.

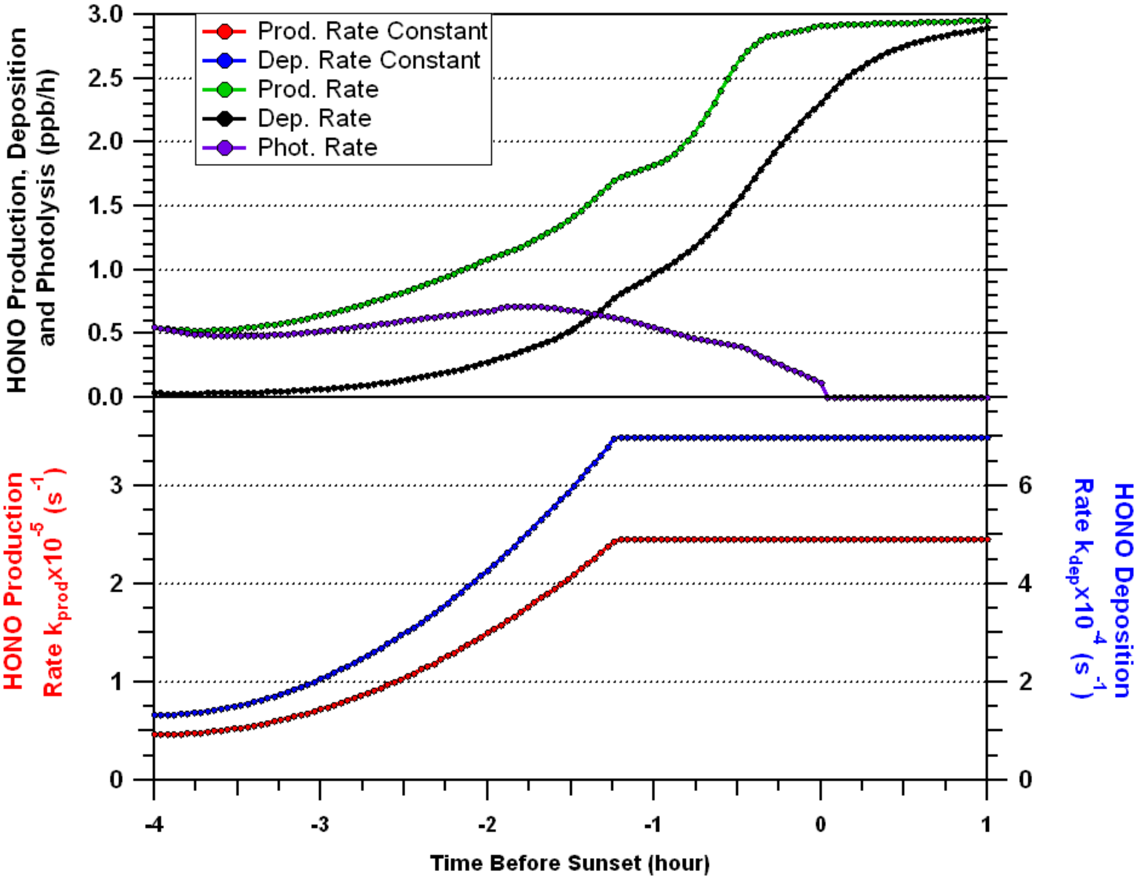

Figure 3.58: Model results for the October 7th case study, showing the varying first order production rate constant of HONO (red), first order loss rate constant of HONO (blue), HONO production rate (green), HONO deposition rate (black) and HONO photolysis rate (purple).

The deposition velocity of HONO (υ_{HONO}) can be determined using the following equation:

$$\upsilon_{\text{HONO}} = k_{\text{dep}} \times H \tag{3.38}$$

where H is the height of a well mixed boundary layer. Assuming a constant NBL height of 50 m, expected to form several hours after sunset for stable conditions, and an upper limit deposition rate constant value of $k_{\mathrm{dep}} = 6.99 \times 10^{-4}\,\mathrm{s}^{-1}$, the deposition velocity of HONO was calculated to be 3.5 cm/s. This result is substantially larger than the estimated deposition velocity of 0.077 cm/s made by (Stutz et al., 2002). It is, however, comparable to other published results ranging from $0.5 - 3$ cm/s (Harrison and Kitto, 1994; Harrison et al., 1996; Spindler et al., 1999; Li et al., 2012).

- **Sensitivity Analysis**

A sensitivity analysis was performed on the modeled case study production and loss rate constants of HONO by multiplying the previously obtained rate constants by factors of 0.2, 0.5, 0.8, 1.2, 2 and 5. The resulting HONO mixing ratios for the sensitivity analysis are shown in Figure 3.59, while calculations of the variance and mean error are shown in Table 3.13. The initial HONO concentration was observed to strongly dependent on the initial set kinetics. For very large initial rate constants such as 5.0 × Rate, the modeled HONO concentration abruptly increases, while for relatively slow kinetics, a decrease in the concentration is observed.

- **Modeled HONO Lifetimes**

The lifetime of HONO (τ_{HONO}) was calculated from the case study results with respect to deposition and photolysis, as shown in Figure 3.60. The HONO lifetime was 7 minutes at the beginning of the model run and was dominated by photolysis effects, while the deposition of HONO at this time was slow due to the slow initial production rate. The predominant sink of HONO transitions ~1.3 hours prior to sunset from photolysis to deposition, as the photolysis rate decreases with a descending SZA and the deposition rate increases. The net HONO lifetime was <25 minutes for

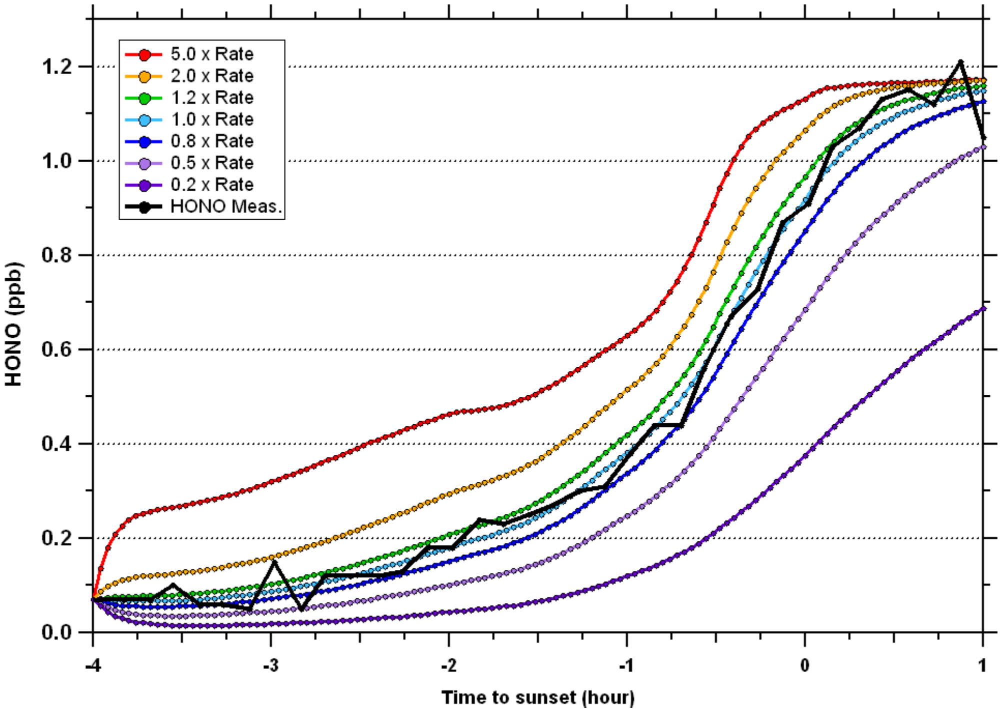

Figure 3.59: Sensitivity results for the October 7th case study showing the modeled HONO mixing ratio for multiple production rate constants (colored) along with the measured HONO (black line) mixing ratio.

the 5 hour modeled period, comparable to that of a previous study which determined the HONO lifetime to be ~10 minutes during solar noon (Sorgel et al., 2011a). No other nocturnal lifetimes of HONO have been reported in literature.

- **Time dependent Production and Loss Rate Constants**

In summary, the results pertaining to the time dependent rate constants were not foreseen and can be further investigated. Firstly, the first order production of HONO from NO_2 may not be the only source of HONO and a reservoir may be

Table 3.13: Sensitivity analysis including the variance and mean error for various HONO production and loss rate constants.

Factor	$k_{\text{prod,initial}}$ (s^{-1})	$k'_{\text{prod,rise}}$ (s^{-2})	$k_{\text{prod,upper}}$ (s^{-1})	Variance	Mean Error (ppb)
×0.2	9.32×10^{-7}	7.96×10^{-14}	4.89×10^{-6}	6.392	0.322
×0.5	2.33×10^{-6}	1.99×10^{-13}	1.22×10^{-5}	1.266	0.137
×0.8	3.73×10^{-6}	3.18×10^{-13}	1.96×10^{-5}	0.213	0.052
×1.0	4.66×10^{-6}	3.98×10^{-13}	2.45×10^{-5}	0.104	0.033
×1.2	5.59×10^{-6}	4.78×10^{-13}	2.94×10^{-5}	0.181	0.045
×2.0	9.32×10^{-6}	7.96×10^{-13}	4.89×10^{-5}	1.157	0.112
×5.0	2.33×10^{-5}	1.99×10^{-12}	1.22×10^{-4}	6.136	0.230

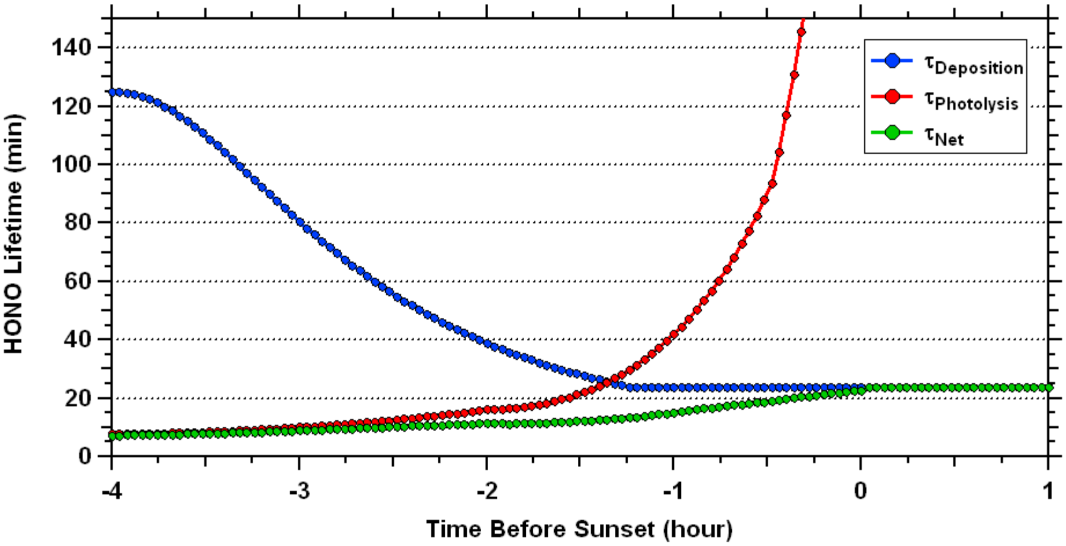

Figure 3.60: Calculations of the HONO lifetime with respect to deposition and photolysis during the October 7th, 2011 case study.

contributing to the rapid rise during the early evening. Secondly, a decreasing BL may also be responsible for the time dependent first order rate. However, the evolution of the NBL was previously studied and it was found that nocturnal inversions at urban locations generally formed ~2.5 hours after sunset, compared to rural sites where formation generally occurred 1 hour prior to sunset (Godowitch et al., 1985). The delayed formation of the inversion was attributed to the highly inhomogeneous thermal structure of urban environments. The MET data for the modeled case study, previously shown in Figure 3.44, exhibited wind speeds between 2−3 m/s and $\Delta T_{9.5-1}$ ~0.5 °C for the first 2 hours after sunset, indicating that a stable NBL was not present during the modeling period. After 22:00, wind speeds decreased to 0 m/s and $\Delta T_{9.5-1}$ was > 2°C, indicating the formation of a stable NBL at this time. Although a sharp rise in NO_2 was observed during the modeling period, it was also accompanied by a simultaneous decrease in O_3, leading to a constant level of odd oxygen and suggesting that the NO_2 concentration likely increased due to NO emissions instead of meteorological effects. $PM_{2.5}$ concentrations from the Ministry of the Environment North station were relatively constant from 16:00 to 21:00, with a large peak occurring between 23:00−0:00, concurring with the formation of a stable NBL during this time. From these observations, boundary layer height changes appear to have negligible effects on the presented model analysis.

The changing rate may be due to the availability of surface adsorbed water necessary for the heterogeneous HONO production reaction to occur. A few hours before sunset, surfaces are still heated by incoming solar radiation which presumably limits the surface capability to form mono-layers of water. As the sun sets and the surfaces cool, the temperature drops and relative humidity increases, leading to more favorable conditions for the condensation of water onto surfaces. Initially, water may be the limiting reagent in the heterogeneous formation of HONO, however, as water is continuously adsorbed onto surfaces, the reaction is expected to proceed at a faster rate. Therefore, the linear rate constant increase resulting from the model is potentially associated with a linear increase in water availability on surfaces. It is also possible that when insufficient surface adsorbed water is available, the surface becomes too acidic, significantly slowing down the HONO formation reaction.

From this hypothesis, the concept of an upper limit rate constant may be linked to the saturation of surface adsorbed water. Thus, during periods when surface adsorbed water is not a limiting factor in the heterogeneous formation of HONO, the formation is predicted to be governed by the upper limit rate constant. Since significant amounts of surface adsorbed water are expected in urban environments during periods with snow ground cover or after rainfall, this theory was investigated by selecting a night from the data set with significant snow ground cover and a stable NBL. As previously discussed, atmospherically stable nights were not frequently observed during the winter. In fact, only 2 out of the 40 most stable nights exhibited significant snow cover, from which only the evening of February 16, 2011 had observations collected during the sunset period.

Stable Night with Snow - Case Study on February 16, 2011

February 16, 2011 was chosen as an additional case study to test the hypothesis that surface water is the limiting reagent in the heterogeneous conversion of NO_2 to HONO. A mix of clear and cloudy overhead conditions was observed early in the evening, with low and decreasing wind speeds overnight, accompanied by the formation of a stable NBL ∼1.5 hours after sunset, determined from $\Delta T_{9.5-1}$ measurements. The temperature remained at 3°C and the relative humidity increased from 60% to 65 % during the modeled period.

The modeled photolysis of HONO for this case study was more elaborate due to the presence of clouds 2 to 4 hours prior to sunset. In order to account for the cloudy conditions, the percentage reduction of the incoming solar radiation was determined by comparing the downwelling short wavelength irradiance measurements from the EMOS station at York University during the cloudy period of the case study to the previous day with clear sky conditions. The radiation reduction was found to be ∼50% for the first two hours of the modeled period and was taken into account for the photolysis calculation. During the case study, 22 cm of snow ground cover were present and incorporated into the photolysis calculation by setting the surface albedo to 0.8, according to the recommendations from (Schwander et al., 1999) for fresh snow. An increase of approximately 96% is obtained for the photolysis rate constant when varying the albedo from 0.2 to 0.8, determined by the Tropospheric Ultraviolet and Visible (TUV) radiative transfer column model. The $k_{\mathrm{prod}}/k_{\mathrm{dep}}$ ratio was set to

4.6% for this case study, based on the average $HONO/NO_2$ ratio from the measured data in the evening.

The measurements and model results obtained using the previously determined rate constants are shown in Figure 3.61. The NO_2 mixing ratio was observed to increase from 30 to 55 ppb over a 5 hour period in the early evening, while the O_3 mixing ratio decreased from 10 to 0 ppb by sunset (not shown). The HONO mixing ratio was modeled using the upper limit rate constant ($k_{\mathrm{prod,upper}} = (2.45 \pm 0.20) \times 10^{-5}\,\mathrm{s}^{-1}$) determined from the previous October 7th case study, with a variance of 0.85 and a mean error of 0.11 ppb. As observed from the results, the upper limit rate constant captures the HONO temporal profile for the majority of the modeled period, but overestimates the HONO mixing ratio by ∼0.2 ppb for a 1.5 hour period ∼2 hours before sunset. A noticeable plateau can be observed in the modeled HONO temporal profile when using the upper rate limit, ∼2 hours prior to sunset, coinciding with a transition to clear sky conditions. The time dependent rate constant was also used to model HONO (variance of 0.81 and mean error of 0.10).

From Figure 3.61, the time dependent rate constant underestimates the HONO mixing ratio by ∼0.2 ppb for the first 1.5 hours of the model run, but captures the HONO concentration thereafter. Excellent agreement is obtained between the measured and modeled HONO 1.5 hours prior to sunset when both production rates are at the upper limit. It is important to note that the combined effect of snow ground cover and cloudy conditions greatly complicates the model, adding further uncertainties and assumptions. Therefore, the results obtained can only be used as

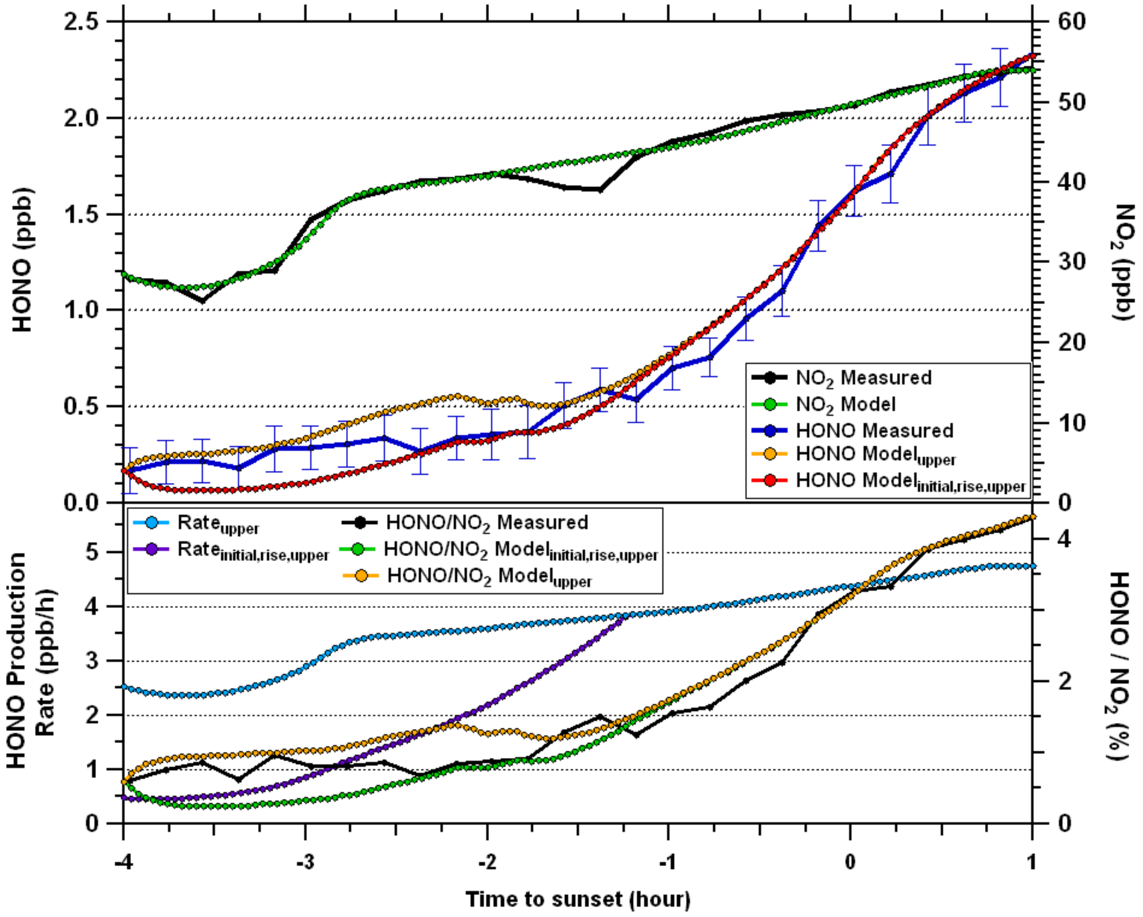

Figure 3.61: Upper panel: Modeled (yellow/red) and measured (blue) HONO along with measured (black) and fit (green) NO_2 mixing ratios during sunset on February 16, 2011. Lower panel: Modeled HONO production rates (blue/purple) along with measured (black) and modeled (yellow/green) HONO/NO_2 ratios. Modeled results were obtained using the previously determined upper limit and time dependent rate constants.

an estimate of the kinetics but may still provide insightful information.

As shown in the lower panel in Figure 3.61, the HONO production rate using the time dependent rate constant increased from 0.5 − 4 ppb/h over a 3 hour period, while the resulting production rate using the upper limit rate constant increased from 2.5 − 4 ppb/h. A production rate of HONO as high as 4.5 ppb h^{-1} was determined in the presence of 54 ppb of NO_2 for this case study.

These findings are not entirely conclusive in determining whether water availability is the limiting factor in the heterogeneous conversion of HONO to NO_2 early in the evening, however, a larger initial production rate constant is needed for this study as compared to the previous case study without snow. Thus, the time dependent rate constant was insufficient to capture the measured HONO in the beginning of the modeled period, suggesting that a snow surface may not hinder the reaction, assuming that the first-order heterogeneous production of HONO from NO_2 is the only source. It is important to note that additional sources and/or sinks of HONO may have been unaccounted for in the model, which could explain the observed levels of HONO. It is also possible that multiple HONO formation mechanisms occur simultaneously during this period, such as the photolysis of surface adsorbed HNO_3 (Zhou et al., 2011) and photolytic substrates that reduce NO_2 to HONO such as humic acid (Stemmler et al., 2006), organic films (Broske et al., 2003), and soot (Aubin and Abbatt, 2007). Furthermore, additional unforeseen factors variant among the two case studies could lead to distinct production rates and/or other uncertainties.

3.4.4.4 HONO Production and Loss Rates for Unstable Nights

Modeling studies were also performed to reproduce the observed formation of a steady-state of HONO during unstable nights. As expected, a first-order production of

HONO from NO_2 was unable to capture the steady-state profile of HONO. Although not shown, the observed $d[\mathrm{HONO}]/dt = 0$ behavior could be reproduced by a constant source of HONO that is independent of the NO_2 concentration and is balanced by HONO deposition. Alternatively, a steady-state of HONO could be established given that the HONO formation and deposition become inactive after a rapid rise of HONO during sunset, however, this scenario seems unlikely.

The source of HONO during unstable nights can be estimated based on reasonable assumptions. During the steady-state periods of HONO ($d[\mathrm{HONO}]/dt$=0), the sources (S_{HONO}) and losses of HONO (L_{HONO}) are equal. The only known significant loss of HONO during the nighttime is dry deposition as shown below, also expressed in terms of the deposition velocity of HONO, υ_{HONO}, and the height of the NBL, H:

$$S_{\mathrm{HONO}} = L_{\mathrm{HONO}} = k_{\mathrm{dep}}[\mathrm{HONO}] = \frac{\upsilon_{\mathrm{HONO}}[\mathrm{HONO}]}{H} \tag{3.39}$$

During unstable nights, atmospheric mixing is very efficient and large deposition velocities and NBL heights are expected. The production rate of HONO was estimated according to Equation 3.39, using the highest reported deposition velocity of HONO (3.0 ± 1.5 cm s^{-1}) (Harrison et al., 1996), an unstable NBL height of 250 ± 100 m, and the median HONO concentration during steady-state periods (0.7 ppb). As a result, the production rate of HONO during unstable nights was found to range from 0.11 − 0.76 ppb/h. These rates are significantly lower than the HONO production rates modeled during stable nights, which ranged from 0.5 − 5 ppb/h.

4 Conclusions and Future Work

4.1 Overall Conclusions

NO_3 and N_2O_5 at Saturna Island

Active-DOAS measurements of NO_3, NO_2 and O_3 were performed and levels of N_2O_5 were calculated at Saturna Island. The overnight median mixing ratios of NO_3, NO_2 and N_2O_5 were 10.2 ppt, 5.2 ppb and 76 ppt, respectively. Using the forward and reverse equilibrium rate constants for the reaction $NO_2 + NO_3 \rightleftharpoons N_2O_5$, the lifetimes of NO_3 and N_2O_5 with respect to their equilibrium reaction at Saturna were calculated to be 6 and 53 seconds, respectively. The lifetime of NO_3 was calculated for non steady-state conditions, arising due to the high levels of NO_2 encountered in the study, possibly inhibiting the approach to steady-state. The lifetimes were calculated based on the rate of change of NO_3 and N_2O_5 with time, and were compared to calculated steady-state lifetimes of NO_3. Minor differences were observed between the steady-state and non steady-state assumptions for the NO_3 lifetimes, with median values ranging from $1 - 4$ minutes. The high turnover times of NO_3 and N_2O_5 along with the similarities between the steady-state and non steady-state lifetimes of NO_3

validate the calculation of N_2O_5 by showing that the NO_2-NO_3-N_2O_5 system is in equilibrium for the warm temperatures experienced in the study.

Assuming a combined pool of $NO_3 + N_2O_5$, the direct (via NO_3, k_x) and indirect (via N_2O_5, k_y) rate loss constants of NO_3 from the combined nocturnal reservoir were determined as a function of time of night. Direct loses of NO_3 dominated in the early evening with a maximum rate loss coefficient of $k_\mathrm{x} = 0.021\ \mathrm{s}^{-1}$ and decreased throughout the night, consistent with a overnight decline of VOCs and/or NO in the MBL. The indirect losses via N_2O_5 were low early in the evening and dominated shortly after midnight with a maximum rate loss coefficient of $k_\mathrm{y} = 1.6 \times 10^{-3}\,\mathrm{s}^{-1}$, consistent with the loss of N_2O_5 via heterogeneous reactions on deliquesced aerosols with increasing relative humidity overnight. The direct loss of NO_3 was found to comprise $50.4 \pm 13.2\%$ of the total sinks from the $NO_3 + N_2O_5$ pool, while the loss via N_2O_5 accounted for $49.6 \pm 9.6\%$ of the total overnight loss.

Temporally integrated overnight N_2O_5 mixing ratios were calculated to range from $0.038 - 0.275$ ppb $\cdot$ night and were correlated with the 1-hour maximum O_3 concentration measured at the following day at stations within the LFV. The analysis was performed for days which exhibited signs of a significant sea breeze and the correlation was extended to two days following the overnight N_2O_5 accumulation calculation. Statistically significant positive correlations between the overnight integrated N_2O_5 concentration at Saturna and 1-hour maximum O_3 concentration were observed only on the two days following the accumulation. The average peak O_3 enhancement on Day 0.5 was $\mathrm{d}O_3/\mathrm{d}\int[N_2O_5]\mathrm{d}t = 30.3 \pm 7.7\,\mathrm{ppb}\,O_3 \times\ \mathrm{ppb}\,{N_2O_5}^{-1}\,\mathrm{night}^{-1}$, corresponding to a increase in peak ozone of +1.1 ppb to +8.3 ppb based on the range of the overnight N_2O_5 integral. Spatially the highest correlation was seen in the eastern side of the valley on Day 1 while higher correlations were subsequently observed in the western side of the valley on Day 2, perhaps associated with downward mixing of O_3 in the residual layer.

HONO and NO_2 at Saturna Island

HONO was also measured at Saturna Island using active-DOAS. The data set is the first reported measurements of HONO in a polluted MBL and offer a unique environment to study the formation of HONO in a truly aqueous environment. The temporal profile of HONO over the ocean showed the rapid formation of a steady-state which persisted throughout the night until sunrise. During the steady-state period, $d[\mathrm{HONO}]/dt \approx 0$, HONO was independent of the air mass source and the NO_2 concentration, leading to a HONO formation which was zero-order with respect to NO_2. The median HONO/NO_2 ratio during the steady-state period was 0.16 with ratios >1.0 observed late in the night. These observations suggest that a reservoir of HONO and/or nitrogen precursors exists and/or a dynamic equilibrium takes place where deposited HONO is reversibly lost to the surface.

Potential reservoirs of HONO such as the sea surface micro-layer, aerosols, or the air-sea surface interface were explored. Based on reasonable assumptions from previous studies about the nature and properties of each potential reservoir, it was concluded that the air-sea surface interface was the most likely candidate for a reservoir of HONO which can support the steady-state HONO mixing ratios at Saturna Island. A conceptual model was presented for HONO formation in aqueous systems encompassing the observations made at Saturna Island and with the aid of observations from literature. The model assumes a reservoir of N(IV) species concentrated on the surface of the ocean in a few mono-layers which react to produce HNO_3 (N(V)) and HONO (N(III)). HNO_3 is highly soluble and diffuses into the underlying SML and bulk water. HONO produced at the surface remains in a dynamic equilibrium balanced by deposition back to the reservoir. A correlation between temperature and HONO was observed during the steady-state period which is consistent with the enthalpy for release of HONO from the surface with $\Delta H_{\mathrm{vap,SNL}} = 58.1 \pm 5.8\,\mathrm{kJ\,mol^{-1}}$; relatively close to HONO vaporization from pure water $\Delta H_{\mathrm{vap}} = 40.7 \pm 1.2\,\mathrm{kJ\,mol^{-1}}$.

The conceptual model is predicted to be representative of all aqueous surfaces in polluted environments, potentially including surfaces with snow ground cover. The HONO formation mechanism may continue during the daytime with a first-order dependence on NO_2. It is predicted that significant amounts of OH-radicals will be generated near the surface through photolysis of HONO, while a depletion of odd oxygen close to the surface will simultaneously occur.

NO_3 at York University

Measurements of NO_3 and NO_2 were made in the nocturnal urban atmosphere at York University, Toronto, with overnight median mixing ratios of 6.0 ppt and 16.6 ppb, respectively. The overnight NO_3 mixing ratio was highly variable and generally exhibited multiple short time-scale peaks, presumably due to NO_x emissions. In addition, a positive correlation between NO_3 and temperature was observed, likely due to the temperature dependence of N_2O_5. Furthermore, the overnight NO_3 temporal profile was analyzed for atmospherically stable and unstable conditions. During stable nights, levels remained below detection limit due to the rapid depletion O_3 early in the evening, while for unstable nights, the NO_3 concentration was highly variable and production of N_2O_5 and HNO_3 was expected to occur.

The steady-state and non steady-state assumption lifetimes of NO_3 were calculated for two case studies with distinct overnight temperatures. The warmer case study indicated only minor differences between the two NO_3 lifetimes, which ranged from $0.5 - 3.5$ minutes. For the colder case study, significant differences were observed in the first half of the night, with non steady-state lifetimes ranging from $0.5 - 2$ minutes and steady-state lifetimes ranging from $1.5 - 4$ minutes. The lifetimes during the second half of the night were coincident, ranging from $0.5 - 4$ minutes. The observed differences between the steady-state and non steady-state assumption lifetimes can be attributed to the increased lifetime of N_2O_5 during colder temperatures, which slows the NO_2-NO_3-N_2O_5 system approach to equilibrium and steady-state. This emphasizes the fact that the steady-state assumption is not always valid when calculating lifetimes of NO_3, and that non-steady state lifetimes of NO_3 should be used when appropriate.

HONO and NO_2 at York University

Measurements of HONO and NO_2 were collected at York University, Toronto over a 1-year period. The overnight median mixing ratios of HONO and NO_2 were 1.02 ppb and 15.76 ppb, respectively and the median HONO/NO_2 ratio was 6.32% with a overnight range of $1 - 36\%$. No significant correlation was observed between nighttime HONO, NO_2, and the HONO/NO_2 ratio with relative humidity, temperature, and wind direction. However, a strong correlation with wind speed and $\Delta T_{9.5-1}$ was identified for the three parameters. During nights with high winds speeds and low $\Delta T_{9.5-1}$ values, indicative of a well mixed NBL, the HONO and NO_2 mixing ratios were relatively low. In turn, for nights with low winds speeds and high $\Delta T_{9.5-1}$ values, indicative of a low and stable nocturnal inversion, the HONO and NO_2 mixing ratios were measurably higher.

During atmospherically stable nights, the concentration of HONO was observed to strongly correlate with NO_2, where $d([\text{HONO}]/[\text{NO}_2])/dt \approx 0$. For the 39 most stable nights, the NO_2 concentration increased from a median mixing ratio of 15 ppb to 30 ppb, 5 hours after sunset. The HONO concentration closely followed the NO_2 concentration with median nighttime levels of 1.5 ppb. The HONO/NO_2 ratio rapidly rose to $\sim 4 - 6\%$ during sunset and remained stable for the duration of the night. These nights are also characterized by warmer temperatures, occurring more frequently on summer nights, and by a frequently observed titration of O_3 with the formation of a low nocturnal inversion. The relative humidity on stable nights was generally low during sunset (median RH = 40%), increasing to 70% approximately 6 hours after sunset.

During atmospherically unstable nights, steady-states of HONO were observed with $d[\text{HONO}]/dt \approx 0$ and HONO mixing ratios independent of NO_2, as observed at Saturna Island. During these types of nights, the HONO mixing ratio rapidly increased during sunset and remained constant throughout the night with a median of ~0.7 ppb for the 41 most stable nights. The NO_2 mixing ratio was highest early in the evening (median $NO_2 = 11$ ppb) and slowly decreased overnight while the median HONO/NO_2 ratio increased from 5% at sunset to 10% by the end of the night. These nights generally occurred during the wintertime and the overnight O_3 mixing ratio remained at background levels, $20 - 30$ ppb. The relative humidity on these nights was ~70% at sunset, remaining high overnight. According to the level of atmospheric stability, a smooth transition was observed between the steady-state HONO nights and the NO_2−HONO correlated nights.

The conceptual model presented to describe steady-states of HONO at Saturna Island can be extended to explain the observed steady-states of HONO at York University. Steady-states of HONO were observed in both atmospheres during unstable conditions. An abundance of surface water due to the high relative humidity during unstable nights at York University may mimic the ocean surface at Saturna, supporting steady-states of HONO over terrestrial environments. The atmospheric stability and persistent aqueous surface may be the key feature linking the steady-state observations from the two studies.

The conceptual model cannot be extended to explain HONO observations during stable nights, where the HONO and NO_2 concentrations were strongly correlated. The model would only predict a correlation between the HONO and NO_2 concentrations given a continuous depletion of the surface reservoir. However, it is important to note that during stable conditions, the relative humidity was generally low at the beginning of the night, potentially inhibiting the formation of a HONO reservoir, in contrast to the observations made for unstable nights at York University. Thus, for stable conditions, the HONO reservoir is not expected to form due to insufficient surface water, leading to a highly acidic surface from the formation of HNO_3 and to the release of HONO directly into the gas phase. This proposal is in accordance to the results shown in Figure 3.46, where a leveling off was observed for HONO once the relative humidity reached $\sim$75% during stable nights. This suggests that with enough surface water, the reservoir of HONO is able to form during the night, supporting HONO steady-states. In order to verify these hypotheses, measurements of surface acidity and water coverage are required.

The HONO and NO_2 mixing ratios were modeled for stable night conditions during sunset. During stable nights, it was assumed that a balance is achieved between the heterogeneous production of HONO from NO_2, with a first-order dependence, and the deposition of HONO where $k_{\text{prod}}/k_{\text{dep}} = 0.04$. Based on the timescale required to reach a steady HONO/NO_2 ratio, typically established within 1.5 hours during sunset, it was determined that a HONO production $\geq$3.0 ppb h^{-1} was required in the presence of 25 ppb of NO_2 in the early evening.

Modeling studies for a stable night case study required a time dependent rate of HONO production in order to match the observations. The production rate was determined to increase from $0.5 - 3.0$ ppb h^{-1} over a 4 hour period prior to sunset. The varying production rate was attributed to surface water acting as a limiting factor in the heterogeneous conversion of NO_2 to HONO. This hypothesis was tested for another stable night, this time with 22 cm of snow ground cover. Agreement was obtained when using the upper limit of the HONO production rate constant, $k_{\mathrm{prod,upper}} = 2.45(\pm 0.20) \times 10^{-5}\,\mathrm{s}^{-1}$, during the initial hour of the modeled period and the last 2.5 hours. However, the upper limit rate constant overestimated the HONO mixing ratio by ∼0.2 ppb for a ∼1.5 hour period. Modeled results were also produced using the time dependent rate constant, which was found to underestimate the HONO mixing ratio by ∼0.2 ppb for the initial 1.5 hours. A production rate of HONO as high as 4.5 ppb h^{-1} was determined in the presence of 54 ppb of NO_2 for the case study. In addition, HONO production rates between $0.11 - 0.76$ ppb/h were estimated for unstable nights.

4.2 Future Work

An extension to the presented work may include vertical profile measurements of HONO using active-DOAS, by utilizing two retro-reflectors at different heights. This would allow for the determination of the vertical variability of the concentration of HONO. Sharp gradients of HONO may be observed when above the nocturnal inversion and significant differences may be observed between the HONO concentration at ground level and at a height of 15 meters, the height of the beam at York University.

For the presented analysis, concentrations of N_2O_5 were experimentally unavailable and were instead calculated based on the temperature dependent equilibrium constant. However, it was uncertain whether the equilibrium assumption for the NO_2-NO_3-N_2O_5 system was valid at all times. In order to explore possible differences between steady-state and non steady-state assumption lifetimes under non equilibrium conditions, simultaneous measurements of NO_2, NO_3, N_2O_5 and O_3 must be performed. In conjunction with techniques capable of quantifying NO_2 and O_3, cavity ring-down spectroscopy can be used to measure NO_3 and N_2O_5 simultaneously.

The ground surface has been shown to be a important factor in the heterogeneous conversion of NO_2 to HONO. Improvements to the presented work may include better quantification of the ambient ground surfaces during measurement periods in order to verify whether a dry or aqueous surface affects the levels of HONO. In addition, experimental confirmation for the presence of a nitrogen reservoir at the air-water interface is required to support the conceptual model proposed in order to explain steady-state observations of HONO.

Measurements of HONO during the daytime would be useful to investigate the daytime HONO production, providing a link to the nocturnal heterogeneous formation of HONO. In order to collect daytime HONO data, the current active-DOAS instrument would require modifications, allowing one to collect alternating spectra of measured lamp and stray light (without the lamp); necessary for the correction of strong daytime solar features.

The modeling studies could also be extended to account for the daytime period in order to determine whether the ratio between HONO production and loss rates is constant and to identify the conditions or limits of the time dependent rate constants. Future work can also be directed towards the determination of an underlying mechanism which simultaneously explains the HONO behavior during stable and unstable nights.

A DOASIS JScripts

A.1 Automated Offset and Dark Current Correction Jscript

This JScript will automatically subtract offset and dark current spectrum from ambient spectra. The uncorrected ambient spectra must be saved in sequence.

```
import DoasCore.Math;
import DoasCore.IO;
import DoasCore.Device;
import DoasCore.Script;
import DoasCore.HMI;

var uiwWriter : UserInterfaceWriter = new UserInterfaceWriter();

var filenumber;

var mFile;

var MeasSpec : ISpectrum = Specbar.GetSpectrum("Measurement Spectrum");
//creates Spectrum object
MeasSpec.Name = "Measurement Spectrum";
MeasSpec.MinChannel = 1;
MeasSpec.MaxChannel = 2048;

var MeasFile : AutoFileName = new AutoFileName();
//creates File object
MeasFile.BasePath = "C:\\Documents and Settings\\RawSpectraFolder\\";
//specifies folder containing raw spectra
MeasFile.FilesPerFolder = 300;
//sets number of files per folder
MeasFile.Prefix = "RawSpec";
MeasFile.Suffix = ".sp2";
```

```
MeasFile.NumberOfDigits = 5;
//identify name of raw spectra to be corrected
var Offset: ISpectrum = Specbar.GetSpectrum("Offset");
var DC: ISpectrum = Specbar.GetSpectrum("Darkcurrent");

Offset.Open("C:\\Documents and Settings\\Sample\\Offset.sp2");
DC.Open("C:\\Documents and Settings\\Sample\\DarkCurrent.sp2");

var CorrFile : AutoFileName = new AutoFileName();
CorrFile.BasePath = "C:\\Documents and Settings\\Sample\\
        AmbientSpecCorr\\";
CorrFile.FilesPerFolder = 300;
CorrFile.Prefix = "CorrSpec";
CorrFile.Suffix = ".sp2";
CorrFile.NumberOfDigits = 5;
//name of outputted corrected ambient spectra
function extract_filenumber(filename)
//function which extracts the filenumber
{
        var iLastIndex = filename.lastIndexOf("\\");
        if(iLastIndex+1 >=0)
        {
                filenumber = filename.substr(iLastIndex +1,8);
                return(filenumber);
        }
        return(filenumber);
};

function innerLoop()
{
        while(MeasFile.Open(MeasSpec))
//begins a loop which opens all the MeasSpec
        {
                mFile=0;
                if(!Script.StopAllScripts)
                Specbar.CurrentSpectrum = MeasSpec;
//makes sure that the MeasSpec is in the active window sheet

                SpecMath.Sub(MeasSpec, Offset);
                SpecMath.Sub(MeasSpec, DC);
                CorrFile.Save(MeasSpec);
//saves the corrected MeasSpec in a folder named "Corrected"
        }
```

```
        mFile++;
}

function main()
{
        uiwWriter.Status = "Opening:Offset Spec, Darkcurrent and
                Measurement Spec";
//writes into the output window
        if(Offset.Open("C:\\Documents and Settings\\SampleSpectra\\
                Offset.sp2")==false)
//opens the offset spectrum and tells you if anything went wrong
        System.Console.WriteLine("Error while trying to open offset
                spectrum");

        if(DC.Open("C:\\Documents and Settings\\SampleSpectra\\
                DarkCurrent.sp2")==false)
//opens the darkcurrent spectrum and tells you if anything went wrong
        System.Console.WriteLine("Error while trying to open dark
                current spectrum");

        MeasFile.CurrentFileNumber = 0;
        CorrFile.CurrentFileNumber = MeasFile.CurrentFileNumber;

        System.Console.WriteLine(MeasFile.CurrentSubFolder);
        mFile=0;

        while(mFile<=100)
        {
                innerLoop();
                System.Console.Write("Missing filenumber ");
                System.Console.WriteLine(MeasFile.CurrentFileNumber);
                MeasFile.CurrentFileNumber++;
                CorrFile.CurrentFileNumber = MeasFile.CurrentFileNumber;
        }
}
main();
```

A.2 Automated Fits and Output JScript

This JScript will automatically perform fits using a previously determined fit scenario. The JScript will output the column densities for the first species listed in the fit scenario. The corrected ambient spectra which are being fit must be saved in sequence.

```
import System.Threading;
import DoasCore;
import DoasCore.Spectra;
import DoasCore.Math;
import DoasCore.IO;
import DoasCore.Device;
import DoasCore.Script;
import DoasCore.HMI;

var uiwWriter : UserInterfaceWriter = new UserInterfaceWriter();

var filenumber;

var mFile;

var MeasSpec : ISpectrum = Specbar.GetSpectrum("Measurement Spectrum");
//creates Spectrum object
MeasSpec.Name = "Measurement Spectrum";
MeasSpec.MinChannel = 1;
MeasSpec.MaxChannel = 2048;

var MeasFile : AutoFileName = new AutoFileName();
//creates File object
MeasFile.BasePath = "C:\\Documents and Settings\\Sample\\
        SequenceSpecFolder\\";
//specifies folder containing spectra
MeasFile.FilesPerFolder = 300;
//sets number of files per folder
MeasFile.Prefix = "CorrSpec";
MeasFile.Suffix = ".sp2";
MeasFile.NumberOfDigits = 5;


var CorrFile : AutoFileName = new AutoFileName();

function extract_filenumber(filename)
//function which extracts the filenumber
{
        var iLastIndex = filename.lastIndexOf("\\");
        if(iLastIndex+1 >=0)
```

```
        {
                filenumber = filename.substr(iLastIndex +1,8);
                return(filenumber);
        }
        return(filenumber);
};

function innerLoop()
{
        while(MeasFile.Open(MeasSpec))
//begins a loop which opens all the MeasSpec
        {
                mFile=0;
                if(!Script.StopAllScripts)
                Specbar.CurrentSpectrum = MeasSpec;
//makes sure that the MeasSpec is in the active window sheet
// open an empty spectrum sheet with the title "FitResult"
// in which the fit result will be shown later
                var ResultSpec : ISpectrum = Specbar.GetSpectrum
                        ("FitResult");
                var fitfile = "C:\\Documents and Settings\\Sample\\
                        SampleFitScenario.fs";
// open fit scenario
                var fit:DoasFit = new DoasFit;
                fit=DoasFit.Open(fitfile);
// execute the fit, DoFit returns "true" if the fit was succesfull
                if(fit.DoFit(MeasSpec))
                {
// display the fit result windows in the spectrum "ResultSpec"
                        fit.PrepareFitResultSpectrum(ResultSpec);
// display the fit results an the active spectrum sheet
                        Specbar.CurrentSpectrum = ResultSpec;
// display the fit coefficient of the first reference spectrum
// write fit results into file
                        var Data = ("Fit Coefficient:
                        "+fit.ReferencesInfo[0].FitCoefficient+"
                                Fit Coefficient Error:
                                "+fit.ReferencesInfo[0].
                                FitCoefficientError);
                        var textfile
// create an object which enables to create a textfile
                        var dispFileSystem = new ActiveXObject
                                ("Scripting.FileSystemObject");
```

```
// provide access to the text file "C:\\SpeciesFitOutput.dat"
                        textfile = dispFileSystem.OpenTextFile("C:\\
                                Documents and Settings\\Sample\\
                                SpeciesFitOutput.dat",8,true);
                        textfile.WriteLine(Data);
                        textfile.Close();
                }
                else
                {
                        System.Console.WriteLine("Error while fitting!");
                }

                CorrFile.Save(MeasSpec);
//saves the corrected MeasSpec in a folder named "Corrected"
        }
        mFile++;
}
        function main()
{
        MeasFile.CurrentFileNumber = 0;
        CorrFile.CurrentFileNumber =          MeasFile.CurrentFileNumber;
        System.Console.WriteLine(MeasFile.CurrentSubFolder);

        mFile=0;

        while(mFile<=100)
        {
                innerLoop();
                System.Console.Write("Missing filenumber "):
                System.Console.WriteLine(MeasFile.CurrentFileNumber);
                MeasFile.CurrentFileNumber++;
                CorrFile.CurrentFileNumber = MeasFile.CurrentFileNumber;
        }
}
main();
```

Bibliography

Acker, K., Spindler, G., and Brüggemann, E.: Nitrous and nitric acid measurements during the INTERCOMP2000 campaign in Melpitz, Atmospheric Environment, 38, 6497 – 6505, 2004.

Acker, K., Mfller, D., Auel, R., Wieprecht, W., and Kalag, D.: Concentrations of nitrous acid, nitric acid, nitrite and nitrate in the gas and aerosol phase at a site in the emission zone during ESCOMPTE 2001 experiment, Atmospheric Environment, 74, 507–524, 2005.

Alicke, B.: The role of nitrous acid in the boundary layer, PhD Thesis, University of Heidelberg, Heidelberg, 2000.

Alicke, B., Hebestreit, K., Stutz, J., and Platt, U.: Iodine oxide in the marine boundary layer, Nature, 397, 572–573, 1999.

Alicke, B., Platt, U., and Stutz, J.: Impact of nitrous acid photolysis on the total hydroxyl radical budget during the Limitation of Oxidant Production/Pianura Padana Produzione di Ozono study in Milan, Journal of Geophysical Research: Atmospheres, 107, LOP 9–1–LOP 9–17, 2002.

Alicke, B., Geyer, A., Hofzumahaus, A., Holland, F., Konrad, S., Ptz, H. W., Schfer, J., Stutz, J., Volz-Thomas, A., and Platt, U.: OH formation by HONO photolysis during the BERLIOZ experiment, Journal of Geophysical Research: Atmospheres, 108, PHO 3–1–PHO 3–17, 2003.

Allan, B., Plane, J., and McFiggans, G.: Observations of OIO in the remote marine boundary layer, Geophysical research letters, 28, 1945–1948, 2001.

Allan, B. J., McFiggans, G., Plane, J. M. C., Coe, H., and McFadyen, G. G.: The nitrate radical in the remote marine boundary layer, Journal of Geophysical Research: Atmospheres, 105, 24 191–24 204, 2000.

Ambrose, J. L., Mao, H., Mayne, H. R., Stutz, J., Talbot, R., and Sive, B. C.: Nighttime nitrate radical chemistry at Appledore Island, Maine during the 2004 International Consortium for Atmospheric Research on Transport and Transformation, Journal of Geophysical Research: Atmospheres, 112, 2007.

Amedro, D., Parker, A. E., Schoemaecker, C., and Fittschen, C.: Direct observation of OH radicals after 565nm multi-photon excitation of NO_2 in the presence of H_2O, Chemical Physics Letters, 513, 12–16, 2011.

Ammann, M., Kalberer, M., Jost, D., Tobler, L., Rössler, E., Piguet, D., Gäggeler, H., and Baltensperger, U.: Heterogeneous production of nitrous acid on soot in polluted air masses, Nature, 395, 157–160, 1998.

Andreae, M. O. and Raemdonck, H.: Dimethyl sulfide in the surface ocean and the marine atmosphere: a global view, Science, 221, 744–747, 1983.

Andres-Hernandez, M., Notholt, J., Hjorth, J., and Schrems, O.: A DOAS study on the origin of nitrous acid at urban and non-urban sites, Atmospheric Environment, 30, 175–180, 1996.

Anlauf, K., Li, S.-M., Leaitch, R., Brook, J., Hayden, K., Toom-Sauntry, D., and Wiebe, A.: Ionic composition and size characteristics of particles in the Lower Fraser Valley: Pacific 2001 field study, Atmospheric Environment, 40, 2662 – 2675, 2006.

Atkinson, R.: Gas-phase tropospheric chemistry of volatile organic compounds: 1. Alkanes and alkenes, Journal of Physical and Chemical Reference Data, 26, 215–290, 1997.

Atkinson, R., Winer, A., and Pitts Jr, J.: Estimation of night-time N_2O_5 concentrations from ambient NO_2 and NO_3 radical concentrations and the role of N_2O_5 in night-time chemistry, Atmospheric Environment, 20(2), 331–339, 1986.

Atkinson, R., Baulch, D., Cox, R., Crowley, J., Hampson, R., Hynes, R., Jenkin, M., Rossi, M., and Troe, J.: Evaluated kinetic and photochemical data for atmospheric chemistry: Volume I–gas phase reactions of O_x, HO_x, NO_x and SO_x species, Atmos. chem. phys, 4, 1461–1738, 2004.

Atkinson, R., Baulch, D. L., Cox, R. A., Crowley, J. N., Hampson, R. F., Hynes, R. G., Jenkin, M. E., Rossi, M. J., Troe, J., and Subcommittee, I.: Evaluated kinetic and photochemical data for atmospheric chemistry: Volume II – gas phase reactions of organic species, Atmospheric Chemistry and Physics, 6, 3625–4055, 2006.

Aubin, D. G. and Abbatt, J. P.: Interaction of NO_2 with hydrocarbon soot: Focus on HONO yield, surface modification, and mechanism, The Journal of Physical Chemistry A, 111, 6263–6273, 2007.

Becker, K. H., Kleffmann, J., Kurtenbach, R., and Wiesen, P.: Solubility of nitrous acid (HONO) in sulfuric acid solutions, The Journal of Physical Chemistry, 100, 14 984–14 990, 1996.

Beine, H. J., Amoroso, A., Domine, F., King, M. D., Nardino, M., Ianniello, A., and France, J. L.: Surprisingly small HONO emissions from snow surfaces at Browning Pass, Antarctica, Atmospheric Chemistry and Physics, 6, 2569–2580, 2006.

Bell, M. L., Davis, D. L., and Fletcher, T.: A retrospective assessment of mortality from the London smog episode of 1952: the role of influenza and pollution., Environmental Health Perspectives, 112, 6, 2004a.

Bell, M. L., McDermott, A., Zeger, S. L., Samet, J. M., and Dominici, F.: Ozone and short-term mortality in 95 US urban communities, 1987-2000, the Journal of the American Medical Association, 292(19), 2372–2378, 2004b.

Bongartz, A., Kames, J., Schurath, U., George, C., Mirabel, P., and Ponche, J.: Experimental determination of HONO mass accommodation coefficients using two different techniques, Journal of Atmospheric Chemistry, 18, 149–169, 1994.

Brook, J. R., Strawbridge, K., Snyder, B., Boudries, H., Worsnop, D., Sharma, S., Anlauf, K., Lu, G., and Hayden, K.: Towards an understanding of the fine particle variations in the LFV: integration of chemical, physical and meteorological observations, Atmospheric Environment, 38, 5775 – 5788, 2004.

Broske, R., Kleffmann, J., and Wiesen, P.: Heterogeneous conversion of NO_2 on secondary organic aerosol surfaces: A possible source of nitrous acid (HONO) in the atmosphere?, Atmospheric Chemistry and Physics, 3(3), 469–474, 2003.

Brown, S., Dubé, W., Osthoff, H., Wolfe, D., Angevine, W., and Ravishankara, A.: High resolution vertical distributions of NO_3 and N_2O_5 through the nocturnal boundary layer, Atmos. Chem. Phys, 7, 139–149, 2007.

Brown, S. S., Stark, H., and Ravishankara, A. R.: Applicability of the steady state approximation to the interpretation of atmospheric observations of NO_3 and N_2O_5, Journal of Geophysical Research: Atmospheres, 108, 2003a.

Brown, S. S., Stark, H., Ryerson, T. B., Williams, E. J., Nicks, D. K., Trainer, M., Fehsenfeld, F. C., and Ravishankara, A. R.: Nitrogen oxides in the nocturnal boundary layer: Simultaneous in situ measurements of NO_3, N_2O_5, NO_2, NO, and O_3, Journal of Geophysical Research: Atmospheres, 108, 2003b.

Brown, S. S., Dibb, J. E., Stark, H., Aldener, M., Vozella, M., Whitlow, S., Williams, E. J., Lerner, B. M., Jakoubek, R., Middlebrook, A. M., DeGouw, J. A., Warneke, C., Goldan, P. D., Kuster, W. C., Angevine, W. M., Sueper, D. T., Quinn, P. K., Bates, T. S., Meagher, J. F., Fehsenfeld, F. C., and Ravishankara, A. R.: Nighttime removal of NO_x in the summer marine boundary layer, Geophysical Research Letters, 31, 2004.

Brown, S. S., Dub, W. P., Karamchandani, P., Yarwood, G., Peischl, J., Ryerson, T. B., Neuman, J. A., Nowak, J. B., Holloway, J. S., Washenfelder, R. A., Brock, C. A., Frost, G. J., Trainer, M., Parrish, D. D., Fehsenfeld, F. C., and Ravishankara, A. R.: Effects of NO_x control and plume mixing on nighttime chemical processing of plumes from coal-fired power plants, Journal of Geophysical Research, 117, D07 304, 2012.

Calvert, J., Yarwood, G., and Dunker, A.: An evaluation of the mechanism of nitrous acid formation in the urban atmosphere, Research on Chemical Intermediates, 20, 463–502, 1994.

Calvert, J. G. and Stockwell, W. R.: Deviations from the O_3 - NO - NO_2 photostationary state in tropospheric, Canadian Journal of Chemistry, 61, 983–992, 1983.

Carroll, M. A. and Thompson, A. M.: NO_x in the non-urban troposphere, in Progress and Problems in Atmospheric Chemistry, Chapter 7, World Scientific, Singapore, 1995, 1995.

Chameides, W. L. and Stelson, A. W.: Aqueous-Phase Chemical Processes in Deliquescent Seasalt Aerosols, Berichte der Bunsengesellschaft fr physikalische Chemie, 96, 461–470, 1992.

Chan, W. H., Nordstrom, R. J., Calvert, J. G., and Shaw, J. H.: Kinetic study of nitrous acid formation and decay reactions in gaseous mixtures of nitrous acid, nitrogen oxide (NO), nitrogen oxide (NO_2), water, and nitrogen, Environmental Science & Technology, 10, 674–682, 1976.

Chance, K. V. and Spurr, R. J.: Ring effect studies: Rayleigh scattering, including molecular parameters for rotational Raman scattering, and the Fraunhofer spectrum, Applied Optics, 36, 5224–5230, 1997.

Charlson, R. J., Lovelock, J. E., Andreae, M. O., Warren, S. G., et al.: Oceanic phytoplankton, atmospheric sulphur, cloud albedo and climate, Nature, 326, 655–661, 1987.

Cheung, J., Li, Y., Boniface, J., Shi, Q., Davidovits, P., Worsnop, D., Jayne, J., and Kolb, C.: Heterogeneous interactions of NO_2 with aqueous surfaces, The Journal of Physical Chemistry A, 104, 2655–2662, 2000.

Coheur, P.-F., Fally, S., Carleer, M., Clerbaux, C., Colin, R., Jenouvrier, A., Mrienne, M.-F., Hermans, C., and Vandaele, A. C.: New water vapor line parameters in the 26000-13000 cm^{-1} region, Journal of Quantitative Spectroscopy and Radiative Transfer, 74, 493 – 510, 2002.

Crowley, J., Thieser, J., Tang, M., Schuster, G., Bozem, H., Hosaynali Beygi, Z., Fischer, H., Diesch, J., Drewnick, F., Borrmann, S., et al.: Variable lifetimes and loss mechanisms for NO_3 and N_2O_5 during the DOMINO campaign: contrasts between marine, urban and continental air, Atmospheric Chemistry and Physics Discussions, 11, 17 825–17 877, 2011.

Dentener, F. J. and Crutzen, P. J.: Reaction of N_2O_5 on tropospheric aerosols: Impact on the global distributions of NO_x, O_3, and OH, Journal of Geophysical Research: Atmospheres, 98, 7149–7163, 1993.

Dimitroulopoulou, C. and Marsh, A.: Modelling studies of NO_3 nighttime chemistry and its effects on subsequent ozone formation, Atmospheric Environment, 31, 3041 – 3057, 1997.

EC: Environment Canada, 2011 air pollutant emission summaries and historical emission trends, 2012.

Fan, Q. and Dasgupta, P. K.: Continuous automated determination of atmospheric formaldehyde at the parts per trillion level, Analytical Chemistry, 66(4), 551–556, 1994.

Farman, J., Gardiner, B., and Shanklin, J.: Large losses of total ozone in Antarctica reveal seasonal ClO_x/NO_x interaction, Nature, 315, 207–210, 1985.

Ferm, M. et al.: Measurements of nitrous acid in an urban area, Atmospheric Environment (1967), 19, 985–992, 1985.

Finlayson-Pitts, B.: The tropospheric chemistry of sea salt: A molecular-level view of the chemistry of NaCl and NaBr, Chemical reviews, 103, 4801–4822, 2003a.

Finlayson-Pitts, B., Ezell, M., and Pitts, J.: Formation of chemically active chlorine compounds by reactions of atmospheric NaCl particles with gaseous N_2O_5 and $ClONO_2$, Nature, 337, 241–244, 1989.

Finlayson-Pitts, B., Wingen, L., Sumner, A., Syomin, D., and Ramazan, K.: The heterogeneous hydrolysis of NO_2 in laboratory systems and in outdoor and indoor atmospheres: An integrated mechanism, Physical Chemistry Chemical Physics, 5, 223–242, 2003b.

Finlayson-Pitts, B. J. and Pitts Jr, J. N.: Chemistry of the upper and lower atmosphere: Theory, experiments, and applications, Academic press, 1999.

Finley, B. D. and Saltzman, E. S.: Measurement of Cl_2 in coastal urban air, Geophysical Research Letters, 33, 2006.

George, C., Strekowski, R., Kleffmann, J., Stemmler, K., and Ammann, M.: Photoenhanced uptake of gaseous NO_2 on solid organic compounds: a photochemical source of HONO?, Faraday discussions, 130, 195–210, 2005.

Geyer, A. and Stutz, J.: Vertical profiles of NO_3, N_2O_5, O_3, and NO_x in the nocturnal boundary layer: 2. Model studies on the altitude dependence of composition and chemistry, Journal of Geophysical Research: Atmospheres, 109, 2004.

Geyer, A., Alicke, B., Konrad, S., Schmitz, T., Stutz, J., and Platt, U.: Chemistry and oxidation capacity of the nitrate radical in the continental boundary layer near Berlin, Journal of Geophysical Research: Atmospheres, 106, 8013–8025, 2001.

Godowitch, J., Ching, J., and Clarke, J.: Evolution of the nocturnal inversion layer at an urban and nonurban location., Journal of Applied Meteorology, 24, 791–805, 1985.

Goodman, A., Underwood, G., and Grassian, V.: Heterogeneous reaction of NO_2: Characterization of gas-phase and adsorbed products from the reaction, $2NO_{2(g)} + H_2O_{(a)} \rightarrow HONO_{(g)} + HNO_{3(a)}$ on hydrated silica particles, The Journal of Physical Chemistry A, 103, 7217–7223, 1999.

Grasshoff, K.: The hydrochemistry of landlocked basins and fjords, Chemical oceanography, 2, 455–597, 1975.

Haagen-Smit, A.: Chemistry and physiology of Los Angeles smog, Industrial & Engineering Chemistry, 44, 1342–1346, 1952.

Halla, J. D.: The application of MAX-DOAS to the measurement of tropospheric gases and aerosols in marine and continental environments, PhD Thesis, York University, Toronto, 2013.

Halla, J. D., T.Wagner, Beirle, S., Brook, J. R., Hayden, K. L., OBrien, J. M., Ng, A., Majonis, D., O.Wenig, M., and McLaren, R.: Determination of tropospheric vertical columns of NO_2 and aerosol optical properties in a rural setting using MAX-DOAS, Atmospheric Chemistry and Physics, 11, 12 475–12 498, 2011.

Hardy, J. T.: The sea surface microlayer: biology, chemistry and anthropogenic enrichment, Progress in Oceanography, 11, 307–328, 1982.

Harris, G. W., Carter, W. P., Winer, A. M., Pitts, J. N., Platt, U., and Perner, D.: Observations of nitrous acid in the Los Angeles atmosphere and implications for predictions of ozone-precursor relationships, Environmental Science & Technology, 16, 414–419, 1982.

Harrison, R. M. and Kitto, A.-M. N.: Evidence for a surface source of atmospheric nitrous acid, Atmospheric Environment, 28, 1089–1094, 1994.

Harrison, R. M., Peak, J. D., and Collins, G. M.: Tropospheric cycle of nitrous acid, Journal of Geophysical Research: Atmospheres, 101, 14 429–14 439, 1996.

He, Y., Zhou, X., Hou, J., Gao, H., and Bertman, S. B.: Importance of dew in controlling the air-surface exchange of HONO in rural forested environments, Geophysical research letters, 33, 2006.

Hedley, M. and Singleton, D.: Evaluation of an air quality simulation of the Lower Fraser Valley-I. Meteorology, Atmospheric Environment, 31, 1605 – 1615, 1997.

Heintz, F., Platt, U., Flentje, H., and Dubois, R.: Long-term observation of nitrate radicals at the Tor Station, Kap Arkona (Rgen), Journal of Geophysical Research: Atmospheres, 101, 22 891–22 910, 1996.

Hermans, C., Vandaele, A. C., Carleer, M., Fally, S., Colin, R., Jenouvrier, A., Coquart, B., and Mérienne, M.-F.: Absorption cross-sections of atmospheric constituents: NO_2, O_2, and H_2O, Environmental Science and Pollution Research, 6, 151–158, 1999.

Hönninger, G., Friedeburg, C. v., and Platt, U.: Multi axis differential optical absorption spectroscopy (MAX-DOAS), Atmospheric Chemistry and Physics, 4, 231–254, 2004.

IPCC: Summary for Policymakers, in Climate Change 2007: Impacts, Adaptation and Vulnerability. Contribution of Working Group II to the Fourth Assessment Report of the Intergovernmental Panel on Climate Change, Cambridge University Press, Cambridge, UK, pp. 1–73, 2007.

Jenkin, M. E., Cox, R. A., and Williams, D. J.: Laboratory studies of the kinetics of formation of nitrous acid from the thermal reaction of nitrogen dioxide and water vapour, Atmospheric Environment (1967), 22, 487 – 498, 1988.

Jiang, W., Singleton, D. L., Hedley, M., McLaren, R., Dann, T., and Wang, D.: Comparison of Organic Compound Compositions in the Emissions Inventory and Ambient Data for the Lower Fraser Valley, Journal of the Air & Waste Management Association, 47, 851–860, 1997.

Johnston, H.: Reduction of stratospheric ozone by nitrogen oxide catalysts from supersonic transport exhaust, Science, 173, 517–522, 1971.

Kasting, J. F.: Earth's early atmosphere, Science, 259, 920–926, 1993.

Kessler, C. and Platt, U.: Nitrous acid in polluted air massessources and formation pathways, in: Physico-Chemical Behaviour of Atmospheric Pollutants, pp. 412–422, Springer, 1984.

Kitto, A.-M. N. and Harrison, R. M.: Nitrous and nitric acid measurements at sites in South-East England, Atmospheric Environment. Part A. General Topics, 26, 235 – 241, 1992.

Kleffmann, J., Becker, K., and Wiesen, P.: Heterogeneous NO_2 conversion processes on acid surfaces: possible atmospheric implications, Atmospheric Environment, 32(16), 2721–2729, 1998.

Kleffmann, J., Becker, K. H., Lackhoff, M., and Wiesen, P.: Heterogeneous conversion of NO_2 on carbonaceous surfaces, Physical Chemistry Chemical Physics, 1, 5443–5450, 1999.

Kleffmann, J., Kurtenbach, R., Lörzer, J., Wiesen, P., Kalthoff, N., Vogel, B., and Vogel, H.: Measured and simulated vertical profiles of nitrous acid - Part I: Field measurements, Atmospheric Environment, 37, 2949 – 2955, 2003.

Knipping, E. M. and Dabdub, D.: Impact of chlorine emissions from sea-salt aerosol on coastal urban ozone, Environmental science & technology, 37, 275–284, 2003.

Kraus, S.: DOASIS: A Framework Design for DOAS, Ph.D. thesis, University of Mannheim, 2006.

Kurtenbach, R., Becker, K., Gomes, J., Kleffmann, J., Lrzer, J., Spittler, M., Wiesen, P., Ackermann, R., Geyer, A., and Platt, U.: Investigations of emissions and heterogeneous formation of HONO in a road traffic tunnel, Atmospheric Environment, 35, 3385 – 3394, 2001.

Lammel, G.: Formation of nitrous acid: parameterisation and comparison with observations, Max-Planck-Institut fuer Meteorologie, Hamburg (Germany), 1999.

Lammel, G. and Cape, J. N.: Nitrous acid and nitrite in the atmosphere, Chemical Society Reviews, 25, 361–369, 1996.

Lefohn, A. S., Husar, J. D., and Husar, R. B.: Estimating historical anthropogenic global sulfur emission patterns for the period 1850–1990, Atmospheric Environment, 33, 3435–3444, 1999.

Lenner, M.: Nitrogen dioxide in exhaust emissions from motor vehicles, Atmospheric Environment, 21, 37–43, 1987.

Levenberg, K.: A method for the solution of certain non-linear problems in least squares, Quarterly of Applied Mathematics, 2, 164–168, 1944.

Li, S., Matthews, J., and Sinha, A.: Atmospheric hydroxyl radical production from electronically excited NO_2 and H_2O, Science, 319, 1657–1660, 2008.

Li, X., Brauers, T., Haseler, R., Bohn, B., Fuchs, H., Hofzumahaus, A., Holland, F., Lou, S., Lu, K. D., , Rohrer, Hu, M., Zeng, L. M., Zhang, Y. H., Garland, R. M., Su, H., Nowak, A., Wiedensohler, A., Takegawa, N., Shao, M., and Wahner, A.: Exploring the atmospheric chemistry of nitrous acid (HONO) at a rural site in Southern China, Atmospheric Chemistry and Physics, 12, 1497–1513, 2012.

Liao, W., Case, A. T., Mastromarino, J., Tan, D., and Dibb, J. E.: Observations of HONO by laser-induced fluorescence at the South Pole during ANTCI 2003, Geophysical Research Letters, 33, L09 810, 2006.

Liggio, J., Li, S.-M., Vlasenko, A., Sjostedt, S., Chang, R., Shantz, N., Abbatt, J., Slowik, J. G., Bottenheim, J. W., Brickell, P. C., Stroud, C., and Leaitch, W. R.: Primary and secondary organic aerosols in urban air masses intercepted at a rural site, Journal of Geophysical Research: Atmospheres, 115, D21 305, 2010.

Likens, G. E., Wright, R. F., Galloway, J. N., and Butler, T. J.: Acid rain, Sci. Am.;(United States), 241, 1979.

Lovei, M.: Phasing out lead from gasoline: worldwide experiences and policy implications, vol. 397, World Bank Publications, 1998.

Lu, G., Brook, J. R., Alfarra, M. R., Anlauf, K., Leaitch, W. R., Sharma, S., Wang, D., Worsnop, D. R., and Phinney, L.: Identification and characterization of inland ship plumes over Vancouver, BC, Atmospheric Environment, 40, 2767 – 2782, 2006.

Martinez, M., Perner, D., Hackenthal, E.-M., Klzer, S., and Schütz, L.: NO_3 at Helgoland during the NORDEX campaign in October 1996, Journal of Geophysical Research: Atmospheres, 105, 22 685–22 695, 2000.

Matsumoto, J., Imagawa, K., Imai, H., Kosugi, N., Ideguchi, M., Kato, S., and Kajii, Y.: Nocturnal sink of NO_x via NO_3 and N_2O_5 in the outflow from a source area in Japan, Atmospheric Environment, 40, 6294 – 6302, 2006.

McCarthy, J. J.: Climate change 2001: impacts, adaptation, and vulnerability: contribution of Working Group II to the third assessment report of the Intergovernmental Panel on Climate Change, Cambridge University Press, 2001.

McLaren, R., Salmon, R. A., Liggio, J., Hayden, K. L., Anlauf, K. G., and Leaitch, W. R.: Nighttime chemistry at a rural site in the Lower Fraser Valley, Atmospheric Environment, 38, 5837 – 5848, 2004.

McLaren, R., Wojtal, P., Majonis, D., McCourt, J., Halla, J., and Brook, J.: NO_3 radical measurements in a polluted marine environment: links to ozone formation, Atmos. Chem. Phys, 10, 4187–4206, 2010.

McLaren, R., Wojtal, P., Halla, J. D., Mihele, C., and Brook, J. R.: A survey of NO_2:SO_2 emission ratios measured in marine vessel plumes in the Strait of Georgia, Atmospheric Environment, 46, 655–688, 2012.

Mertes, S. and Wahner, A.: Uptake of nitrogen dioxide and nitrous acid on aqueous surfaces, The Journal of Physical Chemistry, 99, 14 000–14 006, 1995.

Metro-Vancouver: Lower Fraser Valley Air Emissions Inventory and Forecast and Backcast, Burnaby, BC, Metro Vancouver Policy and Planning Department, Air Quality Policy and Management Division, 2007.

Middleton, J. T., Kendrick Jr, J., and Schwalm, H.: Injury to herbaceous plants by smog or air pollution, Plant Dis.;(United States), 34, 1950.

Miyazaki, K., Eskes, H. J., and Sudo, K.: Global NO_x emission estimates derived from an assimilation of OMI tropospheric NO_2 columns, Atmospheric Chemistry and Physics, 12, 2263–2288, 2012.

Molina, M. J. and Rowland, F. S.: Stratospheric sink for chlorofluoromethanes: chlorine atomc-atalysed destruction of ozone, Nature, 249, 811, 1974.

Munger, J. W., Jacob, D., Daube, B., Horowitz, L., Keene, W., and Heikes, B.: Formaldehyde, glyoxal, and methylglyoxal in air and cloudwater at a rural mountain site in central Virginia, Journal of Geophysical Research: Atmospheres (1984–2012), 100, 9325–9333, 1995.

Murfachaew, G., Varner, M., Phillips, L., Finlayson-Pitts, B., and Gerber, B.: Nitrogen dioxide at the air-water interface: trapping, adsorption, and salvation in the bulk and at the surface, Physical Chemistry Chemical Physics, 15, 204–212, 2013.

Naudet, J., Huguenin, D., Rigaud, P., and Cariolle, D.: Stratospheric observations of NO_3 and its experimental and theoretical distribution between 20 and 40 km, Planetary and Space Science, 29, 707–712, 1981.

Ndour, M., DAnna, B., George, C., Ka, O., Balkanski, Y., Kleffmann, J., Stemmler, K., and Ammann, M.: Photoenhanced uptake of NO_2 on mineral dust: Laboratory experiments and model simulations, Geophysical Research Letters, 35, L05 812, 2008.

Noxon, J.: Nitrogen dioxide in the stratosphere and troposphere measured by ground-based absorption spectroscopy, Science, 189, 547–549, 1975.

Noxon, J. F., Whipple, E., and Hyde, R.: Stratospheric NO_2: 1. Observational method and behavior at mid-latitude, Journal of Geophysical Research: Oceans (1978–2012), 84, 5047–5065, 1979.

Osthoff, H. D., Pilling, M. J., Ravishankara, A. R., and Brown, S. S.: Temperature dependence of the NO_3 absorption cross-section above 298 K and determination of the equilibrium constant for $NO_3 + NO_2 \leftrightarrow N_2O_5$ at atmospherically relevant conditions, Phys. Chem. Chem. Phys., 9, 5785–5793, 2007.

Osthoff, H. D., Roberts, J. M., Ravishankara, A., Williams, E. J., Lerner, B. M., Sommariva, R., Bates, T. S., Coffman, D., Quinn, P. K., Dibb, J. E., et al.: High levels of nitryl chloride in the polluted subtropical marine boundary layer, Nature Geoscience, 1, 324–328, 2008.

Park, J. Y. and Lee, Y. N.: Solubility and decomposition kinetics of nitrous acid in aqueous solution, The Journal of Physical Chemistry, 92, 6294–6302, 1988.

Park, S. S., Hong, S. B., Jung, Y. G., and Lee, J. H.: Measurements of PM_{10} aerosol and gas-phase nitrous acid during fall season in a semi-urban atmosphere, Atmospheric Environment, 38, 4265–4265, 2004.

Penner, J. E.: Aviation and the Global Atmosphere: Special Report of the IPCC Working Groups I and III in Collaboration with the Scientific Assessment Panel to the Montreal Protocol on Substances that Deplete the Ozone Layer, Cambridge University Press, 1999.

Perner, D. and Platt, U.: Detection of nitrous acid in the atmosphere by differential optical absorption, Geophysical Research Letters, 6, 917–920, 1979.

Perner, D., Ehhalt, D., Pätz, H., Platt, U., Röth, E., and Volz, A.: OH-Radicals in the lower troposphere, Geophysical Research Letters, 3, 466–468, 1976.

Pitts, J. N., Sanhueza, E., Atkinson, R., Carter, W. P., Winer, A. M., Harris, G. W., and Plum, C. N.: An investigation of the dark formation of nitrous acid in environmental chambers, International journal of chemical kinetics, 16, 919–939, 1984.

Plane, J. and Smith, N.: Atmospheric monitoring by differential optical absorption spectroscopy, Advances in Spectroscopy, 24, 223–223, 1995.

Platt, U.: The origin of nitrous and nitric acid in the atmosphere, Chemistry of multiphase atmospheric systems, pp. 299–319, 1986.

Platt, U. and Stutz, J.: Differential optical absorption spectroscopy, Springer, 2008.

Platt, U., Perner, D., and Pätz, H.: Simultaneous measurement of atmospheric CH_2O, O_3, and NO_2 by differential optical absorption, Journal of Geophysical Research: Oceans (1978–2012), 84, 6329–6335, 1979.

Platt, U., Perner, D., Harris, G., Winer, A., and Pitts, J.: Observations of nitrous acid in an urban atmosphere by differential optical absorption, Nature, 285, 312–314, 1980a.

Platt, U., Perner, D., Winer, A. M., Harris, G. W., and Pitts, J. N.: Detection of NO_3 in the polluted troposphere by differential optical absorption, Geophysical Research Letters, 7, 89–92, 1980b.

Qin, M., Xie, P. H., Liu, W. Q., Li, A., Dou, K., Fang, W., Liu, H. G., and Zhang, W. J.: Observation of atmospheric nitrous acid with DOAS in Beijing, China, Journal of Environmental Sciences, 18, 69–75, 2006.

Raff, J. D., Njegic, B., Chang, W. L., Gordon, M. S., Dabdub, D., Gerber, R. B., and Finlayson-Pitts, B. J.: Chlorine activation indoors and outdoors via surface-mediated reactions of nitrogen oxides with hydrogen chloride, Proceedings of the National Academy of Sciences, 106, 13 647–13 654, 2009.

Rappenglück, B., Ackermann, L., Alvarez, S., Golovko, J., Buhr, M., Field, R., Soltis, J., Montague, D. C., Hauze, B., Adamson, S., Risch, D., Wilkerson, G., Bush, D., Stoeckenius, T., and Keslar, C.: Strong wintertime ozone events in the Upper Green River Basin, Wyoming, Atmospheric Chemistry and Physics Discussions, 13, 17 953–18 005, 2013.

Sakamaki, F., Hatakeyama, S., and Akimoto, H.: Formation of nitrous acid and nitric oxide in the heterogeneous dark reaction of nitrogen dioxide and water vapor in a smog chamber, International journal of chemical kinetics, 15, 1013–1029, 1983.

Saliba, N. A., Yang, H., and Finlayson-Pitts, B. J.: Reaction of gaseous nitric oxide with nitric acid on silica surfaces in the presence of water at room temperature, The Journal of Physical Chemistry A, 105(45), 10,339–10,346, 2001.

Sander, S. P., Golden, D., Kurylo, M., Moortgat, G., Wine, P., Ravishankara, A., Kolb, C., Molina, M., Finlayson-Pitts, B., Huie, R., et al.: Chemical kinetics and photochemical data for use in atmospheric studies evaluation number 15, JPL Publication, 2006.

Sanders, R., Solomon, S., Carroll, M., and Schmeltekopf, A.: Ground-Based Measurements of O_3, NO_2, OClO and BrO during the 1987 Antarctic Ozone Depletion Event, in: Ozone in the Atmosphere, vol. 1, p. 65, 1989.

Schnell, R. C., Oltmans, S. J., Neely, R. R., Endres, M. S., Molenar, J. V., and White, A. B.: Rapid photochemical production of ozone at high concentrations in a rural site during winter, Nature Geoscience, 2, 120–122, 2009.

Schwander, H., Mayer, B., Ruggaber, A., Albold, A., Seckmeyer, G., and Koepke, P.: Method to determine snow albedo values in the ultraviolet for radiative transfer modeling, Applied Optics, 38(18), 3869–3875, 1999.

Seinfeld, J. H. and Pandis, S. N.: Atmospheric chemistry and physics: from air pollution to climate change, Wiley-Interscience, 2012.

Sharma, S., Vingarzan, R., Barrie, L. A., Norman, A., Sirois, A., Henry, M., and DiCenzo, C.: Concentrations of dimethyl sulfide in the Strait of Georgia and its impact on the atmospheric sulfur budget of the Canadian West Coast, Journal of Geophysical Research: Atmospheres, 108, 2003.

Simon, H., Kimura, Y., McGaughey, G., Allen, D. T., Brown, S. S., Osthoff, H. D., Roberts, J. M., Byun, D., and Lee, D.: Modeling the impact of $ClNO_2$ on ozone formation in the Houston area, Journal of Geophysical Research: Atmospheres, 114, 2009.

Simpson, W. R., Kinga, M. D., Beine, H. J., Honrath, R. E., and Zhou, X.: Radiation-transfer modeling of snow-pack photochemical processes during ALERT 2000, Atmospheric Environment, 36, 2663–2670, 2002.

Snyder, B. and Strawbridge, K.: Meteorological analysis of the Pacific 2001 air quality field study, Atmospheric Environment, 38, 5733 – 5743, 2004.

Solomon, S.: Stratospheric ozone depletion: A review of concepts and history, Reviews of Geophysics, 37, 275–316, 1999.

Song, C.: An overview of new approaches to deep desulfurization for ultra-clean gasoline, diesel fuel and jet fuel, Catalysis today, 86, 211–263, 2003.

Sorgel, M., Trebs, I., Seramovich, A., Moravek, A., Held, A., and Zetzsch, C.: Simultaneous HONO measurements in and above a forest canopy: inuence of turbulent exchange on mixing ratio differences, Atmospheric Chemistry and Physics, 11, 841–855, 2011a.

Sörgel, M., Regelin, E., Bozem, H., Diesch, J.-M., Drewnick, F., Fischer, H., Harder, H., Held, A., Hosaynali-Beygi, Z., Martinez, M., et al.: Quantification of the unknown HONO daytime source and its relation to NO_2, Atmospheric Chemistry and Physics, 11, 10 433–10 447, 2011b.

Spindler, G., Bruggemann, E., and Herrmann, H.: Nitrous acid concentration measurements and estimation of dry deposition over grassland in Eastern Germany, Proceedings of the EUROTRAC Symposium 1998, 2, 218–222, 1999.

Stemmler, K., Ammann, M., Donders, C., Kleffmann, J., and George, C.: Photosensitized reduction of nitrogen dioxide on humic acid as a source of nitrous acid, Nature Letters, 440(9), 195–198, 2006.

Stull, R. B.: An introduction to boundary layer meteorology, International Geophysics Series, Kluwer Academic Publishers, Dordrecht, The Netherlands, 1988.

Stutz, J. and Platt, U.: Improving long-path differential optical absorption spectroscopy with a quartz-fiber mode mixer, Applied optics, 36, 1105–1115, 1997.

Stutz, J., Alicke, B., and Neftel, A.: Nitrous acid formation in the urban atmosphere: Gradient measurements of NO_2 and HONO over grass in Milan, Italy, Journal of Geophysical Research: Atmospheres, 107, LOP 5–1–LOP 5–15, 2002.

Stutz, J., Alicke, B., Ackermann, R., Geyer, A., Wang, S., White, A. B., Williams, E. J., Spicer, C. W., and Fast, J. D.: Relative humidity dependence of HONO chemistry in urban areas, Journal of Geophysical Research: Atmospheres, 109, 2004.

Su, H., Cheng, Y. F., Cheng, P., Zhang, Y. H., Dong, S., Zeng, L. M., Wang, X., Slanina, J., Shao, M., and Wiedensohler, A.: Observation of nighttime nitrous acid (HONO) formation at a non-urban site during PRIDE-PRD2004 in China, Atmospheric Environment, 42, 6219–6232, 2008.

Su, H., Cheng, Y., Oswald, R., Behrendt, T., Trebs, I., Meixner, F. X., Andreae, M. O., Cheng, P., Zhang, Y., and Pschl, U.: Soil nitrite as a source of atmospheric HONO and OH radicals, Nature, 333, 1616–1618, 2011.

Svensson, R., Ljungstrm, E., and Lindqvist, O.: Kinetics of the reaction between nitrogen dioxide and water vapour, Atmospheric Environment, 21(7), 1529–1539, 1987.

Tang, I. N., Tridico, A. C., and Fung, K. H.: Thermodynamic and optical properties of sea salt aerosols, Journal of Geophysical Research: Atmospheres, 102, 23 269–23 275, 1997.

Taylor, K. C.: Automobile catalytic converters, Springer, 1984.

Thomas, K., Volz-Thomas, A., Mihelcic, D., Smit, H. G., and Kley, D.: On the exchange of NO_3 radicals with aqueous solutions: Solubility and sticking coefficient, Journal of atmospheric chemistry, 29, 17–43, 1998.

Valente, R. J., Imhoff, R. E., Tanner, R. L., Meagher, J. F., Daum, P. H., Hardesty, R. M., Banta, R. M., Alvarez, R. J., McNider, R. T., and Gillani, N. V.: Ozone production during an urban air stagnation episode over Nashville, Tennessee, Journal of Geophysical Research: Atmospheres, 103, D17, 22 555–22 568, 1998.

Vandaele, A., Hermans, C., Simon, P., Carleer, M., Colin, R., Fally, S., Mérienne, M., Jenouvrier, A., and Coquart, B.: Measurements of the NO_2 absorption cross-section from 42000cm^{-1} to 10000cm^{-1} (238-1000 nm) at 220 K and 294 K, Journal of Quantitative Spectroscopy and Radiative Transfer, 59, 171 – 184, 1998.

VandenBoer, T. C.: Atmospheric chemistry of trace nitrogeneous bases and acids: alkyl amines in the gas and particulate phases and nitrous acid interactions with the ground surface, PhD Thesis, University of Toronto, Toronto, 2012.

Veitel, H.: Vertical profiles of NO_2 and HONO in the planetary boundary layer, PhD Thesis, University of Heidelberg, Heidelberg, 2002.

Večeřa, Z., Mikuška, P., Smolík, J., Eleftheriadis, K., Bryant, C., Colbeck, I., and Lazaridis, M.: Shipboard Measurements of Nitrogen Dioxide, Nitrous Acid, Nitric Acid and Ozone in the Eastern Mediterranean Sea, Water, Air, & Soil Pollution: Focus, 8, 117–125, 2008.

Voigt, S., Orphal, J., and Burrows, J.: The temperature and pressure dependence of the absorption cross-sections of NO_2 in the 250-800 nm region measured by Fourier-transform spectroscopy, Journal of Photochemistry and Photobiology A: Chemistry, 149, 1 – 7, 2002.

Vrekoussis, M., Kanakidou, M., Mihalopoulos, N., Crutzen, P., Lelieveld, J., Perner, D., Berresheim, H., and Baboukas, E.: Role of the NO_3 radicals in oxidation processes in the eastern Mediterranean troposphere during the MINOS campaign, Atmos. Chem. Phys, 4, 169–182, 2004.

Vrekoussis, M., Mihalopoulos, N., Gerasopoulos, E., Kanakidou, M., Crutzen, P., and Lelieveld, J.: Two-years of NO_3 radical observations in the boundary layer over the Eastern Mediterranean, Atmos. Chem. Phys, 7, 315–327, 2007.

Wagner, T., Otten, C., Pfeilsticker, K., Pundt, I., and Platt, U.: DOAS moonlight observation of atmospheric NO_3 in the Arctic winter, Geophysical research letters, 27, 3441–3444, 2000.

Wagner, T., Chance, K., Frieß, U., Gil, M., Goutail, F., Hönninger, G., Johnston, P., Karlsen-Tørnkvist, K., Kostadinov, I., Leser, H., et al.: Correction of the Ring effect and I0-effect for DOAS observations of scattered sunlight, in: 1st DOAS Workshop, Heidelberg, Germany, pp. 13–14, 2001.

Walcek, C.: A theoretical estimate of O_3 and H_2O_2 dry deposition over the northeast United States, Atmospheric Environment (1967), 21, 2649–2659, 1987.

Wängberg, I., Etzkorn, T., Barnes, I., Platt, U., and Becker, K.: Absolute determination of the temperature behavior of the NO_2+ NO_3+(M) ↔ N_2O_5+(M) equilibrium, The Journal of Physical Chemistry A, 101, 9694–9698, 1997.

Wayne, L. G. and Yost, D. M.: Kinetics of the Rapid Gas Phase Reaction between NO, NO, and HO, The Journal of Chemical Physics, 19, 41, 1951.

Wayne, R., Barnes, I., Biggs, P., Burrows, J., Canosa-Mas, C., Hjorth, J., Bras, G. L., Moortgat, G., Perner, D., Poulet, G., Restelli, G., and Sidebottom, H.: The nitrate radical: Physics, chemistry, and the atmosphere, Atmospheric Environment. Part A. General Topics, 25, 1 – 203, 1991.

Wilkins, E.: Air pollution aspects of the London fog of December 1952, Quarterly Journal of the Royal Meteorological Society, 80, 267–271, 1954.

Winer, A. and Biermann, H.: Long pathlength differential optical absorption spectroscopy (DOAS) measurements of gaseous HONO, NO_2 and HCNO in the California South Coast Air Basin, Research on Chemical Intermediates, 20, 423–445, 1994.

Wojtal, P., Halla, J., and McLaren, R.: Pseudo steady states of HONO measured in the nocturnal marine boundary layer: a conceptual model for HONO formation on aqueous surfaces, Atmos. Chem. Phys, 11, 3243–3261, 2011.

Wong, K., Oh, H.-J., Lefer, B., Rappenglück, B., and Stutz, J.: Vertical profiles of nitrous acid in the nocturnal urban atmosphere of Houston, TX, Atmospheric Chemistry and Physics, 11, 3595–3609, 2011.

Wong, K., Tsai, C., Lefer, B., Haman, C., Grossberg, N., Brune, W., Ren, X., Luke, W., and Stutz, J.: Daytime HONO vertical gradients during SHARP 2009 in Houston, TX, Atmospheric Chemistry and Physics, 12, 635–652, 2012.

Wong, K. W. and Stutz, J.: Influence of nocturnal vertical stability on daytime chemistry: A one-dimensional model study, Atmospheric Environment, 44, 3753–3760, 2010.

Yabushita, A., Enami, S., Sakamoto, Y., Kawasaki, M., Hoffmann, M., and Colussi, A.: Anion-catalyzed dissolution of NO_2 on aqueous microdroplets, The Journal of Physical Chemistry A, 113, 4844–4848, 2009.

Young, C. J., Washenfelder, R. A., Roberts, J. M., Mielke, L. H., Osthoff, H. D., Tsai, C., Pikelnaya, O., Stutz, J., Veres, P. R., Cochran, A. K., et al.: Vertically resolved measurements of nighttime radical reservoirs in Los Angeles and their contribution to the urban radical budget, Environmental science & technology, 46, 10 965–10 973, 2012.

Yu, Y., Galle, B., Panday, A., Hodson, E., Prinn, R., and Wang, S.: Observations of high rates of NO_2-HONO conversion in the nocturnal atmospheric boundary layer in Kathmandu, Nepal, Atmos. Chem. Phys, 9, 6401–6415, 2009.

Zafiriou, O. C. and True, M. B.: Nitrite photolysis in seawater by sunlight, Marine Chemistry, 8, 9 – 32, 1979.

Zhang, Z., Liu, L., Wu, Z., Li, J., and Ding, H.: Physicochemical studies of the sea surface microlayer: I. Thickness of the sea surface microlayer and its experimental determination, Journal of Colloid and Interface Science, 204, 294–299, 1998.

Zhang, Z., Liu, C., and Liu, L.: Physicochemical Studies of the Sea-Surface Microlayer, Frontiers of Chemistry in China, 1, 1–14, 2006.

Zhang, Z.-B., Pan, M.-X., Wang, Z.-D., Zhao, W., Huang, H.-H., Wei, G.-F., Gao, H.-L., Peng, Y.-H., Zhu, Z.-H., and Li, L.: Biological and chemical studies of sea-surface microlayer (SML) in Daya Bay, China IIA., Chinese Journal of Oceanology and Limnology, 19, 272–281, 2001.

Zhou, X., Civerolo, K., Dai, H., Huang, G., Schwab, J., and Demerjian, K.: Summertime nitrous acid chemistry in the atmospheric boundary layer at a rural site in New York State, Journal of Geophysical Research: Atmospheres, 107, ACH 13–1–ACH 13–11, 2002.

Zhou, X., Zhang, N., TerAvest, M., Tang, D., Hou, J., Bertman, S., Alaghmand, M., Shepson, P. B., Carroll, M. A., Grifth, S., Dusanter, S., and Stevens, P. S.: Nitric acid photolysis on forest canopy surface as a source for tropospheric nitrous acid, Nature Geoscience, 4, 440–443, 2011.